Constitutive Modelling of the Skin Accounting for Chronological Ageing

Damien Pond

Dissertation Presented in Fulfilment for the Degree of Master of Science
in Mechanical Engineering University of Cape Town

Department of Mechanical Engineering
University of Cape Town
2016

Declaration

I know the meaning of plagiarism and declare that all the work in the document, save for that which is properly acknowledged, is my own. This thesis/dissertation has been submitted to the Turnitin module (or equivalent similarity and originality checking software) and I confirm that my supervisor has seen my report and any concerns revealed by such have been resolved with my supervisor.

Signed by candidate

Acknowledgements

I would like to express my deepest gratitude to my supervisor, Dr Andrew McBride, whose patience and expertise have made this all achievable.

I am thankful to Prof. George Limbert for his support and collaboration on the project, as well as for his generosity in hosting me on my visits to the University of Southampton. I am also thankful to Prof. Lester Davids for sharing his knowledge on what was a difficult task to unravel.

Much appreciation must be given to my family for the support they have provided throughout my studies.

Finally, sincere thanks are given to Prof. Daya Reddy and the Centre for Research in Computational and Applied Mechanics, the University of Cape Town and the Royal Society for the financial assistance that has made it possible to complete this Master's degree.

Abstract

The skin is the largest organ in the human body. It is the first line of contact with the outside world, being subject to a harsh array of physical loads and environmental factors. In addition to this, the skin performs numerous physiological tasks such as thermo-regualtion, vitamin D synthesis and neurotransduction. The skin, as with all biological tissue, is subject to chronological ageing, whereby there is a general breakdown of tissue function and a decline in mechanical properties. In addition to this, skin undergoes extrinsic forms of ageing through exposure to external factors such as ultraviolet radiation, air pollution and cigarette smoking.

Skin modelling is an area of biomechanics that, although medical in nature, has expanded into areas such as cosmetics, military, sports equipment and computer graphics. Skin can be approximated at the macroscopic continuum scale as an anisotropic, nearly-incompressible, viscoelastic and non-linear material whose material properties are highly dependent on the ageing process. Through the literature, several phenomenologically based models have been satisfactorily employed to capture the behaviour inherent to the skin, but despite the intrinsic link to age, to date no constitutive model for the UV-induced ageing/damage of skin has been developed that is both capable of capturing the material and structural effects, and is embedded in the rigorous framework of non-linear continuum mechanics. Such a mechanistic model is proposed here.

The macroscopic response of the skin is due to microscopic components such as collagen, elastin and the surrounding ground substance and the interaction between them. An overview on the structure of the skin helps motivate the form of the continuum model and identifies which aspects of the skin need to be captured in order to replicate the macroscopic response. Furthermore, the ageing process is explored and a firm understanding of the influence of ageing on the substructures is established. Over time, elastin levels tend to decrease which results in a loss of skin elasticity. Collagen levels drop with age, but tend to flatten out which results in an overall increase in skin stiffness and loss of anisotropy.

A worm-like chain constitutive model, arranged in an 8-chain configuration, is employed to capture the mechanical response of the skin. The use of such a micro-structurally-motivated model attempts to connect the underlying substructures (collagen, elastin and ground substance) present in the skin to the overall mechanical response. The constitutive model is implemented within a finite element scheme. Simple uniaxial tests are employed to ascertain the validity of the model, whereby skin samples are stretched to elicit the typical anisotropic locking response. A more complex loading condition is applied through bulge tests where a pressure is applied to an in vitro skin specimen. This more complex test is subsequently used to conduct a series of ageing numerical experiments to ascertain the response of the model to changes in material properties associated with ageing.

A modified model is then proposed to capture the ageing response of the skin. The key microscopic biophysical processes that underpin ageing are identified, approximated and adapted sufficiently to be of use in the macroscopic continuum model. Aspects of open-system thermodynamics and mixture theory are adapted to the context of ageing in order to capture a continuous ageing response.

Contents

1

Introduction

The human skin is an organ that is often taken for granted when considering general human biology. Consisting of 3 main layers, the epidermis, dermis and hypodermis, the skin is on average only a few millimetres thick, with a surface area of 1.5-2m^2, making it the largest organ of the human body. Considering the diverse range of loading that the skin experiences everyday, be it thermo-mechanical loads, chemical and bacterial agents and UV rays from the sun, the skin's interaction with the environment has been the subject of much experimental investigation ever since the defining study of Langer (1861).

One of the aspects of skin development that does receive much attention is its built in link with ones age. In a world where youth is one of the most sought after commodities, the fight against ageing has become a billion dollar industry whereby numerous corporations have flooded the market with creams and treatments aimed at maintaining the appearance of youth. Chronological ageing is one of lifes undeniable truths and generally accompanied by a gradual decline in the structure of skin tissue which leads to increased stiffness, loss of elasticity and the development of fine wrinkles. These effects are exacerbated by exposure to ultraviolet (UV) radiation from the sun in what is termed *photoageing*. UV rays have be shown to increase oxidative damage within the skin, and chronic UV exposure leads to photoageing, characterised by skin dyspigmentation, a leathery appearance and deep wrinkles.

In order to understand the macroscopic response of the skin and how chronological ageing and photoageing contribute, it is necessary to establish a firm understanding of the microstructure and the interactions at the microscopic scale. The skin is composed of multiple constituents, such as collagen and elastin, each of which contribute toward the mechanical properties of the skin. Furthermore, it is the alterations to these constituents and the shift in balance between synthesis and degradation that governs the effects elicited through the different ageing processes.

In the literature, multiple mechanical skin tests have been proposed, each of which aimed at characterising the skin response to loading. The variety of skin tests and devised methods through which to perform them as well as the natural skin variation that exists through factors such as race, gender, age and anatomical site has resulted in a broad characterisation of skin behaviour. In general the skin displays nonlinearity, anisotropy, viscoelasticity and incompressibility, but despite the overall mechanical response being consistent, the extent to which these characteristics are elicited is highly variable. This makes developing a representative skin model extremely difficult.

The goal of this project is to develop an experimentally based mathematical and computational model to study the complex interplay of the material and structural properties of the skin with incorporation of a chronological ageing process. The macroscopic response of the skin can be described using continuum mechanics where a wealth of sophisticated constitutive relations based on micro-mechanical features of skin have been developed. Through the use of a structurally-based constitutive relation the microstructural aspects of the skin are linked to the macroscopic behaviour.

To be valid, a model must capable of replicating the physical response observed experimentally. Through various frameworks such as the the finite element method (FEM), computational models are used to simulate chosen physical experiments. The FEM approach can accommodate a range of physically relevant loading scenarios and geometries which makes it highly applicable for the goal of characterising the response of skin to various loading conditions. Furthermore, the incorporation of chronological ageing presents a difficult task. Naturally, skin is a very complex living system where the effects of chronological ageing vary in nature and intensity within the body and within the inner structures of the skin. It is very difficult to understand how a change in one parameter affects the overall mechanical response of the skin. This is an area where a computational model can be of tremendous help by allowing one to isolate the contributions of each parameter of the system and study how their variations affect the system.

To date, very few constitutive models for the chronological ageing of skin have been developed that are capable of capturing the material and structural effects, and are embedded in the rigorous framework of non-linear continuum mechanics. A mechanistic constitutive model of ageing in the human skin, detailing the age-related accumulation of degradation on the mechanical and structural aspects of the skin, is proposed here. Due to the range of macroscopic loading conditions and the variability across the population, in addition to the micro-level effects, developing a predictive ageing model is not an easy task. Exploitation of the modelling framework requires its implementation in a non-linear finite element platform capable of accounting for multifield formulations. Special emphasis will be placed on capturing the mechanical and structural alterations occurring in the collagenous/elastin network of the dermis and the model will be parametrised to also include age-dependent material and structural properties. The constitutive formulation will be informed by data extracted from the literature.

The structure of the thesis is as follows. In Chapter 2 an overview of the structure of the skin is detailed. The various layers and the constituents therein are explored, with emphasis on the major constituents of the dermal layer, namely collagen, elastin and ground substance. The factors that play a role in the synthesis and degradation of these constituents is described in some depth. In Chapter 3 the synthetic and degradative processes of collagen and elastin are elaborated upon within the contexts of chronological ageing and photoageing. In Chapter 4, the relevant notation and concepts of nonlinear continuum mechanics are introduced in order to provide a framework within which to model the skin. In Chapter 5, the macroscopic mechanical response of the skin is reviewed from results in the literature. Furthermore, the macroscopic response is linked to the microstructure which motivates the form of the free energy function presented. In Chapter 6, the development of a numerical solution scheme is detailed. Aspects of the finite element method are introduced as well as the implementation of the pressure loading condition. In Chapter 7, chosen mechanical tests are detailed and simulated in order to validate the chosen constitutive model. The tension and bulge tests provide two very different loading conditions with which to compare the simulated results to experimental results. In Chapter 8, the mechanical response of the skin within the context of chronological ageing is discussed and reviewed in an attempt to inform associated modifications to the constitutive model. In Chapter 9, the microstructural changes that occur through ageing are linked to the constitutive model. Various parameters are motivated to be age-dependent and the proposed modifications discussed. These alterations are incorporated into the bulge test at various simulated ages. In Chapter 10, a discussion is presented with some concluding remarks. To conclude the thesis, an extension to the model is proposed with further application to photoageing.

The work presented here forms part of a larger project into the characterisation of skin under the influence of chronological and photoageing. Aspects of the numerical model developed in this thesis have been applied to understand the thermomechanical response of skin in McBride, Bargmann, Pond, and Limbert (2016).

2

The Structure of the Skin

Prior to proposing a continuum model for the skin, it is necessary to fully understand the structure of the skin. It is important that a firm grasp of the microstructural components that contribute towards the mechanics of the skin be established so as to guide the development of a structurally-based model of the skin. Within this chapter, such an understanding will presented. The primary components of the skin will be discussed, as well as the aspects that dictate their prevalence and structural integrity, such as synthesis and degradation. This overview will ultimately guide the form of a mechanical model with the intent to include ageing through remodelling of age-dependent constituents.

2.1 Layers of the Skin

The human skin is the largest organ of the human anatomy. With a surface area of approximately 1.5-2m^2, it comprises around a sixth of the body's total weight. It is comprised of distinct layers, providing protection for the underlying muscles, ligaments and bones. Being in direct contact with the environment, the skin plays a key role in immunity, water retention, insulation, sensation and vitamin synthesis. The skin is comprised of three primary layers, the epidermis, the dermis and the hypodermis as depicted by the histological section in Fig. 2.1.

2.1.1 Epidermis

The *epidermis* is the outer most layer. At approximately around 40-150μm thick, it is thus largely responsible for retaining water and pathogen protection, as opposed to structural support. The primary cells that make up the epidermis and their function are:

- Kerotinocytes are primarily responsible for keratin which provides the structural support for the epidermal layer, with around 95% of the epidermal volume taken up by kerotinocytes.
- Melanocytes synthesise melanin which provide UV protection.
- Langerhans cells process and introduce antigens.
- Merkels cells serve as sensory receptors.

These cells are created at the innermost part of the epidermis, referred to as the *stratum basale*. As the cells age, they move up through the epidermis, defining 5 distinct strata: *stratum basale, stratum spinosum, stratum granulosum, stratum lucidum, stratum corneum.* The cells make their way from the basale to corneum, where they are shed as dead cells.

The epidermis is also the site of skin pigmentation, whereby melanocytes are responsible for the synthesis of the pigment melanin. Melanocytes reside within the basal layer of the epidermis where, in normal skin, they are regularly dispersed. Within the melanocytes, specialised organelles called melanosomes produce melanin through a process known as *melanogenesis.*

The tanning response in skin is due to the up-regulation of melanin production after UV-exposure. Upon exposure, the pituatary-adrenal gland is stimulated to produce *melanocyte-stimulating hormone* (MSH). MSH activates melanocortin-1 receptors located in the cell membrane of melanocytes, which thus stimulates the production of black/brown melanin, or eumelanin. Also following UV-exposure there is stimulation of melanocyte dendrite growth. These dendrites allow for the transfer of melanosomes to surrounding kerotinocytes thus allowing for the distribution of melanin (Querleux, 2014).

2.1.2 Dermis

The layer beneath the epidermis is referred to as the *dermis*. At around 1-4mm thick, it is the thickest of the skin layers and consists of connective tissue which offers support and gives the skin its structure. The dermis is also the site for many features such as nerve endings, hair follicles, sweat glands and blood vessels. The dermis is subdivided into two areas:

- The *papillary region* is the area just below the epidermis, to which it is tightly connected by a basement membrane. It is named for the characteristic projections, called papillae, that extend toward the epidermis creating a corrugated surface that strengthens the bond with the epidermal layer. This region makes up around 10% of the dermal thickness and is primarily characterised by small-diameter collagen fibrils and oxytalan fibres, which are elastic-like fibres that extend perpendicular to the skin surface and attach to the junction between the dermal and epidermal layers (Choi, 2005).
- The *reticular region* lies below the papillary region and is much thicker in comparison. The connective tissue in this region provides strength and elasticity to the skin and is comprised of a dense network of large-diameter collagen fibres. Elastin fibres form a network around the collagen bundles.

The dermis is also composed of three major types of cells: *macrophages, adipocytes* and *fibroblasts*. Fibroblasts are responsible for the synthesis of collagen and elastin.

The wavy interface between the dermal and epidermal layers is referred to as the *dermal-epidermal junction* (DEJ). The DEJ provides an adhesion site between the layers, thus playing a role in the structural integrity of the skin.

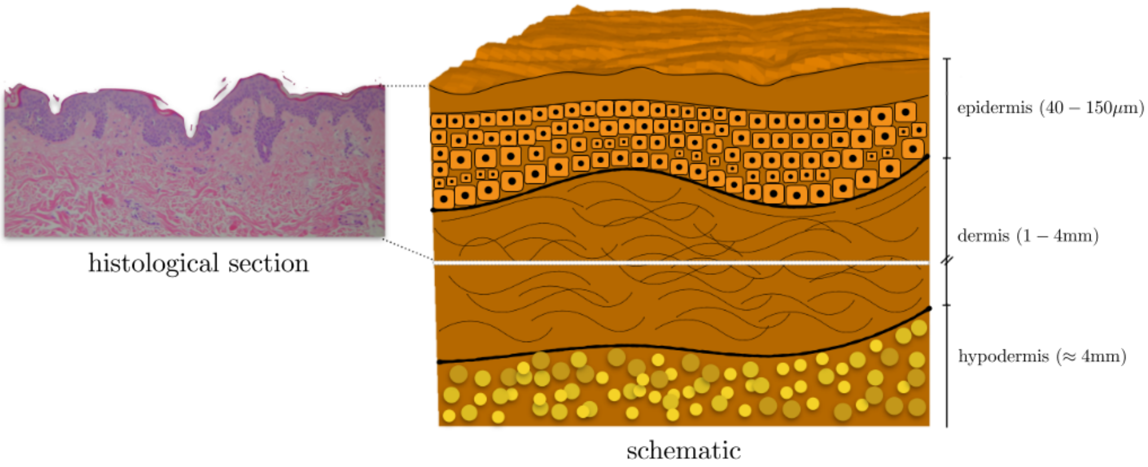

histological section

schematic

Fig. 2.1: Skin profile. Left: histological section (section courtesy of Maria Fabiola Leyva-Mendivil, University of Southampton). Right: schematic profile.

2.1.3 Hypodermis

Below the dermis, there is the *hypodermis.* Technically not part of the skin, the hypodermis connects the skin to the underlying muscle. Making up around 10% of the total body weight, the hypodermis consists predominately of fat, up to 50%, and consists of the same cells as the dermis, with a loose network of connective tissue. The hypodermal tissue is highly compliant, thus does not offer much in terms of structure.

2.2 Microstructural Constituents

The structural integrity of the skin is primarily restricted to the dermal layer where three micro-constituents are of concern: collagen, elastin and ground substance, as shown in Fig. 2.2.

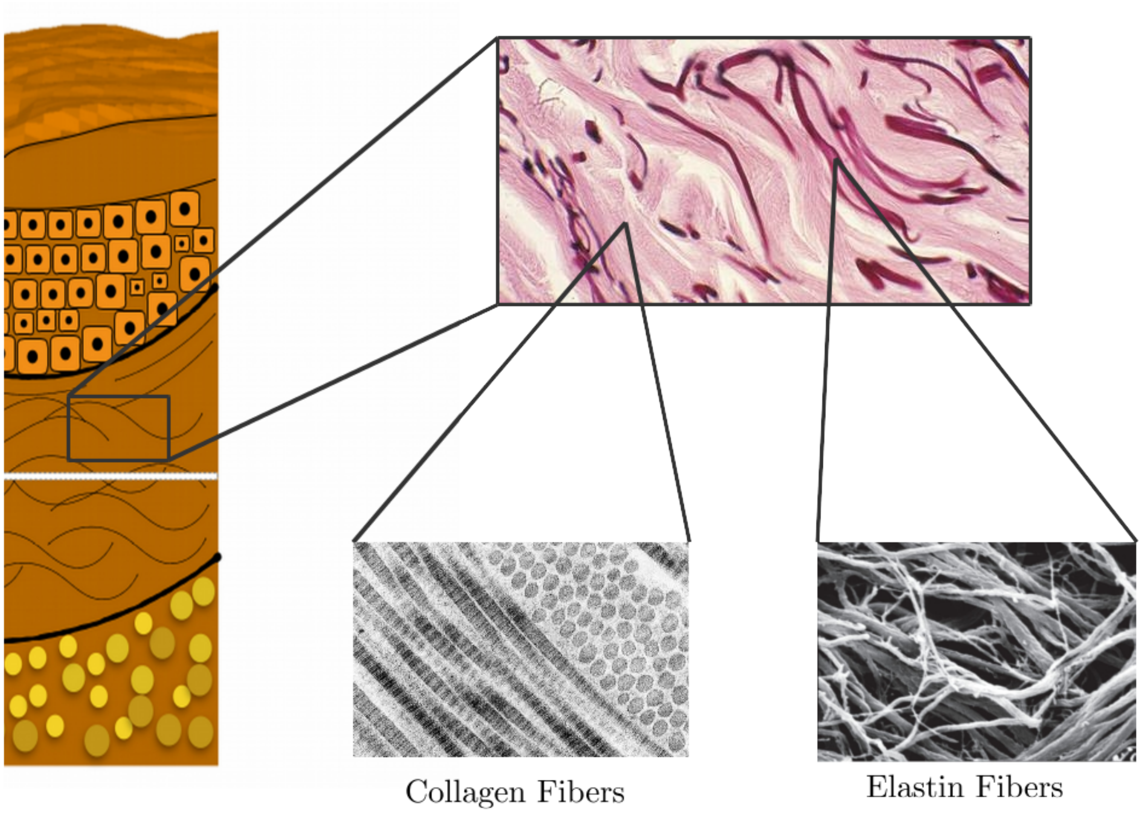

Fig. 2.2: Microscopic view of the dermis with arrangement of collagen and elastin, images found at Kulbitska (2015) and Green et al. (2014).

2.2.1 Collagen

Collagen makes up around 80% of the skin's total proteins. Due to this, it is reasonable to assume to make that the majority of the skin's tensile strength is due to collagen. Collagen is thus a key component in the quantification of the structural integrity in skin. The dermis, the volume of which is comprised of 18-30% collagen, primarily consists of type I (80 - 90%) and III (8 -12%) collagen, but types V and VII are also present, where type VII helps with the stabalisation of the DEJ. Type I collagen offers mechanical strength under tension, while type III allows for flexibility (Choi, 2005).

Triple helix molecules linked together through intramolecular crosslinks form collagen fibrils of around 50nm in diameter, as shown in Fig. 2.3. This parallel arrangement provides the tensile strength to the skin. Fibrils in turn arrange to form fibres of around 0.2micro to 12micro in diameter. Wavy collagen bundles form an irregular network with preferred directions parallel to the skin's surface.

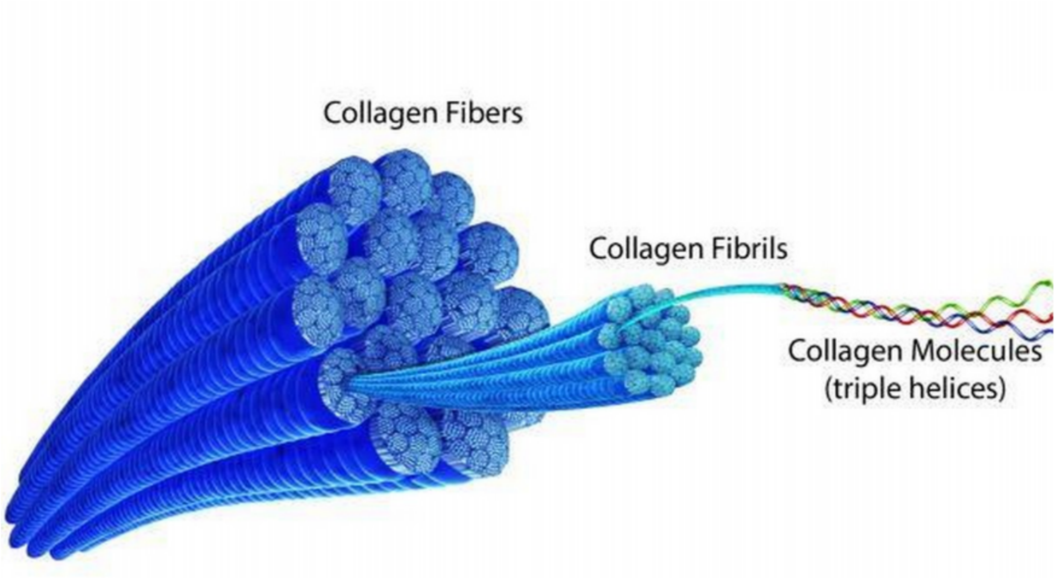

Fig. 2.3: The microscopic structure of a collagen fibre (Harbour MedTech, 2016).

The primary source of collagen in the skin is from fibroblasts, which are the most common cell in connective tissue. Fibroblasts are primarily responsible for the synthesis of procollagen, the precursor to collagen which forms mature collagen through the process of proteolysis.

The key regulators of collagen production (Helfrich et al., 2008; Varani, 2010) are:

- Transforming growth factor$-\beta$ (TGF-β) is a multi-functional cytokine that helps regulate many biological functions such as cellular growth, differentiation and extracellular matrix synthesis, such collagen and elastin constituents.
- Activator protein-1 (AP-1) is a transcription factor that inhibits collagen production and up-regulates matrix metalloproteinase (MMP) enzymes which act to break down extracellular matrix constituents.

Each of these play crucial roles in the proliferation of fibroblasts as well as regulating the synthesis and destruction of connective tissue components, such as collagen and elastin. Understanding the processes involved will thus lend to the understanding of the microscopic processes involved in collagen turnover.

2.2.2 Collagen Synthesis

All fibroblasts have the capacity to synthesise collagen. Thus one of the main contributing factors to collagen synthesis is the proliferative capacity of resident fibroblasts. Platelet derived growth factor (PDGF) is a substance that promotes fibroblast growth and proliferation, known as a mitogen. PDGF binds to cell surface receptors, which activates mitogen-activated protein (MAP) kinase signalling. The result of this is the signalling of downstream effectors, such as the activation of extracellular signal-related kinase (ERK), that promote cell growth and proliferation (Varani, 2010).

It has also been found that synthesis is promoted through mechanical tension applied to dermal fibroblasts. Fibroblasts attach to dermal collagen exert contractile force. Resistance to this generates the tension in the collagen. The rate of collagen synthesis is proportional to the level of mechanical tension (Fisher et al., 2002).

(TGF)-β has a minor role in the down-regulation of MMP production and in the up-regulation of TIMP. The primary role of TGF-β is in the synthesis of a wide range of matrix proteins. Of importance, TGF-β increases the synthesis of procollagen. TGF-β is produced within the extracellular matrix and when in active form is able to associate with TGF-β signalling receptors on the cell surface of dermal fibroblasts, referred to as type I and type II receptors, or TβRI and TβRII respectively. This results in the activation of downstream pathways, notably the Smad protein pathways. Smads 2,3 and 4 transduce the signals, while Smad 7 acts as an inhibitor. Together with interaction with MAP kinase signalling, collagen synthesis is promoted (Choi, 2005).

2.2.3 Collagen Degradation

The main contributor to the destruction of collagen is matrix metalloproteinase (MMP), a family of zinc-centred enzymes. Several MMPs are produced in healthy skin at low levels, with MMP-1 being the main contributor to the degradation of intact collagen. MMP-3 and MMP-9 are generally produced with MMP-1, but are only able to degrade collagen that has been cleaved by other MMPs, including MMP-1 (Rittié and Fisher, 2002; Varani, 2010).

MAP kinase activation is an important mediator of MMP production. Along with activation of the ERK pathway, signalling of the jun-N-terminal kinase (JNK) are necessary for the regulation of MMPs. Activation of the JNK pathway results in the production of c-jun, while ERK signalling results in the production of c-fos, both of which are necessary for the production of AP-1. AP-1 is key to the production of MMP.

Fortunately, there do exist proteins that allow for the inhibition and regulation of MMPs, known as tissue inhibitors of metalloproteinases (TIMPs). TIMP-1 is prominant in the skin. TIMPs are also regulated by downstream signalling through the MAP kinase.

2.2.4 Collagen Crosslinking

During the process of collagen assembly, there are various inter-molecular crosslinks that form to stabalise the helical supramolecular structures. These crosslinks play a crucial role in the overall tissue mechanics, matrix damage accumulation and tissue repair.

Crosslinks are broadly classified into enzymatic and non-enzymatic, where enzymatic crosslinking refers to the step in the development and repair of collagen connective tissues through the interaction with *lysyl oxidase*, an enzyme key to the regulation of crosslinking during maturation[1]. In tests where lysyl oxidase was restricted through dietary inhibition, it was found that overall crosslinking was reduced and there was a corresponding reduction in tendon strength. It is thus broadly accepted that crosslinking, through prevention of molecular slippage, contributes to the tensile strength of healthy, mature collagen fibrils (Snedeker and Gautieri, 2014).

2.2.5 Elastin

One of the major constituents of the dermal layer are the elastic fibres. Elastic fibres form between 2-4% of the dermal volume, offering resiliency and elasticity to the skin. The reticular dermis has a horizontal network of thick fibres that confer the majority of the mechanical strength. The papillary dermis is comprised of thinner fibres, as well as oxytalan fibres that run perpendicular to the surface

---

[1] Maturation refers to the end of puberty, generally around the end of the second decade of life.

and connects to the dermal-epidermal junction.

Elastic fibres consist of several components, but are primarily composed of elastin and microfibrils, called fibrilin. Tropoelastin is the soluble precursor to mature elastin and is secreted by human fibroblasts (Giro et al., 1985). Once secreted, the tropoelastin accumulates around the 10-12nm microfibrils, where it bonds to form functional, insoluable elastin (Choi, 2005; Mecham, 1991). Mature elastic fibres thus consist of a reinforcing outer layer of fibrillin with an inner core of packed, thin elastin (Choi, 2005; Uitto, 2008), where elastin takes up 90% of the total fibre volume (Sherratt, 2009). The process whereby elastic fibres are synthesised is highly regulated, with very little turnover following maturation.

Elastin on a microstructural level is highly crosslinked, which makes it icredibly stable and extremely insoluable. It has been found that under normal physiological conditions that elastin has a half life of up to the age of the organism. (Choi, 2005; Mecham, 1991; Mecham et al., 1997). When isolated, elastic fibres behave in a rubber-like manner, with the ability to rapidly stretch to over 3 times their length, with a equally rapid recoil (Mecham, 1991).

2.2.6 Elastin Synthesis

The majority of elastic fibre assembly occurs during early development. During gestation, an increase in elastin mRNA results in a rapid deposition of elastin throughout the developing body, but the exact secretory pathways involved in elastin synthesis are poorly understood. It has been found that TGF-β is able to stimulate elastin synthesis (Choi, 2005; Choi et al., 2009).

Choi (2005) states that once elastic fibre synthesis has ceased in early development, there is essentially no more turnover. Choi (2005) also reports that any loss of or injury to elastic tissue often does not result in the formation of new, orderly elastic fibre deposition. Various reports show the role of TGF-β in the up-regulation of elastin synthesis. Choi (2005) further mentions how in cases of Cutis laxa, a connective tissue disorder due to little or no presence of functional elastin, the patient can be treated with TGF-β to promote elastin synthesis.

In Choi et al. (2009), the effects of TGF-β on dermal fibroblasts were investigated, in vitro. It was found that tropoelastin mRNA increased 4 hours after TGF-β was administered. The levels remained elevated for 24 hours, reaching maximum at 8-12 hours.

There is also evidence that tumour necrosis factor (TNF)-α plays a role in the downregulation of fibrillin synthesis (Choi, 2005; Kossodo et al., 2004).

2.2.7 Elastin Degradation

Elastin and elastic tissue in general is highly resistant to degradation by MMP's. Due to its crosslinked nature, healthy elastin is stable and highly insoluble. But this is not to say that it is not capable of incurring degradative damage through the action of MMP. MMP's capable of degrading mature, insoluble elastin are referred to as elastases. It has been shown that 8 MMP's are capable of degrading elastic fibres (Mecham et al., 1997; Sherratt, 2009). The pathways involved in the regulation of elastases are similar to those discussed before in Sec. 2.2.3.

Sherratt (2009) shows that elastase increase in response to fibrillin fragmentation, possibly allowing for a mechanism of sustained degradation, although Sephel and Davidson (1986) suggests that tropoelastin production in normal cells is largely unaffected through degradative processes. As with collagen, TIMP is also capable of inhibiting the action of such elastase degradation.

2.2.8 Ground Substance

Proteoglycans (PGs) and glycosaminoglycans (GAGs) collectively form what is referred to as the *ground substance*. The ground substance surrounds the elastic and collagenous fibres and is responsible for the water retention within the dermal layer. Although not structurally important, as the ground substance makes up between 70-90% of the skins volume, it contributes significantly to the compressibility characteristics of the dermal layer. Bailey (2001) reports that such PGs do not show any distinguishable age-related changes. The only major changes are those that refer to the changes in water content, thus hydration may be the only factor to consider.

3

Ageing of the Human Skin: A Microscopic Perspective

In the previous chapter, the structure of the skin was discussed. Furthermore, the aspects which contribute to the synthesis and degradation, i.e. the turnover, of the primary micro-constituents were detailed. Often within the context of biological tissue, change in structure and composition occurs through some stimulus that perturbs the natural equilibrium of the tissue. Examples can be seen in bone and arterial tissue where a stimulus in the form of a modified stress state drives adjustment to the turnover rates of various constituents.

In this chapter, the micro-constituent processes discussed in Chapter 2 are elaborated upon within the contexts of chronological- and UV-ageing. This is done in an attempt to establish a continuous means by which to “age” the skin, ideally through some driving stimulus. UV- and chronological ageing are discussed separately and their actions combined at the end of the chapter through a proposed outline for an ageing model.

3.1 UV-Exposure

Ultraviolet radiation (UVR) enters the Earth’s atmosphere from the sun and thus is something people are exposed to on a day to day basis. There are three forms of UVR:

- UVA radiation has a wavelength of between 320-400 nm and is able to penetrate down to the dermal layer of the skin. As discussed, the dermal layer is responsible for skin strength through a network of collagen and elastin fibres. UVA thus leads to alterations in the structure of these networks, changing the molecular structure and density.
- UVB radiation has a wavelength of between 280-320 nm and is mainly absorbed in the epidermal layer. This exposure severely damages the mechanical properties of the upper layers of the skin, resulting in physical damage such as inflammation and possible scarring.
- UVC radiation has a wavelength of between 200-290 nm. At this wavelength, UVC would be highly damaging to human skin. Fortunately it is fully absorbed by the ozone layer.

3.1.1 UV-Exposure and Photoageing

Long term exposure to UV results in chronically damaged skin that replicates and exaggerates the effects shown by ageing, hence the term photoageing. Photoageing is associated with skin dyspigmentation, laxity, deep wrinkles and a leathery appearance. Chronically exposed skin suffers from inflammation, or heliodermatitis. Sun exposed skin has a greater epidermal thickness, specifically of the basal layer, and an accelerated flattening of the dermal-epidermal junction as when compared to sun protected skin (Rabe et al., 2006).

The following components of the skin undergo various changes as a result of UV exposure:

- Dermal fibroblasts are generally observed to be elongated and flattened after UV exposure. They are as numerous as in sunprotected skin, but show signs of hyperplasia (Fisher et al., 2002).
- There is an accelerated loss of type I and III collagen in sun exposed skin as compared to sun protected skin. Collagen fibrils are also disorganised.
- Type VII collagen is also severely reduced, which contributes to the destabilisation of the dermal-epidermal junction (Choi, 2005).
- Elastin content is increased in sun exposed skin (Jenkins, 2002; Rabe et al., 2006). This UV-induced elastin seems to take up the space previously occupied by collagen and suffers from solar elastosis, whereby it appears inflamed and structurally disorganised.

3.1.2 Photoageing and Collagen

The net decrease in collagen is the result of increased collagen degradation accompanied by the loss of the ability to synthesis new collagen. These factors and processes are now discussed and summarised in Fig. 3.1.

Increased Collagen Degradation

Around 50% of UV damage is due to direct cellular injury, whereby UV activates cell surface cytokine and growth factor receptors that result in downstream MAP signalling. The rest of the damage occurs through the formation of radicals. When skin absorbs UV, it has been shown to increase production of reactive oxygen species (ROS) within 15 minutes of exposure. ROS has the ability to damage cell walls, lipid membranes, cellular mitochondria and DNA (Helfrich et al., 2008; Rittié and Fisher, 2002).

ROS generation is mainly through UVA exposure and is expressed primarily through superoxide anion, peroxide and singlet oxygen. The singlet oxygen leads to what is referred to as *common deletion* of mitochondrial DNA and is often taken as a sign of UV-damage. This common deletion in turn increases ROS sensitivity, thus increasing ROS production (Benedetto, 1998; Rabe et al., 2006).

The upregulation of ROS, is thought to amplify MAP signalling. This leads to increased activation of the pathways involved in AP-1 expression (Rittié and Fisher, 2002; Varani, 2010). ROS, in the form of hydrogen peroxide, has been shown to increase MMP-1 production (Fisher et al., 2002), as stimulated by AP-1. Transcription of MMP-1, 3 and 9 increases 8 hours after UV exposure. MMP-1 cleaves fibrillar collagen types I, II and III, which allows for further degradation through MMPs -3 and -9. There is evidence that ROS plays a role in the inactivation of tissue inhibitors of metalloproteases or TIMPS. This ultimately leads to an even greater increase in MMP expression.

It has been shown that even minimal UV-exposure, only a tenth of the amount necessary to cause sunburn, up-regulates MMP levels. In fact, just 5-15 minutes of midday UV-exposure every other day is enough to sustain elevated MMP levels (Rabe et al., 2006). This leads to increased degradation of intact collagen.

Reduced Collagen Synthesis

Post UV-exposure, there is a drop in the amount of procollagen in the skin within 24 hours of exposure. Choi (2005) and Choi et al. (2009) report an upregulation of TGF-β through ROS accumulation. Despite this it has been found that UV exposure causes cells to be less responsive to TGF-β with an increase in the inhibitory Smad 7 protein (Varani, 2010) and a downregulation of TGF-β cell receptors. Thus, the increase in TGF-β is countered by a loss of sensitivity to TGF-β. These factors have thus reduce type I procollagen expression.

Interestingly, there is evidence to suggest that fibroblasts in sundamaged skin do not lose their procollagen synthetic ability. In Griffiths et al. (1993), it was shown that collagen formation was 56% less in UV-damaged skin versus sunprotected skin, but it was also shown that the synthetic capabilities of the fibroblasts was not decreased. This was further shown by Bernstein et al. (1996) and in Varani et al. (2001), where the synthetic capabilities of fibroblasts from sundamaged skin and sunprotected skin were extracted and compared in vitro. The production rates of healthy procollagen were observed to be very similar.

Not only is collagen degraded through MMP exposure, there is increasing evidence to support the claim that degraded collagen itself down regulates collagen synthesis. Dermal fibroblasts when incubated in contact with MMP degraded collagen have decreased levels of type I procollagen synthesis(Rabe et al., 2006; Varani et al., 2001). As shown by Varani et al. (2001), collagen fragmentation is 3 to 4 times higher in photodamaged skin when compared to photoprotected skin. Thus, it is clear that although fibroblasts are still capable to synthesising normal amounts of procollagen, this is inhibited through contact with partially degraded collagen.

Dermal degradation is only part of the process that leads to more permanent, visible damage. The subsequent process of *dermal repair* following degradation is likely to be responsible for the majority of visible change. The repair process, much like wound healing, is not perfect and introduces defects that account for permanent changes. Termed *imperfect repair*, there are observed changes in the structure and organisation of dermal collagen and elastin fibre networks following repair. More visibly, this imperfect repair may account for the deeper wrinkles associated with photoageing (Jenkins, 2002).

3.1.3 Photoageing and Elastin

One of the hallmarks of photoageing is the accumulation of highly disorganised, amorphous elastic-like fibres. This deposition of what is termed elastotic tissue is characterised by the process of solar elastosis. This elastotic material is composed of all the same components of normal elastic fibres, but aggregated in a highly non-regular and disorganised fashion. It is also found that previously healthy elastin becomes fragmented post chronic UV exposure.

Bernstein et al. (1994) report an increase in elastin mRNA promotor activity post UV-exposure. There is further evidence that fibroblasts extracted from photoaged skin show increased levels of elastin and fibrillin mRNAs, as compared to fibroblasts extracted from sun protected skin of the same individuals. When tested directly, Bernstein et al. (1994) found that elastin promotor activity is elevated after a single UVB dose. These elevated levels were sustained for 72 hours, with a maximal 4-5 fold increase over controls at about 24 hours. It was further shown that higher UV doses elicit a higher response.

Kawaguchi et al. (1997) found that direct UV exposure had no effect of elastin mRNA, a finding that was backed up by Bernstein et al. (1996) and Imokawa and Ishida (2015). This finding shows that secondary effects of UV exposure are responsible for solar elastosis. Kawaguchi et al. (1997) show that ROS elicited a dose-dependent response in elastin mRNA promotion. Scharffetter-Kochanek et al. (2000) reports a similar link between ROS and increased elastin/tropoelastin deposition. There have also been reports to show that UV exposure increases the expression of TGF-β (Choi, 2005). In the same report, it was suggested that increased TGF-β results in increased ROS levels, while other studies (Choi et al., 2009; Ibbotson et al., 1999; Wang and Kochevar, 2005) report that ROS is the driving factor behind increased TGF-β. In the context of the model postulated in the present dissertation, it is more convenient to take ROS as the driving factor that elicits an upregulation in TGF-β.

An upregulation of TGF-β results in the upregulation of elastin synthesis. As mentioned previously, there is an inhibition of TGF-β receptor due to ROS that results in the downregulation of collagen. Choi et al. (2009) and Kucich et al. (2002) offer an explanation as to how TGF-β may operate on an alternate pathway to illicit an upregulation of elastin through TGF-β while collagen is downregulated.

The increase in elastin is the result of increased synthesis, but this new elastotic material is highly irregular. Kossodo et al. (2004) show that the increased ROS levels also result in an increase in elastase and TNF-α. Kossodo et al. (2004) thus postulate that, due to the fragmentation of healthy elastic tissue through MMP action, the decreased fibrillin through TNF-α action, and the rapid deposition of elastin leads to the accumulation of highly irregular, disorganised elastotic material. As mentioned, normal elastic fibres need a highly coordinated balance between fibrillin and elastin. This forced dysfunction thus results in the elastotic material characteristic of solar elastosis. Fig. 3.1 summarises the key factors that occur within the dermal layer through exposure to UV, primarily through processes that occur within the fibroblasts.

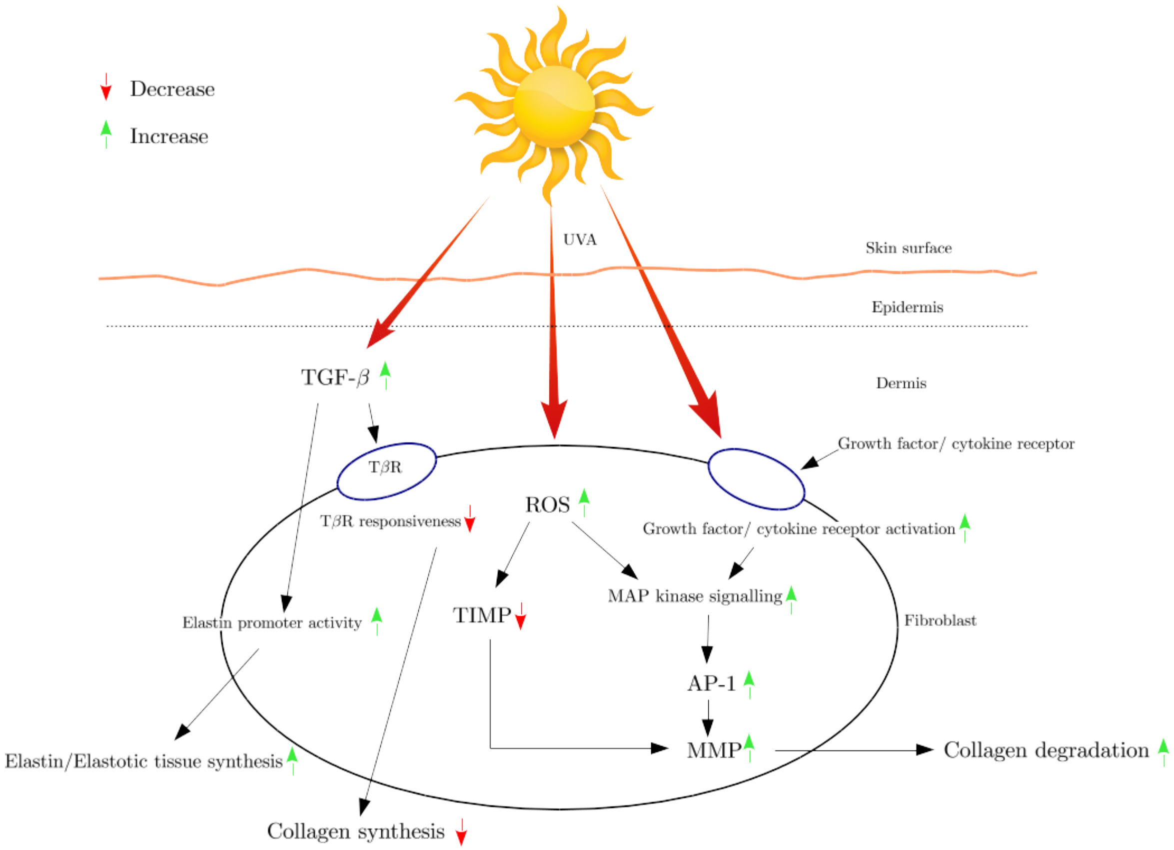

Fig. 3.1: The process of photoageing within a dermal fibroblast. Green arrows indicate an increase. Red arrows indicate a decrease.

3.2 Chronological Ageing

As with internal organs, the skin displays slow deterioration of tissue function over time. Although the stratum corneum remains relatively unchanged, the rest of the epidermis and dermis undergo larger changes. The dermal and epidermal layers thin over time with a flattening of the dermal-epidermal junction, whereby the finger-like papillae smooth out.

3.2.1 Chronological Ageing and Collagen

As skin ages, there is a reduction in the number and synthesis capabilities of fibroblasts, which correlates to a progressive reduction in the collagen content in the dermal layer (Chung et al., 2000; Jenkins, 2002). This reduction has been attributed to the result of fibroblast ageing, in which there is a reduction in the responsiveness to growth factor and thus a reduction in ERK signalling (Varani, 2010). Chung et al. (2000) reports that ERK protein levels in young and old skin were similar, but ERK activity and responsiveness was reduced by 45% in old skin. A further contributing factor to the reduction in collagen is the loss of mechanical tension in the skin. As shown by Varani et al. (2006), when skin of 18-29 year olds was compared to that of 80+ years old, collagen production decreased by around 75%. This was attributed to several factors. Firstly, the amount of healthy procollagen was decreased by 68% in aged skin when compared to young skin, which corresponds to a 30% decrease in procollagen production and a 35% reduction in the number of fibroblasts. Around 30% of the loss of collagen can be attributed to a reduction in mechanical tension. Fligiel et al. (2003) report a 30% reduction in total collagen in old (80+) versus young (18-29) skin. Qualitatively, collagen fibre bundles become thicker and more dense and take on a more random orientation with age. The fibres become thin and tangled while fibroblasts lose orientation and shape.

In aged skin, elevated levels of AP-1 exist when compared to young skin (Fisher et al., 2002; Helfrich et al., 2008; Rittié and Fisher, 2002). This has been attributed to increased JNK activation with age (Varani, 2010), with c-jun levels twice as high in old skin (Chung et al., 2000). Correspondingly, there is increased MMP activity in aged skin, with levels up to four times greater in older skin when compared to younger skin. In particular, MMP-1 and MMP-9 have been recorded at higher levels in aged skin. As expected, the amount of degraded collagen is greater in aged skin as opposed to younger skin. The fragmented collagen was seen to be qualitatively similar to that observed in sundamaged skin, but far less pervasive (Fligiel et al., 2003).

Rittié and Fisher (2002) report reduced levels of TGF-β responsiveness in aged skin. This is similar to that reported in UV damaged skin, but to a lesser extent. This reduction leads to impaired type I collagen production.

Enzyme driven crosslinking of collagen plateaus during maturation. With age though, there is an increase in non-enzymatic formation of crosslinking through oxidative reactions between glucose and collagen. Such reactions lead to the formation of *advanced glycationend-products* or AGEs. AGEs are able to bridge between the free amino groups of neighbouring proteins to form crosslinks. Despite little experimental evidence, it is largely accepted that AGEs are responsible for the increased crosslinking. There is also evidence that AGEs contribute towards ROS production (Snedeker and Gautieri, 2014).

3.2.2 Chronological Ageing and Elastin

The majority of elastic tissue synthesis and deposition occurs during late gestation (Choi, 2005), following which further turnover essentially ceases. Unlike collagen, under normal ageing conditions, elastin does not undergo any extensive remodelling. Damaged elastic tissue does not undergo any significant repair or replacement (Choi, 2005). As reported by Uitto (2008), elderly individuals show diminished capacity to replace elastic tissue damaged through ageing.

Due to the highly stable nature of elastic tissue, under the normal chronological ageing elastic tissue is highly resilient and is generally found to last up to the lifespan of the organism (Choi, 2005; Mecham, 1991). This means that despite the low synthetic capabilities, biosynthesis remains stable for the first 30-40 years of life (Uitto, 2008). Following this there is a gradual decrease in the amount of elastin content in the skin. Sephel and Davidson (1986) reports that decreased synthesis as well as increased degradation of elastin are likely to contribute to the overall loss. As explored for the case of collagen, reduced antioxidant defence with age results in the gradual increase in oxidative damage. A similar mechanism through gradual accumulation of elastase activity could account for the increased degradation (Imokawa and Ishida, 2015). Bailey (2001) mentions that the elastin synthetic capabilities of fibroblasts decreases with age, and Sephel and Davidson (1986) further report that after the 6th decade of life, there is a 70-85% decrease in tropoelastin synthesis. Fig. 3.2 details the processes that occur during chronological ageing, particularly the effects on the fibroblasts of the dermal layer.

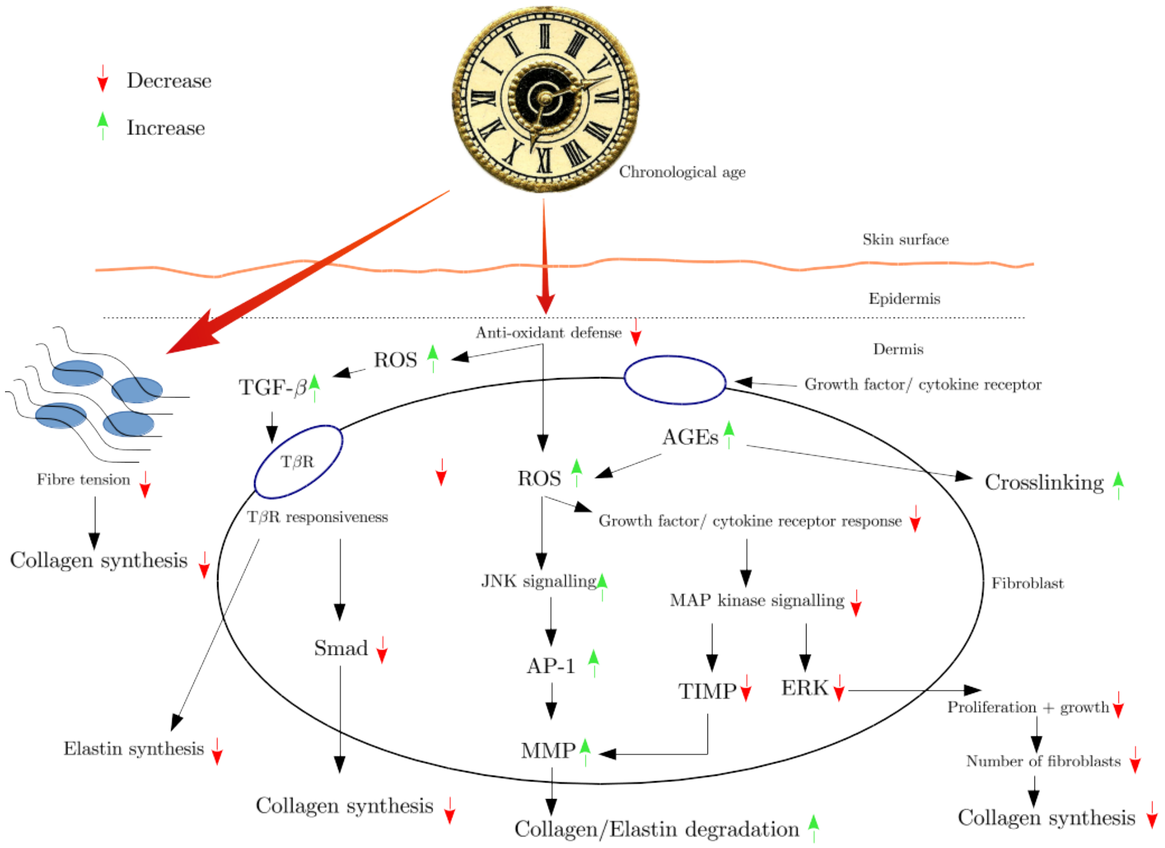

Fig. 3.2: The process of chronological ageing within a dermal fibroblast. Green arrows indicate an increase. Red arrows indicate a decrease.

3.2.3 Theories of Ageing

Although the changes that occur under chronological ageing are well documented, the processes involved are largely not understood. There are two main theories that attempt to understand the chronological ageing process.

Cellular Senescence

According to the theory of cellular senescence, the ageing process is a result of a combination of (Jenkins, 2002):

- Decreased proliferation ability.
- Decreased matrix synthesis.
- Increased expression of degrading enzymes of the collagenous matrix.

It has been repeatedly shown that keratinocytes, fibroblasts and melanocytes all display an age-associated decrease in proliferative ability and irreversible cell arrest, which is a process termed as *cellular senescence.*

Essentially, cellular senescence is a change in the state of a cell, and not a deterioration of cell capabilities with time. Cells undergo a change that reduces, or completely arrests, cell growth and proliferation. Cell division plays a role in the gradual loss of replicative ability. On each cell division, there is a shortening cellular telomeres. Telomeres are the end bits of DNA strands that have been shown to play a crucial part in ageing. This gradual change alters the physical expression of a cell's genotype, known as its phenotype (Jeyapalan and Sedivy, 2008).

As observed in senescent fibroblasts, there is a selective repression of genes involved in growth regulation. Essentially, this change results in the end of the replicative lifespan as the cell is no longer able to enter the first stages of mitosis.

In pre-senescent fibroblasts, the level of MMP-1 and MMP-3 have been observed to expressed at very low levels. Additionally TIMP levels have been shown to be high, further reducing MMP expression. The is reversed in senescent skin, where there is increased MMP and reduced TIMP expression. Coupled to this is the decreased rate of collagen synthesis in older skin, which further compounds the observed disorganisation and reduced presence of dermal collagen.

Free Radical Theory of Ageing

An alternate, and more popular view of ageing is that due to oxidative stress. Ageing results as an accumulation of oxidative damage due to a build up of ROS. This ROS production is a result of aerobic metabolism. There has been significant research that supports the role of ROS and cumulative oxidative damage as a major contributor to the ageing process (Fisher et al., 2002; Jenkins, 2002; López-Otín et al., 2013).

The main source of ROS in ageing is that through mitochrondrial oxidative energy generation. Over the course of ageing, damage accumulation due to ROS results in reduced antioxidant capacity through mitochrondrial deterioration which furthers ROS generation. This view of ageing is backed up by the observed higher levels of ROS in aged skin.

Over the last couple of years there have been several conflicting results in studies on the effects of ROS (Hekimi et al., 2011):

- Increased ROS may prolong the lifespan of yeast cells and *C.elegans* (a type of ringworm).
- Genetic manipulations in mice to increase mitochrondrial ROS does not accelerate ageing.
- Mice with increased antioxidant defence do not represent and increased lifespan.

There has also been research in the field of intracellular signalling that provides evidence that the role of ROS may in fact be as a survival response to physiological signals.

3.2.4 Theory of Ageing Proposed in this Study

In order to consolidate these theories with the damaging properties of ROS established in previous studies, the following hypothesis has been proposed in this work:
The primary effect of ROS is to trigger homoeostatic responses, such as cellular proliferation, in response to physiological stress. As chronological age advances, cellular damage increases while ROS levels increase as well in an attempt to maintain survival. Beyond a certain threshold, ROS eventually

starts to aggravate age-associated damage.

Whether the traditional theory of oxidative damage is adhered to or whether this new hypothesis is adopted, the cellular processes are the same. As a person ages, cells undergo a morphological change similar to that described in cellular senescence. Through the accumulation of ROS, the structural and functional capabilities degenerate, which only accelerates with advancing age. In skin, fibroblasts undergo this morphological change from mitotic cells to ones that are no longer able to undergo mitosis. This change is likely, as with senescence, to alter the phenotypical behaviour of the cell, thus negatively affecting type I procollagen production. Additionally, as mentioned, ROS has a direct impact on dermal collagen through the upregulation of AP-1 and MMPs.

There is further evidence to support reduced antioxidant activity within the skin. Although results have been conflicting, in general they show that there is a reduction of antioxidant enzymes with age. It has also been demonstrated that aged fibroblasts are far more susceptible to the accumulation of oxidised proteins following oxidative stress, whereas young fibroblasts were able to remove these proteins more effectively (Merker et al., 2000).

Although the theory of cellular senescence has its value, the free radical theory of ageing is far more relevant in terms of ageing in skin. By adopting this theory, a convenient and logical link is established between chronological and UV ageing. As shown in Fig. 3.3, increased ROS production is a common process in chronological and photoageing. This process can be modelled and if influence of the micro-processes on the macro-processes can be quantified this would constitute the basis for a continuum description of ageing.

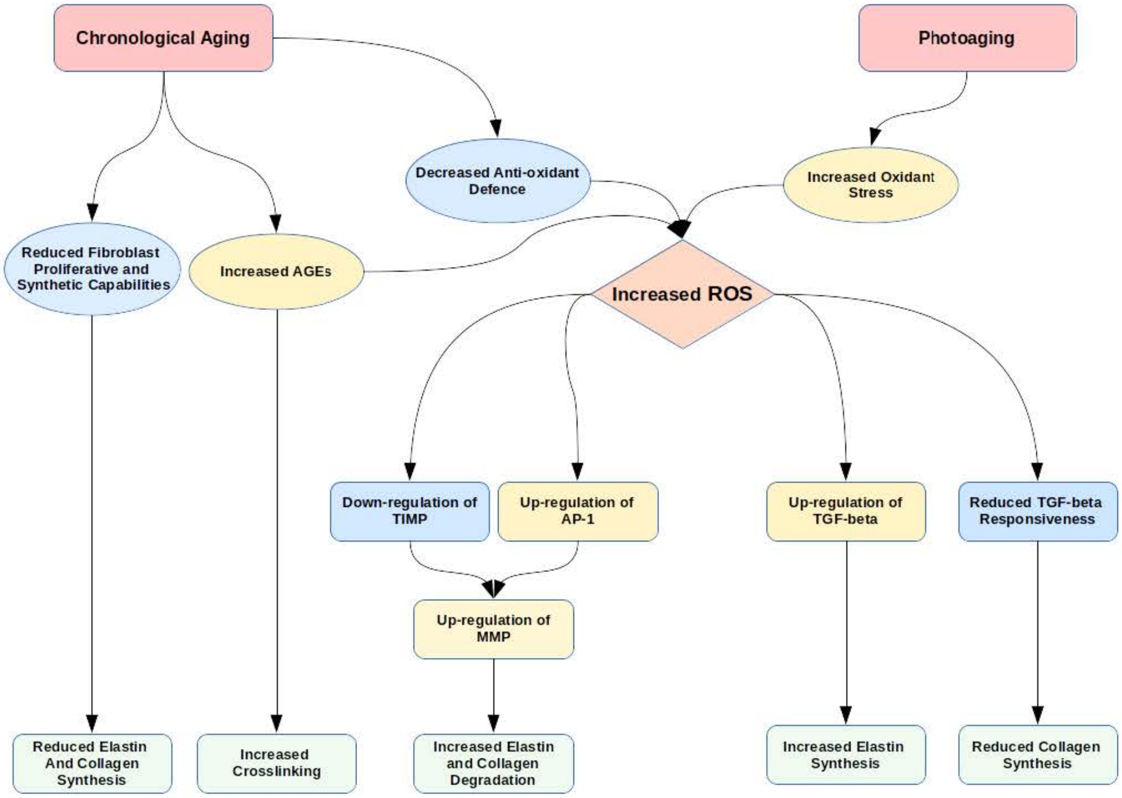

Fig. 3.3: Nanoscopic processes that lead to microscopic synthesis and degradation during chronological ageing and photoageing.

4

Continuum Description of Skin: A Macroscopic Perspective

In Chapters 2 and 3, the key constituents of the skin were identified and discussed. The primary sources of mechanical integrity within the skin are in the form of dense collagen and elastin networks, embedded in a ground substance. These constituents will be used to form a structurally-motivated continuum model with which to simulate the skin.

Before aspects discussed in the previous chapters can be incorporated into a continuum model, some basic and relevant aspects of nonlinear continuum mechanics need be presented and the notation introduced. The concepts and relations discussed in this chapter will serve as the framework within which the skin will be modelled. Continuum theory is well established with numerous texts oo the subject. Here, the relevant aspects of continuum theory are described in some detail. General concepts on constitutive modelling are then discussed before various models for skin are reviewed. For an extensive overview of continuum mechanics the reader is referred to Holzapfel (2000); Marsden et al. (1984).

4.1 Nonlinear Continuum Mechanics

For general engineering applications, viewing physical objects as discrete points on an atomistic scale is not adequate and does not provide a useful framework from which to analyse the kinematics of motion. Thus, a more macroscopic view is adopted that allows for a very powerful method through which to explain engineering phenomena. This method is known as *continuum mechanics*. Within a continuum approach, objects are characterised through continuous field quantities, such as density, temperature and displacement.

Continuum mechanics can be loosely divided into the following concepts :

- The kinematics of motion and deformation.
- The concept of stress.
- Fundamental balance principles that encapsulate the conservation of mass, momentum and energy.

These concepts hold true for all continuum bodies. In order to distinguish one material from another, *constitutive models* are employed to approximate the observed physical behaviour of a certain material under a motion of interest.

4.1.1 Vector Algebra

This section provides a general overview of the notation and algebra required for the skin models developed here. For a more detailed description of the mathematics of vectors and tensors, the reader is referred to many introductory texts on the subject of continuum mechanics.

Lower case letters will be used to describe scalar values, while bold face letters will be used to indicate a vector in $\mathbb{R}^3$, that is

$$a, b, c, ... \qquad \text{scalars}, \qquad\qquad \mathbf{a},\ \mathbf{b},\ \mathbf{c}... \qquad \text{vectors}.$$

It should be noted though that it will become necessary to deviate from this general notation when describing values in different configurations (see the section on the *Kinematics of Motion*), but what is meant will be obvious from the context.

A frame of reference of right-handed, rectangular coordinates with a fixed origin $\mathcal{O}$ will be considered. This reference frame is defined by a set of orthonormal basis vectors $\mathbf{e}_a$, $a = 1, 2, 3$, commonly referred to as a Cartesian basis, with the properties that

$$\mathbf{e}_1 \cdot \mathbf{e}_2 = \mathbf{e}_1 \cdot \mathbf{e}_3 = \mathbf{e}_2 \cdot \mathbf{e}_3 = 0, \qquad \mathbf{e}_1 \cdot \mathbf{e}_1 = \mathbf{e}_2 \cdot \mathbf{e}_2 = \mathbf{e}_3 \cdot \mathbf{e}_3 = 1. \tag{4.1}$$

Thus any vector $\mathbf{a}$ can be defined as a linear combination of these basis vectors by

$$\mathbf{a} = a_1\mathbf{e}_1 + a_2\mathbf{e}_2 + a_3\mathbf{e}_3 = \sum_{i=1}^{3} a_i\mathbf{e}_i,$$

where $a_i, i = 1, 2, 3$ are the real components of vector $\mathbf{a}$ in the directions $\mathbf{e}_1, \mathbf{e}_2, \mathbf{e}_3$. Employing the Einstein summation convention, the summation can be alternatively written as

$$\mathbf{a} = \sum_{i=1}^{3} a_i\mathbf{e}_i = a_i\mathbf{e}_i,$$

where summation over the repeated index is implied. This convention will be employed unless otherwise stated.

Eq. (4.1) can alternatively be expressed as

$$\mathbf{e}_i \cdot \mathbf{e}_j = \delta_{ij} = \begin{cases} 1, \ \text{if } i = j \\ 0 \text{ if } i \neq j \end{cases} \qquad ,$$

where δ_{ij} is the *Kronecker delta*. The Kronecker delta serves as a replacement operator in that it has the property

$$\delta_{ij}u_j = u_i. \tag{4.2}$$

With Eq. (4.2), the vector *dot product* can defined by:

$$\begin{aligned} \mathbf{u} \cdot \mathbf{v} &= u_i\mathbf{e}_i \cdot v_j\mathbf{e}_j \\ &= u_iv_j\mathbf{e}_i \cdot \mathbf{e}_j \\ &= u_iv_j\delta_{ij} \\ &= u_iv_i. \end{aligned}$$

Additionally, the *vector cross product* is defined in terms of the basis vectors by

$$\mathbf{e}_i \times \mathbf{e}_j = \varepsilon_{ijk}\mathbf{e}_k,$$

where the *permutation symbol* ε_{ijk} is defined by

$$\varepsilon_{ijk} = \begin{cases} 1, \text{for } \textbf{even} \text{ permutations of } ijk, \ \text{i.e. 123, 231, 312} \\ -1, \text{for } \textbf{odd} \text{ permutations of } ijk, \ \text{i.e. 132, 213, 321} \\ 0, \ \text{for repeated indices.} \end{cases}$$

Thus the cross product of two arbitrary vectors $\mathbf{u}$ and $\mathbf{v}$ is given in terms of the cross product by

$$\begin{aligned}\mathbf{u} \times \mathbf{v} &= u_i \mathbf{e}_i \times v_j \mathbf{e}_j \\ &= u_i v_j \mathbf{e}_i \times \mathbf{e}_j \\ &= u_i v_j \varepsilon_{ijk} \mathbf{e}_k.\end{aligned}$$

4.1.2 Tensor Algebra

Second-order tensors will be denoted by bold-faced upper-case letters and fourth-order tensors by upper-case blackboard letters, that is

$$\mathbf{A},\mathbf{B},\mathbf{C}... \quad \text{second-order tensor}, \qquad \mathbb{A}, \mathbb{B}, \mathbb{C}... \quad \text{fourth-order tensor}.$$

Second order tensors have the property of acting like a linear operator, in that if it acts on some vector $\mathbf{u}$, a vector $\mathbf{v}$ will be generated:

$$\mathbf{A}\mathbf{u} = \mathbf{v}. \tag{4.3}$$

As second order tensors are linear operators, the various properties of linear operators apply (see Holzapfel (2000) for further details).

The tensor product of two vectors results in a second order tensor. Generally referred to as the dyad, or *dyadic product*, the tensor product of vectors $\mathbf{u}$ and $\mathbf{v}$ is denoted by $\mathbf{u} \otimes \mathbf{v}$. This product linearly transforms a vector $\mathbf{w}$ into a vector through the relation:

$$(\mathbf{u} \otimes \mathbf{v})\mathbf{w} = (\mathbf{v} \cdot \mathbf{w})\mathbf{u}.$$

Expressed in terms of Cartesian coordinates, a tensor $\mathbf{A}$ may be expressed as a tensor product of the basis vectors, that is

$$\mathbf{A} = A_{ij} \mathbf{e}_i \otimes \mathbf{e}_j,$$

where A_{ij} are the components of the tensor $\mathbf{A}$.

With reference to Eq. (4.2):

$$A_{ij} \delta_{jk} = A_{ik}.$$

The linear transformation given by Eq. (4.3) can be better represented by

$$\begin{aligned}\mathbf{A}\mathbf{u} &= A_{ij} (\mathbf{e}_i \otimes \mathbf{e}_j) u_k \mathbf{e}_k \\ &= A_{ij} u_k (\mathbf{e}_j \cdot \mathbf{e}_k) \mathbf{e}_i \\ &= A_{ij} u_k \delta_{jk} \mathbf{e}_i \\ &= A_{ij} u_j \mathbf{e}_i \\ &= v_i \mathbf{e}_i \\ &= \mathbf{v},\end{aligned}$$

where $A_{ij} u_j = v_i$.

Consider a tensor $\mathbf{A}$, if there exist a set of nonzero normalised vectors $\{\mathbf{n}_i\}$ such that

$$\mathbf{A}\mathbf{n}_i = \lambda_i \mathbf{n}_i,$$

then $\mathbf{n}_i$ and λ_i are referred to as the eigenvectors and eigenvalues of tensor $\mathbf{A}$. Eigenvalues do not depend on the coordinate system and characterise the physical nature of a tensor.

The *tensor product* between two second-order tensors, $\mathbf{A}$ and $\mathbf{B}$ results in a second-order tensor, $\mathbf{C}$. Using the identity

$$(\mathbf{a} \otimes \mathbf{b})(\mathbf{c} \otimes \mathbf{d}) = (\mathbf{b} \cdot \mathbf{c})\mathbf{a} \otimes \mathbf{d},$$

the tensor product $\mathbf{C} = \mathbf{A} \otimes \mathbf{B}$ is given by

$$\begin{aligned}\mathbf{C} &= A_{ij}B_{mn}(\mathbf{e}_i \otimes \mathbf{e}_j)(\mathbf{e}_m \otimes \mathbf{e}_n)\\ &= A_{ij}B_{mn}\delta_{jm}(\mathbf{e}_i \otimes \mathbf{e}_n)\\ &= A_{ij}B_{jn}(\mathbf{e}_i \otimes \mathbf{e}_n),\end{aligned}$$

where $C_{in} = A_{ij}B_{jn}$.

The *double contraction* of two tensors, $\mathbf{A}$ and $\mathbf{B}$, denoted by $\mathbf{A} : \mathbf{B}$, produces a scalar. Using the identity

$$(\mathbf{a} \otimes \mathbf{b}) : (\mathbf{c} \otimes \mathbf{d}) = (\mathbf{a} \cdot \mathbf{c})(\mathbf{b} \cdot \mathbf{d}),$$

the scalar product **A:B** is given by

$$\begin{aligned}\mathbf{A{:}B} &= A_{ij}B_{mn}(\mathbf{e}_i \otimes \mathbf{e}_j) : (\mathbf{e}_m \otimes \mathbf{e}_n)\\ &= A_{ij}B_{mn}\delta_{im}\delta_{jn}\\ &= A_{ij}B_{ij}.\end{aligned}$$

A fourth order tensor $\mathbb{A}$ may be expressed in terms of the Cartesian basis vectors as:

$$\mathbb{A} = A_{ijkl}\mathbf{e}_i \otimes \mathbf{e}_j \otimes \mathbf{e}_k \otimes \mathbf{e}_l.$$

A useful relationship is given by

$$(\mathbf{a} \otimes \mathbf{b} \otimes \mathbf{c} \otimes \mathbf{d}) : (\mathbf{u} \otimes \mathbf{v}) = (\mathbf{c} \cdot \mathbf{u})(\mathbf{d} \cdot \mathbf{v})(\mathbf{a} \otimes \mathbf{b}).$$

With this relationship, the double contraction between a fourth-order tensor $\mathbb{A}$ and a second-order tensor $\mathbf{B}$ is defined by

$$\begin{aligned}\mathbb{A} : \mathbf{B} &= A_{ijkl}B_{ab}(\mathbf{e}_i \otimes \mathbf{e}_j \otimes \mathbf{e}_k \otimes \mathbf{e}_l) : (\mathbf{e}_a \otimes \mathbf{e}_b)\\ &= A_{ijkl}B_{ab}\delta_{ka}\delta_{lb}(\mathbf{e}_i \otimes \mathbf{e}_j)\\ &= A_{ijkl}B_{kl}(\mathbf{e}_i \otimes \mathbf{e}_j),\end{aligned}$$

where the result is a second-order tensor with components $A_{ijkl}B_{kl}$.

The scope of tensor and vector algebra is incredibly broad, but the aspects described above will allow for a general understanding of the continuum theory used in this dissertation.

4.1.3 Kinematics of Motion

Consider a continuum body defined in relation to the Cartesian reference frame. The reference (or material) configuration is defined as the placement of this body at time $t = 0$, with that region denoted as Ω_0. As the body deforms, this region takes on subsequent configurations. At a current time t, the body occupies an arbitrary region, Ω, referred to as the current (spatial) configuration.

A material point in the reference configuration is identified by the position vector $\mathbf{X} = X_A\mathbf{E}_A$. Similarly, a point in the current configuration is found through the position vector $\mathbf{x} = x_a\mathbf{e}_a$[1] (see Fig. 4.1). It should be noted that as a fixed basis is considered, $\mathbf{E}_A \equiv \mathbf{e}_a$.

It is assumed that there exists a mapping $\boldsymbol{\chi}$ such that each point $\mathbf{X} \in \Omega_0$ uniquely maps to a point $\mathbf{x} \in \Omega$ at time t, i.e.

$$\mathbf{x} = \boldsymbol{\chi}(\mathbf{X}, t) \qquad \forall \mathbf{X} \in \Omega_0.$$

The motion $\boldsymbol{\chi}$ is assumed to possess continuous derivatives both in space and time. The inverse map is given by:

---

[1] As demonstrated, values with upper case indices are those defined on the reference configuration, whereas lower case represents current configuration quantities.

$$\mathbf{X} = \boldsymbol{\chi}^{-1}(\mathbf{x}, t) \qquad \forall \mathbf{x} \in \Omega.$$

The deformation of the body can characterised by the the *deformation gradient* **F** defined by:

$$\mathbf{F}(\mathbf{X}, t) = \frac{\partial \boldsymbol{\chi}(\mathbf{X}, t)}{\partial \mathbf{X}} = \mathrm{Grad}\boldsymbol{\chi}(\mathbf{X}, t) = \mathrm{Grad}\mathbf{x}(\mathbf{X}, t).$$

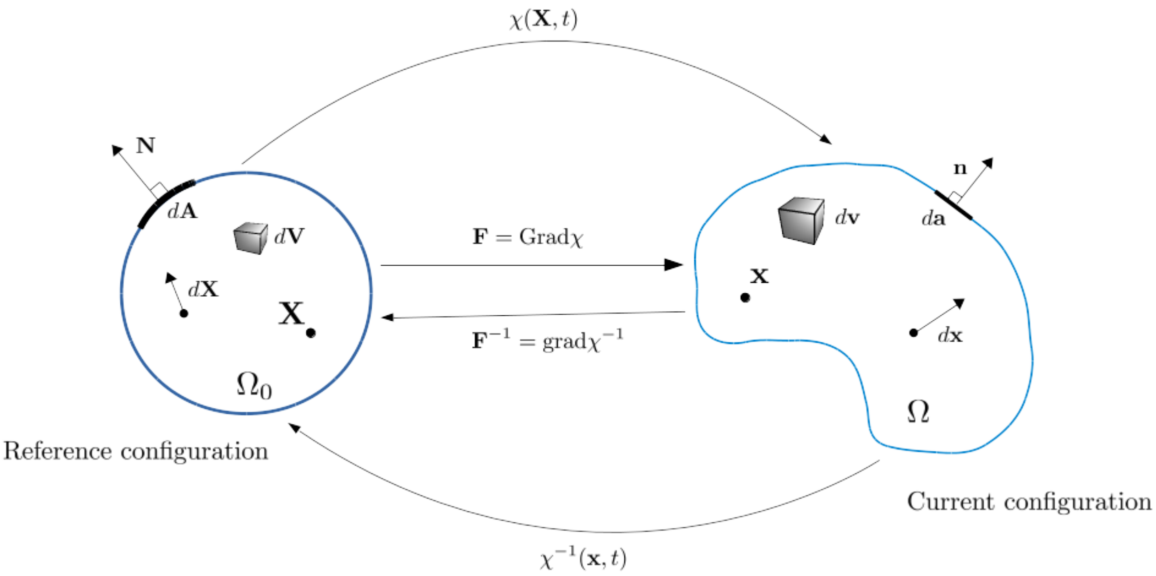

Fig. 4.1: The motion of the continuum body and the various kinematic descriptors used to describe the deformation.

The deformation gradient characterises the behaviour of the motion in the neighbourhood of a point. Accordingly:

$$\mathbf{F}^{-1}(\mathbf{x}, t) = \frac{\partial \boldsymbol{\chi}^{-1}(\mathbf{x}, t)}{\partial \mathbf{x}} = \mathrm{grad}\boldsymbol{\chi}^{-1}(\mathbf{x}, t) = \mathrm{grad}\mathbf{X}(\mathbf{x}, t),$$

defines the inverse deformation gradient[2]. The deformation gradient is a *two-point tensor*, meaning that it has placement in both the current and reference configurations.

The determinant of **F** is defined by

$$J(\mathbf{X}, t) = \det\mathbf{F}(\mathbf{X}, t),$$

where J is referred to as the Jacobian determinant or volume ratio. As **F** is invertible, $J \neq 0$. Given that J relates the reference and current volume elements (as will be shown shortly), negative volumes are mathematically and physically impossible, thus

$$J(\mathbf{X}, t) > 0.$$

Similarly:

---

[2] $\mathrm{Grad}(\cdot) := \frac{\partial(\cdot)}{\partial \mathbf{X}}$ is the gradient of field $(\cdot)$ with respect to the reference position **X**. Similarly, $\mathrm{grad}(\cdot) := \frac{\partial(\cdot)}{\partial \mathbf{x}}$ is the gradient of field $(\cdot)$ with respect to the current position **x**.

$$J^{-1}(\mathbf{X}, t) = \det\mathbf{F}^{-1}(\mathbf{x}, t) > 0.$$

$\mathbf{F}$ and J provide the following relations.

$\mathbf{F}$ relates line elements $d\mathbf{x}$ and $d\mathbf{X}$ within the current and reference configurations respectively by

$$d\mathbf{x} = \mathbf{F}d\mathbf{X}.$$

The cofactor[3] of $\mathbf{F} := \mathrm{cof}\mathbf{F} = J\mathbf{F}^{-T}$ relates infinitesimal surface vector elements $d\mathbf{a}$ and $d\mathbf{A}$ within the current and reference configurations respectively by

$$d\mathbf{a} = J\mathbf{F}^{-T}d\mathbf{A}. \tag{4.4}$$

Infinitesimal volume elements $d\mathbf{v}$ and $d\mathbf{V}$ within the current and reference configurations are related by

$$dv = JdV. \tag{4.5}$$

A further quantity of interest is the *right Cauchy-Green* tensor, $\mathbf{C}$ defined by

$$\mathbf{C} = \mathbf{F}^T\mathbf{F},$$

which provides an important stretch measure in the reference configuration. Introducing a set of mutually orthogonal, normalised eigenvectors $\{\mathbf{N}_i\}$ and the corresponding eigenvalues λ_i^2, $i = 1, 2, 3$, of the tensor $\mathbf{C}$ such that:

$$\mathbf{C}\mathbf{N}_i = \lambda_i^2\mathbf{N}_i \qquad i = 1, 2, 3, \tag{4.6}$$

then $\{\mathbf{N}_i\}$ is referred to as the *principle referential directions* and λ_i referred to as the *principle stretches.*

4.1.4 The Concept of Stress

Within the framework of continuum mechanics, stress is the physical quantity that results from the internal forces that neighbouring particles of a continuum body exert on one another.

Consider a body at time t occupying region Ω with boundary surface $\partial\Omega$, as depicted in Fig. 4.2. In order to conceptualise the internal forces, this body is separated and an "internal surface" is observed. Consider a point $\mathbf{x}$ on this surface, with surface unit normal $\mathbf{n}$. At $\mathbf{x}$, it is postulated that there exists a traction, $\mathbf{t}(\mathbf{x}, t, \mathbf{n})$, referred to as the *Cauchy traction* vector, acting as a force per current surface area, da. The values $\mathbf{x}$, $\mathbf{n}$ and da are inversely mapped to values $\mathbf{X}$, $\mathbf{N}$ and dA, respectively. At $\mathbf{X}$, a "pseudo" traction $\mathbf{T}(\mathbf{X}, t, \mathbf{N})$ is defined as the force per unit reference surface area, dA such that:

$$\mathbf{t}da = \mathbf{T}dA. \tag{4.7}$$

$\mathbf{T}$ is referred to as the *first Piola-Kirchhoff traction* vector. Note that $\mathbf{T}$ acts in the same direction as $\mathbf{t}$.

Cauchy's stress theorem asserts that there exist unique second-order tensor fields $\boldsymbol{\sigma}$ and $\mathbf{P}$ such that:

$$\mathbf{t}(\mathbf{x}, t, \mathbf{n}) = \boldsymbol{\sigma}(\mathbf{x}, t)\mathbf{n}, \tag{4.8}$$

$$\mathbf{T}(\mathbf{X}, t, \mathbf{N}) = \mathbf{P}(\mathbf{X}, t)\mathbf{N}, \tag{4.9}$$

where $\boldsymbol{\sigma}$ is referred to as the Cauchy stress tensor and $\mathbf{P}$ is referred to as the first Piola-Kirchhoff stress tensor.

---

[3] $(\cdot)^{-T} = ((\cdot)^{-1})^T = ((\cdot)^T)^{-1}$

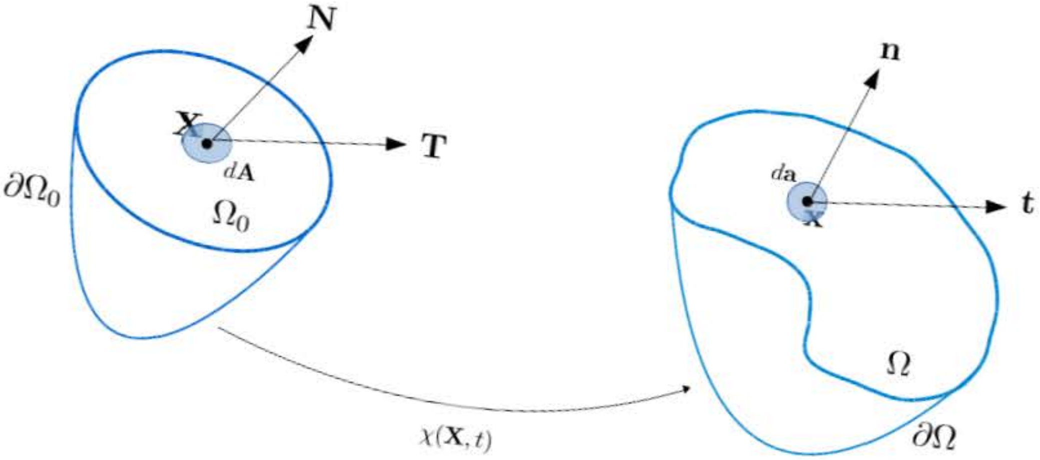

Fig. 4.2: Representation of traction vectors acting of infinitesimal surface elements.

Using equations Eq. (4.7) and Eq. (4.4) and where $d\mathbf{a} = da\mathbf{n}$ and $d\mathbf{A} = dA\mathbf{N}$, the following relation between $\boldsymbol{\sigma}$ and $\mathbf{P}$ can be derived

$$\mathbf{P} = J\boldsymbol{\sigma}\mathbf{F}^{-T}.$$

The Cauchy stress $\boldsymbol{\sigma}$ lies entirely in the current configuration, whereas $\mathbf{P}$ is a two-point tensor. Another useful stress measure that lies entirely in the reference configuration is the *second Piola-Kirchhoff* stress tensor, $\mathbf{S}$, defined by

$$\mathbf{S} = \mathbf{F}^{-1}\mathbf{P} = J\mathbf{F}^{-1}\boldsymbol{\sigma}\mathbf{F}^{-T}.$$

It can be shown through the balance of angular momentum that $\boldsymbol{\sigma} = \boldsymbol{\sigma}^T$. As a result of this, $\mathbf{S} = \mathbf{S}^T$ but $\mathbf{P} \neq \mathbf{P}^T$.

4.1.5 Balance Principles

Conservation of Mass:

Mass is a physical property defined as a measure of the amount of material contained in a body. Before the *conservation of mass* is discussed, it is important within the scope of this project to distinguish between *open* and *closed* systems, where a system is defined as a collection of matter in space. Exterior to the system is referred to as the *surroundings*, while the *boundary* separates the system from the surroundings.

Within a *closed system*, mass is a fixed quantity. No mass can move across the boundary, whereas energy is free to exchange with the surroundings. The thermodynamic state of a closed system is defined through its motion $\chi(\mathbf{X}, t)$ and its absolute temperature θ.

Within a *open system*, mass and energy are free to move across the boundary. The thermodynamic state of an open system is characterised through its motion $\chi(\mathbf{X}, t)$ its temperature θ, and the density, ρ.

For now, the balance equations will be detailed within the context of a closed system. The relevance of open system thermodynamics will become apparent later.

Consider a corresponding continuum body at time t distributed over an arbitrary region Ω, with boundary $\partial\Omega$, where the reference configuration and boundary are denoted Ω_0 and $\partial\Omega_0$, respectively. Under the assumption of a closed system, mass m is a *conserved quantity*, thus

$$m(\Omega_0) = m(\Omega) \qquad \forall t. \tag{4.10}$$

Eq. (4.10) is what is referred to as the *conservation of mass.*

Considering an infinitesimal mass element dm, the differential form of the above reads as:

$$dm(\mathbf{X}) = dm(\mathbf{x}, t). \tag{4.11}$$

The mass of the bodies Ω and Ω_0 can be characterised through the continuous scalar fields, $\rho(\mathbf{x}, t)$ and $\rho_0(\mathbf{X})$, respectively. ρ and ρ_0 are referred to as the spatial and reference *mass densities*, respectively. It can be noted that the reference mass density is time-independent, where as the spatial mass density has the ability to evolve with time.

The mass densities are defined such that:

$$dm(\mathbf{X}) = \rho_0(\mathbf{X})dV, \qquad \text{and} \qquad dm(\mathbf{x}, t) = \rho(\mathbf{x}, t)dv, \tag{4.12}$$

where dV and dv are infinitesimal volume elements in the reference and current configurations, respectively. Using the above and Eq. (4.11), the following relation is established:

$$\rho_0(\mathbf{X})dV = \rho(\mathbf{x}, t)dv. \tag{4.13}$$

Using Eq. (4.13) and Eq. (4.12) and integrating over the corresponding configuration, the global form of the conservation of mass is established as

$$m = \int_{\Omega_0} \rho_0 dV = \int_{\Omega} \rho dv = \text{constant}.$$

From this, and using relation (4.5), the following is established:

$$\begin{aligned} &\int_{\Omega_0} \rho_0(\mathbf{X})dV = \int_{\Omega} \rho(\mathbf{x}, t)dv \\ \Rightarrow &\int_{\Omega_0} [\rho_0(\mathbf{X}) - \rho(\chi(\mathbf{X}, t), t)J(\mathbf{X}, t)]dV = 0 \\ \Rightarrow &\rho_0(\mathbf{X}) = \rho(\chi(\mathbf{X}, t), t)J(\mathbf{X}, t) \qquad \forall \mathbf{X} \in \Omega_0. \end{aligned}$$

The identity $\rho_0 = J\rho$ is referred to as the *continuity mass equation.*

Momentum Balance Principles

The *linear momentum* $\mathbf{L}$ of the body is defined by

$$\mathbf{L}(t) = \int_{\Omega} \rho(\mathbf{x}, t)\mathbf{v}(\mathbf{x}, t)dv = \int_{\Omega_0} \rho_0(\mathbf{X})\mathbf{V}(\mathbf{X}, t)dV, \tag{4.14}$$

where $\mathbf{v}(\mathbf{x}, t)$ and $\mathbf{V}(\mathbf{X}, t)$ are the spatial and material velocity fields, respectively.

Taking the material time derivative of Eq. (4.14), the *balance of linear momentum* is postulated as:

$$\mathbf{F}^{\text{ext}}(t) = \dot{\mathbf{L}}(t) = \frac{D}{Dt}\int_{\Omega} \rho(\mathbf{x}, t)\mathbf{v}(\mathbf{x}, t)dv = \frac{D}{Dt}\int_{\Omega_0} \rho_0(\mathbf{X})\mathbf{V}(\mathbf{X}, t)dV,$$

where $\mathbf{F}^{\text{ext}}(t)$ is the *resultant force* due to applied tractions and body forces at time t.

Using the fact that Ω_0 is time-independent and the continuity of mass, it can be found that (dropping arguments):

$$\mathbf{F}^{\text{ext}} = \int_{\Omega} \rho \dot{\mathbf{v}} dv = \int_{\Omega_0} \rho_0 \dot{\mathbf{V}} dV.$$

In the current configuration, the resultant force can be defined as having additive contributions from forces acting on Ω. On the boundary $\partial\Omega$, Cauchy traction vectors $\mathbf{t} = \boldsymbol{\sigma}\mathbf{n}$, where $\mathbf{n}$ is the outward unit normal to an infinitesimal surface element *da* of $\partial\Omega$ contribute, while spatial *body force* vectors $\mathbf{b} = \mathbf{b}(\mathbf{x}, t)$ act per unit current volume of Ω. Thus,

$$\mathbf{F}^{\text{ext}}(t) := \int_{\partial\Omega} \mathbf{t} da + \int_{\Omega} \mathbf{b} dv = \frac{D}{Dt} \int_{\Omega} \rho \mathbf{v} dv.$$

Using Eq. (4.8) and the divergence theorem[4], the above equation can be used to establish the global form of *Cauchy's first equation of motion* as

$$\int_{\Omega} (\text{div}\boldsymbol{\sigma} + \mathbf{b} - \rho\dot{\mathbf{v}}) dv = \mathbf{0}. \tag{4.15}$$

As this equation holds for any volume, the local form of Eq. (4.15) is deduced as

$$\text{div}\boldsymbol{\sigma} + \mathbf{b} = \rho\dot{\mathbf{v}}, \tag{4.16}$$

for each point $\mathbf{x}$ and for all times t, where *Cauchy's equation of equilibrium* is established if the spatial acceleration $\dot{\mathbf{v}}$ is assumed to be $\mathbf{0}$.

Noting that $\dot{\mathbf{v}}(\mathbf{x}, t) = \dot{\mathbf{V}}(\mathbf{X}, t)$ and $\mathbf{B}(\mathbf{X}, t) := J(\mathbf{X}, t)\mathbf{b}(\mathbf{x}, t)$, and using the Piola identity[5], yields following

$$\text{Div}\mathbf{P} = J\text{div}\boldsymbol{\sigma},$$

and using identity Eq. (4.5) the material description of Eq. (4.15) can be established as

$$\int_{\Omega_0} (\text{Div}\mathbf{P} + \mathbf{B} - \rho_0\dot{\mathbf{V}}) dV = \mathbf{0},$$

with the local form of the balance of momentum in the material configuration given by

$$\text{Div}\mathbf{P} + \mathbf{B} = \rho_0\dot{\mathbf{V}}, \tag{4.17}$$

for each point $\mathbf{X}$ and for all times t.

Balance of Mechanical Energy

In a system where forms of energy from thermal, electric, magnetic and nuclear sources are neglected, only mechanical energy need be considered. As a consequence of the balance of linear momentum, the balance of mechanical energy states that the rate of change of the kinetic energy of a mechanical system plus the rate of internal mechanical work done by internal stresses is equal to the rate of external mechanical work done on the system by surface tractions and body forces.

Defined in the reference configuration, the balance of mechanical energy is simply stated as

$$\frac{D}{Dt} K(t) + P^{\text{int}}(t) = P^{\text{ext}}(t)$$

where

---

[4] $\int_{\partial\Omega} \mathbf{u} \cdot \mathbf{n} da = \int_{\Omega} \text{div}\mathbf{u} dv$

[5] $\text{Div}J\mathbf{F}^{-T} = \mathbf{0}$

$$
\begin{aligned}
K(t) &= \frac{1}{2}\int_{\Omega_0} \rho_0 \mathbf{V}^2 dV \\
P^{\text{int}} &= \int_{\Omega_0} \mathbf{P} : \dot{\mathbf{F}} dV \\
P^{\text{ext}} &= \int_{\Omega_0} \mathbf{B}\cdot\mathbf{V} dV + \int_{\partial\Omega_0} \mathbf{T}\cdot\mathbf{V} dA.
\end{aligned}
$$

Furthermore, the internal energy $e = e(\mathbf{X}, t)$ is introduced as the sum of all the microscopic forms of energy. Integrated over a reference region Ω_0, the internal energy possessed by a continuum body is denoted by $\varepsilon(t)$:

$$\varepsilon(t) = \int_{\Omega_0} e(\mathbf{X}, t) dV.$$

As only mechanical energy is considered, the rate of internal mechanical work done P^{int} is equal to the rate of internal energy ε, that is

$$P^{\text{int}}(t) = \frac{D}{Dt}\varepsilon(t).$$

Stated fully, the balance of mechanical energy in the reference configuration the form

$$\frac{D}{Dt}\int_{\Omega_0}\left(\frac{1}{2}\rho_0\mathbf{V}^2 + e\right) dV = \int_{\Omega_0}\mathbf{B}\cdot\mathbf{V} dV + \int_{\partial\Omega_0}\mathbf{T}\cdot\mathbf{V} dA.$$

Conservative System

Define the quantities $\varPi^{\text{ext}}$ and $\varPi^{\text{int}}$ as the *external potential energy* and the *internal potential energy* of the body, respectively. The *total potential energy* $\varPi$ can thus be defined as

$$\varPi(t) = \varPi^{\text{ext}}(t) + \varPi^{\text{int}}(t).$$

A mechanical system is thus known as *conservative* if P_{ext} and P^{int} are expressible as

$$
\begin{aligned}
P^{\text{ext}}(t) &= -\frac{D}{Dt}\varPi^{\text{ext}}(t) \\
P^{\text{int}}(t) &= \frac{D}{Dt}\varPi^{\text{int}}(t),
\end{aligned}
$$

where $\varPi^{\text{int}} = \int_{\Omega_0} \varPsi dV$.
$\varPsi$ is referred to as the *free energy* defined per unit reference volume, more of which will be dealt with in later sections.

4.1.6 Entropy Inequality Principle

Here the *second law of thermodynamics* is introduced, a principle responsible for the direction of the flow of energy within a thermodynamic process. Before the second law of thermodynamics is stated, the concept of *entropy* need be defined. Entropy is the degree of microscopic randomness and disorder representing the thermal energy not available for mechanical work. Denoted per unit reference volume as $\eta = \eta(\mathbf{X}, t)$ the total entropy possessed by a region Ω_0 is defined as

$$S(t) = \int_{\Omega_0} \eta(\mathbf{X}, t) dV.$$

Furthermore, the rate of entropy input, $\tilde{Q}$, into a region is governed the contribution from entropy sources $\tilde{R} = \tilde{R}(\mathbf{X}, t)$ per unit time and per unit reference volume as well as entropy fluxes $\mathbf{H} = \mathbf{H}(\mathbf{X}, t)$. Here, $\mathbf{H}$ is referred to as the *Piola-Kirchhoff entropy flux*, defined per unit reference surface area. Thus the total contribution is given by

$$\tilde{Q}(t) = \int_{\Omega_0} \tilde{R} dV - \int_{\partial\Omega_0} \mathbf{H} \cdot \mathbf{N} dS,$$

where $\mathbf{N}$ is the outward unit normal to $\partial\Omega_0$.

From these considerations, the *total production of entropy*, denoted Γ_{ent}, is defined as the difference between the rate on change of entropy and the entropy input. Furthermore, it is postulated that the total production of entropy is never negative, thus

$$\Gamma_{\text{ent}}(t) = \frac{D}{Dt} S(t) - \tilde{Q}(t) \geq 0. \tag{4.18}$$

This is what is known as the *second law of thermodynamics.*

Very often, it is assumed that the entropy flux $\mathbf{H}$ and the entropy source $\tilde{R}$ are proportional to the heat flux $\mathbf{Q}$ and heat source R, respectively through

$$\mathbf{H} = \frac{\mathbf{Q}}{\theta} \qquad \tilde{R} = \frac{R}{\theta},$$

where $\theta = \theta(\mathbf{X}, t) \geq 0$ refers to the absolute temperature.

With this, Eq. (4.18) can be written in full as

$$\Gamma_{\text{ent}}(t) = \frac{D}{Dt} \int_{\Omega_0} \eta dV + \int_{\Omega_0} \frac{R}{\theta} dV - \int_{\partial\Omega_0} \frac{\mathbf{Q}}{\theta} \cdot \mathbf{N} dS \geq 0,$$

which is known as the *Clausius-Duhem inequality*, presented here in the material description. Through the use of the divergence theorem and the fact that the reference volume V is arbitrary and independent of time, the local form of the Clausius-Duhem inequality can be derived

$$\theta\dot{\eta} - R + \text{Div}\mathbf{Q} - \frac{\mathbf{Q} \cdot \text{Grad}\theta}{\theta} \geq 0. \tag{4.19}$$

The last term is referred to as the *entropy production by conduction of heat*, where through experimental motivation, it is generally asserted that $\mathbf{Q} \propto -\text{Grad}\theta$, and that this term need always be positive:

$$-\frac{\mathbf{Q} \cdot \text{Grad}\theta}{\theta} \geq 0.$$

With this restriction, Eq. (4.19) leads to a stronger form of the second law of thermodynamics given by

$$D_{\text{int}} = \theta\dot{\eta} - R + \text{Div}\mathbf{Q} \geq 0. \tag{4.20}$$

This is referred to as the *Clausius-Planck inequality*, where D_{int} is the internal dissipation. In general, $D_{\text{int}} = 0$ for reversible processes. The inequality must hold for all irreversible processes.

From the first law of thermodynamics it can be shown (Holzapfel, 2000) that the rate of change of the internal energy density e can be given by

$$\dot{e} = \mathbf{P} : \dot{\mathbf{F}} - \text{Div}\mathbf{Q} + R.$$

Using this, Eq. (4.20) can be reformulated as

$$D_{\text{int}} = \mathbf{P} : \dot{\mathbf{F}} - \dot{e} + \theta\dot{\eta} \geq 0. \tag{4.21}$$

Within the context of elastic materials, it proves convenient to work with the free energy, Ψ as introduced for a conservative system. defined in terms of the Legendre transformation

$$\Psi = e - \theta\eta.$$

Taking the material derivative of Ψ, i.e. $\frac{D}{Dt}\Psi = \dot{\Psi} = \dot{e} - \dot{\theta}\eta - \theta\dot{\eta}$, Eq. (4.21) can be written in the form

$$D_{\text{int}} = \mathbf{P} : \dot{\mathbf{F}} - \dot{\Psi} + \dot{\theta}\eta \geq 0.$$

For the cases where the system is isothermal or purely mechanical, the above equation reduces to

$$D_{\text{int}} = \mathbf{P} : \dot{\mathbf{F}} - \dot{\Psi} \geq 0. \tag{4.22}$$

4.2 Constitutive Modelling

The fundamental equations stipulated previously hold for all branches of continuum mechanics. In order to distinguish one material from another, it is essential that additional *constitutive laws* be established.
Ideally, constitutive laws are designed to best approximate observed behaviour of a material of interest. Through these laws, the state of stress of a continuum body subject to various loading conditions can be determined. There are two main categories of constitutive models: phenomenological models and structural models.

Phenomenological models do not explicitly take into account the structural elements of the material (Limbert, 2014; Limbert et al., 2004; Steinmann et al., 2012). This is to say that the geometric and mechanical response of the material that is due to the underlying microstructure is largely ignored. Such models aim to capture the overall, macroscopic response of the material without consideration of the substructures that may be responsible. In the context of skin mechanics, phenomenological models attempt to capture the highly nonlinear, anisotropic response of the skin without consideration to underlying collagen and elastin networks. Due to this, phenomenologically-based models are generally a set of general mathematical relations with the advantage that it is generally always possible to find a set of parameters that will fit a set of experimental data. These models are frequently of polynomial form, and can thus be easily increased in order to fit more complex data. The drawback of such models is the disconnect between the parameters and their interpretation in relation to the physical response.

Structural models, alternatively referred to as micro-mechanical models, assume that the material is composed of various microstructural elements responsible for the overall mechanical response (such as collagen networks in the skin). Structural models also attempt to capture the interaction between various substructures. Such models often derive from arguments in statistical mechanics and require knowledge of the mechanical properties of each of the individual microscopic structures. Additionally, the interaction between and the arrangement of the constituents needs to be known in order to capture the full, macroscopic material response. This ultimately leads to the disadvantage of intrinsically higher computational costs. The advantage though, one that is seen as highly desirable over phenomenological models, is that the constitutive parameters are directly related to the mechanical and geometric properties of the micro-structure.

4.2.1 Hyperelastic Materials

Within the context of solid mechanics, a *hyperelastic material* is one for which a free energy function, $\varPsi$, defined per unit reference volume exists and acts as a potential for the stress. $\varPsi$ is alternatively referred to as the free energy function, or more simply the *free energy.*

For homogeneous materials, $\varPsi$ is purely a function of the deformation gradient $\mathbf{F}$, and acts as a potential for the Piola-Kirchhoff stress via

$$\mathbf{P} = \frac{\partial \varPsi}{\partial \mathbf{F}}. \tag{4.23}$$

That is, the stress state of a hyperelastic model is derived from a scalar-valued free energy. Alternatively, according to definition, a perfectly elastic material is one that for every admissible process the internal dissipation, $D_{\text{int}} = 0$. With the assumption of an isothermal system and $\dot{\varPsi}(\mathbf{F}) = \frac{\partial \varPsi}{\partial \mathbf{F}} : \dot{\mathbf{F}}$, Eq. (4.22) yields

$$D_{\text{int}} = \left(\mathbf{P} - \frac{\partial \varPsi}{\partial \mathbf{F}} \right) : \dot{\mathbf{F}} = 0.$$

Thus for arbitrary $\dot{\mathbf{F}}$, the $\left(\mathbf{P} - \frac{\partial \varPsi}{\partial \mathbf{F}}\right) = \mathbf{0}$. This gives expression Eq. (4.23).

In order to ensure that no stresses are elicited in the initial configuration, it is generally required that:

$$\Psi(\mathbf{I}) = 0.$$

Furthermore, based on observation, it is also require that:

$$\Psi(\mathbf{F}) \geq 0.$$

Ψ also needs to obey certain growth conditions:

$$\begin{aligned} \Psi(\mathbf{F}) &\longrightarrow \infty \text{ as } J \longrightarrow \infty, \\ \Psi(\mathbf{F}) &\longrightarrow \infty \text{ as } J \longrightarrow 0, \end{aligned}$$

where $J = \det\mathbf{F}$. This physically translates to saying that it requires infinite energy to expand a volume to infinity or compress a volume to a point. Refer to Marsden et al. (1984) for a more extensive review on the requirements on the free energy.

4.2.2 Isotropic Materials

A material that has the same constitutive response in all directions is referred to as *isotropic*. Alternatively put, consider some orthogonal tensor $\mathbf{Q}$ that imposes a rigid body translation and/or rotation on a body. Thus if it can be shown that for an arbitrary deformation gradient $\mathbf{F}$ that the material response under $\mathbf{F}$ is the same as the response if the motion is superimposed by $\mathbf{Q}$,

$$\Psi(\mathbf{F}) = \Psi(\mathbf{F}\mathbf{Q}^T),$$

then the material is said to be isotropic.

Under the assumption of hyperelasticity an invariant[6] free energy of the form:

$$\Psi = \Psi(\mathbf{F}) = \Psi(\mathbf{C}),$$

is proposed. It is often convenient to pose the free energy in terms of the principle invariants of its argument. In the context of isotropic materials, Ψ may be expressed by the set of strain invariants of the right Cauchy-Green tensor $\mathbf{C}$

$$\begin{aligned} I_1(\mathbf{C}) &= \mathrm{tr}(\mathbf{C}) = \mathbf{I} : \mathbf{C} \\ I_2(\mathbf{C}) &= \frac{1}{2}\left[\mathrm{tr}(\mathbf{C})^2 - \mathrm{tr}(\mathbf{C}^2)\right] \\ I_3(\mathbf{C}) &= \det(\mathbf{C}), \end{aligned}$$

where $\mathbf{I} = \delta_{ij}\mathbf{e}_i \otimes \mathbf{e}_j$ is the identity tensor.

Thus the free energy can be expressed as

$$\Psi = \Psi(I_1(\mathbf{C}), I_2(\mathbf{C}), I_3(\mathbf{C})). \tag{4.24}$$

This form provides a basis for deriving the necessary constitutive relations as follows

$$\mathbf{P} = \frac{\partial\Psi}{\partial\mathbf{F}} = \frac{\partial\Psi}{\partial\mathbf{C}}\frac{\partial\mathbf{C}}{\partial\mathbf{F}} = 2\mathbf{F}\frac{\partial\Psi}{\partial\mathbf{C}}, \tag{4.25}$$

where

$$\frac{\partial\Psi}{\partial\mathbf{C}} = \frac{\partial\Psi}{\partial I_1}\frac{\partial I_1}{\partial\mathbf{C}} + \frac{\partial\Psi}{\partial I_2}\frac{\partial I_2}{\partial\mathbf{C}} + \frac{\partial\Psi}{\partial I_3}\frac{\partial I_3}{\partial\mathbf{C}}. \tag{4.26}$$

---

[6] A detailed discussion on the invariance of Ψ can be found in Holzapfel (2000).

The derivatives of the invariants are given by

$$\begin{aligned} \frac{\partial I_1}{\partial \mathbf{C}} &= \mathbf{I} \\ \frac{\partial I_2}{\partial \mathbf{C}} &= I_1\mathbf{I} - \mathbf{C} \\ \frac{\partial I_3}{\partial \mathbf{C}} &= I_3\mathbf{C}^{-1}. \end{aligned} \tag{4.27}$$

4.2.3 Incompressible Hyperelasticity

Certain materials, particularly biological materials, undergo deformation without any noticeable volume change. For such materials, assuming incompressibility is often reasonable. For incompressible materials, the volume is constant throughout the motion and is characterised by the incompressibility constraint

$$\det\mathbf{F} = J = 1.$$

From this constraint, free energy functions for incompressible materials are given by

$$\Psi = \Psi(\mathbf{F}) - p(J-1),$$

The scalar-value p is known as a *Lagrange multiplier*, and has the interpretation of a hydrostatic pressure. From Eq. (4.23), the first Piola-Kirchhoff stress can be found as

$$\mathbf{P} = \frac{\partial \Psi}{\partial \mathbf{F}} - p\mathbf{F}^{-T}.$$

For the case of incompressible isotropy, expressing the free energy in terms of the invariants as in Eq. (4.37) is slightly modified. With the consideration of the incompressibility constraint, it follows that

$$I_3 = \det\mathbf{C} = 1.$$

Thus, only I_1 and I_2 need be considered. The free energy function for incompressible isotropic hyperelastic materials is accordingly given by

$$\Psi = \Psi(I_1(\mathbf{C}), I_2(\mathbf{C})) - \frac{1}{2}p(I_3 - 1). \tag{4.28}$$

With reference to Eq. (4.25) and Eq. (4.26) as well as the identities (4.27), $\mathbf{P}$ can be fully described by

$$\mathbf{P} = -\frac{p}{2}\mathbf{F}^{-T} + 2\mathbf{F}\left[\frac{\partial \Psi}{\partial I_1}\mathbf{I} + \frac{\partial \Psi}{\partial I_2}(I_1\mathbf{I} - \mathbf{C})\right]. \tag{4.29}$$

4.2.4 Compressible Hyperelasticity

In general, soft tissue represents a quasi-incompressible or near-incompressible hyperelastic material. Thus is makes sense to pose the model in the context of compressible hyperelasticity where the free energy Ψ is additively decomposed into *volumetric* and *isochoric* parts as

$$\Psi = \Psi_{vol} + \Psi_{iso}.$$

Ψ_{vol} characterises the volumetric part of the energy. Ψ_{iso} characterises the isochoric part of the energy which preserves volume. The volumetric-isochoric decomposition can further be parametrised through the multiplicative split of the deformation gradient $\mathbf{F}$ and the right Cauchy-Green tensor $\mathbf{C}$ as

$$\mathbf{F} = J^{\frac{1}{3}}\overline{\mathbf{F}} \qquad \text{and} \qquad \mathbf{C} = J^{\frac{2}{3}}\overline{\mathbf{C}},$$

where $J^{\frac{1}{3}}\mathbf{I}$ and $J^{\frac{2}{3}}\mathbf{I}$ capture the volume changes while $\overline{\mathbf{F}}$ and $\overline{\mathbf{C}} = \overline{\mathbf{F}}^T\overline{\mathbf{F}}$ are associated with volume preservation such that:

$$\det(\overline{\mathbf{F}}) = 1 \qquad \text{and} \qquad \det(\overline{\mathbf{C}}) = 1.$$

With reference to Eq. (4.6), the modified principle stretches can be shown to be:

$$\overline{\lambda}_a = J^{-\frac{1}{3}}\lambda_a$$

for $a = 1, 2, 3$.

Furthermore, the strain invariants of the modified right Cauchy-Green tensor, $\overline{\mathbf{C}}$ are defined by:

$$\begin{aligned} \overline{I}_1 &= \operatorname{tr}(\overline{\mathbf{C}}) = J^{-\frac{2}{3}} I_1 \\ \overline{I}_2 &= \frac{1}{2}\left[\operatorname{tr}(\overline{\mathbf{C}})^2 - \operatorname{tr}(\overline{\mathbf{C}}^2)\right] = J^{-\frac{4}{3}} I_2 \\ \overline{I}_3 &= \det(\overline{\mathbf{C}}) = 1. \end{aligned}$$

The free energy then takes the form:

$$\Psi = \Psi_{vol}(J) + \Psi_{iso}(\overline{I}_1, \overline{I}_2).$$

Correspondingly, the various stress measures are given by

$$\mathbf{P} = \frac{\partial \Psi}{\partial \mathbf{F}} = \frac{\partial \Psi_{vol}}{\partial \mathbf{F}} + \frac{\partial \Psi_{iso}}{\partial \mathbf{F}} = \mathbf{P}_{vol} + \mathbf{P}_{iso}.$$

4.2.5 Examples of Incompressible Isotropic Models

Numerous forms of Ψ have been proposed to capture the behaviour of isotropic elastic materials. Several primary examples are now detailed and compared under two simple loading conditions. The procedure detailed here can be found in Steinmann et al. (2012). The analytical formulation of the stress-strain relation for arbitrary free energy functions are derived according to the equations set out in the previous sections. These analytical formulations are then used to evaluate the legitimacy of the chosen models in their ability to replicate given data. The data as provided by Steinmann et al. (2012) are extracted from the classical experimental data of Treloar (1944) who extensively studied the behaviour for vulcanised rubber containing 8% sulphur. Steinmann et al. (2012) were able to extract the stretch data with the corresponding nominal stress values for cases of uniaxial and equibiaxial tension.

Uniaxial Tension

For the case of uniaxial tension

$$\mathbf{F} = \begin{bmatrix} \lambda & 0 & 0 \\ 0 & \dfrac{1}{\sqrt{\lambda}} & 0 \\ 0 & 0 & \dfrac{1}{\sqrt{\lambda}} \end{bmatrix} \Longrightarrow \mathbf{C} = \begin{bmatrix} \lambda^2 & 0 & 0 \\ 0 & \dfrac{1}{\lambda} & 0 \\ 0 & 0 & \dfrac{1}{\lambda} \end{bmatrix}.$$

The first and second invariants can accordingly be found as

$$I_1 = 2\lambda^{-1} + \lambda^2, \qquad\qquad I_2 = \lambda^{-2} + 2\lambda.$$

As contraction in the y and z directions is unhindered, only P_{11} contributes to the stress response. This can be used to calculate the pressure term p by setting either P_{22}, $P_{33} = 0$ in Eq. (4.29), yielding

$$p = \frac{2}{\lambda}\frac{\partial \Psi}{\partial I_1} + 2\left[\lambda + \frac{1}{\lambda^2}\right]\frac{\partial \Psi}{\partial I_2}.$$

Thus the first principal stress has the form:

$$P_{11} = 2\left[\frac{\partial \Psi}{\partial I_1} + \frac{1}{\lambda}\frac{\partial \Psi}{\partial I_2}\right]\left[\lambda - \frac{1}{\lambda^2}\right]. \tag{4.30}$$

Equibiaxial Tension:

For the case of equibiaxial tension

$$\mathbf{F} = \begin{bmatrix} \lambda & 0 & 0 \\ 0 & \lambda & 0 \\ 0 & 0 & \dfrac{1}{\lambda^2} \end{bmatrix} \Longrightarrow \mathbf{C} = \begin{bmatrix} \lambda^2 & 0 & 0 \\ 0 & \lambda^2 & 0 \\ 0 & 0 & \dfrac{1}{\lambda^4} \end{bmatrix}.$$

The first and second invariants can accordingly be found as

$$I_1 = 2\lambda^2 + \lambda^{-4}, \qquad\qquad I_2 = \lambda^4 + 2\lambda^{-2}.$$

As contraction in the z direction will be unhindered, P_{11} and P_{22} will contribute to the stress response, where $P_{11} = P_{22}$. This can be used to calculate the pressure term p by setting $P_{33} = 0$ in Eq. (4.29), yielding

$$p = \frac{2}{\lambda^4}\frac{\partial \Psi}{\partial I_1} + \frac{4}{\lambda^2}\frac{\partial \Psi}{\partial I_2}.$$

Thus the first and second principal stress has the form:

$$P_{11} = P_{22} = 2\left[\frac{\partial \Psi}{\partial I_1} + \lambda^2 \frac{\partial \Psi}{\partial I_2}\right]\left[\lambda - \frac{1}{\lambda^5}\right]. \tag{4.31}$$

For comparison, three models were chosen for Ψ: a Neo-Hookean model, a Mooney-Rivlin model and a Yeoh model. With reference to Eq. (4.28), where the first term of the free energy is given by:

Neo-Hookean model:

$$\Psi(I_1, I_2) = \frac{\mu}{2}\left(I_1 - 3\right), \tag{4.32}$$

where μ denotes the shear modulus.

Mooney-Rivlin model:

$$\Psi(I_1, I_2) = c_{10}\left(I_1 - 3\right) + c_{01}\left(I_2 - 3\right), \tag{4.33}$$

where c_{10} and c_{01} are parameters similar to the shear modulus, and relate to the shear modulus through $\mu = 2(c_{10} + c_{01})$.

Yeoh model:

$$\Psi(I_1, I_2) = c_1\left(I_1 - 3\right) + c_2\left(I_1 - 3\right)^2 + c_3\left(I_1 - 3\right)^3. \tag{4.34}$$

where c_1, c_2 and c_3 are material parameters of shear modulus type.

These are examples of phenomenological models will increasing complexity. The models were optimised using a built in global optimisation routine, called GlobalSearch, provided by Mathematica (Wolfram, 2016) in order to determine the relevant model parameters. Errors were calculated according to:

$$E^2 = \frac{1}{N}\sum_{i=2}^{N} \frac{\left(P_{\text{sim}}(\lambda_i^{\text{exp}}) - P_{\text{exp}}(\lambda_i^{\text{exp}})\right)^2}{(P_{\text{exp}}(\lambda_i^{\text{exp}}))^2}, \tag{4.35}$$

where P_{sim} and P_{exp} are the stress component values of the simulation (Eq. (4.30) and Eq. (4.31)) and the experimental Treloar data, respectively, λ_i^{exp} are the experimental Treloar stretch values and N the number of data points (i starts at 2 to avoid zero stress values).

As per the process detailed in Steinmann et al. (2012), in order to validate the models each set of model parameters obtained for the cases of uniaxial and equibiaxial tension are used to simulate the other deformation mode. The results are plotted in against the experimental data Fig. 4.3 - Fig. 4.5. The respective parameters and corresponding errors are given Table 4.1 - Table 4.3.

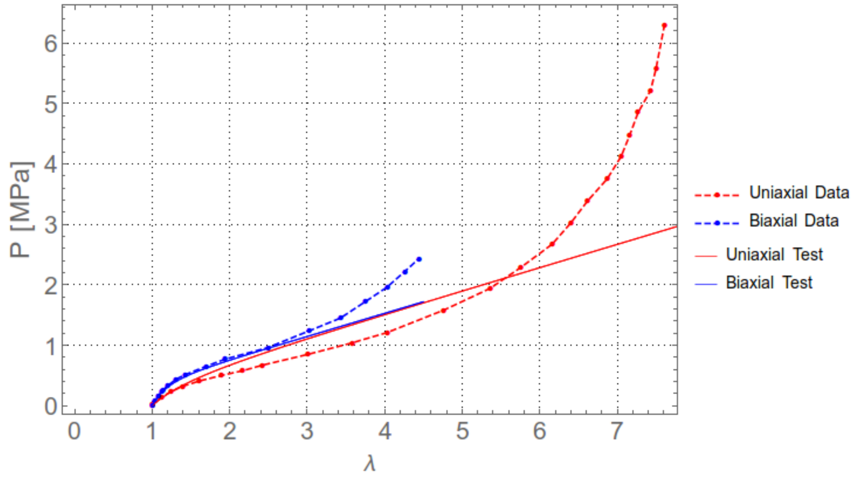

(a) Uniaxial fit

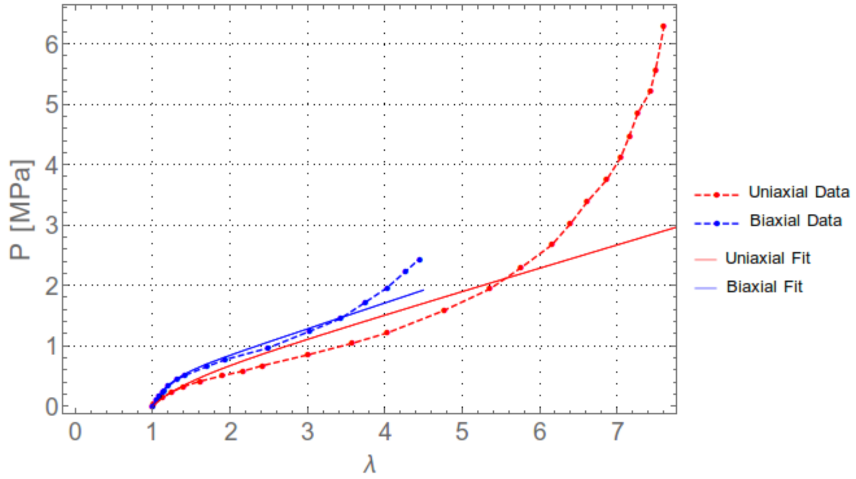

(b) Equibiaxial fit

Fig. 4.3: Neo-Hookean model fit against Treloar data.

	Uniaxial Test	Equibiaxial Test
μ [MPa]	0.3822	0.4267
$E_{\text{uniaxial fit}}$	0.3036	0.3224
$E_{\text{equibiaxial fit}}$	0.1334	0.0874

Table 4.1: Parameter and error values for Neo-Hookean model

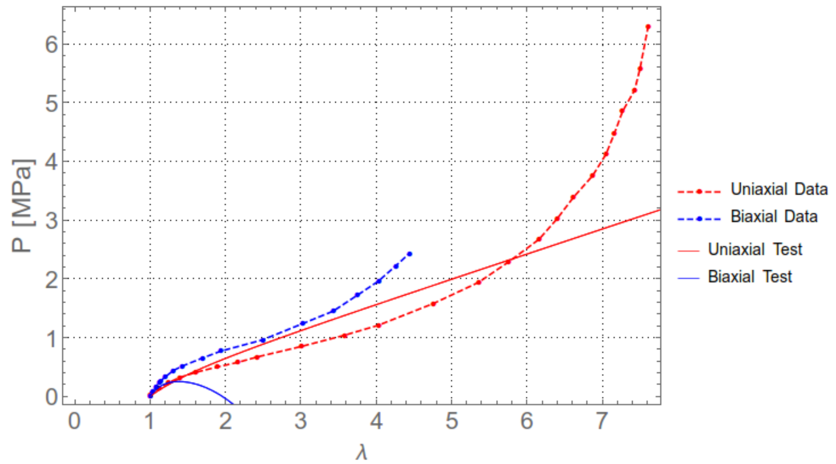

(a) Uniaxial fit

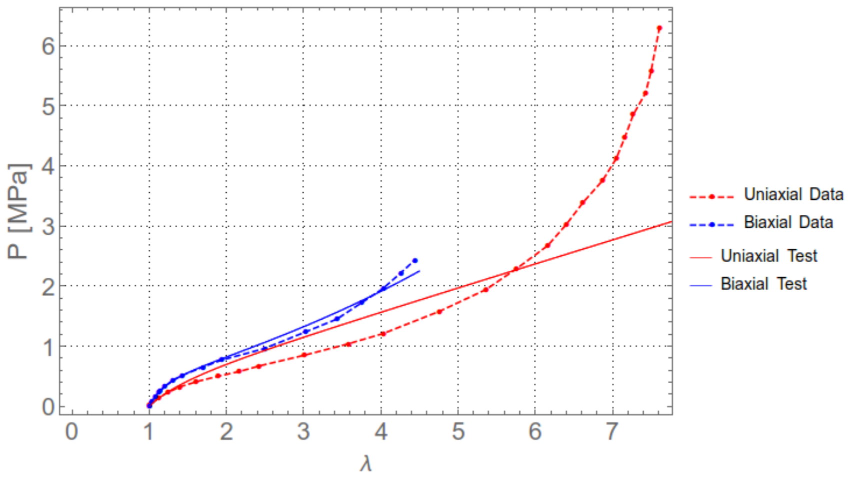

(b) Equibiaxial fit

Fig. 4.4: Mooney-Rivlin model fit against Treloar data.

	Uniaxial Test	Equibiaxial Test
c_{10} [MPa]	0.2118	0.1978
c_{01} [MPa]	-0.0552	0.0026
$E_{\text{uniaxial fit}}$	0.2976	0.3064
$E_{\text{equibiaxial fit}}$	2.1824	0.0527

Table 4.2: Parameter and error values for Mooney-Rivlin model

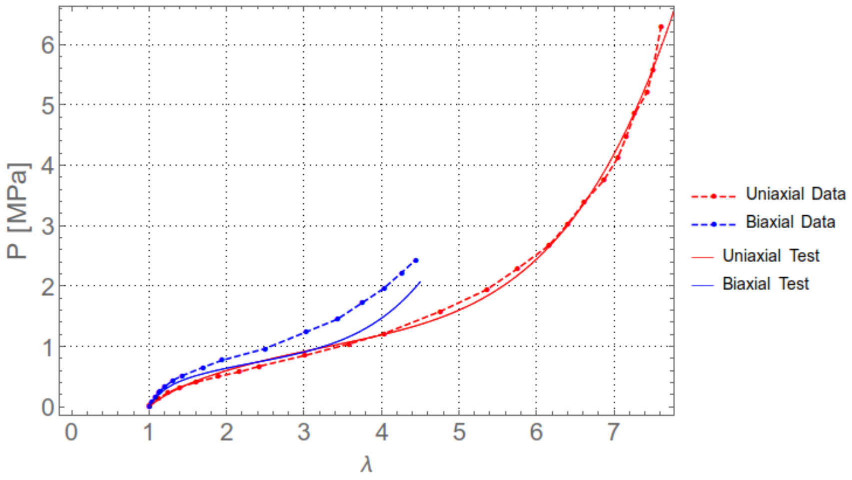

(a) Uniaxial fit

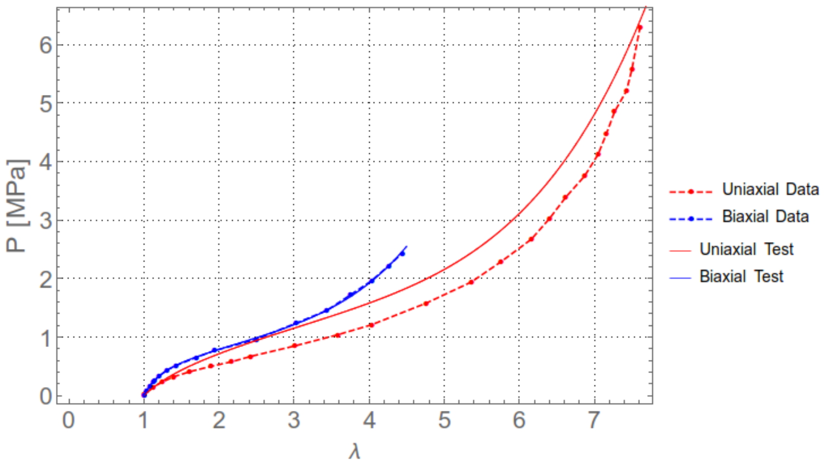

(b) Equibiaxial fit

Fig. 4.5: Yeoh model fit against Treloar data.

	Uniaxial Test	Equibiaxial Test
c_1 [MPa]	0.1785	0.2077
c_2 [MPa]	-0.002	-0.00097
c_3 [MPa]	4.7052e-5	3.5182e-5
$E_{\text{uniaxial fit}}$	0.1457	0.2541
$E_{\text{equibiaxial fit}}$	0.1878	0.0174

Table 4.3: Parameter and error values for Yeoh model

What is clear from Fig. 4.3a and Fig. 4.3b is that the Neo-Hookean model provides an extremely poor fit to the experimental data, for both the uniaxial and equibiaxial tension tests. The simple model is unable to capture the S-shaped nature of the experimental data. It can be said though that for small stretch values, $\lambda < 2$, the Neo-Hookean model may be seen as adequate.

From Fig. 4.4a, the Mooney-Rivlin model performs very poorly under uniaxial tension. From Table 4.2 it is clear that the parameters found under uniaxial tension lack generality in that large error in generated when used to fit the equibiaxial data. The equibiaxial test generates a satisfactory fit to the equibiaxial data, which can be attributed to the relative linearity of the data, but poor generality leads to an inadequate fit to the uniaxial data.

The Yeoh model provides a very good fit to the data, which is not surprising as the cubic nature of the model is expected to capture the S-shape of the data. It is also notable that the generated parameter sets provide good generality in that the simulations yield reasonable fits to the complementary deformation mode.

It should be noted that under uniaxial tension, both the Mooney-Rivlin and Yeoh models produce parameter sets different to that presented in Steinmann et al. (2012). This is to be expected as it becomes difficult to find a single ideal parameter set the more flexible the models become. Without any physical interpretation to the parameters, choosing one set over another is difficult to motivate.

4.2.6 Anisotropic Materials

Many soft tissue materials are composed of a ground substance with an embedded family or families of fibres. These *fibre-reinforced* composite materials exhibit strong directional properties with respect to the fibre direction(s), which manifests as a strong anisotropic response to loading. A material with a single family of fibres in a single preferred direction is referred to as *transversely isotropic* with respect to the preferred direction.

Consider a body with reference configuration Ω_0 at time $t = 0$. In this configuration a family of fibres is embedded at point $\mathbf{X} \in \Omega_0$ with a preferential direction characterised by $\mathbf{v}_0(\mathbf{X}), |\mathbf{v}_0| = 1$.
At later time $t > 0$, Ω_0 has undergone a deformation to the current configuration Ω where the fibres have a current preferential direction $\mathbf{v}(\mathbf{x}, t), |\mathbf{v}| = 1$, at the associated point $\mathbf{x} \in \Omega$. The fibres can be said to have undergone a deformation induced stretch denoted by λ such that:

$$\begin{aligned} &\lambda \mathbf{v}_0 = \mathbf{F}\mathbf{v}_0 \\ \Rightarrow &\lambda^2 = \mathbf{v}_0 \cdot \mathbf{F}^T\mathbf{F}\mathbf{v}_0 = \mathbf{v}_0 \cdot \mathbf{C}\mathbf{v}_0. \end{aligned}$$

Due to the directional dependence on the deformation, it is necessary for the free energy to have dependence on the preferential direction vector $\mathbf{v}_0$. Thus:

$$\Psi = \Psi(\mathbf{C}, \mathbf{v}_0 \otimes \mathbf{v}_0).$$

In the context of transversely isotropic materials, Ψ may be expressed by the set of strain invariants of the right Cauchy-Green tensor $\mathbf{C}$ as detailed for isotropic materials, with the addition of a fourth invariant defined by

$$I_4(\mathbf{C}, \mathbf{v}_0) = \mathbf{v}_0 \cdot \mathbf{C}\mathbf{v}_0 = \lambda^2, \tag{4.36}$$

where $\mathbf{v}_0$ is the fibre direction in the reference configuration[7].

The free energy is accordingly modified to included this dependence:

$$\Psi = \Psi(I_1(\mathbf{C}), I_2(\mathbf{C}), I_3(\mathbf{C}), I_4(\mathbf{C}, \mathbf{v}_0)). \tag{4.37}$$

With reference to Eq. (4.25)

---

[7] Note that a fifth invariant of the form $I_5 = \mathbf{v}_0 \cdot \mathbf{C}^2\mathbf{v}_0$ is often included but is not relevant to the scope of the project.

$$\mathbf{P} = 2\mathbf{F}\frac{\partial \Psi}{\partial \mathbf{C}},$$

where the additional dependence on I_4 extends equation Eq. (4.26) to

$$\frac{\partial \Psi}{\partial \mathbf{C}} = \frac{\partial \Psi}{\partial I_1}\frac{\partial I_1}{\partial \mathbf{C}} + \frac{\partial \Psi}{\partial I_2}\frac{\partial I_2}{\partial \mathbf{C}} + \frac{\partial \Psi}{\partial I_3}\frac{\partial I_3}{\partial \mathbf{C}} + \frac{\partial \Psi}{\partial I_4}\frac{\partial I_4}{\partial \mathbf{C}},$$

where the derivative of I_4 with respect to $\mathbf{C}$ is given by

$$\frac{\partial I_4}{\partial \mathbf{C}} = \mathbf{v}_0 \otimes \mathbf{v}_0.$$

4.2.7 Examples of Anisotropic Models

Examples of phenomenologically based anisotropic models were taken from Tonge et al. (2013b) for modelling bulge tests conducted on in vitro skin specimens (see Sec. 7.1). These models were based on the observation that the skin consists of an anisotropic collagen matrix embedded in an incompressible isotropic matrix of elastin and ground substance. Thus the models are composed of three terms

$$\Psi = -\frac{p}{2}(I_3 - 1) + \Psi_{iso} + \Psi_{aniso}.$$

The first term describes the incompressibility where p represents a Lagrange multiplier to enforce incompressibility, the second term the isotropic part, often taken as a standard Neo-Hookean, (Eq. (4.32)) and the last term describes the anisotropic collagen contribution.

The model considered is an example of a transversely isotropic model referred to as the *3D Gasser-Ogden-Holzapfel (GOH)* model. For a more detailed discussion on the model the reader is referred to Tonge et al. (2013b). The anisotropic part of the model has the form

$$\Psi_{aniso} = \frac{k_1}{2k_2}(\exp[k_2(I_\alpha - 1)^2] - 1),$$

where k_1 is a stiffness parameter, k_2 describes the nonlinearity of the fibres and I_α is a pseudo-invariant defined by

$$I_\alpha = \mathbf{C} : \mathbf{A},$$

where $\mathbf{A} = \kappa\mathbf{I} + (1 - 3\kappa)\mathbf{e}_f \otimes \mathbf{e}_f$, $\mathbf{e}_f$ being the vector describing the dominant fibre direction and $\kappa \in [0, \frac{1}{3}]$ a dispersion parameter. For a case of uniaxial tension applied in the direction of the collagen fibres, I_α reduces to:

$$I_\alpha = \kappa I_1 + (1 - 3\kappa)\lambda^2.$$

For the case of skin tests, a plane stress assumption is used to find a value for p:

$$\sigma_{33} = 0 \Longrightarrow p = 2(F_{33})^2\left(\frac{\partial \Psi}{\partial I_3} + \frac{\partial \Psi}{\partial I_\alpha}A_{33}\right).$$

Anisotropic data was found through tensile tests conducted on rabbit skin by Lanir and Fung (1974) as depicted by the dots in Fig. 4.6. Table 4.4 gives the parameter values obtained through the same optimisation routine run for the isotropic models and Fig. 4.6 shows the resulting fit. The error was calculated by

$$E^2 = w_1 E^2_{\text{parallel}} + w_2 E^2_{\text{perpendicular}} \tag{4.38}$$

where E^2_{parallel} and $E^2_{\text{perpendicular}}$ are Eq. (4.35) along the parallel and perpendicular directions, respectively. w_1 and w_2 are weighting parameters where preference can be given to a certain direction. The model gives a very satisfactory fit to the rabbit skin data in the parallel and perpendicular directions.

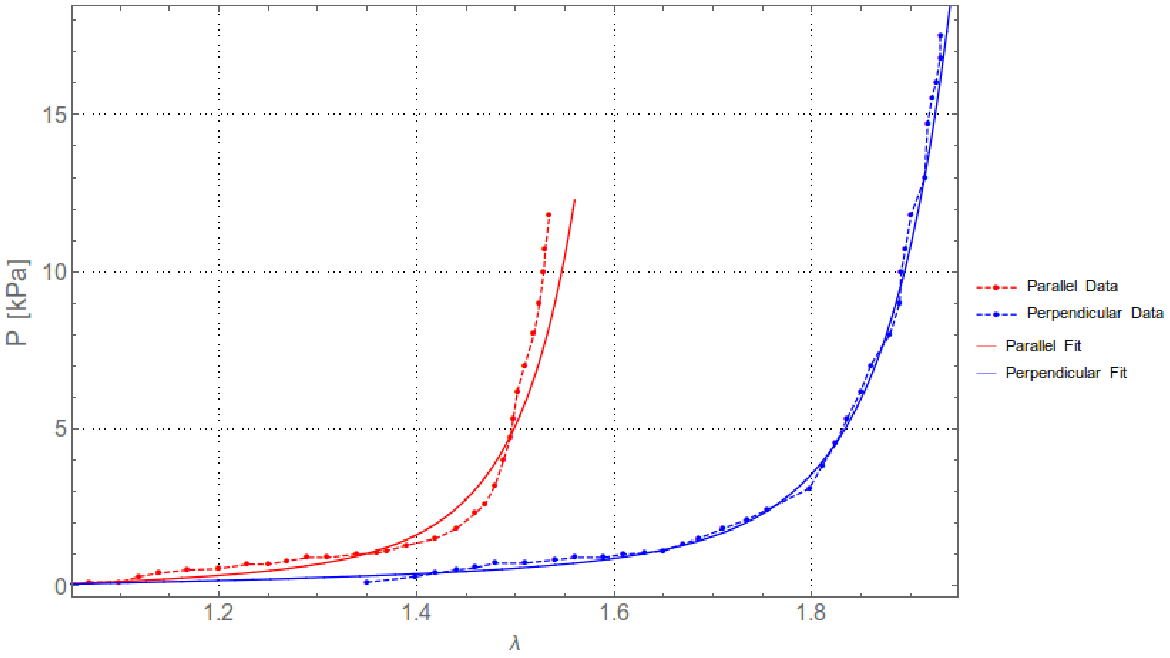

Fig. 4.6: 3D-GOH model fit to rabbit skin data, Lanir and Fung (1974)

	Uniaxial Test
μ (kPa)	0.3076
κ	0.2862
k_1(kPa)	0.2525
k_2	14.2063
w_1	5
w_2	1
E_{fit}	0.7035

Table 4.4: Parameter values for 3D-GOH model

5

Linking the Microscopic Structure to the Macroscopic Response

In general, soft tissue is a highly complex material. In Chapter 2 the intricate microstructure that makes up the skin was explored in detail and key constituents identified. Individually, collagen, elastin and ground substance have different mechanical response under loading, but it is their combined response and the interaction between them that elicits the macroscopic response of the skin.

Displaying properties such as anisotropy, incompressibility, nonlinearity, time dependence, rate dependence and non-homogeneity, while subject to large deformations, characterising the response of soft tissue is a very challenging task. Various mechanical tests have been performed in order to quantify the mechanical properties of soft tissue, and are broadly divided into two categories:

- In vivo - Conducted on living tissue.
- In vitro (ex vivo) - Conducted on tissue that has been removed.

In vitro and in vivo tests have their advantages and disadvantages. In vivo tests account for factors such as the presence of living cells and attachment to underlying tissue which alter the overall skin response. The advantage of testing the true skin response is that it accounts for the active processes that may influence skin deformation. The disadvantage of such tests is that it becomes difficult to isolate various constituent and physiological contributions, such as through the presence of blood vessels and muscle attachments. It is also difficult to develop appropriate boundary conditions and the control of loading conditions is imprecise due to complex geometry, skin tension and apparatus attachment.

In vitro tests have the advantage that boundary conditions can be controlled. Additionally, it is easier to isolate the skin response, as it is removed from underlying tissue and variability in skin tension is avoided. The argument against such tests is that the response is not the true skin response.

There has been much research into the the overall stiffness of the skin. From the summary of the literature in Table 5.1, there is very little agreement on the stiffness of the skin. Such variation has been attributed to a variety of factors intrinsic to the skin and environment, including

- Anatomical site.
- Patient age.
- Gender.
- Skin thickness.
- Hormones.
- Cumulative ultraviolet and infra-red exposure.
- Humidity.
- Connection to underlying muscle.
- Initial skin tension.

- Anisotropy.

These factors have all been linked with the extreme variation of results. Additionally, external factors such as the effect of the chosen test set-up (in vivo vs in vitro), the effect of the test rig on the natural state of stress, lack of control of test environment, not accounting for effect and mobility of underlying tissue, not accounting for initial skin tension and the chosen analytical model to interpret the data may further explain such discrepancies.

Author	Young's modulus	Test
Lapeer et al. (2010)	129 ± 88 kPa	suction (in vivo)
	56 - 177.6 kPa	suction (in vivo)
	7 - 33 kPa	indentation(in vivo)
	1.586 - 3.164 MPa	(in vitro)
Pawlaczyk et al. (2013)	4.6 - 20 MPa	
	0.05 - 0.15 MPa	suction (in vivo)
	60-70 MPa	tension
Agache et al. (1980)	4.2 $\times 10^2$ MPa	torsion (in vivo)
Silver et al. (2002)	2.1 -4.3 MPa ($<$ 20% strain)	tension (in vitro)
	41 - 45 MPa ($>$ 30% strain)	tension(in vitro)
Hendriks et al. (2003)	56 kPa (small strains)	suction (in vivo)
Hendriks et al. (2006)	0.96 MPa (small strains)	suction (in vivo)
Diridollou et al. (2001)	0.08 - 0.26 MPa	suction (in vivo)

Table 5.1: Values for Young's modulus of human skin in the literature

Skin displays a typical *J-curve* under loading (see Fig. 4.6). This curve is divided into three distinct regions during loading as represented in Fig. 5.1. The characteristics represented in this typical curve logically depends of the interaction between the various layers of the skin, and the comprising components therein.

The stiffness of the low modulus portion of the curve has been recorded at values of 0.1 MPa (Daly and Odland, 1979), 2.1 - 4.3 MPa (Silver et al., 2002), 0.96 MPa (Hendriks et al., 2006) and 56 kPa (Hendriks et al., 2003). The Young's modulus increases exponentially at higher strains with Silver et al. (2002) reporting values of 41-45 MPa for this final portion of the curve. This nonlinear response may further explain the large differences in reported values.

Much research has been on the contributions of the individual layers to the overall skin response. Despite this, there is still a great deal of uncertainty. The uppermost layer of the skin is the epidermal layer. Of great interest in the literature is the sub-layer referred to as the stratum corneum. This interest arises as the stratum corneum is the outer most sublayer of the epidermis and is thus in direct contact with the environment. Additionally, the stratum corneum despite being only $10 - 25$µm thick (Geerligs, 2006), is an extremely stiff layer of "dead cells" called corneocytes. Thus it has been hypothesised that the stratum corneum contributes significantly to the overall skin stiffness. Unfortunately, there has been significant difficulty in developing a conclusive answer to this thought due to the vast variability in quoted stiffnesses through the literature. The Young's modulus has been quoted anywhere from a few MPa to on the order of GPa. Reasons for such variation could be due to anatomical heterogeneity, species variation, environmental influence, errors in sample preparation and differences in testing apparatus.

The stratum corneum has been shown to be highly dependent on the relative humidity of the testing environment. From Fig. 5.2 (Geerligs, 2006), the loading behaviour is very different depending on the

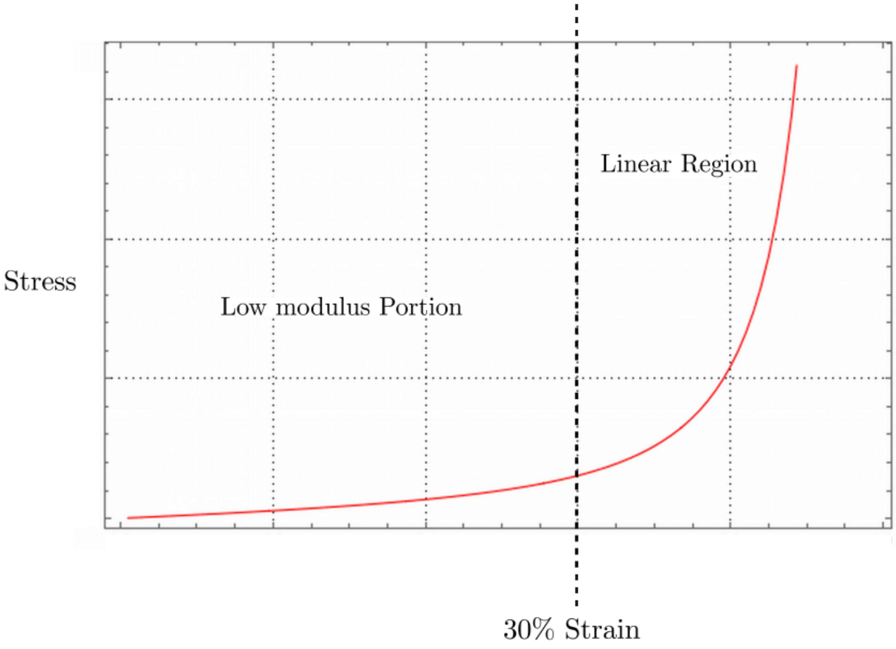

Fig. 5.1: Schematic of typical skin stress-strain behaviour

relative humidity (RH). At 32% RH, the stratum corneum behaves purely elastically with rupture at around 30% elongation. At 76% RH, the stratum corneum behaves elastically up till 30% elongation before entering a phase of irreversible (plastic) elongation. At 98% RH the stratum corneum is able to extend to a zone of strain hardening with rupture occurring at around 200% elongation.

It's noticeable that at higher RH levels the stratum corneum is significantly less stiff. Levi (2009) was able to find that the Young's modulus of the stratum corneum varied with RH:

- 370 MPa at 30% RH.
- 114 MPa at 50% RH.
- 63 MPa at 70% RH.
- 3 MPa at 100% RH.

Similarly to RH, stratum corneum stiffness shows significant dependence on the hydration level of the sample tested. Geerligs (2006) mentions that results of 10 MPa were recorded for wet porcine skin whereas up to 1 GPa was found for dried human skin. Levi (2009) shows that for a constant RH of 15%, the Young's modulus of wet skin was found to be 28.4 MPa while dry skin measured at 272 MPa. It was also mentioned that at low strain the stratum corneum behaves linear elastically but displayed increasingly viscoelastic behaviour for increasing hydration levels. Further values for the Young's modulus of the stratum corneum can be found in Geerligs (2006)

Often the choice of testing apparatus to measure skin properties has been questioned. One such technique is that of nano-indentation. Sharp tips used for indentation can cause damage to the skin samples which would give false data. Secondly, indentation tips varies from $1-10$µm whereas corneocytes range from $26-45$µm in diameter. It is thus likely that such tests measured the local stiffness of individual cells, rather than the tissue as a whole (Geerligs, 2006).

As the stratum corneum is so thin, making up around $\frac{1}{40}$ of the skin thickness, its overall contribution to the stiffness of the epidermis and the skin as a whole has often been questioned. Geerligs (2006)

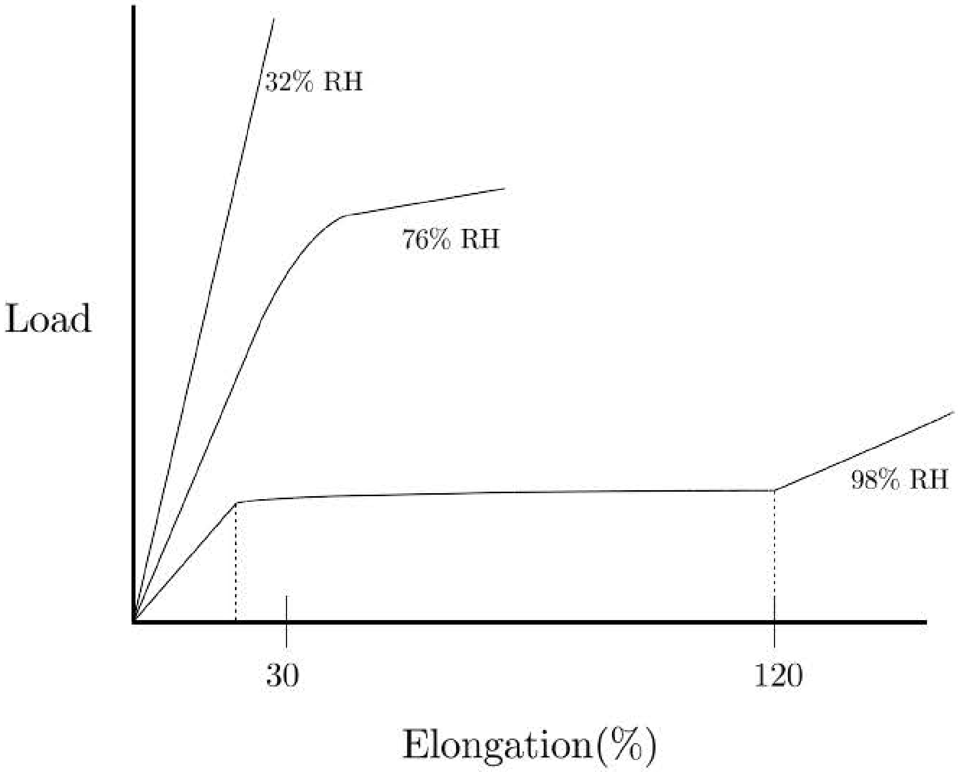

Fig. 5.2: Typical force-elongation curve for the stratum corneum at different relative humidity (RH) levels (Geerligs, 2006)

tested the contribution of the stratum corneum to the whole epidermis. It was found that the Young's modulus of the stratum corneum was double that of the whole epidermis. This suggests that the overall contribution to the epidermis is negligible. Through FE simulations, Geerligs (2006) found that the Young's modulus of the stratum corneum was comparable to that of the rest of the epidermis and that varying the stiffness of the stratum corneum hardly had any effect on the overall stiffness. Hendriks et al. (2006) similarly found that at low strains the contribution of the stratum corneum is negligible. Xu et al. (2008) mentions that there is no observable difference in the stretch response of the skin with and without the stratum corneum.

Similar tests have been carried out to establish the effect of the whole epidermis on the overall skin response. Hendriks et al. (2006) reported that the upper layers of the skin (the epidermis and the papillary dermis) have a Young's modulus of 0.11 kPa while the reticular dermis was measured at 0.16 MPa, suggesting that the epidermis plays little role in the overall response. This assertion has been backed by Tregear (1969) who found that the removal of the epidermis had little effect on the overall Young's modulus and no effect on the viscoelastic response, when compared to the skin as a whole. Thus despite the stiffness of the epidermal layer being greater than that of the dermis, the epidermis is often neglected in skin tests. Tregear (1969) additionally found that the hypodermis did not contribute to the skin stiffness, which is unsurprising, given a Young's modulus measured at between a few kPa to 100 kPa (Geerligs, 2006).

Thus it has been generally accepted that the bulk of the material response is due to that of the dermal layer. Silver et al. (2001, 2002) reports that the mechanical properties of the skin and the dermis were not statistically different. Comprised of a matrix of collagen, elastin and ground substance, the expression of the mechanical properties of the skin is due to these components, their structural organisation and the interaction between them.

Collagen has been found to make up approximately 66-69% of the fractional volume of the dermis (Silver et al., 2002). This results in around 34% (Leveque et al., 1980) and 73% (Reihsner et al., 1995) of the wet weight and dry weight of the skin, respectively. Tonge et al. (2013a) mentions that collagen contributes 70-80 % of the dry weight of skin. In experiments where collagen was isolated through enzymatic treatment (Oxlund and Andreassen, 1980; Oxlund et al., 1988; Pailler-Mattei et al., 2008), the relative contribution of collagen to the overall skin mechanical behaviour has been assessed. Such tests conclude that collagen was indeed responsible for the tensile strength of the skin. In tests where collagen was fully degraded, the remaining skin sample lost all mechanical integrity. Furthermore, Xu et al. (2008) mentions that a denser collagen network lead to a greater stiffness at high strains.

The angular distribution of collagen fibres and the non-uniform fibre geometry means that under stretch not all fibres are straightened and stretched. This accounts for the anisotropic stiffness response when load is applied along versus across the "preferential" fibre direction. Furthermore, under tension, collagen networks are shown to reorientate along the line of tension, resulting in the typical nonlinear load-extension curve.

Contributing approximately 2-4 % of the dry weight of skin (Tonge et al., 2013a), elastin fibres are highly compliant with the ability to stretch to two times their original length and return to their initial length. Silver et al. (1992) was able to show that when the skin is stretched, the elastin fibres are the first to take on stretch, thus displaying that the elastin contribution is important at low strain levels. Stress-strain curves of elastin-free skin (Oxlund et al., 1988) show that elastin supports the entire load up to 50% strain after which the slope rapidly increases due to collagen response.

The elastic modulus of elastin has been found at around 1MPa which agrees with the Young's modulus of skin at low strain and the fact that elastin is not strong enough to provide much tensile strength at higher strains (Tregear, 1969). Reihsner et al. (1995) states that elastin is especially responsible for the recoiling of the skin and collagen after stress is applied. Oxlund et al. (1988) showed that after degradation of the elastin through the use of elastase, the large strain response occurs sooner for a given tensile load. This seems to suggest that in the absence of elastin, collagen fibres take on load at lower strain levels than when elastin is present.

The ground substance has been shown to play a role mainly in the viscoelastic properties of the skin. Oxlund and Andreassen (1980) was able to show that the removal of various macromolecules within the ground substance has no effect on the stress-strain curve of rat skin. Oomens et al. (1987) suggests that ground substance probably only plays a major when soft tissue is subject to compression.

With reference to Fig. 5.1, each portion can be related to the dermal constituents as follows

1. Low Modulus Portion:
    - This occurs during the gradual straightening of crimped collagen fibres.
    - During this stage, the greatest resistance to loading is generated by the elastin and ground substance, with collagen offering very little resistance.
    - The low modulus portion can be further divided into two phases:
        a) Phase 1: wavy collagen is still relaxed and elastin takes on the majority of the load.
        b) Phase 2: collagen starts to uncrimp and elongate and take on load.
2. Linear Region:
    - Collagen straightens and align with the load direction.
    - Straightened collagen strongly resist loading. This results in the rapid stiffening of the skin.

    - The steep linear stress-strain relation is due to stretching and slippage between fibrils and molecules.
3. Final Yield Region:
    - Tensile strength is reached and fibres begin to break (Not shown in Fig. 5.1).

It is well recognised that the skin has certain directional properties. The discovery of this phenomenon has been attributed to the Austrian anatomist Karl Langer, in his study "On the Anatomy and Physiology of the Skin"(Langer, 1861). Although Langer notes that such skin behaviour was first noted by Baron Dupuytren, he was the first to conduct a series of in-depth experiments into the subject. Langer used a 2mm diameter spike in the majority of his experiments and found that instead of a round stab wound, a "linear cleft" was produced. He was thus able to map this directionality over the entire body, producing lines of tension referred to as *Langer lines* (Fig. 5.3).

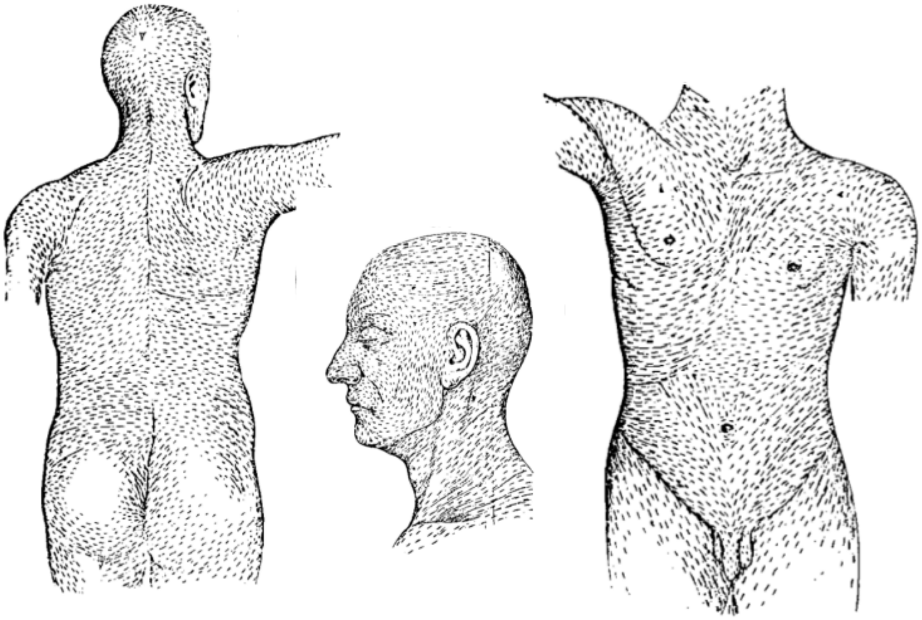

Fig. 5.3: Langer lines as observed by Langer (1861)

As quoted from Langer (1861):

> "I began on the assumption that, if the clefts were placed as closely as possible, they would show a definite relationship to each other in the various parts of the body and it would be possible to group the clefts into lines and areas arranged topographically in a similar way to the already known pattern of the hairs. These lines which, as was realised from the outset, were an expression of the fibre pattern of the skin, would furnish much, until now unknown, information not only about the texture of the skin but about its elasticity and capacity for swelling because they provide a technique of orientating the dermal tissue and differentiating the lengthwise incision from the transverse."

At the time, Langer argued that this observed directionality was due to the directional orientation of the fibres in the dermis. More recent studies (Pawlaczyk et al., 2013; Xu and Lu, 2011) have confirmed that collagen fibres lie predominantly along Langer lines, with elastin showing similar orientation but to a lesser extent.

The magnitude of these directional effects have been the subject of several modern studies. Lapeer et al. (2010) found that the Young's modulus parallel to the Langer lines was greater than that perpendicular to the Langer lines by a ratio of around 2.21:1. Reihsner et al. (1995) found that the degree of anisotropy differs across anatomical site, an observation similarly made by Langer in his original study. Reihsner et al. (1995) found in situ stresses range from 0.2-1.6 $\mathrm{N\,m\,g^{-1}}$ along Langer lines and 0.1 - 1.3 $\mathrm{N\,m\,g^{-1}}$ perpendicularly, with the degree of anisotropy differing between principle stress components from 0.1 - 0.3 $\mathrm{N\,m\,g^{-1}}$.

5.1 Skin Model

The primary aim of the constitutive relation used in this dissertation is to link the macroscopic skin behaviour to the underlying microstructure. As discussed, only the dermal layer contributes significantly to the overall skin response. For this reason, the proposed free energy needs to reflect the contributions from the primary constituents of the dermal layer i.e. collagen, elastin and ground substance. In Sec. 4.2, the distinction between phenomenological and structurally-motivated models was made, where structural models have the advantage of a more direct link to the microstructure. Developing such a model is desirable in its ability to link the microscopic constituent contributions to the macroscopic response. Furthermore, the incorporation of ageing will be more natural to motivate.

As per the framework detailed in Chapter 4 a free energy is proposed of the additive form

$$\Psi = \Psi_{\text{gs}} + \Psi_{\text{elas}} + \Psi_{\text{col}}, \tag{5.1}$$

where $\Psi_{\text{gs}}, \Psi_{\text{elas}}$ and Ψ_{col} represented the free energy contributions from the ground substance, elastin and collagen, respectively. Often, the contribution of the ground substance and elastin energies are combined. Here, the contributions are separated with the expectation that each may be altered differently according to the ageing response.

As shown in Fig. 5.1, each constituent primarily contributes to a different section of the loading curve. Elastin and ground substance represent the low modulus portion of the curve which is largely linear and isotropic. Collagen essentially plays no part in this region.

To capture the linear, isotropic behaviour at low stretches the elastin and ground substance energies are given forms that capture the near incompressible nature of the bulk material. The coupled form of the compressible neo-Hookean model is given by

$$\Psi_{\text{gs}} = \gamma_{\text{gs}} \left(I_1 - 3 + \frac{1}{\beta_{\text{gs}}} \left(I_3^{-\beta_{\text{gs}}} - 1 \right) \right) \tag{5.2}$$

$$\Psi_{\text{elas}} = \gamma_{\text{elas}} \left(I_1 - 3 + \frac{1}{\beta_{\text{elas}}} \left(I_3^{-\beta_{\text{elas}}} - 1 \right) \right), \tag{5.3}$$

where

$$\gamma = \frac{\mu}{2}, \qquad \beta = \frac{\nu}{1 - 2\nu}.$$

It has been chosen to separate the elastin and ground substance contributions, despite the identical nature of the chosen free-energies. In Garikipati et al. (2004); Kuhl et al. (2005); Kuhl and Holzapfel (2007), the substrate of elastin and proteoglycans is characterised through a single isotropic free energy. Here the separation is motivated by the expected differences in the ageing response of elastin versus the ground substance. Furthermore in Chapter 10.2, this separation will become necessary due

Parameter	Symbol	Units
Poisson's ratio	ν	-
Shear modulus	μ	$\mathrm{N\,m^{-2}}$

Table 5.2: 8-chain constitutive parameters

to a proposed modification to the form of the free energy.

The second region of the loading curve is dominated by the response of collagen. As the collagen fibres straighten and take on load, they exponentially resist further stretch which results in the rapid nonlinear locking behaviour witnessed in skin tests. This behaviour is also strongly anisotropic due the inherent preferred alignment of collagen. As the stiffening response of the skin is so highly dominated by the response of the collagen network, the employment of an effective microstructurally motivated model is essential.

The primary feature of a typical collagen molecule is the assembly of a "chain-like" helical structure. Polymer chains have previously been developed in the context of entropic rubber elasticity (Kuhn and Grün, 1942). Often described by statistical mechanics, such polymer-chain models are typically characterised through a *freely-jointed* chain model based on a "random walk" principle which results in an uncorrelated chain assembly (see Fig. 5.4).

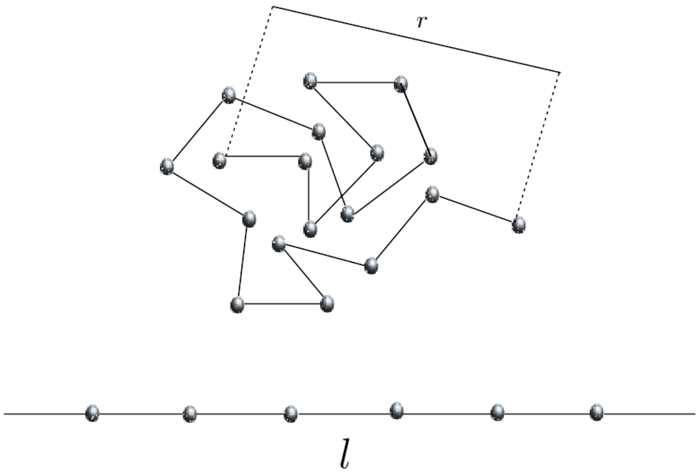

Fig. 5.4: Freely-jointed chain assembly. The orientation of each link in the chain is uncorrelated to neighbouring links.

Biological chains, such as collagen, display a more correlated nature. Such models are referred to as "*wormlike*" chain models where the curvature varies smoothly (Fig. 5.5). The wormlike chain model was developed by Kratky and Porod (1949) (alternatively referred to as the Kratky and Porod model) and successfully applied to the behaviour of DNA molecules by Marko and Siggia (1995). Since then, wormlike chain models have been used to describe the behaviour of collagen in the context of skin modelling (Bischoff et al., 2002; Buganza Tepole et al., 2012; Flynn and McCormack, 2010; Garikipati et al., 2004) and other fibrous soft tissue (Kuhl et al., 2005; Kuhl and Holzapfel, 2007; Saez et al., 2013b).

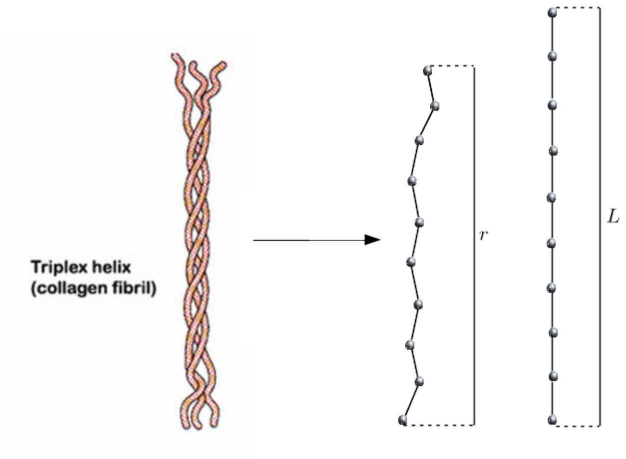

Fig. 5.5: Wormlke chain assembly. The successive chain link is correlated to the chain before it.

5.1.1 Chain Models

Chain models are generally characterised by N rigid bonds, each of equal length, l, referred to as the Kuhn length (Kuhn and Grün, 1942). Stretched out, the contour length of the chain is given by $L = Nl$. The end-to-end distance, r, is defined by the length of the vector pointing from one end of the chain to the other, $0 \leq r \leq L$. Deformation is generally captured through the change in r or through the relative chain stretch defined by

$$\lambda_{\text{chain}} = \frac{r}{L}.$$

Freely-jointed Chain Model

The defining feature of a freely-jointed chain is that each bond is randomly orientated with no relation to the neighbouring bonds and is characterised through the single parameter length L. Defining $p(\lambda_{chain})$ as the probability that a chain characterised by L takes on a configuration governed by r, then, according to the Boltzmann equation, the entropy S of a single chain is described by

$$S = k \ln(p),$$

where $k = 1.3810^{-23} \text{J K}^{-1}$ is the Boltzmann constant.

For a purely entropic chain, the free energy of the chain is expressed by

$$\Psi = -k\theta \ln(p),$$

where θ is the absolute temperature.

In order to specify how the entropy changes with deformation, either classical Gaussian or non-Gaussian statistics are applied. Under the assumption of classical Gaussian statistics, the probability density p is given by

$$p = p_0 \mathrm{exp}\left(-\frac{3}{2}N\frac{r^2}{L^2}\right).$$

This choice results in a free energy, denoted by Ψ_{Gaussian} of the form:

$$\Psi_{\text{Gaussian}} = \Psi_0 + k\theta N\frac{3}{2}\frac{r^2}{L^2},$$

where Ψ_0 is the value of the chain energy in the unperturbed state. From this, the single chain force is derived as

$$\begin{aligned} f_{\text{Gaussian}} &= \frac{\partial \Psi_{\text{Gaussian}}}{\partial r} \\ &= k\theta N 3\frac{r}{L}. \end{aligned}$$

For the case of non-Gaussian statistics, the probability density is defined by

$$p = p_0 \exp\left(-N\mathscr{L}^{-1}\frac{r}{L} - N\ln\left(\frac{\mathscr{L}^{-1}}{\sinh(\mathscr{L}^{-1})}\right)\right),$$

where $\mathscr{L}(\frac{r}{L}) = coth(\frac{r}{L}) - \frac{L}{r}$ is the Langevin function introduced by Kuhn and Grün (1942).

The free energy thus has the form

$$\Psi_{\text{non-Gaussian}} = \Psi_0 + k\theta N\left(\frac{r}{L}\mathscr{L}^{-1} + \ln\left(\frac{\mathscr{L}^{-1}}{\sinh(\mathscr{L}^{-1})}\right)\right),$$

where the single chain force can be found as:

$$f_{\text{non-Gaussian}} = k\theta N\mathscr{L}^{-1}$$

Wormlike Chain

In general, the freely-jointed chain typically overpredicts the locking behaviour characteristic of soft tissue (Kuhl et al., 2005). The freely-jointed chain model has been found to experience difficulties in simultaneously capturing the necessary locking stretches and the shape of the stress-stretch curve. In order to capture both of these characteristics, a *wormlike chain* model was proposed. The wormlike chain has the defining characteristic that the chain segments are correlated and exhibit a smooth curvature along its contour. This correlated form is captured through a second parameter A, known as the persistence length. The persistence length can be thought of as some measure of stiffness. Garikipati et al. (2004) refers to it as a measurement of the degree to which a chain departs from a straight line. Marko and Siggia (1995) describes the persistence length as the characteristic length over which a bend can be made with energy cost $k\theta$.

Originally suggested in the context of DNA by Marko and Siggia (1995), the force-stretch relation for the wormlike chain is given by

$$f_{\text{wormlike}} = \frac{k\theta}{4A}\left(4\frac{r}{L} + \frac{1}{(1-\frac{r}{L})^2} - 1\right).$$

Integrating f_{wormlike} with respect to the chain stretch yields the free energy as

$$\Psi_{\text{wormlike}} = \Psi_0 + \frac{k\theta L}{4A}\left(2\frac{r^2}{L^2} + \frac{1}{(1-\frac{r}{L})} - \frac{r}{L}\right), \tag{5.4}$$

where again Ψ_0 is the value of the chain energy in the unperturbed state (Kuhl and Holzapfel, 2007).

In Fig. 5.6, a comparison between the force-stretch relations of the freely-jointed and wormlike chain models is given. In Fig. 5.6a, $\frac{f}{Nk\theta}$ is plotted against the chain stretch, for both the classical Gaussian and non-Gaussian formulations. At low stretches, the force reactions are nearly identical. For high stretches, the Gaussian formulation maintains a linear gradient while the Langevin model captures the nonlinear locking behaviour that is desired. In Fig. 5.6b, $\frac{f}{k\theta}$ is plotted against the chain stretch for varying values of the persistence length, A. The wormlike model captures the asymptotic behaviour as $\lambda_{chain} \longrightarrow 1$ with a right shift as the persistence length is increased.

5.1.2 Chain Networks

In order to incorporate such chain models into a constitutive framework it is necessary to relate the individual chain stretch to the overall deformation. This is done by assuming a representative chain network structure.

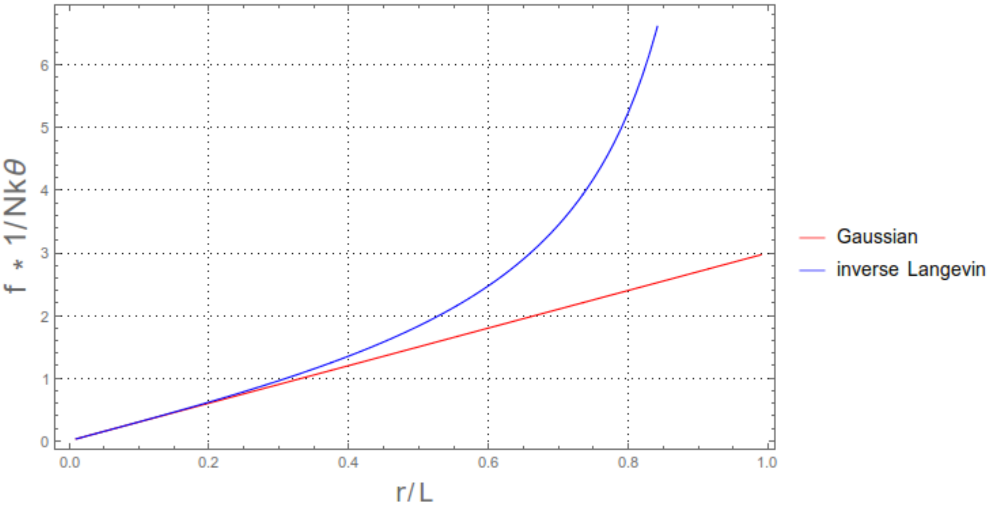

(a) Freely-jointed chain model. Comparison of Gaussian against the non-Gaussian.

Several chain network models have been proposed. The chains are arranged within a unit cell which is taken to deform according to the principal stretches. Each arrangement thus differs in how the deformation of the chains relates to the deformation of the unit cell. For example, the in “3-chain” model (Fig. 5.7a), the chains lie along the axes of the unit cell, thus the chain stretches correspond to the principal stretch values of the unit cell.

The “8-chain” network (Fig. 5.7c), as proposed by Arruda and Boyce (1993), has 8 chains placed along the diagonals of the the unit cell, connecting at a common point at the centre of the cell. Due to the symmetry of the chain structure, the stretch of each chain can be found as a function of the principle stretches.

Through a comparison of uniaxial and biaxial simulations with the Treloar data, Arruda and Boyce (1993) found that the 3- and 4-chain network models were able to capture the uniaxial results, but fail to provide a good prediction under biaxial tension. The 8-chain model was found to predict the

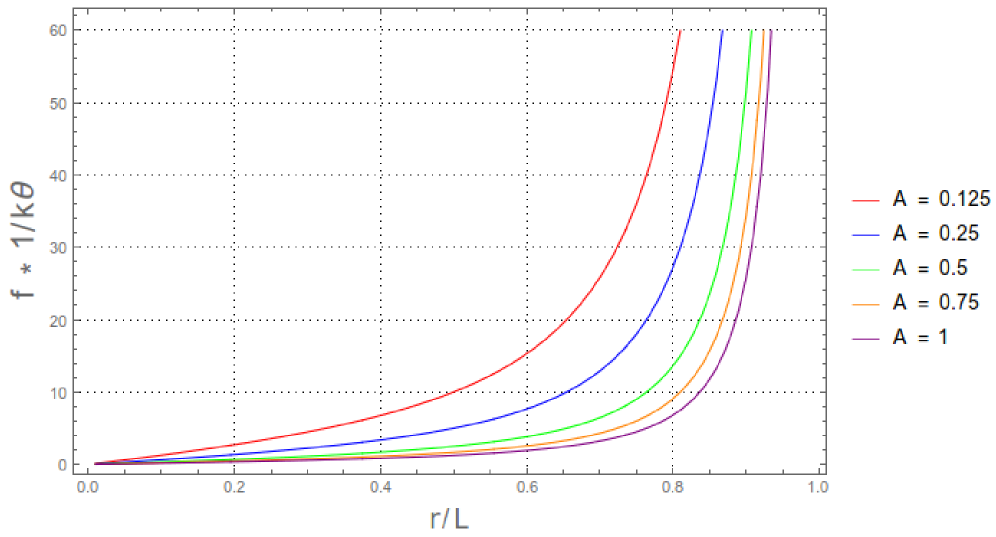

(b) Wormlike chain model at varying values of the persistence length.

Fig. 5.6: Comparison of freely-jointed and wormlike chain models at increasing stretch.

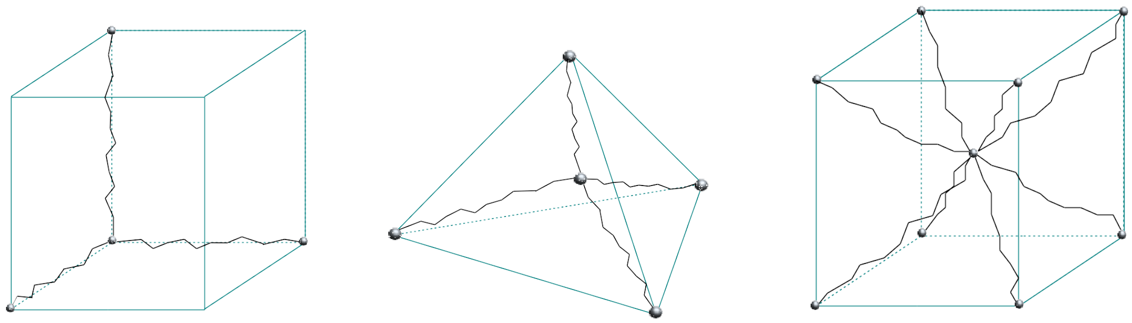

(a) 3-chain network

(b) 4-chain network

(c) 8-chain network

Fig. 5.7: Comparison of chain network assemblies

behaviour under both uniaxial and biaxial tension tests. The predictive ability of the 8-chain arrangement is due to the cooperative manner in which the chains are able to deform and rotate toward the maximum stretch axes. Due to this, the 8-chain network provides a suitable configuration for modelling collagen networks and will be adopted in this work.

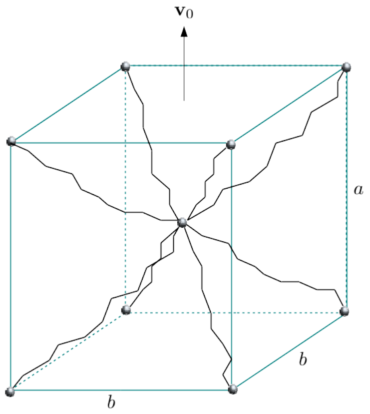

Fig. 5.8: 8-chain network dimensions, a and b, with unit vector $\mathbf{v}_0$ corresponding to the preferred orientation of the collagen network.

In Fig. 5.8, a cell arrangement of dimensions $a \times b \times b$ is depicted. For the case of anisotropy, $a \neq b$. The model is reduced to an isotropic case by setting $a = b$. Additionally, the unit cell is characterised by a unit vector $\mathbf{v}_0$ that corresponds to the preferred orientation of the collagen network. The end-to-end length of the chains is given by

$$r_0 = \frac{1}{2}\sqrt{a^2 + 2b^2}. \tag{5.5}$$

Consider a deformation as depicted in Fig. 5.9 where the cell dimensions undergo a stretch that correspond to the principal stretches. The new end-to-end length can be calculated as:

$$r = \frac{1}{2}\sqrt{\lambda_1^2 a^2 + (\lambda_2^2 + \lambda_3^2) b^2}. \tag{5.6}$$

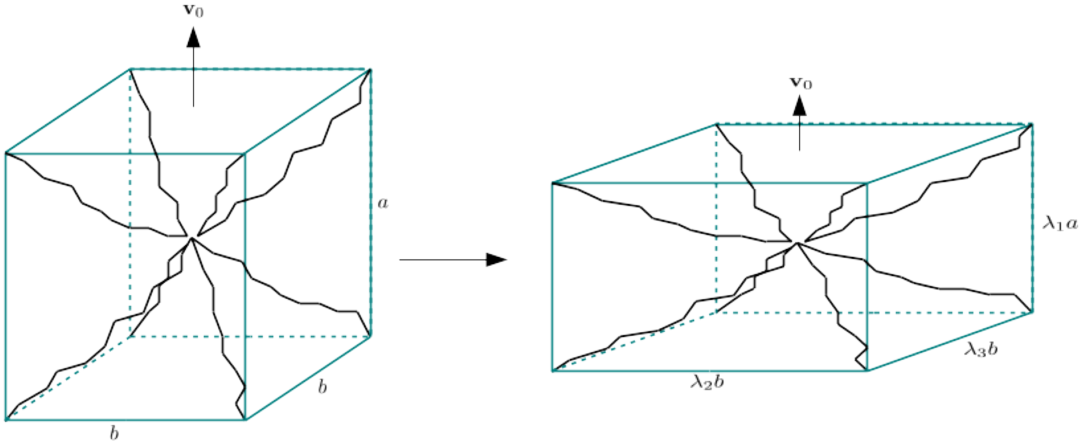

Fig. 5.9: 8-chain network dimensions under deformation. Each dimension is stetched by the corresponding principal stretch value.

With reference to Eq. (4.36), $I_4 = \lambda_1^2$ and noting that $I_1 = \mathbf{I} : \mathbf{C} = \lambda_1^2 + \lambda_2^2 + \lambda_3^2$, Eq. (5.6) can be written as

$$r = \frac{1}{2}\sqrt{I_4 a^2 + (I_1 - I_4) b^2}. \tag{5.7}$$

The final term of Eq. (5.1), $\mathit{\Psi}_{col}$, is further decomposed into the additive form

$$\mathit{\Psi}_{\text{col}} = \mathit{\Psi}_{\text{chn}} + \mathit{\Psi}_{\text{rep}},$$

where $\mathit{\Psi}_{\text{chn}}$ reflects the effective assembly of the eight chain energies, i.e. $\mathit{\Psi}_{\text{chn}} := \gamma_{\text{chn}} \mathit{\Psi}_{\text{wormlike}}$ and $\mathit{\Psi}_{\text{rep}}$ is a repulsive energy that ensures that the initial configuration is stress free and that the chain does not collapse. γ_{chn} denotes the chain density per unit cell. Saez et al. (2013b) interprets this as the number of molecules within a collagen fibril, while Bischoff et al. (2000) describes it as the collagen fibre density and in the context of collagen, this corresponds to the number of fibres within a bundle. Thus

$$\begin{aligned} \mathit{\Psi}_{\text{chn}} &= \frac{\gamma_{\text{chn}} k L \theta}{4A}\left(2\frac{r^2}{L^2} + \frac{1}{1-\frac{r}{L}} - \frac{r}{L}\right), \\ \mathit{\Psi}_{\text{rep}} &= -\frac{\gamma_{\text{chn}} k \theta}{4A}\left(\frac{1}{L} + \frac{1}{4r_0}\frac{1}{1-\frac{r_0}{L}} - \frac{1}{4r_0}\right)\left(\ln\left(I_4^{[a^2-b^2]/2}\right) + \frac{3}{2}\ln\left(I_1^{b^2}\right)\right). \end{aligned} \tag{5.8}$$

All length quantities in Eq. (5.8) have been normalised through division by the link length. The parameter interpretations and units are give in Table 5.3.

Parameter	Symbol	Units
Boltzmann constant	k	$\mathrm{J\,K^{-1}}$
Absolute temperature	θ	K
Chain density	γ_{chn}	$\mathrm{m^{-3}}$
Contour length	L	-
Persistence length	A	-
Unit cell dimensions	a, b	-

Table 5.3: 8-chain constitutive parameters, symbol and units

5.1.3 A Note on Entroptic Elastic vs Energetic Elastic Models

With reference to Holzapfel (2000), for the case of an ideal rubber, where the property of incompressibility is a defining property, the retractive force is purely as a result of changes in entropy. That is also to say that the internal energy does not change during deformation. Such a rubber-like material is what is referred to as a *entropic elastic* material. Counter to this, a material for which deformation occurs through rapid changes in internal energy and where entropy does not change are referred to as *energetic elastic* materials.

Given the structure of collagen, it is appealing to use an entropic elastic material model as discussed, and it might be the case that this is appropriate. But it is not clear whether the highly bonded and hierarchical structure of collagen allows degrees of freedom for all states to be sampled in an entropy-dominated regime. However, energetic elasticity models can also model the stiffening behaviour by to uncoiling of crimps (See Garikipati et al. (2008) for a detailed implementation of energetic elasticity).

6

Numerical Model

In Chapter 4, the equations governing the response of a continuum were derived. The concept of a free energy function, Ψ, was introduced with the idea that the stress state of a hyperelastic material could be derived from a scalar-valued free energy. In Chapter 5, the form of a free energy function for skin was motivated through structural arguments.

In this chapter, in order to solve the governing equations with the constitutive relations appropriate for skin, the finite element method is introduced. Concepts such as the minimisation of a potential and linearisation are discussed and presented within the finite element framework.

6.1 Finite Element Method

Generally an analytical solution to a boundary value problem is not possible to find and approximate solutions need to be generated through strategies such as the finite element method, which are built on the basis of variational principles.

In order to solve the given problem, it is essential that robust discretisation techniques be employed. One such technique is that of the *finite element method*, which has become one of the most widely used numerical techniques for generating approximate solutions to a wide range of initial boundary-value problems.
Variational principles are often applied in the development of the finite element method, thus it is important that the fundamental principles of variational techniques be understood.

6.1.1 Virtual Displacements

Consider a continuum body B with a continuum particle $P \in B$. A particle is described by position vectors $\mathbf{X}$ at time $t = 0$ in the reference configuration and $\mathbf{x}$ at time $t > 0$ in the current configuration. The displacement of P is thus described by $\mathbf{u} = \mathbf{x} - \mathbf{X}$. It must be noted that for ease of notation and due to displacement being frame invariant, $\mathbf{u} = \mathbf{u}(\mathbf{x}, t) = \mathbf{U}(\mathbf{X}, t)$, thus the configuration of interest should be understood from context.

Now consider an arbitrary displacement $\mathbf{w}$ of the current configuration which results in a *virtual* deformed configuration in the neighbourhood of $\mathbf{u}$ characterised by the displacement vector:

$$\bar{\mathbf{u}} = \mathbf{u} + \epsilon \mathbf{w},$$

where ϵ is some infinitesimal scalar value.

The difference between $\bar{\mathbf{u}}$ and $\mathbf{u}$ is referred to as the *virtual displacement* or the *first variation* of field $\mathbf{u}$, which is denoted $\delta \mathbf{u}$:

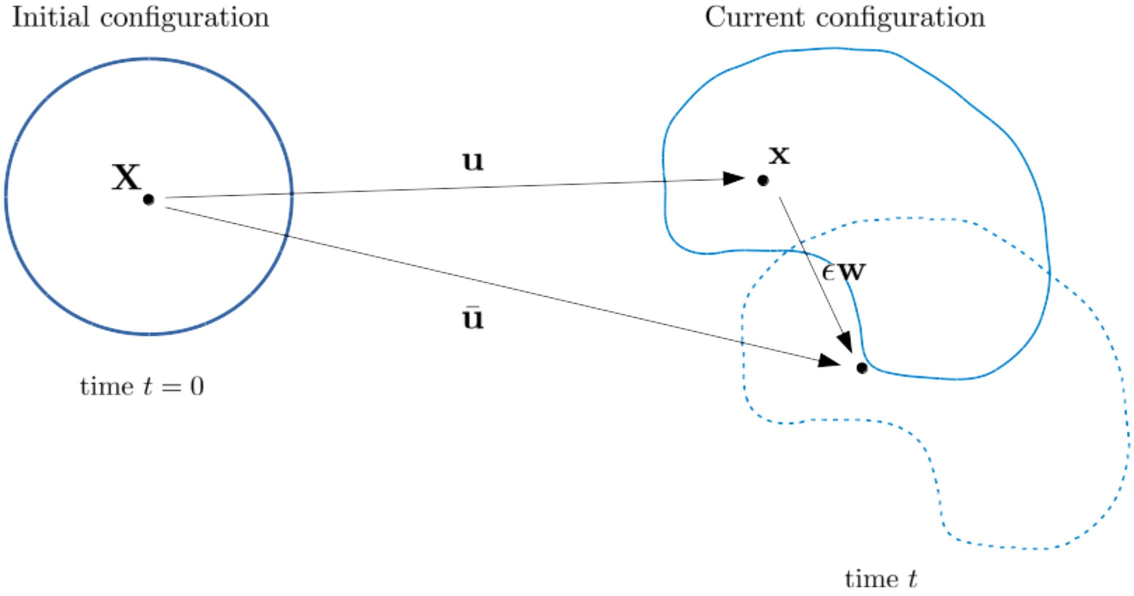

Fig. 6.1: Depiction of virtual displacement.

$$\delta\mathbf{u} = \bar{\mathbf{u}} - \mathbf{u} = \epsilon\mathbf{w}.$$

$\delta\mathbf{u}$ represents an arbitrary, infinitesimal virtual change. It is important to note that similarly to $\mathbf{u}$, $\delta\mathbf{u}$ can be expressed in spatial of material coordinates, i.e. $\delta\mathbf{u} = \delta\mathbf{u}(\mathbf{X}) = \delta\mathbf{u}(\mathbf{x})$.

First Variation of a Function in the Material Description

Let $f = f(\mathbf{u})$ be some smooth vector function of the material displacement vector $\mathbf{u}$. In order to obtain the first variation of f, the directional derivative of $f(\mathbf{u})$ at any fixed $\mathbf{u}$ in the direction $\delta\mathbf{u}$ must be evaluated as

$$\delta f(\mathbf{u}, \delta\mathbf{u}) = \frac{d}{d\epsilon} f(\mathbf{u} + \epsilon\delta\mathbf{u})|_{\epsilon=0}.$$

6.1.2 Principle of Virtual Work

In previous sections, the governing equation was established through the balance of linear momentum in the material configuration, see Eq. (4.17). In what follows, a quasi-static system is assumed; $\dot{\mathbf{V}} = \mathbf{0}$ In order to solve the governing system, the boundary conditions need to be fully defined. The reference boundary $\partial\Omega_0$ is thus assumed to be decomposed into disjoint parts $\partial\Omega_U$ and $\partial\Omega_T$ where:

$$\partial\Omega_0 = \partial\Omega_U \cup \partial\Omega_T \qquad \text{and} \qquad \partial\Omega_U \cap \partial\Omega_T = \emptyset$$

The boundaries $\partial\Omega_U$ and $\partial\Omega_T$ are referred to as *Dirichlet* and *Neumann* boundaries, respectively. On Dirichlet boundaries, a prescribed displacement $\bar{\mathbf{U}}$ is enforced while on Neumann boundaries a surface traction $\bar{\mathbf{T}}$ is imposed. Eq. (4.17) combined with the boundary conditions form what is known as the *strong form* of the problem, stated fully as

$$\begin{aligned} \mathrm{Div}\mathbf{P} + \mathbf{B} &= \mathbf{0} && \\ \mathbf{U} &= \bar{\mathbf{U}} && \text{on} \quad \partial\Omega_U \\ \mathbf{T} = \mathbf{PN} &= \bar{\mathbf{T}} && \text{on} \quad \partial\Omega_T. \end{aligned} \tag{6.1}$$

Equivalently, with reference to Eq. (4.16), the strong form given in the current configuration is stated as

$$\begin{aligned} \mathrm{div}\boldsymbol{\sigma} + \mathbf{b} &= \mathbf{0} \\ \mathbf{u} &= \bar{\mathbf{u}} \qquad \text{on} \qquad \partial\Omega_u \\ \mathbf{t} = \boldsymbol{\sigma}\mathbf{n} &= \bar{\mathbf{t}} \qquad \text{on} \qquad \partial\Omega_t, \end{aligned} \tag{6.2}$$

where the current boundary $\partial\Omega$ is disjointly decomposed into a Neumann boundary $\partial\Omega_t$ and Dirichlet boundary $\partial\Omega_u$

Consider the strong from Eq. (6.1). In order to develop the principle of virtual work, the balance of linear momentum is multiplied by an arbitrary vector-valued function $\mathbf{w} = \mathbf{w}(\mathbf{X})$, with placement in the current configuration but parametrised in terms of the reference configuration, Ω_0. Integration over Ω_0 of the subsequent equation yields

$$G(\mathbf{U}, \mathbf{w}) = \int_{\Omega_0} (\mathrm{Div}\mathbf{P} + \mathbf{B}) \cdot \mathbf{w} dV = 0. \tag{6.3}$$

$\mathbf{w}$ is referred to as a test or weighting function, and is an arbitrary, sufficiently smooth function with $\mathbf{w} = \mathbf{0}$ on $\partial\Omega_u$. As $\mathbf{w}$ is arbitrary, the strong form of the equation is equivalent to Eq. (6.3).

Applying integration by parts to the first term of the integral, Eq. (6.3) can be simplified to

$$G(\mathbf{U}, \mathbf{w}) = \int_{\Omega_0} (\mathbf{P} : \mathrm{Grad}\mathbf{w} - \mathbf{B} \cdot \mathbf{w}) dV - \int_{\partial\Omega_0} \mathbf{P}\mathbf{N} \cdot \mathbf{w} dA = 0.$$

As $\mathbf{w} = \mathbf{0}$ on $\partial\Omega_U$, the last term need only be evaluated over $\partial\Omega_T$. Substituting in the traction boundary condition, the full form of the variational problem is given by

$$G(\mathbf{U}, \mathbf{w}) = \int_{\Omega_0} (\mathbf{P} : \mathrm{Grad}\mathbf{w} - \mathbf{B} \cdot \mathbf{w}) dV - \int_{\partial\Omega_T} \bar{\mathbf{T}} \cdot \mathbf{w} dA = 0.$$

This is referred to as the *weak form* of the boundary value problem.

Note here that the test function $\mathbf{w}$ is arbitrary. Thus $\mathbf{w}$ can be conveniently taken as the virtual displacement $\delta\mathbf{u}$, parametrised in terms of the reference placement. With this, the weak form can be rewritten as:

$$G(\mathbf{U}, \delta\mathbf{u}) = \int_{\Omega_0} (\mathbf{P} : \mathrm{Grad}\delta\mathbf{u} - \mathbf{B} \cdot \delta\mathbf{u}) dV - \int_{\partial\Omega_T} \bar{\mathbf{T}} \cdot \delta\mathbf{u} dA = 0, \tag{6.4}$$

where it is required that $\delta\mathbf{u}$ vanish on boundaries $\partial\Omega_U$ where the displacement is prescribed. This is commonly referred to as the *principle of virtual work.*

For completeness, the principle of virtual work is stated here in the current configuration:

$$g(\mathbf{u}, \delta\mathbf{u}) = \int_{\Omega} (\boldsymbol{\sigma} : \mathrm{grad}\delta\mathbf{u} - \mathbf{b} \cdot \delta\mathbf{u}) dv - \int_{\partial\Omega_t} \bar{\mathbf{t}} \cdot \delta\mathbf{u} ds = 0 \tag{6.5}$$

A Note on Continuity and Completeness

In order for the weak form as given in Eq. (6.4) to be valid, it is necessary that the highest derivatives that appear be integrable. This is to ensure that all integrals exist. Thus for a problem where the highest derivative is of order $m + 1$ it is necessary that variables be C^m continuous, i.e. that all derivatives up to order m exist and are continuous over the whole domain.

In the above problem, the highest order derivative is of first order, thus C^0 functions are required. As a stricter requirement, it is required that all functions be elements of the $H^1(\Omega_0)$ function space:

$$H^1(\Omega_0) = \left\{ f(\mathbf{X}) | f \in L^2, \mathrm{Grad} f \in L^2 \right\},$$

where

$$L^2(\Omega_0) = \left\{ g(\mathbf{X}) | \left(\int_{\Omega_0} |g|^2 dV \right)^{\frac{1}{2}} < \infty \right\}.$$

Additionally, it is required that all variables within the weak form, as well as their derivatives up to the highest order, be capable of assuming constant values. That is to say that all C^m functions be complete up to order $m+1$.

6.1.3 Principle of Stationary Potential Energy

The form of the principle of virtual work as given by Eq. (6.4) does not take into account any particular material or loading and is thus generally applicable to any. Here, a conservative mechanical system is assumed requiring the existence of an energy functional Π for both the stresses and the loads. This is as introduced in Sec. 4.1.5.

For now, it is assumed that all loads are independent of the motion. That is to say that $\bar{\mathbf{T}} \neq \bar{\mathbf{T}}(\mathbf{U})$ and $\mathbf{B} \neq \mathbf{B}(\mathbf{U})$. The total potential energy of the system is thus given as the sum of the internal and external energies, defined in the reference configuration by

$$\Pi(\mathbf{U}) = \Pi_{\text{int}}(\mathbf{U}) + \Pi_{\text{ext}}(\mathbf{U}),$$

where

$$\Pi_{\text{int}}(\mathbf{U}) = \int_{\Omega_0} \Psi(\mathbf{F}(\mathbf{U}))dV \qquad \text{and} \qquad \Pi_{\text{ext}}(\mathbf{U}) = -\int_{\Omega_0} \mathbf{B}\cdot\mathbf{U}dV - \int_{\partial\Omega_T} \bar{\mathbf{T}}\cdot\mathbf{U}dA.$$

As introduced in Sec. 4.2.1, $\Psi = \Psi(\mathbf{F})$ is the free energy defined per unit volume.

It is important to note that the energies are assumed to be purely functions of the displacements vis $\mathbf{F}$. The idea is to find a state for which the potential is stationary which is the same as requiring the directional derivative with respect to $\mathbf{U}$ to vanish in all directions $\delta\mathbf{u}$:

$$\delta\Pi(\mathbf{U}, \delta\mathbf{u}) = \frac{d}{d\epsilon}\Pi(\mathbf{U} + \delta\mathbf{u})|_{\epsilon=0} = 0.$$

This is what is known as the *principle of stationary energy.* It is important to note that the arbitrary vector field $\delta\mathbf{u}$ is consistent with the restrictions imposed on the continuum body in that $\delta\mathbf{u} = \mathbf{0}$ on $\delta\Omega_U$.

Calculating the directional derivative of Π, noting that by assumption $\frac{d}{d\epsilon}\mathbf{B} = 0$ and $\frac{d}{d\epsilon}\bar{\mathbf{T}} = 0$, yields

$$\begin{aligned}
\delta\Pi(\mathbf{U}, \delta\mathbf{u}) &= \frac{d}{d\epsilon}\Pi(\mathbf{U} + \epsilon\delta\mathbf{u})|_{\epsilon=0} \\
&= \frac{d}{d\epsilon}\left[\int_{\Omega_0} \Psi(\mathbf{F}(\mathbf{U} + \epsilon\delta\mathbf{u}))dV - \int_{\Omega_0} \mathbf{B}\cdot(\mathbf{U} + \epsilon\delta\mathbf{u})dV - \int_{\partial\Omega_T} \bar{\mathbf{T}}\cdot(\mathbf{U} + \epsilon\delta\mathbf{u})dA\right]|_{\epsilon=0} \\
&= \int_{\Omega_0} \frac{\partial\Psi}{\partial\mathbf{F}} : \delta\mathbf{F}dV - \int_{\Omega_0} \mathbf{B}\cdot\delta\mathbf{u}dV - \int_{\partial\Omega_T} \bar{\mathbf{T}}\cdot\delta\mathbf{u}dA
\end{aligned}$$

Using $\mathbf{P} = \frac{\partial\Psi}{\partial\mathbf{F}}$ from Sec. 4.2.1 and the following identity:

$$\begin{aligned}
\delta\mathbf{F} &= \delta(\text{Grad}\mathbf{U} + \mathbf{I}) \\
&= \frac{d}{d\epsilon}(\text{Grad}(\mathbf{U} + \epsilon\delta\mathbf{u}) + \mathbf{I})|_{\epsilon=0} \\
&= \text{Grad}\delta\mathbf{u},
\end{aligned}$$

the first variation of Π is given by

$$\delta\Pi = \int_{\Omega_0} \mathbf{P} : \text{Grad}\delta\mathbf{u}dV - \int_{\Omega_0} \mathbf{B}\cdot\delta\mathbf{u}dV - \int_{\partial\Omega_T} \bar{\mathbf{T}}\cdot\delta\mathbf{u}dA.$$

Therefore is has been shown that solving for the stationary point of the potential Π, i.e. $\delta\Pi = 0$, gives the solution for the principle of virtual work Eq. (6.4) for a static body.

6.1.4 Linearisation

Due to the inherent nonlinear nature of problems in biomechanics where nonlinearities occur due to geometric and material sources, a solution cannot be found directly. Therefore it is necessary to reduce the problem to a series of linear problems which can be solved iteratively to approximate the full nonlinear solution.

One such iterative scheme is the *Newton-Raphson* algorithm. Essentially a linear Taylor approximation, the scheme is developed as follows.
Assume some well-defined function $R(\mathbf{d}) = 0$, where $\mathbf{d}$ is a collection of scalar or vector-valued functions. $R(\mathbf{d})$ is expanded as

$$R(\mathbf{d}, \Delta\mathbf{d}) = R(\mathbf{d}) + \Delta R(\mathbf{d}, \Delta\mathbf{d}) + \mathcal{O}(\Delta\mathbf{d}),$$

where $\mathcal{O}(\Delta\mathbf{d}) \to 0$ faster than $\Delta\mathbf{d} \to 0$. $\Delta\mathbf{d}$ is the increment of field $\mathbf{d}$. The first term of the right hand side represents the constant part for a given $\mathbf{d}$ while the second term represents a linear change due to $\Delta\mathbf{d}$. Dropping the higher order terms yields

$$R(\mathbf{d}, \Delta\mathbf{d}) \equiv R(\mathbf{d}) + \Delta R(\mathbf{d}, \Delta\mathbf{d}).$$

It is thus desired that some $\mathbf{d}^*$ be found such that

$$\begin{aligned} &R(\mathbf{d}^*, \Delta\mathbf{d}) \doteq 0 \\ &\Rightarrow 0 = R(\mathbf{d}) + \Delta R(\mathbf{d}, \Delta\mathbf{d}). \end{aligned}$$

In the above, $R(\mathbf{d})$ is referred to as the residual and $\Delta R(\mathbf{d}, \Delta\mathbf{d})$ as the tangent. The tangent is calculated as the directional derivative of R at some fixed $\mathbf{d}$ in the direction $\Delta\mathbf{d}$:

$$\Delta R(\mathbf{d}, \Delta\mathbf{d}) = \frac{d}{d\epsilon} R(\mathbf{d} + \epsilon\Delta\mathbf{d})|_{\epsilon=0}. \tag{6.6}$$

The resulting system is then solved for the increment $\Delta\mathbf{d}$. From this an iterative scheme is developed:

$$\begin{aligned} \Delta R(\mathbf{d}_{(i)}, \Delta\mathbf{d}_{(i)}) &= -R(\mathbf{d}_{(i)}) \\ \Delta\mathbf{d}_{(i)} &= \mathbf{d}_{(i+1)} - \mathbf{d}_{(i)}, \end{aligned} \tag{6.7}$$

where the subscript (i) indicates the current iteration and $(i+1)$ indicates the next iteration. The counter i starts at 0 where $\mathbf{d}_0$ represents an initial guess to the solution. This procedure is repeated until a norm of the residual term comes within some desired tolerance:

$$|R(\mathbf{d}, \Delta\mathbf{d})| \begin{cases} > \text{tolerance, iterate.} \\ < \text{tolerance}, \mathbf{d}_{(i+1)} \text{ is the solution.} \end{cases}$$

The Newton-Raphson scheme offers a robust method, provided that the guess is in the region of convergence, that displays quadratic convergence to the desired solution.

If the principle of virtual work Eq. (6.4) is set as the residual, where $\mathbf{U}$ is the solution variable then

$$R(\mathbf{U}) = \int_{\Omega_0} \mathbf{P} : \text{Grad}\delta\mathbf{u} dV - \int_{\Omega_0} \mathbf{B} \cdot \delta\mathbf{u} dV - \int_{\partial\Omega_T} \bar{\mathbf{T}} \cdot \delta\mathbf{u} dA. \tag{6.8}$$

With reference to Eq. (6.6) and due to the assumption of body forces and traction independent of the deformation, the only contribution to the linearisation of R comes from the first term, thus

$$\begin{aligned} \Delta R(\mathbf{U}, \Delta\mathbf{u}) &= \frac{d}{d\epsilon} R(\mathbf{U} + \epsilon\Delta\mathbf{u})|_{\epsilon=0} \\ &= \frac{d}{d\epsilon}\left[\int_{\Omega_0} \mathbf{P}(\mathbf{F}(\mathbf{U} + \epsilon\Delta\mathbf{u})) : \text{Grad}\delta\mathbf{u} dV\right]|_{\epsilon=0} \\ &= \int_{\Omega_0} \text{Grad}\delta\mathbf{u} : \frac{\partial\mathbf{P}}{\partial\mathbf{F}} : \Delta\mathbf{F}(\mathbf{U}, \Delta\mathbf{u}) dV \\ &= \int_{\Omega_0} \text{Grad}\delta\mathbf{u} : \mathbb{A} : \text{Grad}\Delta\mathbf{u} dV, \end{aligned} \tag{6.9}$$

where $\Delta \mathbf{u}$ is the increment of $\mathbf{U}$ defined in the reference configuration and $\mathbb{A} = \frac{\partial \mathbf{P}}{\partial \mathbf{F}} = \frac{\partial^2 \Psi}{\partial \mathbf{F} \partial \mathbf{F}}$ is a mixed 4^{th} order elasticity tensor[1].

6.1.5 Spatial Discretisation using Finite Elements

As mentioned, there are few problems where an analytical solution may exist. Thus it is essential that robust solution techniques be employed such that a solution can be found. In the previous sections, a variational (weak) form was developed. It can be shown that corresponding to the weak form there exists a solution $\mathbf{U}(\mathbf{X})$ defined on the reference configuration and defined for all $\mathbf{X} \in \Omega_0$. In order to simplify the problem, the domain, which can be arbitrary in shape, needs to be reduced to smaller, repeatable simpler domains. To accomplish this through the finite element method, the domain Ω_0 is subdivided into cells that define a mesh. These cells are alternatively referred to as elements. The full domain is thus approximated through this union of elements $\{\Omega_0^e\}$, such that

$$\Omega_0 \approx \bigcup_e \Omega_0^e,$$

where Ω_0^e refers to element e, as depicted in Fig. 6.2.
The discretisation of the domain results in a discretisation of the boundary into surface elements $\{\partial \Omega_0^{et}\}$:

$$\partial \Omega_0 \approx \bigcup_{et} \partial \Omega_0^{et},$$

where $\partial \Omega_0^{et}$ refers to elemental boundary et.

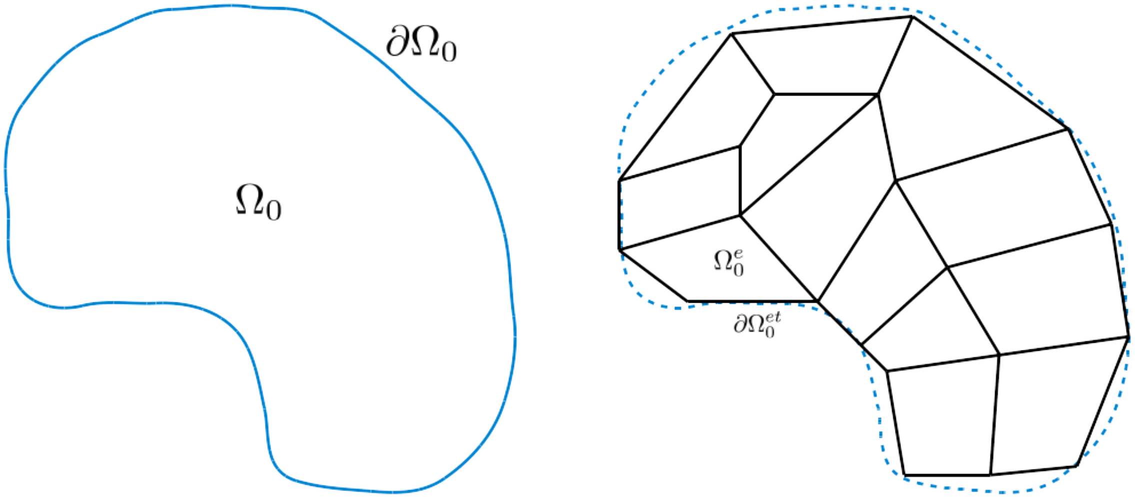

Fig. 6.2: Depiction of the discretisation of the domain into elements.

Thus the weak form can be written as a sum over the elemental domains:

$$\sum_e \left[\int_{\Omega_0^e} (\mathbf{P} : \mathrm{Grad}\delta\mathbf{u} - \mathbf{B} \cdot \delta\mathbf{u}) dV \right] - \sum_{et} \left[\int_{\partial\Omega_T^{et}} \bar{\mathbf{T}} \cdot \delta\mathbf{u} dA \right] = 0,$$

where the summation here is understood as an assembly of the full domain.

---

[1] $\mathbf{B} : \mathbb{A} : \mathbf{C} = (\mathbb{A} : \mathbf{B}) : \mathbf{C}$

Shape Functions

The issue still remains that there exist infinitely many points on the problem domain, which a computer is unable to handle. Thus a discretisation method needs be introduced so as to reduce the problem to a finite dimension.
In order to achieve this the variables within the problem are approximated through a linear combination of polynomial functions of $\mathbf{X}$. Thus for some scalar-valued variable $V(\mathbf{X})$ defined on the reference domain, the following approximation is employed:

$$V(\mathbf{X}) \approx V^h(\mathbf{X}) = \sum_{a=1}^{\mathrm{N}} V_a \varphi_a(\mathbf{X}),$$

and similarly for some vector-valued variable $\mathbf{V}(\mathbf{X})$ defined on the reference domain,

$$\mathbf{V}(\mathbf{X}) \approx \mathbf{V}^h(\mathbf{X}) = \sum_{a=1}^{\mathrm{N}} V_a \boldsymbol{\varphi}_a(\mathbf{X}), \tag{6.10}$$

where $\varphi_a(\mathbf{X})$ and $\boldsymbol{\varphi}_a(\mathbf{X})$ are referred to as shape functions[2] and V_a represent N unknown coefficients defined at discrete points over the domain. These points are referred to as nodal points or nodes and are generally positioned such as to aid continuity.

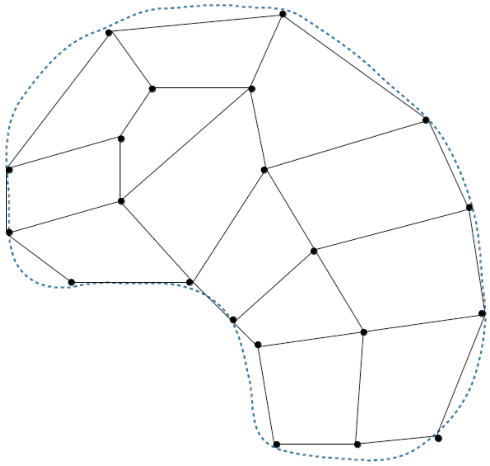

Fig. 6.3: 2D Example of Nodal Positions.

Applying this approximation to the displacement variables and the virtual displacements, yields the following global approximations

---

[2] In 2D, vector-valued shape functions are viewed as follows:

$$\begin{aligned} \mathbf{V}(\mathbf{X}) &= \begin{bmatrix} V_x \\ V_y \end{bmatrix} \\ &\approx \underbrace{\begin{bmatrix} \varphi_1 \\ 0 \end{bmatrix}}_{\boldsymbol{\varphi}_1} V_1 + \underbrace{\begin{bmatrix} 0 \\ \varphi_1 \end{bmatrix}}_{\boldsymbol{\varphi}_2} V_2 + ... + \underbrace{\begin{bmatrix} 0 \\ \varphi_{ndof/2} \end{bmatrix}}_{\boldsymbol{\varphi}_{\mathrm{N}}} V_{\mathrm{N}}, \end{aligned}$$

where φ_j are the scalar-valued shape functions.

$$
\begin{aligned}
&\mathbf{U}(\mathbf{X}) \approx \mathbf{U}^h(\mathbf{X}) = \sum_{a=1}^{\text{ndofs}} \boldsymbol{\varphi}_a(\mathbf{X}) U_a \\
&\delta\mathbf{u}(\mathbf{X}) \approx \delta\mathbf{u}^h(\mathbf{X}) = \sum_{a=1}^{\text{ndofs}} \boldsymbol{\varphi}_a(\mathbf{X}) \delta u_a \\
&\Delta\mathbf{u}(\mathbf{X}) \approx \Delta\mathbf{u}^h(\mathbf{X}) = \sum_{a=1}^{\text{ndofs}} \boldsymbol{\varphi}_a(\mathbf{X}) \Delta u_a \\
&\text{Grad}\delta\mathbf{u}(\mathbf{X}) \approx \text{Grad}\delta\mathbf{u}^h(\mathbf{X}) = \sum_{a=1}^{\text{ndofs}} \text{Grad}\boldsymbol{\varphi}_a(\mathbf{X}) \delta u_a \\
&\text{Grad}\Delta\mathbf{u}(\mathbf{X}) \approx \text{Grad}\Delta\mathbf{u}^h(\mathbf{X}) = \sum_{a=1}^{\text{ndofs}} \text{Grad}\boldsymbol{\varphi}_a(\mathbf{X}) \Delta u_a.
\end{aligned}
$$

where ndofs refers to the global number of degrees of freedom. This is referred to as the *Galerkin method.*

Applying these approximations to the Newton-Raphson scheme Eq. (6.7), with the forms of the residual and tangent given by Eq. (6.8) and Eq. (6.9), respectively, the following scheme element-wise is developed

$$
\begin{aligned}
&\Delta R(\mathbf{X}_{(i)}, \Delta\mathbf{X}_{(i)}) = -R(\mathbf{X}_{(i)}) \\
&\Rightarrow \sum_{a=1}^{\text{ndofs}} \sum_{b=1}^{\text{ndofs}} \int_{\Omega_0} \text{Grad}\boldsymbol{\varphi}_a \delta u_a : \mathbb{A} : \text{Grad}\boldsymbol{\varphi}_b \Delta u_b dV \\
&= - \sum_{a=1}^{\text{ndofs}} \left(\int_{\Omega_0} \text{Grad}\boldsymbol{\varphi}_a \delta u_a : \mathbf{P} dV - \int_{\Omega_0} \boldsymbol{\varphi}_a \delta u_a \cdot \mathbf{B} dV - \int_{\partial\Omega_T} \boldsymbol{\varphi}_a \delta u_a \cdot \bar{\mathbf{T}} dA \right) \\
&\underbrace{\Rightarrow \sum_{a=1}^{\text{ndofs}} \sum_{b=1}^{\text{ndofs}} \int_{\Omega_0} \text{Grad}\boldsymbol{\varphi}_a : \mathbb{A} : \text{Grad}\boldsymbol{\varphi}_b dV}_{\mathbf{K}} \, \Delta u_b = \\
&\underbrace{- \sum_{a=1}^{\text{ndofs}} \left(\int_{\Omega_0} \text{Grad}\boldsymbol{\varphi}_a : \mathbf{P} dV - \int_{\Omega_0} \boldsymbol{\varphi}_a \cdot \mathbf{B} dV - \int_{\partial\Omega_T} \boldsymbol{\varphi}_a \cdot \bar{\mathbf{T}} dA \right)}_{\mathbf{R}} \\
&\mathbf{K}\Delta\mathbf{u} = -\mathbf{R},
\end{aligned}
\tag{6.11}
$$

where **K** and **R** are the tangent and residual matrices, respectively.

Mapping to the Reference Cell

As the shape of physical elements is arbitrary, defining a general form for the shape functions on the spatial domain is a difficult task. Thus it is necessary that the physical elements be mapped to a reference cell, depicted in 2D in Fig. 6.4. This reference element, Ω_ξ with boundary $\partial\Omega_\xi$, is defined on $\hat{\mathbf{x}} = \{\xi_i | i = 1...\text{dim}\}$. Basis functions $\hat{\varphi}(\hat{\mathbf{x}})$ can thus be generally defined[3] and the problem variables similarly approximated on an element through:

$$
V(\hat{\mathbf{x}}) \approx \hat{V}^h(\hat{\mathbf{x}}) = \sum_{a=1}^{\text{ndofe}} V_a \hat{\varphi}_a(\hat{\mathbf{x}}),
$$

---

[3] The form of the basis functions can be found in any introductory text on the FE method (Marsden et al., 1984).

where ndofe are the number of elemental degrees of freedom.

These basis functions $\hat{\varphi}(\hat{\mathbf{x}})$ can be used to define a linear mapping between the reference and physical domains through:

$$\mathbf{X}(\hat{\mathbf{x}}) = \sum_{a=1}^{\text{ndofe}} X_a \hat{\boldsymbol{\varphi}}_a(\hat{\mathbf{x}}),$$

where X_a are the physical nodal coordinates of node a.

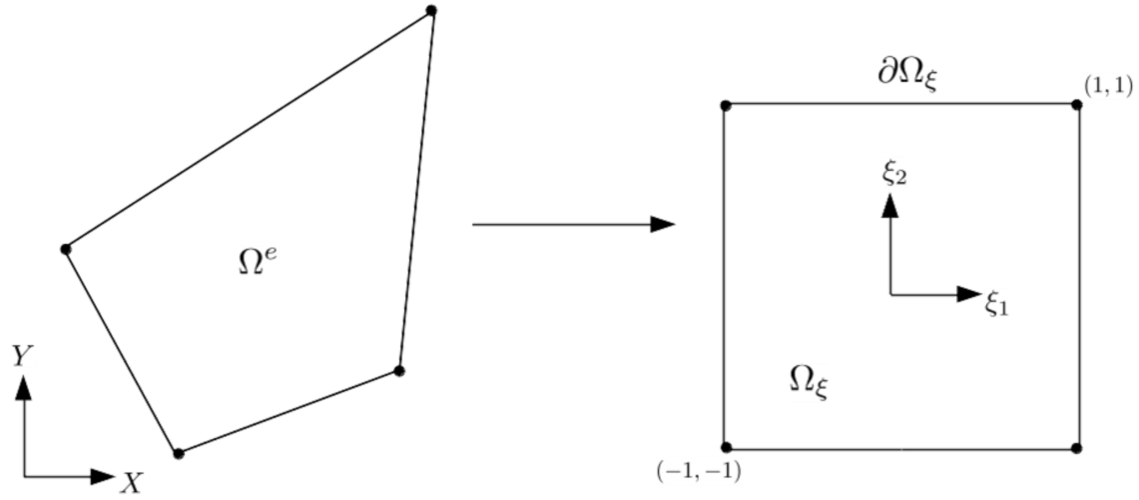

Fig. 6.4: Conversion between physical element to reference element in 2D.

Thus, the relation between the physical and reference shape functions is given by

$$\hat{\boldsymbol{\varphi}}_i(\hat{\mathbf{x}}) = \boldsymbol{\varphi}_i(\mathbf{X}(\hat{\mathbf{x}})).$$

This leads to the following relation of the gradient of $\hat{\boldsymbol{\varphi}}$ with respect to $\hat{\mathbf{x}}$:

$$\begin{aligned} \widehat{\text{Grad}}\hat{\boldsymbol{\varphi}} &= \frac{\partial \hat{\boldsymbol{\varphi}}}{\partial \hat{\mathbf{x}}} \\ &= \frac{\partial \boldsymbol{\varphi}}{\partial \mathbf{X}} \frac{\partial \mathbf{X}}{\partial \hat{\mathbf{x}}} \\ &\Rightarrow \text{Grad}\boldsymbol{\varphi} = \mathbf{J}^{-1}\widehat{\text{Grad}}\hat{\boldsymbol{\varphi}}, \end{aligned}$$

where $\mathbf{J}^{-1} = \frac{\partial \mathbf{x}}{\partial \hat{\mathbf{X}}}$ is the inverse of the Jacobian mapping.

Eq. (6.11) can be written on the reference element as:

$$\begin{aligned} &\Rightarrow \sum_{a=1}^{\text{ndofe}} \sum_{b=1}^{\text{ndofe}} \int_{\Omega_\xi} \mathbf{J}^{-1}\widehat{\text{Grad}}\hat{\boldsymbol{\varphi}}_a : \mathbb{A} : \mathbf{J}^{-1}\widehat{\text{Grad}}\hat{\boldsymbol{\varphi}}_b |\mathbf{J}| dV_\xi \Delta u_b \\ &= -\sum_{a=1}^{\text{node}} \left(\int_{\Omega_\xi} \mathbf{J}^{-1}\widehat{\text{Grad}}\hat{\boldsymbol{\varphi}}_a : \mathbf{P}|\mathbf{J}| dV_\xi - \int_{\Omega_\xi} \hat{\boldsymbol{\varphi}}_a \cdot \mathbf{B}|\mathbf{J}| dV_\xi - \int_{\partial\Omega_\xi^T} \hat{\boldsymbol{\varphi}}_a \cdot \bar{\mathbf{T}} |\text{jac}| dA_\xi \right), \end{aligned} \tag{6.12}$$

where the $\det\mathbf{J} = |\mathbf{J}|$ and $|\text{jac}|$ are the appropriate Jacobian transformations from the physical coordinate system to the reference domain.

6.1.6 Numerical Integration - Gauss Quadrature

In order to numerically compute the integrals that appear in Eq. (6.12), quadrature need be performed. The most convenient quadrature formula for polynomial expressions is that of Gauss-Legendre quadrature, or more commonly referred to as *Gauss quadrature*. Generally, Gauss quadrature performed over the domain $-1 < \xi_i < 1$ which is a further motivation as to why the shape functions are chosen to be defined on a bi-unit domain. Generally stated, Gauss quadrature for the integral of a 3D function $f = f(\xi_1, \xi_2, \xi_3)$ over the domain $\{\xi_i | i = 1...3, -1 < \xi_i < 1\}$ has the form:

$$\int_{-1}^{1}\int_{-1}^{1}\int_{-1}^{1} f(\xi_1,\xi_2,\xi_3)d\xi_1 d\xi_2 d\xi_3 \approx \sum_{j,k,l}^{n} w_i w_j w_k f(\xi_1^i, \xi_2^j, \xi_3^k),$$

where $\sum_{j,k,l}^{n} = \sum_{j}^{n}\sum_{k}^{n}\sum_{l}^{n}$.

The points $\xi_1^i, \xi_2^j, \xi_3^k$ refer to points at which the function is evaluated, and w_i, w_j, w_k are associated weights. The above formula is exact for polynomials less than order $2n$ in any direction.

Applying Gauss quadrature to Eq. (6.12) yields

$$\begin{aligned} &\Rightarrow \sum_{j=1}^{\text{ndofe}}\sum_{i=1}^{\text{ndofe}}\left[\sum_{A,B,C}^{n} w_A w_B w_C \left[\mathbf{J}^{-1}\widehat{\text{Grad}}\hat{\boldsymbol{\varphi}}_j : \mathbb{A} : \mathbf{J}^{-1}\widehat{\text{Grad}}\hat{\boldsymbol{\varphi}}_i|\mathbf{J}|\right]|_{(\xi_1^A,\xi_2^B,\xi_3^C)}\right]\Delta u_i \\ &= -\sum_{j=1}^{\text{ndofe}}\left(\left[\sum_{A,B,C}^{n} w_A w_B w_C \left[\mathbf{J}^{-1}\widehat{\text{Grad}}\hat{\boldsymbol{\varphi}}_j \cdot \mathbf{P}|\mathbf{J}| - \hat{\boldsymbol{\varphi}}_j \cdot \mathbf{B}|\mathbf{J}|\right]|_{(\xi_1^A,\xi_2^B,\xi_3^C)}\right]\right) \\ &+ \sum_{j=1}^{\text{ndofe}}\left(\left[\sum_{A,B}^{n} w_A w_B \left[\hat{\boldsymbol{\varphi}}_j \cdot \bar{\mathbf{T}}|\text{jac}|\right]|_{(\xi_1^A,\xi_2^B,\xi_3^C)}\right]\right). \end{aligned}$$

6.1.7 Pressure Loading Condition

Up until this point, all traction boundary conditions have been considered as *dead loads* where $\bar{\mathbf{T}} \neq \bar{\mathbf{T}}(\mathbf{U})$, $\bar{\mathbf{t}} \neq \bar{\mathbf{t}}(\mathbf{u})$. One important form of a traction condition dependent on the deformation of the body is a *pressure boundary loading*. The discussion here follows that detailed in Holzapfel (2000).

For convenience, consider a pressure applied on the traction boundary $\partial\Omega^t$ of the current configuration, Ω. For the case of a constant pressure, the prescribed traction $\bar{\mathbf{t}}$ is thus described by

$$\bar{\mathbf{t}} = \boldsymbol{\sigma}\mathbf{n} = p\mathbf{n} \tag{6.13}$$

where p is a constant scalar pressure, not dependent on the deformation, and $\mathbf{n} = \mathbf{n}(\mathbf{x})$ is the outward unit normal to $\partial\Omega^t$, see Fig. 6.5. As the orientation of $\mathbf{n}$ is dependent on the deformation of the body, changes in the geometry will result in changes in the equilibrium and an overall contribution to the residual terms.

Applying Eq. (6.13) to the traction term in Eq. (6.5):

$$\int_{\partial\Omega^t} \bar{\mathbf{t}} \cdot \delta\mathbf{u} da = p\int_{\partial\Omega^t} \mathbf{n} \cdot \delta\mathbf{u} da. \tag{6.14}$$

It is possible to perform a pull-back of Eq. (6.14) to the reference configuration using Eq. (4.4):

$$p\int_{\partial\Omega^t} \mathbf{n} \cdot \delta\mathbf{u} da = p\int_{\partial\Omega_0^t} J\mathbf{F}^{-T}\mathbf{N} \cdot \delta\mathbf{u} dA,$$

where $\delta \mathbf{u}$ is defined on the reference configuration. But in terms of the finite element implementation done here[4], it proves convenient to parametrise Eq. (6.14) in terms of the reference domain Ω_ξ, defined in 2D in terms of the coordinates $\hat{\mathbf{x}} = \{\xi_1, \xi_2\}$. By considering $\mathbf{n}da = d\mathbf{s}$ as a vector orientated in the direction normal to the surface:

$$d\mathbf{s} = \frac{d\mathbf{x}}{d\xi_1} \times \frac{d\mathbf{x}}{d\xi_2} d\xi_1 d\xi_2.$$

Applying this transformation to Eq. (6.14):

$$p \int_{\partial\Omega^t} \mathbf{n} \cdot \delta\mathbf{u} da = p \int_{\Omega_\xi} \left(\frac{d\mathbf{x}}{d\xi_1} \times \frac{d\mathbf{x}}{d\xi_2} \right) \cdot \delta\mathbf{u} d\xi_1 d\xi_2.$$

This form of the pressure loading is perfect for finite element discretisations as standard 2D Gauss quadrature can be performed on the reference domain Ω_ξ.

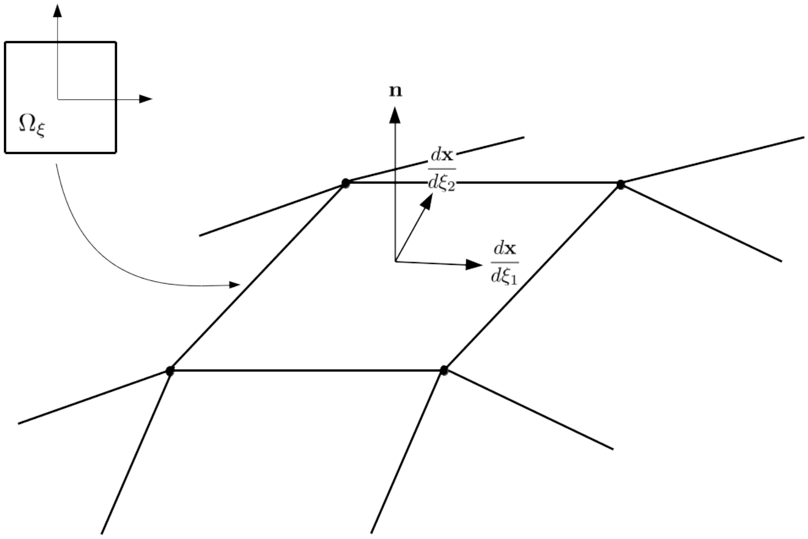

Fig. 6.5: Depiction of unit normal in parametrised domain

Linearisation

For dead loads due to the assumption that $\bar{\mathbf{t}} \neq \bar{\mathbf{t}}(\mathbf{u})$, there was no contribution to the tangent matrix from the traction term in the weak form. With a pressure loading condition this is no longer the case as

$$\frac{d}{d\epsilon} \left[p \int_{\partial\Omega^t} \mathbf{n} \cdot \delta\mathbf{u} da \right] |_{\epsilon=0} = \frac{d}{d\epsilon} \left[p \int_{\Omega_\xi} \left(\frac{d\mathbf{x}}{d\xi_1} \times \frac{d\mathbf{x}}{d\xi_2} \right) \cdot \delta\mathbf{u} d\xi_1 d\xi_2 \right] |_{\epsilon=0}.$$

As the reference domain is not dependent on the deformation, using the identity $\mathbf{x} = \mathbf{u} + \mathbf{X}$,

$$\begin{aligned} &\frac{d}{d\epsilon} \left[p \int_{\Omega_\xi} \left(\frac{d\mathbf{x}}{d\xi_1} \times \frac{d\mathbf{x}}{d\xi_2} \right) \cdot \delta\mathbf{u} d\xi_1 d\xi_2 \right] |_{\epsilon=0} \\ &= p \int_{\Omega_\xi} \frac{d}{d\epsilon} \left[\left(\frac{d}{d\xi_1} (\mathbf{u} + \epsilon \Delta\mathbf{u} + \mathbf{X}) \times \frac{d}{d\xi_2} (\mathbf{u} + \epsilon \Delta\mathbf{u} + \mathbf{X}) \right) \right] |_{\epsilon=0} \cdot \delta\mathbf{u} d\xi_1 d\xi_2 \\ &= p \int_{\Omega_\xi} \left[\left(\frac{d\Delta\mathbf{u}}{d\xi_1} \times \frac{d\mathbf{x}}{d\xi_2} \right) + \left(\frac{d\mathbf{x}}{d\xi_1} \times \frac{d\Delta\mathbf{u}}{d\xi_2} \right) \right] \cdot \delta\mathbf{u} d\xi_1 d\xi_2. \end{aligned}$$

---

[4] In the FE model developed here, the boundary of an element has limited knowledge of the fields within the element, making the computation of $\mathbf{F}$ of $\partial\Omega_0^t$ problematic

It must be noted here that the above contribution is not symmetric in $\delta\mathbf{u}$ and $\Delta\mathbf{u}$. Thus for finite element simulations the tangent matrix is in general not symmetric for cases of pressure loading conditions.

6.2 Numerical Implementation

6.2.1 Incremental Loading

As mentioned previously, the Newton-Raphson scheme offers a robust method that displays quadratic convergence to the desired solution. Convergence though only occurs within some radius of the solution point. Outside of this radius the scheme may diverge or converge to a different stationary point. In order to ensure that the scheme converges to the appropriate solution, incremental loading methods are employed. Through these schemes the traction boundary conditions and body forces are loaded incrementally through a λ^t parameter and solution steps are moderated by an adaptive value $\Delta\lambda^t$

$$\mathbf{d}_{(i+1)} = \mathbf{d}_{(i)} + \Delta\lambda^t \Delta\mathbf{d}_{(i)}.$$

The value λ is increased incrementally through $\lambda^t_{(i+1)} = \lambda^t_{(i)} + \Delta\lambda^t$ until the full boundary and body force loading has been applied, i.e. $\lambda^t = 1$. A Newton scheme is conducted for each increment of λ^t and the solution to the previous Newton scheme is used as the initial guess for the next.

With reference to Eq. (6.8), the modified and adaptive residual can be expressed as

$$R(\mathbf{U}) = \int_{\Omega_0} \mathbf{P} : \mathrm{Grad}\delta\mathbf{u} dV - \int_{\Omega_0} \lambda^t \mathbf{B} \cdot \delta\mathbf{u} dV - \int_{\partial\Omega_T} \lambda^t \bar{\mathbf{T}} \cdot \delta\mathbf{u} dA,$$

where λ^t has been introduced as a scalar parameter on the traction boundary.

6.2.2 Automation in Computational Modelling

With the vast advances in numerical power and methods, the idea of automation of numerical modelling is one that has come to the forefront of computational mechanics. In particular, the FE method is one that lends itself to the concept of automation. The various steps involved in the FE procedure, from the formulation of the strong form to the visualisation of results can be automated, although complete automation is of little use when the problem specific nature of computational mechanics is considered. It is for this reason that automation within FE environments is often, if not always, restricted to parts of the whole, where the outcome is predictable such as differentiation or code generation. The user is still responsible for the assembly of, and decisions made within, the full problem.

In general it is required that the basic equations within a problem to be input in a form that is appropriate for symbolic manipulation. Essentially what this refers to is the way input in the main program is passed into an automatic routine and returned as to the user interface. This is generally done through the use of *external variables*, which are used to form the link between the symbolic-numeric interface. There are numerous benefits to using symbolic formulations, including

- Fewer possibilities for error
- Algebraic operations such as differentiation can be done automatically
- Automatically generated codes are highly efficient and portable

In order to take advantage of symbolic manipulation it is necessary to employ what are known as symbolic and algebraic computational (SAC) systems. SAC systems, such as *Mathematica* (Wolfram, 2016), are tools by which to manipulate mathematical expressions in symbolic form. Despite the high computing power of modern computers, SAC systems for use in the context of computational mechanics are not able to keep up with the efficiency of more specialised libraries. Thus in order to take advantage of SAC systems, the FE method is usually implemented within an additional toolbox/-package. One such package is *AceGen*(Korlec, 2015), a package capable of automatic generation of formulae needed in numerical procedures. As quoted from Korelc and Wriggers (2016):

> The idea implemented in *AceGen* is not to try combine different tools, but to combine different techniques inside one system...

This allows for the combination of techniques to allow for an optimal environment with which to design, code and solve especially challenging problems for which a general strategy to approach numerically has not been established.

AceGen employs what is referred to as the *hybrid symbolic-numeric* (HSN) approach (see Fig. 6.6). This approach attempts to employ the extensive computing power of SAC systems while offering the generality and flexibility often not offered by commercial software. The idea behind the HSN approach is to use SAC systems to derive elemental quantities and employ automatic code generation techniques at the level of a single element. The automatically generated code is thus incorporated into any one of numerous FE environments and assembled within the global solution procedure.

Automatic Generation of Numerical Codes

The automation of the FE method is a subject that has been the topic of extensive study. One common issue with the automatic generation of code for complex FE problems is that of *expression swell*. Expression swell refers to the exponential growth of expressions through iterative procedures such as differentiation and matrix algebra, which leads to highly inefficient and unusable code. Numerous approaches have been taken to solve the issue of expression swell, although most approaches solve the issue at the cost of generality and flexibility of such systems. One such solution is through the identification of common sub-expressions within the given formulae. Expressions are optimised prior to the generation of the code. Although this is often sufficient for smaller FE problems, it proves inadequate for larger codes.

An alternative method, as employed by *AceGen*, is referred to as the *Simultaneous Stochastic Simplification* of numerical code. This method employs *Mathematica*'s symbolic and algebraic capabilities to accomplish a reduction in the extent of expression growth. Additionally, *AceGen* makes use of automatic differentiation and the simultaneous optimisation of expressions through selection and introduction of intermediate variables, where expressions are simplified through the use of auxiliary variables. This is similar to defining common sub-expressions. *AceGen* optimises and simplifies expressions which are then replaced by these auxiliary variables. Post generation of numerical code, re-coding into a variety of languages can be achieved with almost no additional effort, which allows for the exportation of element-level code into any one of multiple large scale FE environments.

AceGen provides elemental routines for a number of cases in linear elasticity, hyperelasticity, plasticity and heat conduction. For more specialised element formulations, such as presented in this dissertation, the elemental code need be constructed following the *AceGen* framework.

Automatic Differentiation

Automatic differentiation is a method to compute the derivative of a function specified by a computer program. It is based on the idea that a computer is able to compute a series of elementary operations on known derivatives through the chain rule. This allows for the exact evaluation of arbitrarily complex derivatives. Through the use of automatic differentiation, expression growth can be avoided as during the process expression optimisation and generation of auxiliary variables can simultaneously

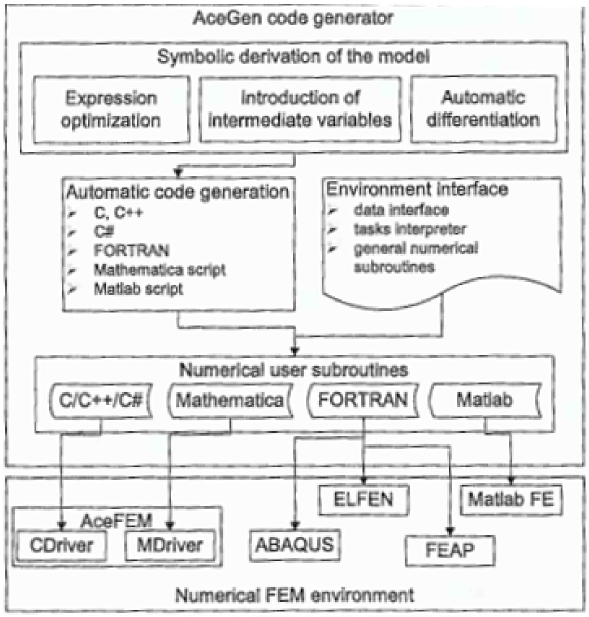

Fig. 6.6: Hybrid symbolic-numeric approach to automation of finite elements (Korelc and Wriggers, 2016)

be performed.

Through the automatic differentiation capabilities of *AceGen* the following are possible:

- Evaluation of (consistent) tangent and residual matrices.
- Sensitivity analysis.
- Optimisation routines

Due to the method through which *AceGen* stores the results and all auxiliary variables with a global vector, there is no limitation to the number of derivatives that can be performed.

There are two primary approaches for automatic differentiation, referred to as *forward* and *reverse* modes. Consider a function $y = f(v)$ defined by the following sequence:

$$\begin{aligned}
&\text{for } i = n+1, n+2, ..., m \\
&\qquad v_i = f_i(v_j)_{j \in A_i} \\
&y = v_m \\
&A_i = \{1, 2, ..., i-1\},
\end{aligned}$$

where f_i depends on v_j, an already computed quantity. $v_i, i = 1, ..., n$ are independent variables and $v_i, i = n+1, ..., m$ are a set of auxiliary variables.

Thus

$$\begin{aligned}
v_{n+1} &= f_{n+1}(v_1, v_2, ..., v_n) \\
v_{n+2} &= f_{n+2}(v_1, v_2, ..., v_n, f_{n+1}) \\
&\vdots \\
y = v_m &= f_m(v_1, v_2, ..., f_{m-1}).
\end{aligned}$$

The goal is thus to find $\nabla y = \{\frac{\partial y}{\partial v_1}, \frac{\partial y}{\partial v_2}, ..., \frac{\partial y}{\partial v_n}\}$ by resolving the dependencies of implicitly contained variables.

The *forward* mode works by accumulating derivatives of auxiliary variables with respect to the independent variables. Taking ∇v_i as the gradient of v_i with respect to independent variables $v_i, i = 1, ..., n$

$$\nabla v_i = \{\frac{\partial v_i}{\partial v_1}, \frac{\partial v_i}{\partial v_2}, ..., \frac{\partial v_i}{\partial v_n}\}_{i=1,...,n} = \{\delta_{ij}\}_{j=1,2,...n} \text{ for } i = 1, 2, ..., n.$$

Through the chain rule:

$$\nabla v_i = \sum_{j=1}^{i-1} \frac{\partial f_i}{\partial v_j} \text{ for } i = n+1, n+2, ..., m.$$

For example,

$$\begin{aligned}
\nabla v_{n+1} &= \{\frac{\partial f_{n+1}}{\partial v_1}, \frac{\partial f_{n+1}}{\partial v_2}, ..., \frac{\partial f_{n+1}}{\partial v_n}\} \\
\nabla v_{n+2} &= \{\frac{\partial f_{n+2}}{\partial v_1}, \frac{\partial f_{n+2}}{\partial v_2}, ..., \frac{\partial f_{n+2}}{\partial v_n}\} + \nabla v_{n+1}\frac{\partial f_{n+2}}{\partial v_{n+1}} \\
\nabla v_{n+3} &= \{\frac{\partial f_{n+3}}{\partial v_1}, \frac{\partial f_{n+3}}{\partial v_2}, ..., \frac{\partial f_{n+3}}{\partial v_n}\} + \nabla v_{n+1}\frac{\partial f_{n+3}}{\partial v_{n+1}} + \nabla v_{n+2}\frac{\partial f_{n+3}}{\partial v_{n+2}} \\
&\vdots \\
\nabla y = \nabla v_m &= \{\frac{\partial f_m}{\partial v_1}, \frac{\partial f_m}{\partial v_2}, ..., \frac{\partial f_m}{\partial v_n}\} + \nabla v_{n+1}\frac{\partial f_m}{\partial v_{n+1}} + ... + \nabla v_{m-1}\frac{\partial f_m}{\partial v_{m-1}}.
\end{aligned}$$

In practice, ∇v_i are relatively sparse.

The *reverse* mode attempts to propagate adjoints[5] with respect to auxiliary variables. Define:

$$\bar{v}_i = \frac{\partial y}{\partial v_i} \text{ for } i = m, m-1, ...n. \tag{6.15}$$

∇y is thus similarly defined by

$$\nabla y = \{\frac{\partial y}{\partial v_i}\} = \{\bar{v}_i\} \text{ for } i = 1, 2, ..., n.$$

By the chain rule,

$$\bar{v}_i = \sum_{j=i+1}^{m} \frac{\partial f_j}{\partial v_i}\bar{v}_j \text{ for } i = 1, 2, ...n.$$

To propagate adjoints the flow of the program must be reversed,

$$\bar{v}_i = \sum_{j=i+1}^{m} \frac{\partial f_j}{\partial v_i}\bar{v}_j \text{ for } i = m, m-1, ..., 1. \tag{6.16}$$

For example,

According to Eq. (6.15):

$$\bar{v}_m = \frac{\partial v_m}{\partial v_m} = 1$$

Then following Eq. (6.16):

---

[5] Derivatives of the final values.

$$\begin{aligned}
\bar{v}_{m-1} &= \frac{\partial f_m}{\partial v_{m-1}} \bar{v}_m \\
\bar{v}_{m-2} &= \frac{\partial f_{m-1}}{\partial v_{m-2}} \bar{v}_{m-1} + \frac{\partial f_m}{\partial v_{m-2}} \bar{v}_m \\
&\vdots \\
\bar{v}_1 &= \frac{\partial f_2}{\partial v_1} \bar{v}_2 + ... + \frac{\partial f_m}{\partial v_1} \bar{v}_m
\end{aligned}$$

In general, the reverse mode often proves to be more efficient.

7

Mechanical Response of the Skin

In the previous chapter, the numerical procedure, based on the FEM, for finding the approximate solution to general nonlinear continuum problems was detailed. The approach can accommodate a range of physically relevant loading scenarios. In this chapter, some mechanical tests are discussed, which aim to characterise the response of skin to various loading conditions. Chosen tests are simulated and results compared to experimental values found in the literature. This section intends to validate the chosen constitutive model developed in Sec. 5.1.1 in its ability to capture macroscopic skin response as discussed in Chapter 5. In particular, the model should capture the anisotropy and nonlinearity inherent to skin behaviour, as well as identify the key parameters that may later inform an ageing type response.

7.1 Mechanical Tests - Overview and Simulation

Mechanical testing of skin aims to characterise the response of skin to the applied loading. As mentioned, the skin is highly anisotropic, nonlinear, heterogeneous and viscoelastic. The expression of these characteristics is dependent on the choice of skin test. The choice of skin test is generally influenced by the desired outcome, as varying characteristics are illicited through different loading conditions.

7.1.1 Torsion Tests

Torsion tests, often applied in vivo, involve a disk that is adhered to the skin and rotated through a controlled angle as depicted in Fig. 7.1. The rotational device measures the torque and the degree of rotation (Agache et al., 1980; Escoffier et al., 1989; Sanders, 1973). A guard ring is often introduced with the proposition that rings of varying diameter control the depth of the mechanical deformation, thus testing the skin response at varying depths. A further advantage of this testing method is that through rotation of the skin sample anisotropic effects are mitigated, thus eliminating variability through directional effects.

7.1.2 Suction Test

Suction tests are commonly used to characterise the mechanical response of skin (Diridollou et al., 2001; Imokawa and Ishida, 2015). The test applies a negative pressure to the surface of the skin and the resulting vertical deformation is measured. Diridollou et al. (2001) claim that this technique enables the measurement of the mechanical response as dictated by the dermal layer without the influence of the hypodermal layer. This form of testing applies a biaxial stress state for the characterisation and determination of anisotropic effects.

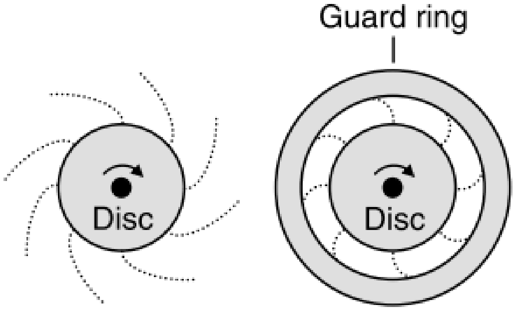

Fig. 7.1: Torsion test set-up, with and without guard ring, extracted from Sherratt (2009)

7.1.3 Tensile Tests

Tensile tests are one of the more frequently used tests when identifying the mechanical properties of the skin, both in vivo and in vitro. Through this test, the skin is loaded parallel to the surface. This test is well suited for identifying the inherent directionality present in the skin, as the skin can be loaded parallel and perpendicular to the Langer lines. Tension tests have also been used to measure the viscoelastic properties through tensile creep tests.

Tensile tests thus offer a simple mechanical test through which to characterise skin behaviour. As extracted from Buganza Tepole et al. (2012), in vitro biaxial mechanical properties of rabbit skin were investigated by Lanir and Fung (1974) (see Fig. 4.6). The test rig as employed by Lanir and Fung (1974) is displayed in Fig. 7.2. A square specimen of soft tissue is connected by silk threads to a displacement motor via a force distributor. The silk threads are connected to all four sides of the sample to allow for a full range biaxial deformations. According to Fung (1974), sample sizes extracted from rabbit skin ranged between 3 × 3cm and 6 × 6cm.

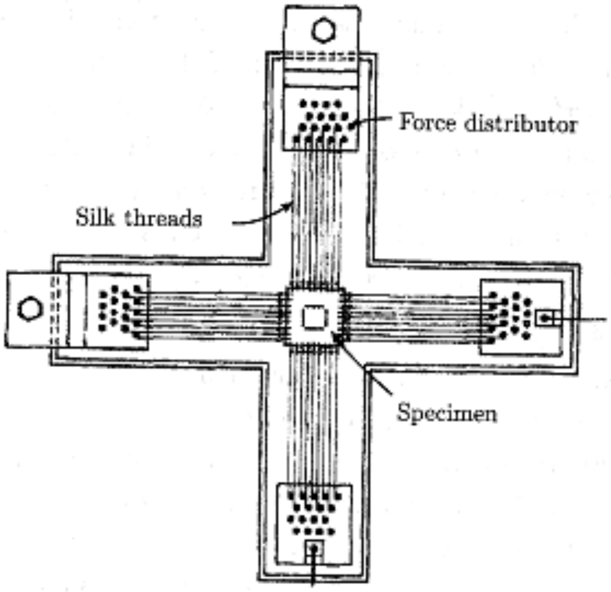

Fig. 7.2: Biaxial tensile test set-up, extracted from Xu and Lu (2011)

The tensile test setup is now simulated using the FEM model described in Sec. 6.1.5. The finite element mesh used for tensile test simulations is as given in Fig. 7.3. l refers to the specimen dimensions, where the specimen was tested at $l = 3$cm and $l = 6$cm. The thickness t was unspecified in the literature and thus set to 4mm. The domain was discretised into $15 \times 15 \times 6$ for a total of 1350 elements. With reference to Fig. 7.3, the boundary conditions are as follows:

$$\begin{aligned} (U, V, W) &= (0, 0, 0) \qquad &\text{on}& \qquad X = 0 \\ (U, V, W) &= (d, 0, 0) \qquad &\text{on}& \qquad X = l \\ V &= 0 \qquad &\text{on}& \qquad Y = 0 \cup Y = l, \end{aligned}$$

where d refers to the prescribed displacement.

The collagen fibres were first aligned along $[1, 0, 0]$ and then along $[0, 1, 0]$ directions to elicit the parallel and perpendicular responses. Stretches were measured at the point $(\frac{l}{2}, \frac{l}{2}, \frac{t}{2})$ to ensure negligible influence from edge effects.

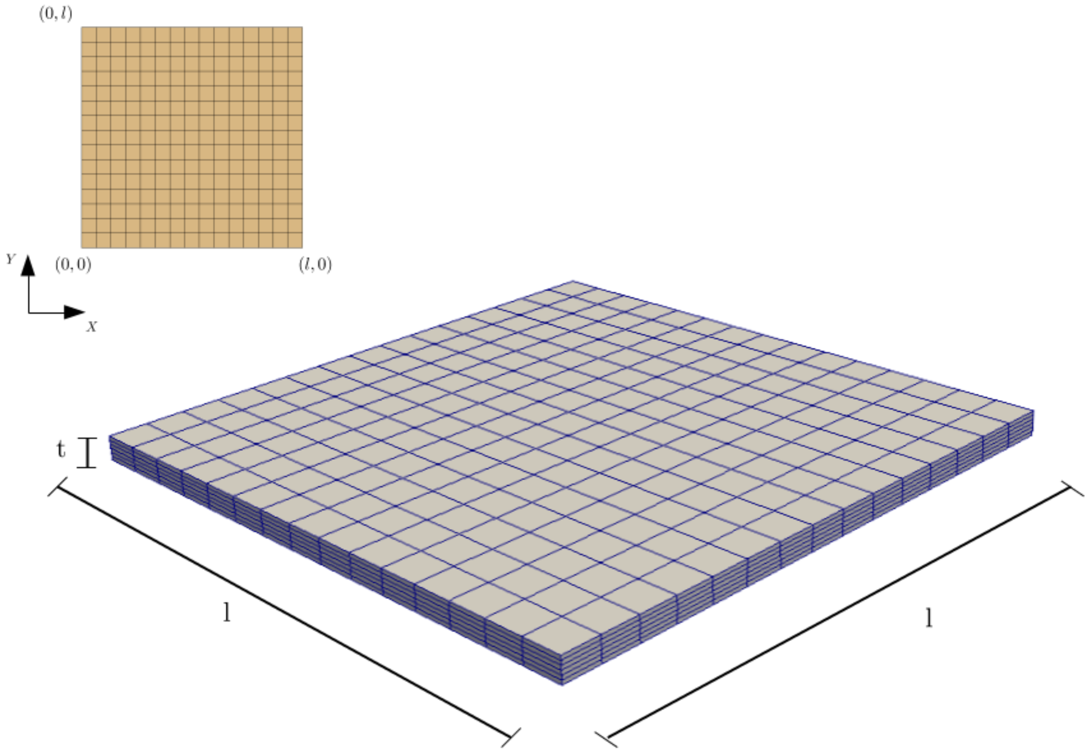

Fig. 7.3: Finite element mesh for tension test

The wormlike 8-chain model was used to replicate the tension test as performed on rabbit skin by Lanir and Fung (1974). The resulting fit and parameters are given in Fig. 7.5 and Table 7.1, respectively and an example of a finite element simulation is shown in Fig. 7.4. It was found that the specimen dimensions did not significantly affect the found parameters. The contour length and persistence length values were extracted from Kuhl et al. (2005) with similar values found in Buganza Tepole et al. (2012). It can be seen that the model provides an exceptional fit to the rabbit skin data, especially along the parallel direction. The model is able to capture the locking stretches of about 1.55 and 1.93 in the parallel and perpendicular directions, respectively. The highly nonlinear and anisotropic shape of the skin response is successfully captured through the 8-chain model under uniaxial loading.

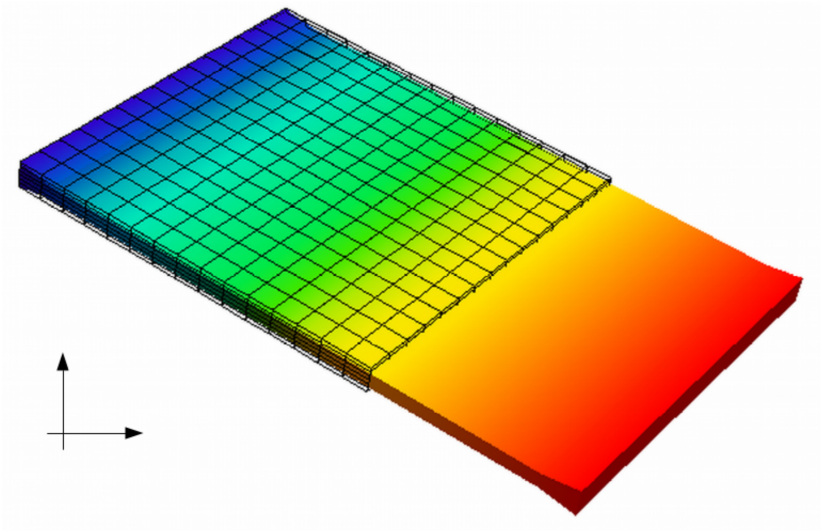

Fig. 7.4: Example of finite element simulation of tension test.

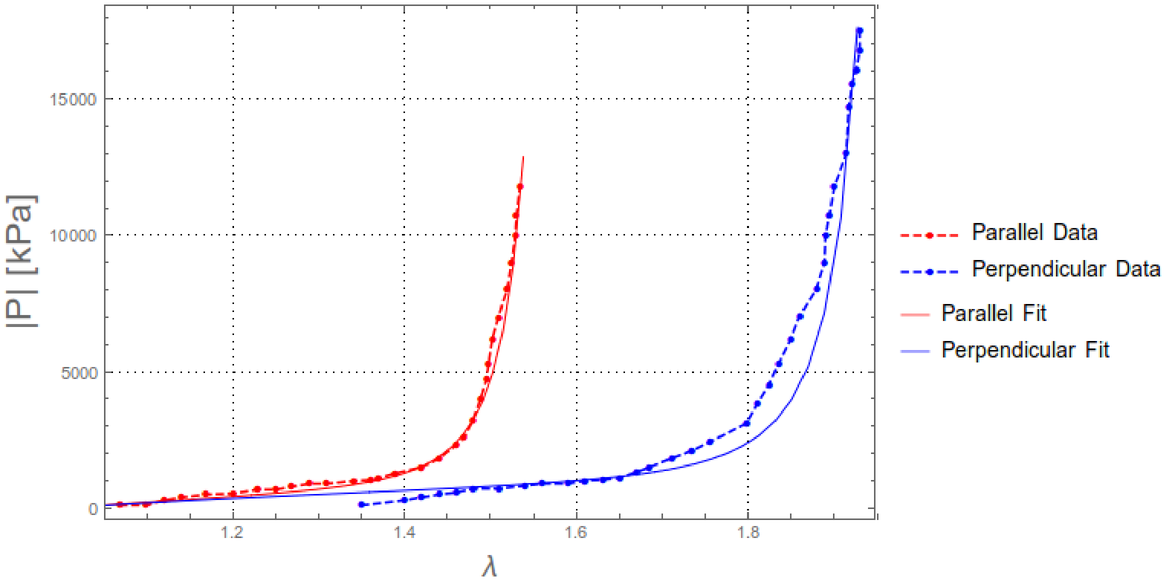

Fig. 7.5: Wormlike 8-chain model fit to rabbit skin data extracted from Buganza Tepole et al. (2012).

Parameter	Value
L	2.125
A	1.82
γ_{chn}	$6.8518 \times 10^{21}\ \mathrm{m}^{-3}$
γ_{gs}	$100\ \mathrm{N\,m}^{-2}$
γ_{elas}	$170\ \mathrm{N\,m}^{-2}$
a	2.38
b	1.74
θ	310 K
β	4.5

Table 7.1: Wormlike 8-chain model parameter values for rabbit skin tensile test.

7.1.4 Bulge Tests

Performed in vitro, the bulge test applies a positive pressure to the underside of an excised skin sample, thus being a similar test to the suction test. The skin sample is held fixed at a specified diameter which allows for a "bulge-like" deformation of the sample.

The procedure for the bulge test follows that detailed in Tonge et al. (2013a). 10cm × 10cm skin specimens were procured from the back torso of donors, ages ranging from 43 to 83 years. After excision, the adipose tissue was removed and tissue thicknesses measured. The thickness, gender, age and anatomical site of the samples is shown in Table 7.2. Thicknesses were measured at the centre of each edge and an average taken from these measurements. This average was used as the uniform thickness of the sample.

Age	Gender	Site	Thickness (mm)
43	Male	Lower back	4.86
44	Male	Lower back	4.38
59	Female	Unknown	5.18
61	Male	Left upper back	2.01
62	Female	Unknown	2.95
83	Male	Unknown	2.43

Table 7.2: Donor and specimen information.

Fig. 7.6: Skin fixed to guard ring, extracted from Tonge et al. (2013a).

The specimens were glued to a ring of 7.5 cm in diameter, with a 9.5 cm outer perimeter, as shown in Fig. 7.6. The complete fixation of the edges of the skin samples aims to prevent structural realignment under loading, and mitigate the effects of preconditioning[1]. The coordinate system for the samples was set such that the Y-axis corresponds with the vertical body axis and the X-axis with the horizontal body axis, as shown in Fig. 7.7. Fibre and perpendicular directions can thus be defined by an angle Φ from the horizontal axis.

The specimens were then mounted onto a customised pressure chamber, see Fig. 7.8. The chamber was controlled for relative humidity and temperature. Inside the chamber samples were inflated through an applied pressure. The pressure and pressure-rate were monitored throughout the process. In order to ensure the skin did not collapse under its own weight, the tissue was brought to equilibrium by a baseline pressure of 0.276 kPa which was held for 15 minutes. Following this, the specimens were

---

[1] In this context, preconditioning refers to the idea that the constituents, primarily the collagen fibres, undergo realignment through loading. With each load and unload phase, the alterations to the microstructure change the mechanical response.

subjected to three load-unload cycles at a rate of 0.069 kPa s^{-1}, with a maximum pressure of 5.516 kPa. Between each load cycle, the sample was brought back to the baseline pressure for 15 minutes. The loading cycles were used to determine the effects of preconditioning on the samples, which was found to negligibly alter the inflation response. Cameras were used to capture the overall deformation.

It was found that upon inflation the skin samples deformed to an elliptical dome, which indicated the presence of the inherent anisotropy in the skin. In order to determine the dominant fibre direction, the deformed surface at the point of maximum pressure was fit to a general ellipsoid. This gave the magnitude and direction of the major and minor radii, corresponding to the least stiff and stiffest material directions, respectively. The dominant fibre direction was then taken along the minor axis and Φ defined accordingly.

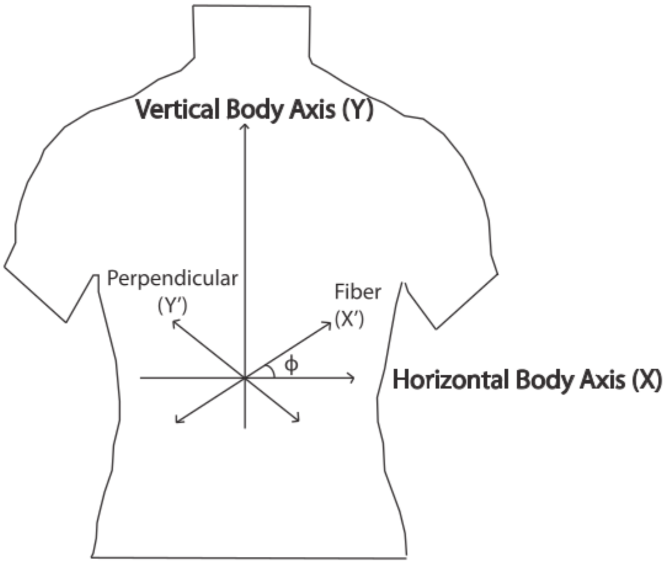

Fig. 7.7: Body axes. Y-axis corresponds with the vertical body axis and the X-axis with the horizontal body axis

The choice of using this test as a comparison for our computational and constitutive models was motivated by the following factors:

- As the experiments are performed in vitro, the boundary conditions on the numerical model are simpler to impose.
- The resulting large deformations would ensure that the various components of the model would play a part. At small deformations the elastin and ground substance will play the dominant role and ultimately the collagen fibres will become active and form the majority of the response at large deformations.
- The specimens were taken from the back of the patients, thus minimising any photoaging effects.
- The experimental results as published in Tonge et al. (2013a,b) gave a range of kinematic measurements with which to compare the model.
- Crucially, the experiments were conducted over a range of ages, which is pertinent to this presentation.

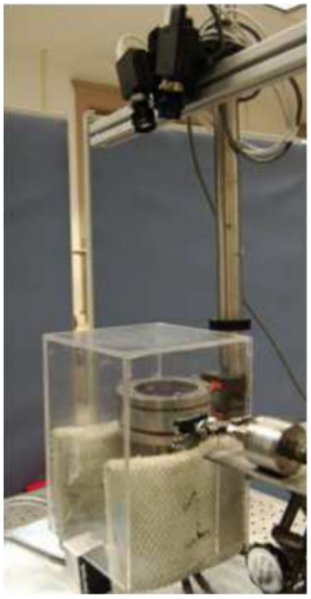

Fig. 7.8: Bulge test set-up, extracted from Tonge et al. (2013a).

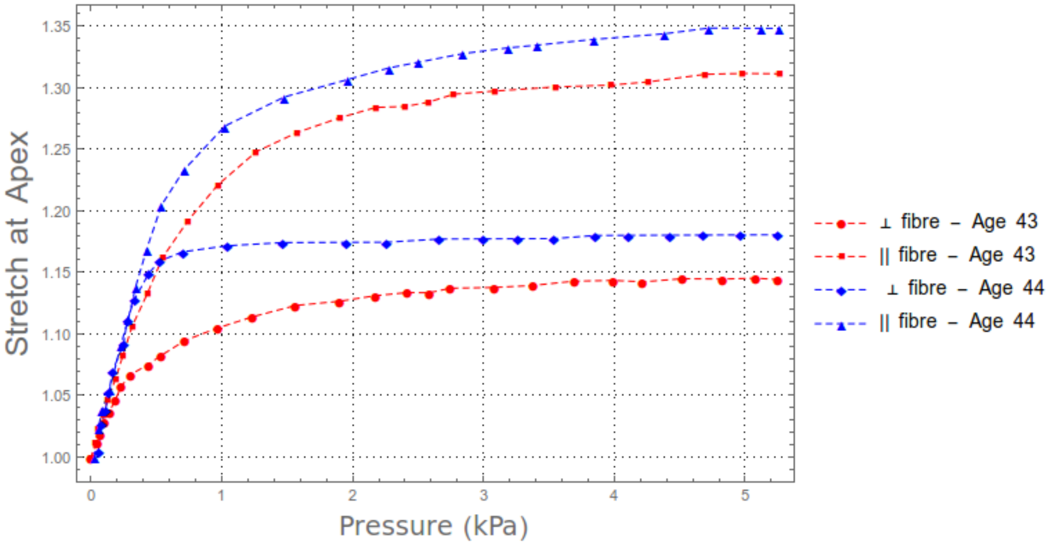

Fig. 7.9: Pressure vs Stretch at Apex, Ages 43 and 44, extracted from Tonge et al. (2013a).

The parameters for the constitutive model employed in this work were determined from the experimental data for the specimens aged 43 and 44. These specimens were both male and from the lower portion of the back, thus eliminating variability between gender, anatomical site and age group.

Fig. 7.9 represents the experimental stretch response of the samples with increasing pressure. It is clear that despite the control over several factors known to influence the skin response there remains a distinct variability between individuals. The age 43 specimen is notably stiffer when compared to the age 44 response, where the maximum stretch obtained by the age 43 specimen is approximately 1.14 and 1.31 in the parallel and perpendicular directions respectively, which is around 0.04 less than that of the age 44 specimen, at 1.18 and 1.348 in the parallel and perpendicular directions, respectively. The perpendicular stretch behaviour profile is very similar for both specimens, whereas the parallel stretch behaviour differs significantly. The age 43 specimen stiffens gradually in the parallel direction, where the age 44 specimen displays the typical locking type behaviour at a stretch of 1.15. This suggests that there is either an additional constituent response or an unexpected influence on the collagen network for the age 43 specimen, possibly by accumulated UV damage. Additionally there could be experimental error.

Tonge et al. (2013b) provides fits to the pressure vs stretch data. The models used are the GOH model as detailed Sec. 4.2.7 and a 2D-FI model, the details of which can be found in Tonge et al. (2013b). It is clear from Fig. 7.10b and Fig. 7.11b that the 3D-GOH model provides an exceptionally bad fit to the data and is unable to capture the inherent skin anisotropy. The 2D-FI model though provides an improved fit to the data, especially in the parallel fibre direction. In Fig. 7.10a, the model struggles to capture the perpendicular behaviour, which is certainly due to the unexpectedly stiffer parallel response.

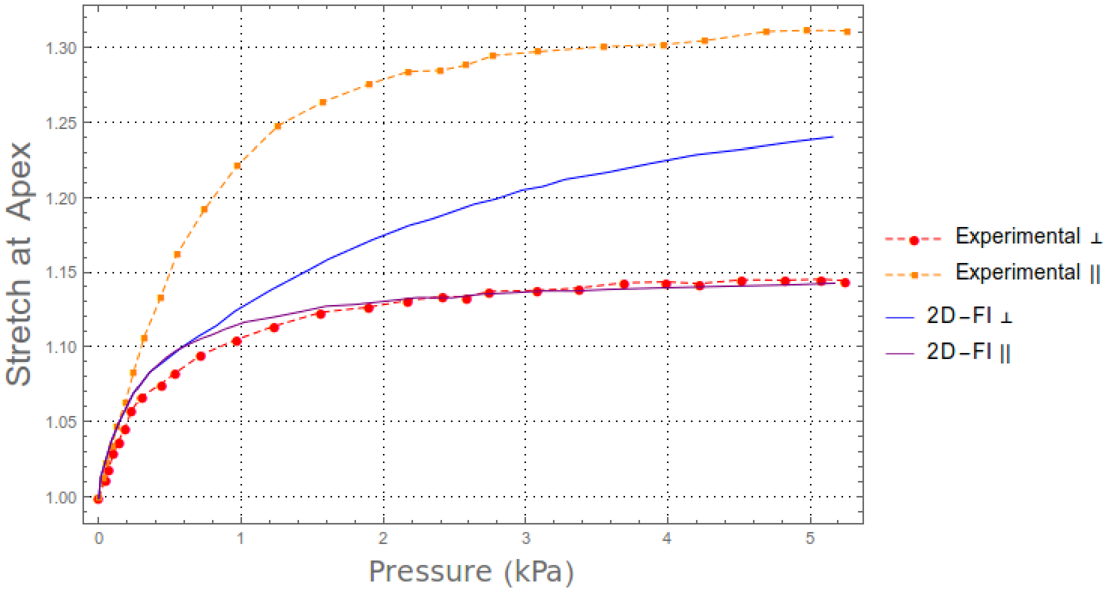

(a) 2D-FI model fit.

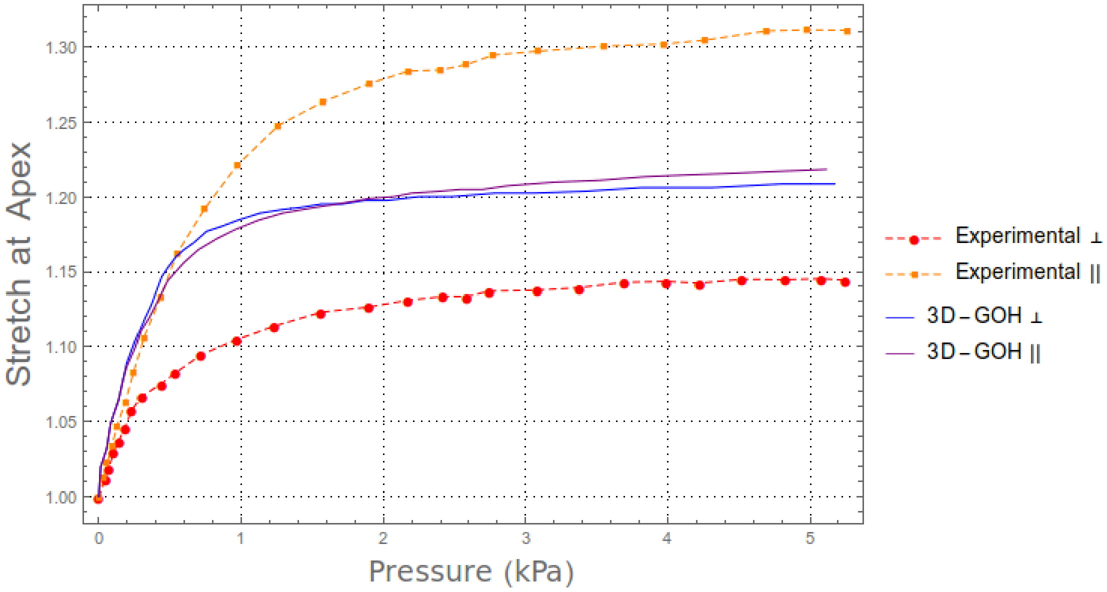

(b) 3D-GOH model fit.

Fig. 7.10: Pressure vs apex stretch fits, age 43.

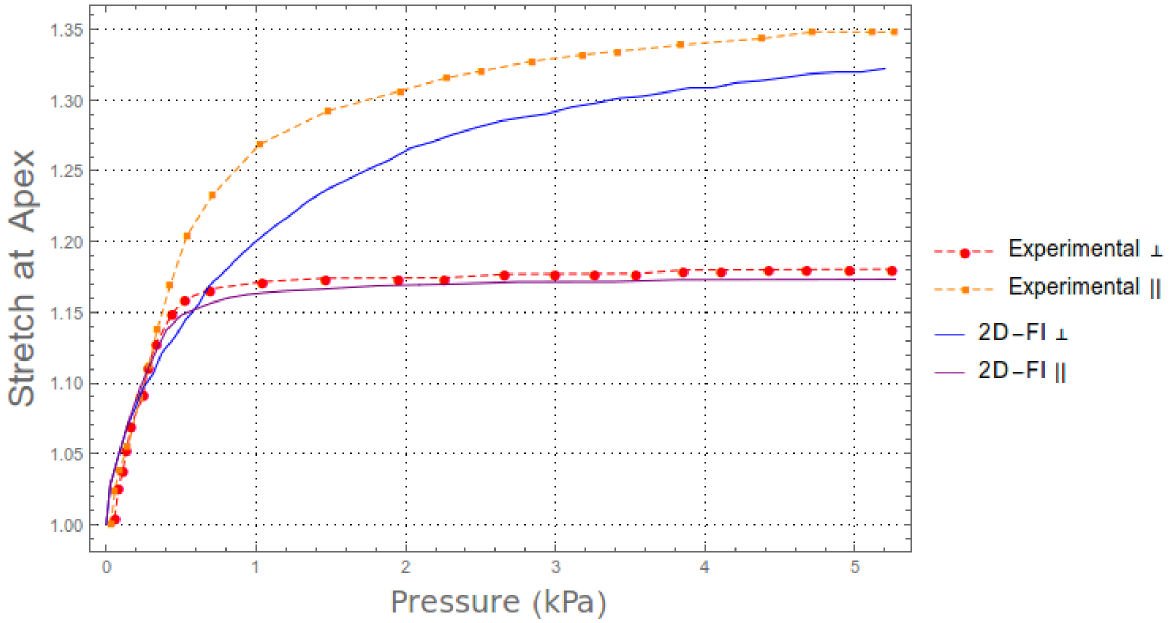

(a) 2D-FI model fit.

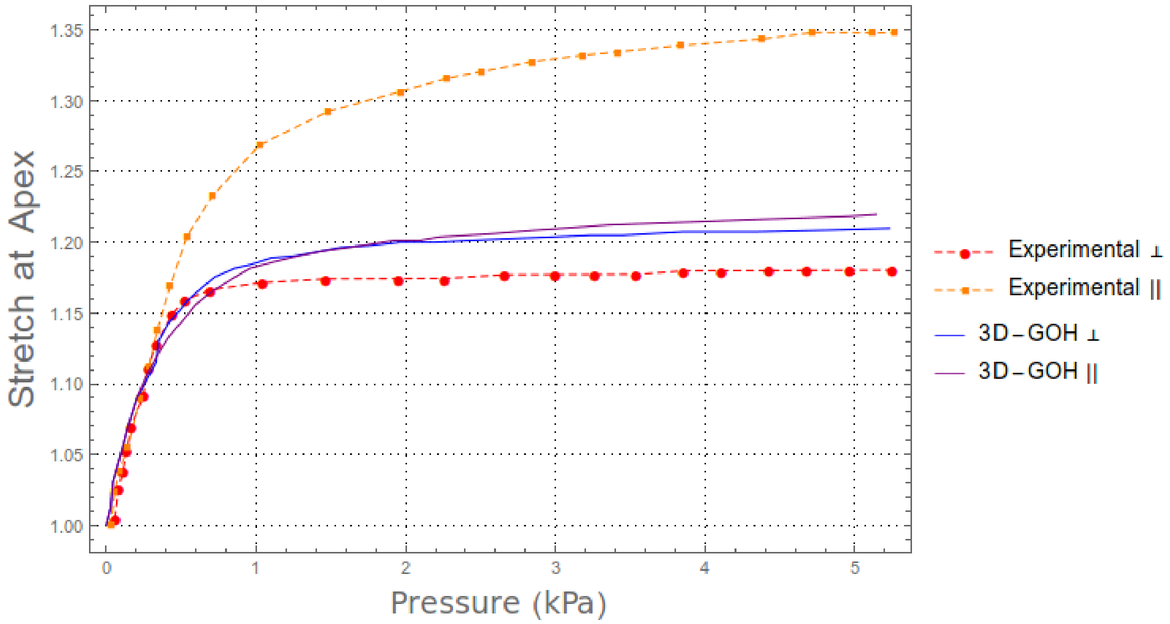

(b) 3D-GOH model fit.

Fig. 7.11: Pressure vs apex stretch fits, age 44.

The bulge test is now simulated using the wormlike 8-chain model. Fig. 7.12 shows the discretisation of the skin sample. The domain follows that described in the experimental set-up, where a 10cm × 10cm domain with uniform dermal thickness t has been discretised. t is set to the dermal thicknesses as specified in Table 7.2. The geometry was discretised using 8-node brick elements, with 5 elements through the thickness. Through a mesh convergence study, the displacements converged in the L_2-norm using 46416 nodes. The displacement components of the nodes on the upper surface outside the bulge diameter of 7.5 cm and the outer edges were held fixed. A pressure loading condition was applied to the bottom surface.

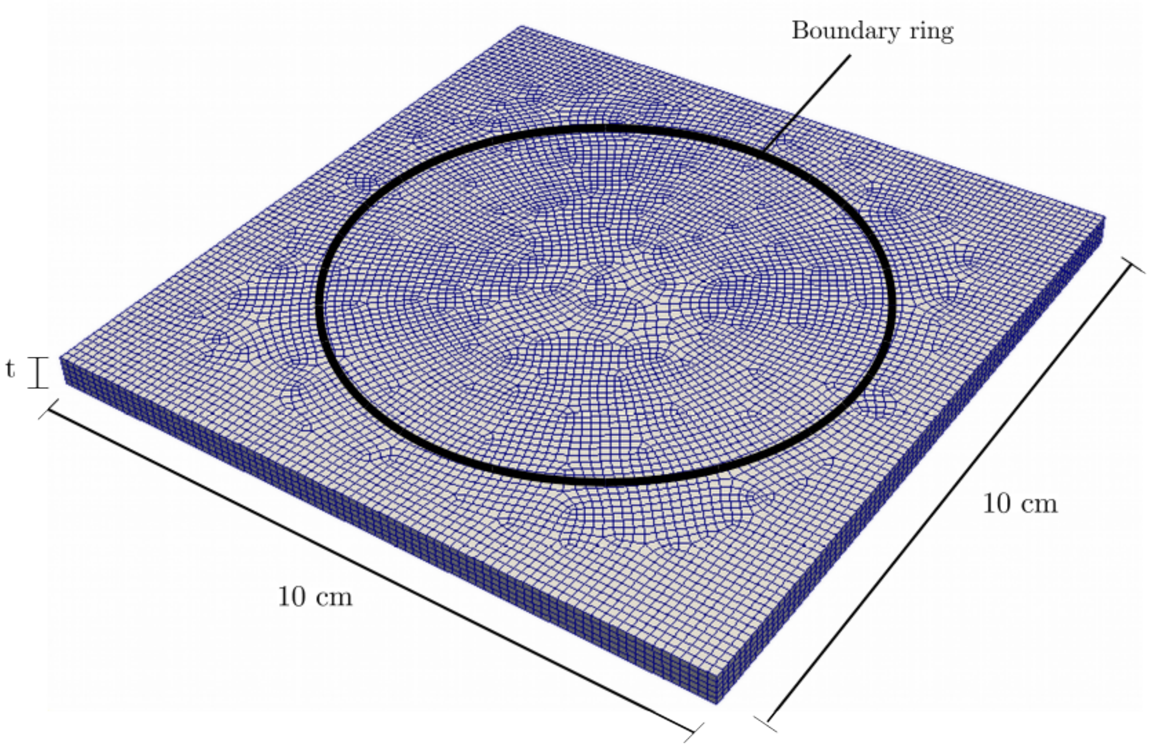

Fig. 7.12: Finite element mesh for bulge test.

Fig. 7.13 and Fig. 7.14 provides the fits obtained through the 8-chain model. In both cases, the model was able to capture the parallel fibre direction behaviour accurately. The perpendicular behaviour was underestimated, similarly to the FI model, although notably improved. Table 7.3 details the parameters obtained for ages 43 and 44. It was postulated that only the original network dimensions a and b, γ_{chn} and γ_{elas} were variable. The rest of the parameters were kept constant at $L = 2.125$, $A = 1.82$, $\gamma_{gs} = 100\text{Pa}$, $\beta = 4.5$, $\theta = 310\text{K}$.

Parameter	Age 43	Age 44
a	3.58	3.45
b	0.5	0.8
γ_{chn}	6×10^{22} m^{-3}	8.56×10^{21} m^{-3}
γ_{elas}	1000Pa	1300Pa

Table 7.3: Wormlike 8-chain model parameter values for age 43 and 44 bulge test.

In general, the parameters obtained for the pressure-stretch fits for both ages are comparable. The network dimensions a and b by Eq. (5.5) result in initial end-to-end lengths of 1.8246 and 1.8154 for the age 43 and 44 simulations, respectively. The minor difference in the end-to-end lengths allows for the difference in maximum stretches observed in the experiments. It is interesting that the initial end-to-end lengths are nearly identical. This suggests that the observed differences between the specimens could be due to differences in fibre dispersion, a factor that, to the authors knowledge, has received little experimental attention in the literature. It can further be noted that the maximum attained stretches are almost entirely dictated by the values of a and b, which will become important within the context of ageing.

A notable difference between the parameters is that of γ_{chn}. γ_{chn} acts as a scaling factor on the strain response of the collagen network. In this case, the higher value of γ_{chn} at age 43 allows for a greater stiffening response at lower strains. This results in the gradual stiffening along the parallel direction of the age 43 specimen. Unfortunately, this parameter has influence over the perpendicular response, which explains the large difference between the the experimental and simulated results along the perpendicular direction at age 43. This suggests that there is an additional directional dependence not captured by the model or a missing constituent contribution. Again, it is possible that experimental error may explain this variation.

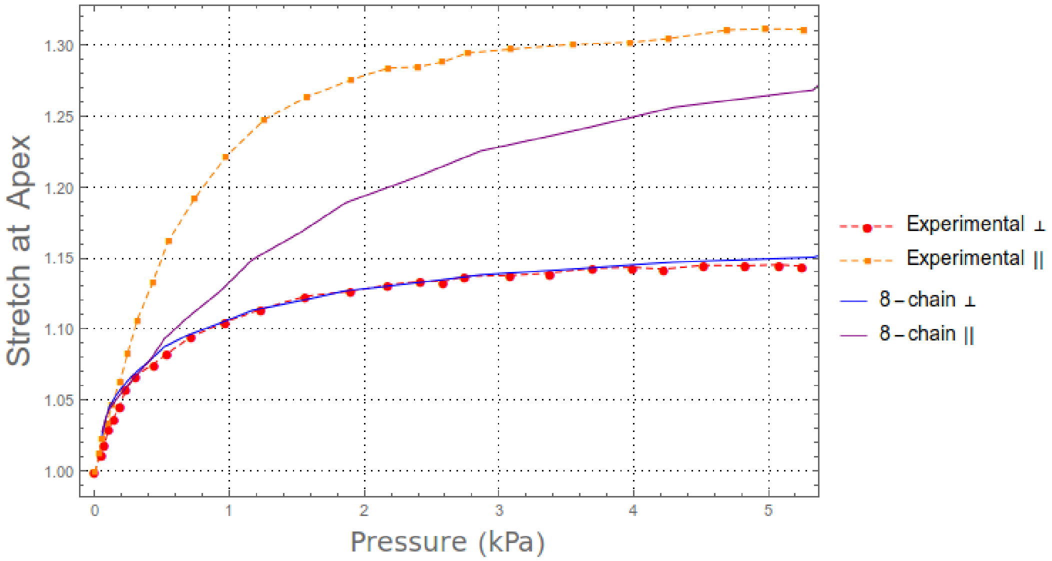

Fig. 7.13: Pressure vs Stretch at Apex, Age 43, 8-chain fit.

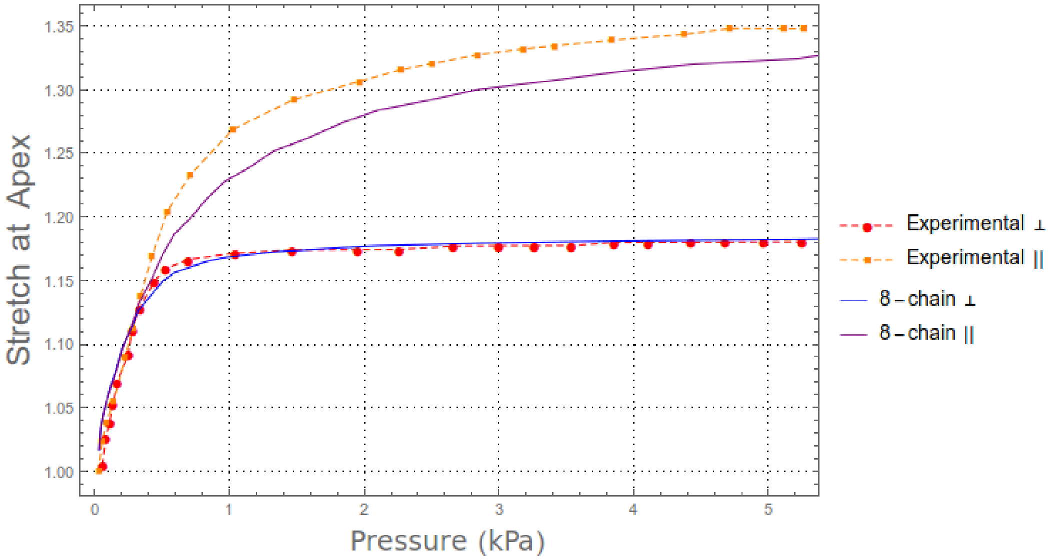

Fig. 7.14: Pressure vs Stretch at Apex, Age 44, 8-chain fit.

In Fig. 7.15 - Fig. 7.22, the profile of the skin obtained from the finite element simulation of the age 44 bulge test is given at increasing stages of the pressure loading. In each figure, the profiles are given along and perpendicular to the fibre direction as illustrated in each subfigure.

The bulge specimen undergoes a rapid initial displacement while the stress state is still within the low modulus portion. This can be seen by Fig. 7.13 and Fig. 7.14 where a small increment in pressure induces a large change in stretch. Similarly, by Fig. 7.23 the apex height initially increased rapidly at low pressure values. During this phase, the elastin and ground substance contributions dominate the response and offer little resistance. This results in the expected isotropic initial deformation as seen in Fig. 7.9. The pressure-stretch lines in the parallel and perpendicular directions coincide up to approximately 200 Pa and 400 Pa applied pressure for the age 43 and 44 specimens, respectively.

Beyond these pressure values, the pressure-stretch lines diverge, which indicates the activation of the anisotropic collagen network. In terms of the material model, the collagen energy contribution is no longer negligible as the end-to-end parameter r takes on significant stretch and approaches the contour length, L. For the age 44 specimen, above 400 Pa further stretch parallel to the fibre direction no longer occurs where perpendicular stretch continues to increase with pressure. This results in the response shown in Fig. 7.18, where at 502 Pa the profiles along the perpendicular and parallel directions differ. The presence of anisotropy is enhanced with increased pressure as the perpendicular stretch increases. As the specimen is displaced, exponentially more pressure is needed to attain further displacement which is characterised by the locking type limit in Fig. 7.23. In Fig. 7.20, Fig. 7.21 and Fig. 7.22 displacement at high pressure occurs laterally in the perpendicular fibre direction.

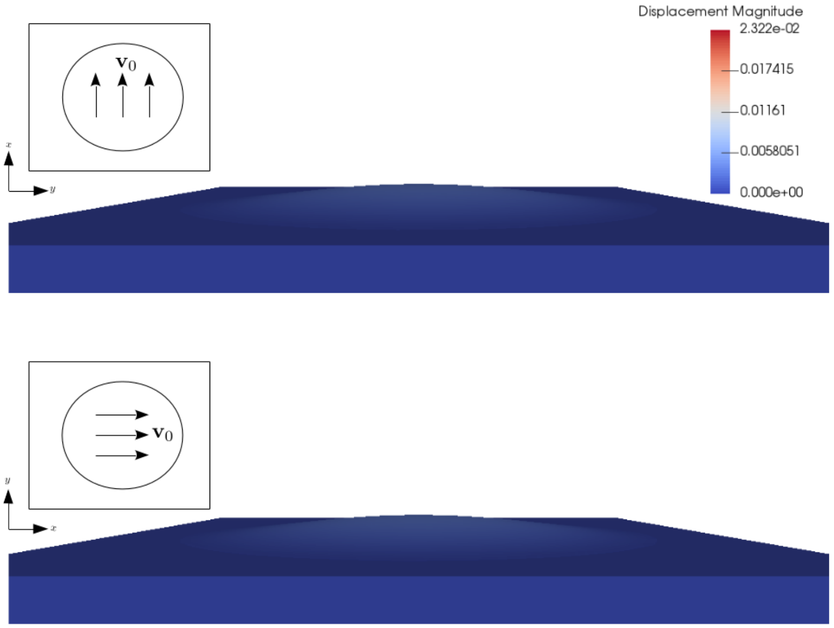

Fig. 7.15: Displacement profile, pressure = 34.37 Pa.

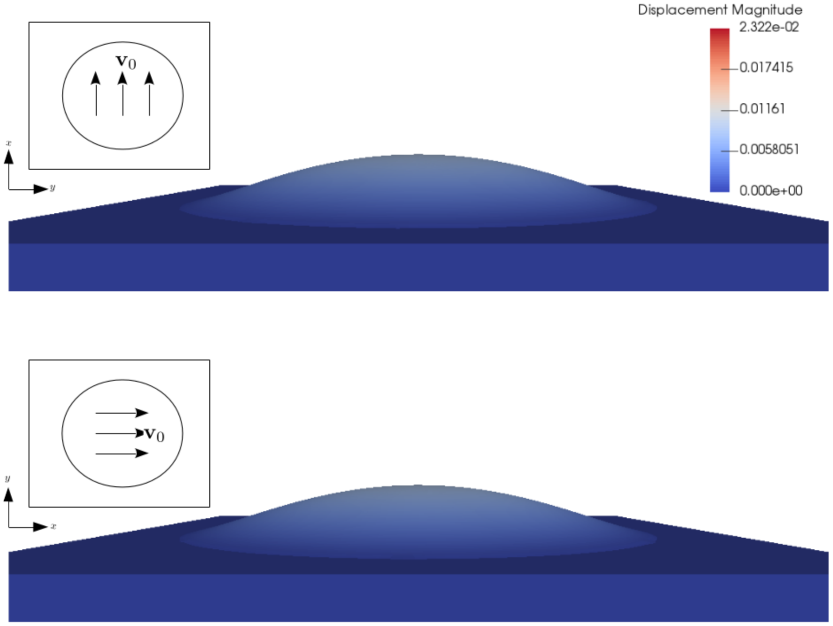

Fig. 7.16: Displacement profile, pressure = 72.16 Pa.

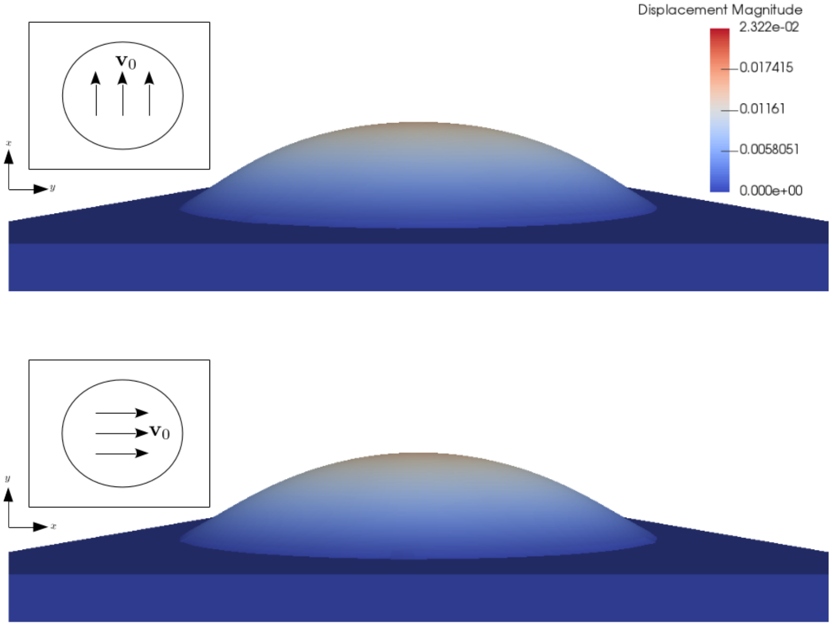

Fig. 7.17: Displacement profile, pressure = 206.4 Pa.

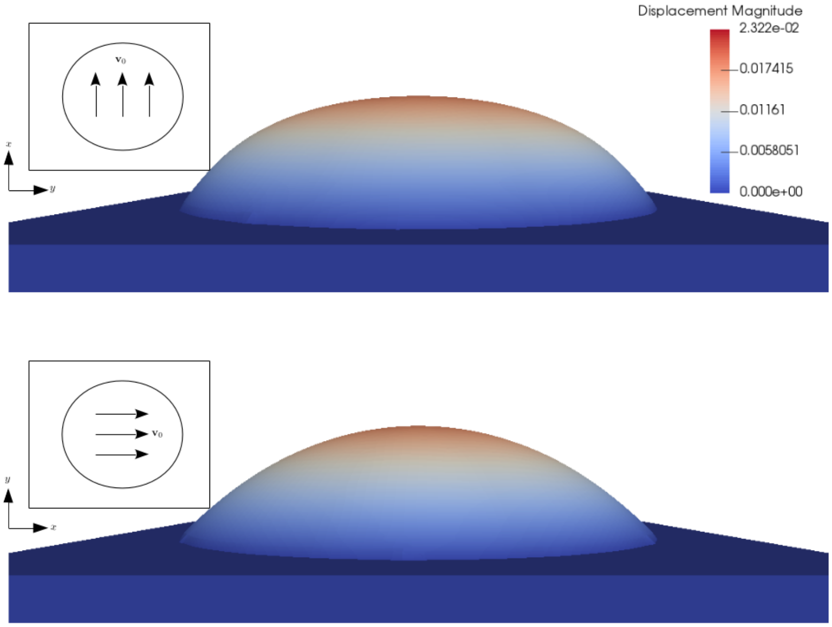

Fig. 7.18: Displacement profile, pressure = 502.1 Pa.

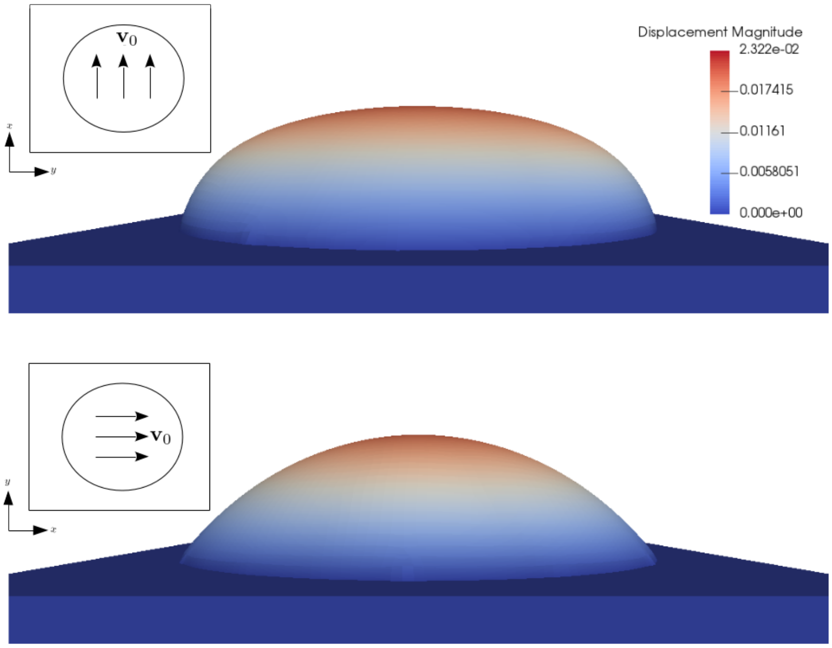

Fig. 7.19: Displacement profile, pressure = 965.4 Pa.

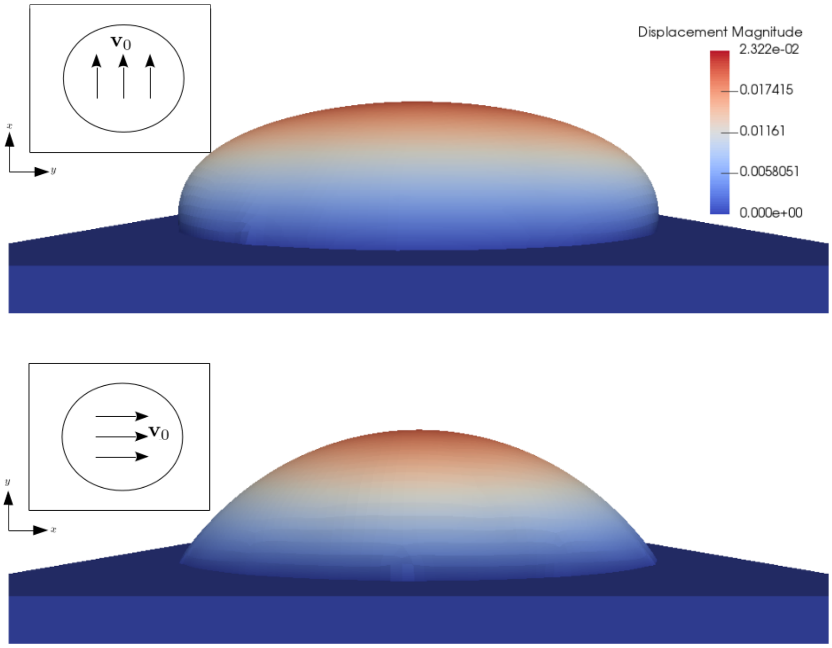

Fig. 7.20: Displacement profile, pressure = 1.84 kPa.

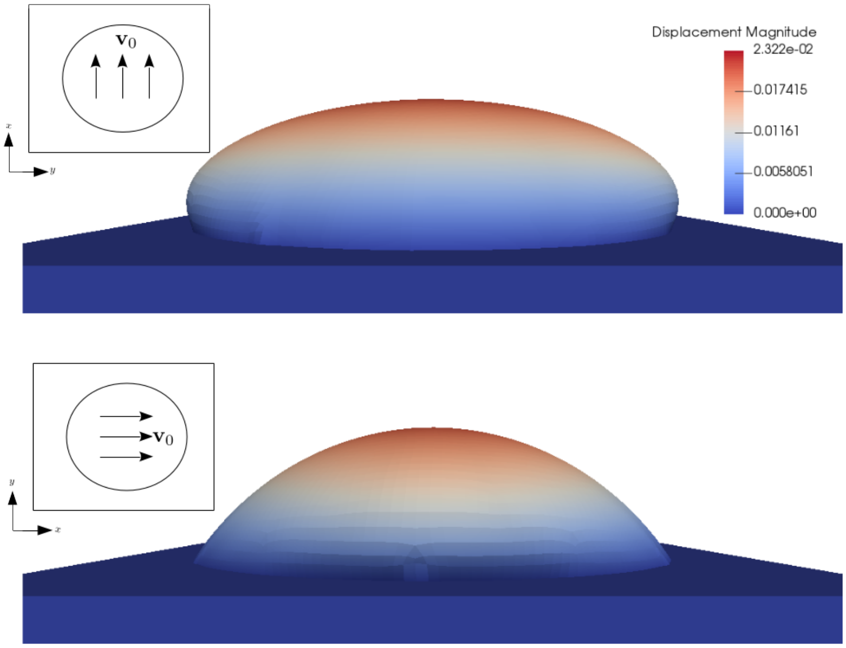

Fig. 7.21: Displacement profile, pressure = 3.38 kPa.

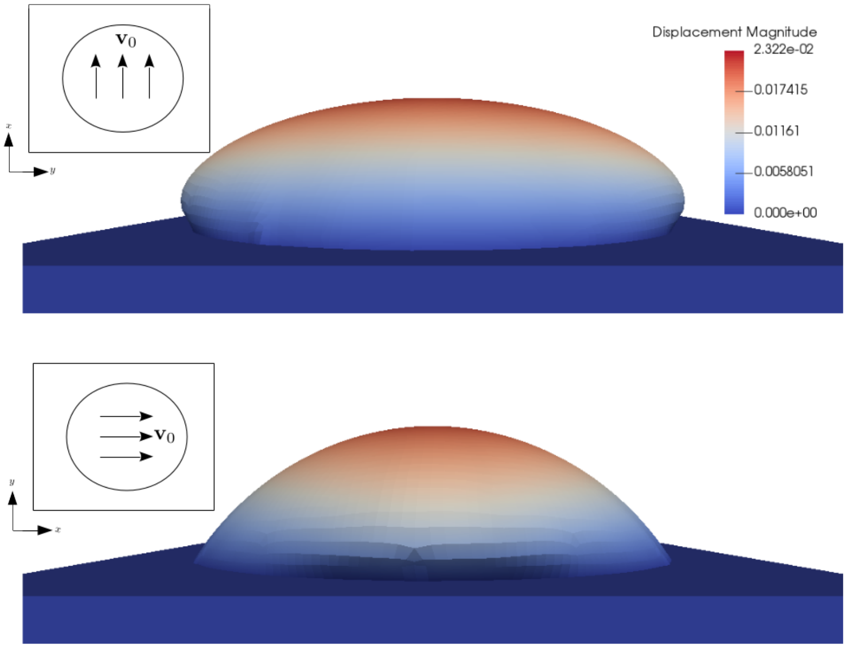

Fig. 7.22: Displacement profile, pressure = 5.52 kPa.

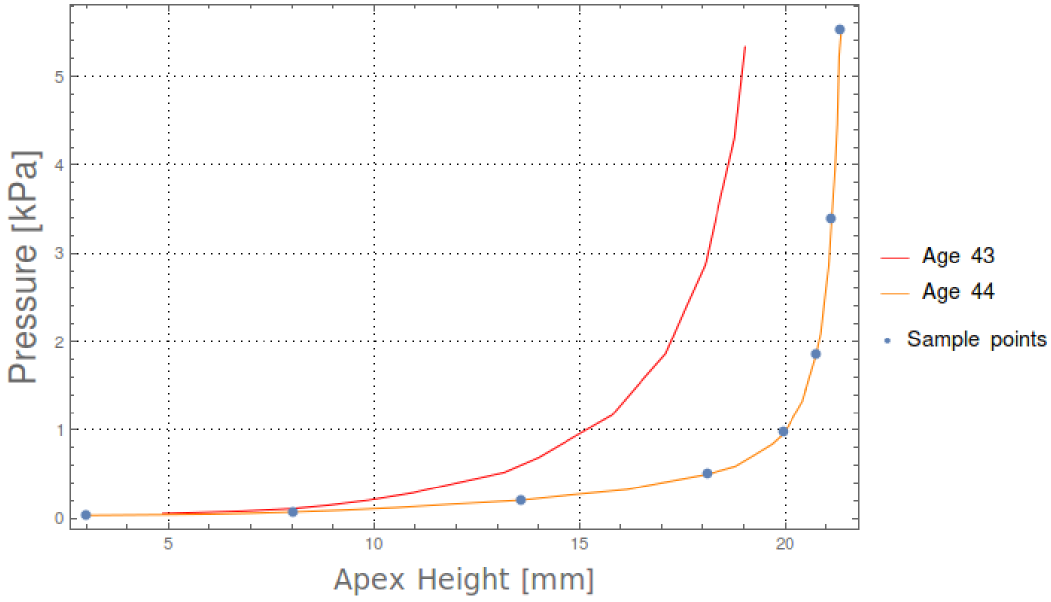

Fig. 7.23: Apex displacement vs pressure, 8-chain simulation. Sample points represent the pressure values at which the displacement profiles were taken.

The contour plots of the displacement components for the age 43 and 44 specimens are displayed in Fig. 7.24 and Fig. 7.25, with the fibre direction along the x-axis. A comparison is given with the experimental results obtained by Tonge et al. (2013a). The contour profiles are highly comparable and the overall behaviour of the simulations matches that of the experimental results. The simulated bulge tests deformed into the characteristic ellipsoid as seen in the experimental results. The age 43 simulations accurately capture the magnitude of displacement in all components. The age 44 simulations accurately capture the displacement in U, but the displacements in V and W are slightly overestimated by approximately 0.5 mm and 2 mm, respectively. This overestimation could be through a constituent contribution not captured in the model. It is also possible that the effect of the rig set-up is not appropriately captured in the simulation. The guard ring may introduce a compressive force through the thickness that would limit the extent of the deformation.

As a check on the results, and to compare to other models used through the literature, the parameter values found through the bulge test were employed in a simulation of a tension test. Through this, stretch-stress curves were generated and a simple Neo-Hookean material model (see Sec. 4.2.5) was then optimised to the data. The Neo-Hookean was fit to three parts of the curve; the curve at small stress values, the curve at large stress values and to the overall curve. This was done in order to capture the stiffness at the low modulus part of the curve, the linear region of the curve and to generate an average over the full stretch range. The low modulus portion of the curves were characterised by stress values < 1000Pa while the linear region was characterised by stress values in the region of 10kPa. Using the optimised value of the shear modulus and a value of 0.48 for the Poisson ratio (McBride et al., 2016; Xu and Lu, 2011), the Young's modulus was obtained for both the 43 and 44 ages. The results are reported in Table 7.1.4.

From Table 7.1.4, it is clear that the Young's moduli obtained vary on the order of magnitudes as shown in Table 5.1. The large degree of difference found between small strain and large strain levels may give an indication as why such varying results have been reported in the literature. It must also be noted that in obtaining the above values that those found for the linear region and average were highly dependent on the simulated stretch. The higher the stretch, and thus the more $r \to L$, the higher the calculated value of the Young's modulus. This may further explain the variability in the literature. Different tests and testing procedures would have obtained inconsistent levels of fibre stretch, and accordingly reported inconsistent stiffnesses.

	Parallel Fibre Direction			Perpendicular Fibre Direction		
	Young's Modulus			Young's Modulus		
Age	Low Modulus Portion	Linear Region	Average	Low Modulus Portion	Linear Region	Average
43	38 kPa	2.251 MPa	97 kPa	8.4 kPa	0.89 MPa	28 kPa
44	15 kPa	7.08 MPa	150 kPa	8.5 kPa	0.56 MPa	17 kPa

Table 7.4: Young's moduli generated at different parts of the stretch curve using the bulge test parameters in a tension test.

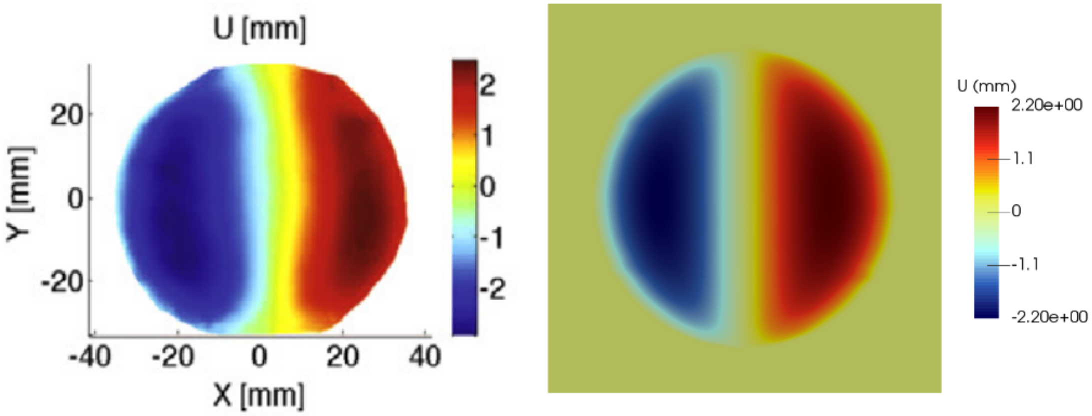

(a) U component of displacement.

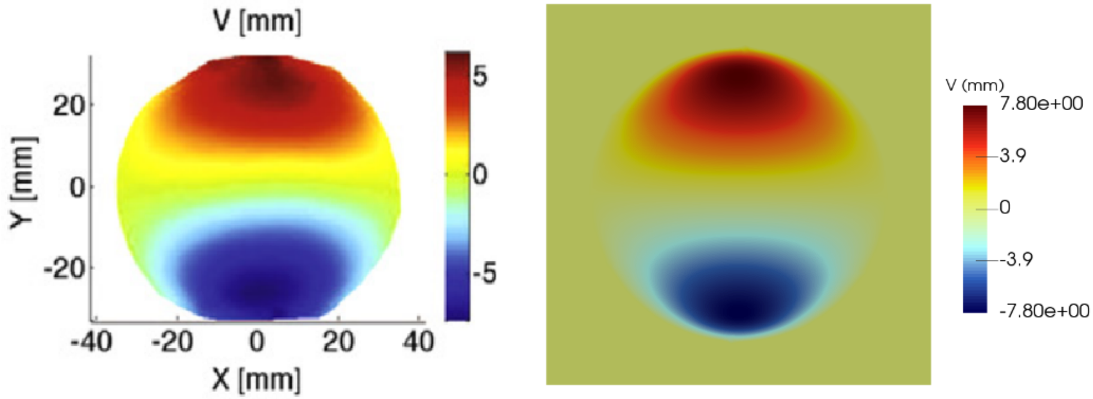

(b) V component of displacement.

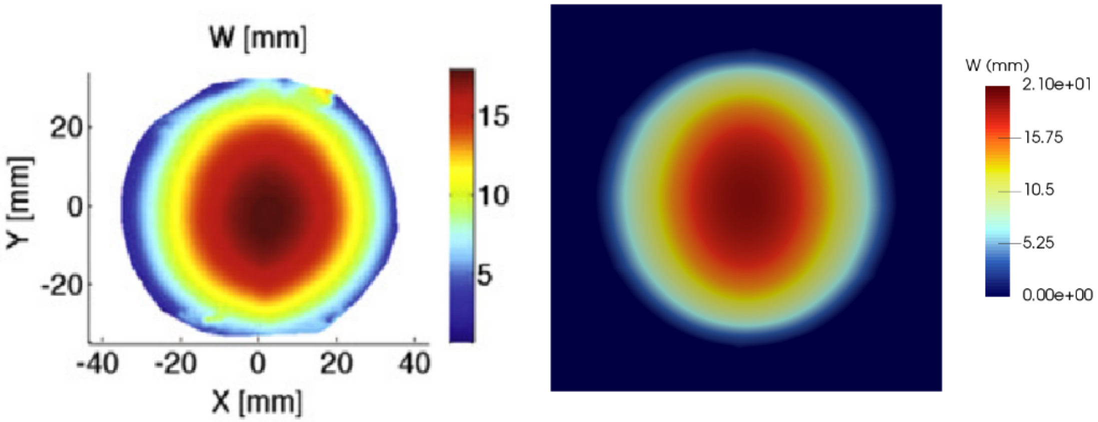

(c) W component of displacement.

Fig. 7.24: Displacement comparison, age 43 (Left: Experimental data. Right: 8-chain simulation).

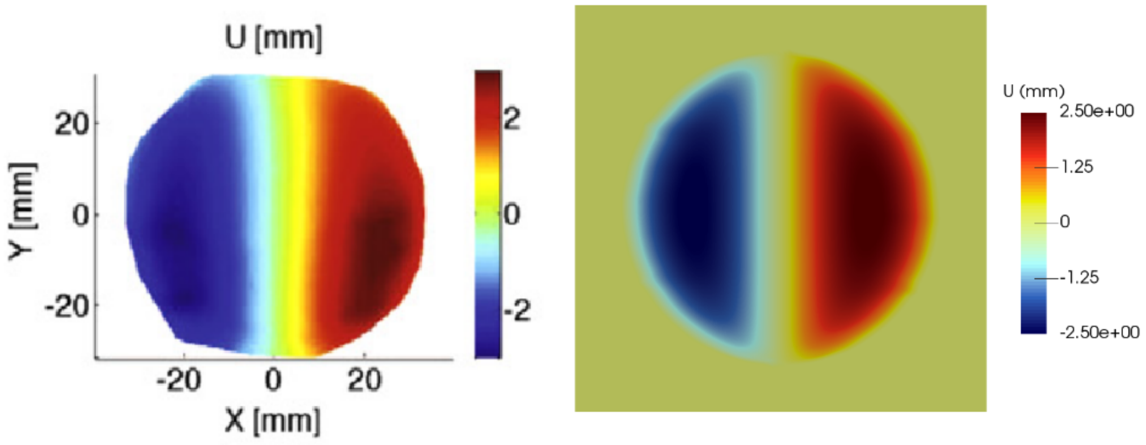

(a) U component of displacement.

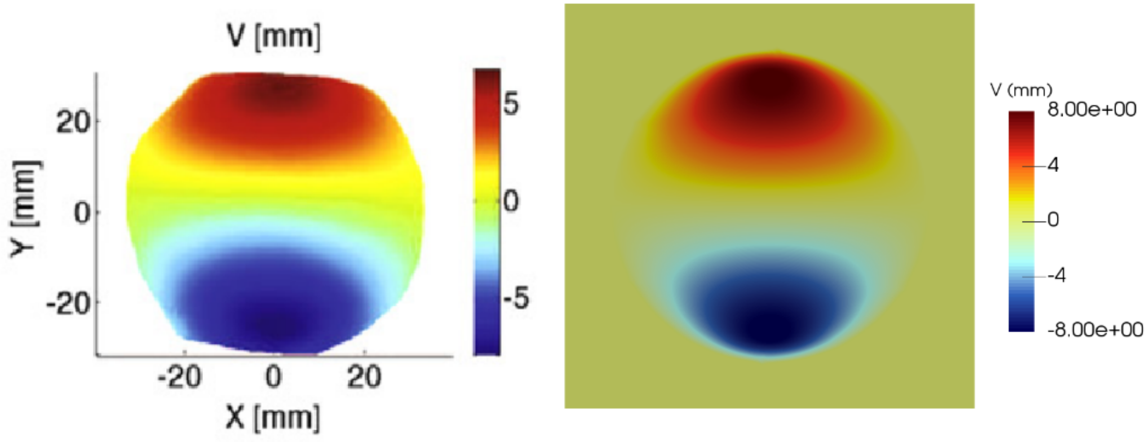

(b) V component of displacement.

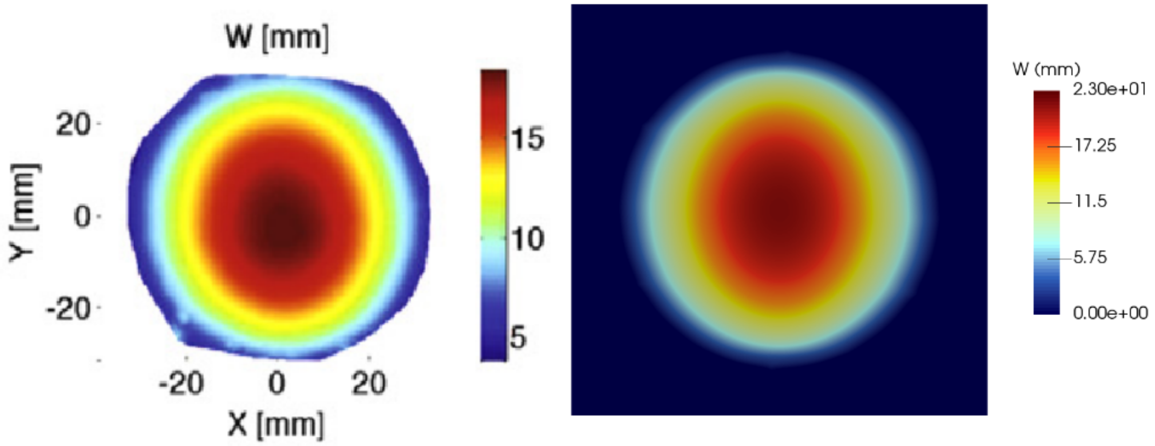

(c) W component of displacement.

Fig. 7.25: Displacement comparison, age 44 (Left: Experimental data. Right: 8-chain simulation).

8

Age Dependent Response of the Skin

In previous chapters, a good understanding of the mechanisms and structures involved in the mechanical response of skin has been developed. The constitutive model developed in Sec. 5.1 incorporated the structurally significant microstructure into a macroscopic model that, through the use of the finite element method, was able to satisfactorily capture the mechanical response of skin for selected skin tests. The modelled skin response has, so far in this thesis, been independent of chronological ageing. In this chapter, ageing is explored using the available experimental data. Several aspects that are key to the ageing process are identified in a hope to inform the modifications to incorporate into the skin model required to account for ageing.

Due to the intrinsic link between age and the appearance and properties of skin, ageing in skin has been the topic of considerable investigation, primarily from an experimental point of view more so than attempting to model the process. Despite this array of data, very little agreement on the general macroscopic behaviour of skin with age has been determined, let alone the link with the microstructure.

It is generally accepted that skin thickness decreases with age (Escoffier et al., 1989; Pailler-Mattei et al., 2008; Pawlaczyk et al., 2013), although some studies have found no significant correlation between skin thickness and chronological age (Reihsner et al., 1995; Xu and Lu, 2011). Pawlaczyk et al. (2013) found that there is an overall loss of 0.7-0.8 mm of thickness in older skin. Leveque et al. (1980) found that skin thickness reaches a maximum around the fourth decade for men and third decade for women after which there is a gradual decrease. Escoffier et al. (1989) suggests that skin thickness remains relatively constant till the seventh decade, after which there is a decrease. This result is backed by Diridollou et al. (2001) who found that after an initial increase during maturation (0-20 years), thickness remains constant to about the age of 60 followed by a decrease according to:

$$t = 1.3\text{mm} - 6 \times 10^{-3}\text{mm} \times \text{age}. \tag{8.1}$$

The rate of decrease is more significant in women.

With age, as shown in Table 8.1, the majority of results suggest that there is an increase in skin stiffness.

The results given by Sanders (1973), where the skin ws observed to decrease in stiffness may be due to the influence of the mobility of underlying tissue. Despite this, it is generally accepted that skin ageing is characterised by an increase in stiffness (Alexander and Cook, 2006; Pawlaczyk et al., 2013; Xu and Lu, 2011), although Alexander and Cook (2006) found that there is a decrease during ages 15-25, which may be due to hormonal changes through puberty. Despite this agreement, the magnitude of the Young's modulus and age of onset of stiffening show very little agreeable trend. Xu and Lu (2011) mentions that there is a sudden increase in the Young's modulus at age 30 by around 50%, whereas others quote an increase from the age of 45. Escoffier et al. (1989) observed an increase of around 20% after the age of 70, which is backed by the findings of Leveque et al. (1980). Alexander and Cook (2006) found that the stiffness of skin starts increasing from the age of 25 but notes that the

Author	Young's modulus	Age Range	Test
Diridollou et al. (2001)	18-57 MPa 0.15 MPa 0.25 MPa	Increase from 20 -70 years Before age 25 After age 60	suction suction (in vivo)
Sanders (1973)	0.11 - 0.02 MPa	Decrease between 6 and 60 years	torsion
Alexander and Cook (2006)	200 - 140 Pa 320 - 540 Pa	Decrease from age 6 -25 Increase after 25	suction
Agache et al. (1980)	0.42 MPa 0.85 MPa	Before age 40 After age 40	torsion
Escoffier et al. (1989)	1.1-1.32 MPa	Increase suddenly after 65 years	torsion

Table 8.1: Values for Young's modulus of human skin with age.

variation in results increases with age. This suggests that the process of skin ageing is a highly patient specific and may explain the large variation in results through the literature. Using linear regression, Diridollou et al. (2001) found that the evolution of the Young's modulus can be described by:

$$\text{Young's modulus} = 79\text{kPa} + 1.7\text{kPa} \times \text{age}, \qquad \text{(for men.)}$$

$$\text{Young's modulus} = 102\text{kPa} + 1\text{kPa} \times \text{age}, \qquad \text{(for women.)}$$

Escoffier et al. (1989) and Leveque et al. (1980) additionally found that intrinsic skin extensibility[1] decreases with age. Escoffier et al. (1989) found that intrinsic extensibility decreases by around 35% after the age of 65 which agrees with the findings of Xu and Lu (2011) in that maximum skin elongation is found between ages 35-55. Similarly skin elasticity decreases with age Escoffier et al. (1989); Xu and Lu (2011). Henry et al. (1997) found that elasticity decreases from an early age, but this may include UV effects.

The causes of such change are often unclear and may be the result of alterations to the mechanical properties or altered amounts of the various constituents. As discussed in previous chapters, the low modulus and linear regions are dictated by the ageing process of the various constituents.

Within the linear region, Agache et al. (1980) found that the behaviour is relatively stable up to 30 years after which there is a rapid drop in immediate distension by around 50%. Alexander and Cook (2006) found a decrease in the initial portion of the elongation-stress curve, with similar results noted by Daly and Odland (1979) and Reihsner et al. (1995) who found a reduced low-modulus portion.

As elastin is primarily responsible for the low stretch response, it is clear that there must be some modification to the elastin network with age. As discussed in the introductory chapters, elastin is a highly stable protein, the biosynthesis of which remains steady for the first 40-50 years, after which there is a decline. Thus, various authors (Alexander and Cook, 2006; Daly and Odland, 1979; Reihsner et al., 1995; Silver et al., 2002) attribute the decrease in the low-modulus portion to the gradual degradation of the elastin network, as well as the deposition of amorphous elastin. This statement is backed by the observation that upon enzymatic removal of elastin from skin samples, similar results were obtained to that of ageing. Furthermore, Silver et al. (2002) found that the elastic modulus of elastin decreases with age. Alexander and Cook (2006) notes that the ageing response of elastin is not common to every individual which may be due to UV and hormonal contributions.

In the linear region, collagen fibre take on tension which results in the typical nonlinear response. Alexander and Cook (2006) reports that the slope of the linear portion of the elongation-stress curve tends to increase with age. This suggests a stiffening of the collagen fibres with age. Counter to this,

---

[1] intrinsic skin extensibility is a standardised mean extensibility to account for varying skin thickness

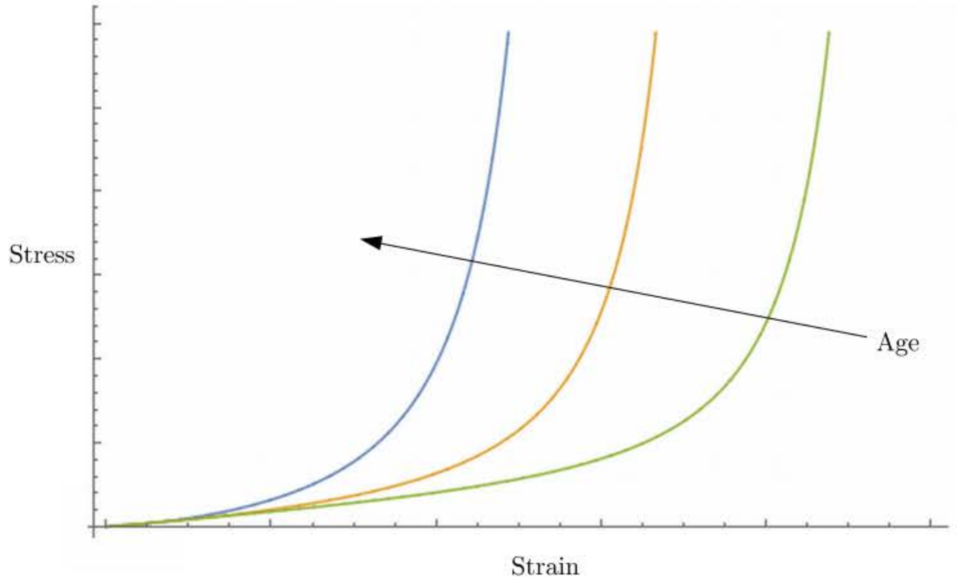

Fig. 8.1: Stress-strain behaviour with age.

Daly and Odland (1979) and Reihsner et al. (1995) note that the final slope remains constant with age, and that the stiffness of the collagen remains constant. There is suggestion that the alteration of the collagen is not due to a stiffening of the fibres, but rather an alteration in the structure of the network. It was found that alterations in total skin thickness were proportional to the alterations in dermal thickness and that due to the compacting of the dermis with age, collagen bundles tend to flatten and unravel (Leveque et al., 1980). Coupled with the loss of elastic integrity, Diridollou et al. (2001) goes on to postulate that due to the dermal thinning, collagen fibres may tend to unfold to some extent, which could further explain the reduction in skin extensibility and the smaller low-modulus portion, as collagen is activated sooner. Agache et al. (1980), Escoffier et al. (1989) and Reihsner et al. (1995) mention that there is increased crosslinking with age, which would reduce any slippage between neighbouring fibres and stiffen up the collagen network. Anisotropy tends to increase with age suggesting that there is an increase in alignment along Langer lines with age (Ruvolo Jr. E et al., 2007; Vexler et al., 1999), although Tonge et al. (2013a) found a decrease in overall anisotropy.

It is generally accepted that the amount of viable collagen in the dermal layer decreases with age. Silver et al. (2002) states that the volume fraction of collagen in the skin decreases from 16.6% to 9.6% in young to old skin. Leveque et al. (1980) mentions that collagen concentration fell from 34% to 18% of the skin wet weight between the ages of 20 and 50, while the percentage of collagen appears to remain constant relative to the fat-free dry weight of skin.

The viscoelastic properties of the skin have also been shown to change with age. Alexander and Cook (2006), Diridollou et al. (2001) and Sanders (1973) show that the viscoelastic properties tend to remain constant during early age and then increase from the age of 40 although other studies have found no significant change in the overall skin viscoelasticity with age (Vexler et al., 1999; Vogel, 1981).

Overall, Xu and Lu (2011) notes three factors that influence biomechanical behaviour of skin with age:

1. Increased cross-linking between collagen fibres - collagen network density increases with age as well as a decrease in fibre free length. Collagen fibres are thus more compact and appear to unravel.

2. The loss of elasticity at low strain is attributed to destruction of the elastin network. Elastic fibres become thinner and fractionated with age. The decreased extensibility properties of skin with age are generally attributed to the loss of elastin in the upper dermis with age.
3. Water content tends to decrease with age, which alters the overall viscoelastic properties.

9

Incorporating Ageing into the Macroscopic Model

In the previous chapter, a reasonable understanding of the underlying mechanical alterations that occur with ageing was presented. As to be expected, ageing is not a simple mechanism and the response of the skin varies greatly. Additionally, the chronological ageing response is often masked by additional factors, such as UV exposure and hormonal changes. In this chapter, an attempt to capture the ageing response of skin is presented. In order to incorporate an ageing type response into the mechanical model presented in Chapter 5, several "age-dependent" constitutive parameters are identified according to the structural changes discussed previously.

In Table 9.1, the key age related changes are listed with their link to the mechanical constitutive parameters introduced in Sec. 5.1. As the ground substance is primarily responsible for the viscoelastic response which is not captured in the present model, no alterations to the parameters in Eq. (5.2) were justified. The observed loss of elasticity and destruction of the elastin network could be captured by changes to the shear modulus of elastin through the parameter γ_{elas}. The loss of collagen and increased crosslinking do not have natural analogues within the current model, but could be captured through γ_{chn}. Alterations in the network dimension and structure are naturally captured through the chain network dimensions, a and b. Similarly, the ratio between the two will affect the anisotropy of the of the material response. Additionally, the dermal thickness changes with age which is captured through the thickness of the mesh as shown in Fig. 7.12.

Constituent	Ageing Response	Reactive Parameter
Ground Substance	Increased water content results in increased viscoelasticity	N/A
Elastin	Loss of elasticity	γ_{elas}
	Destruction of elastin network	γ_{elas}
Collagen	Loss of mature collagen	γ_{col}
	Increased crosslinking	γ_{chn}
	Flattening and unravelling of collagen network	a, b
	Alterations in anisotropy	a, b

Table 9.1: Parameters related to age.

In order to investigate the effect of these parameters on the model's response, tension tests were run by individually varying the value of each parameter while keeping the rest fixed at the values established by in Table 7.1.

As the influence of elastin is largely restricted to low stretches, it could be expected that by varying values of γ_{elas} the small stretch response is predominantly affected. This can be seen in Fig. 9.1 where the slope of the curve is greater for greater values of γ_{elas}. At higher stretches, where the collagen response is dominant, the effect is minor and the lines converge. From Table 9.2, γ_{elas} has little affect on the level of anisotropy of the material response, which is to be expected as the elastin contribution makes up the isotropic aspect of the model.

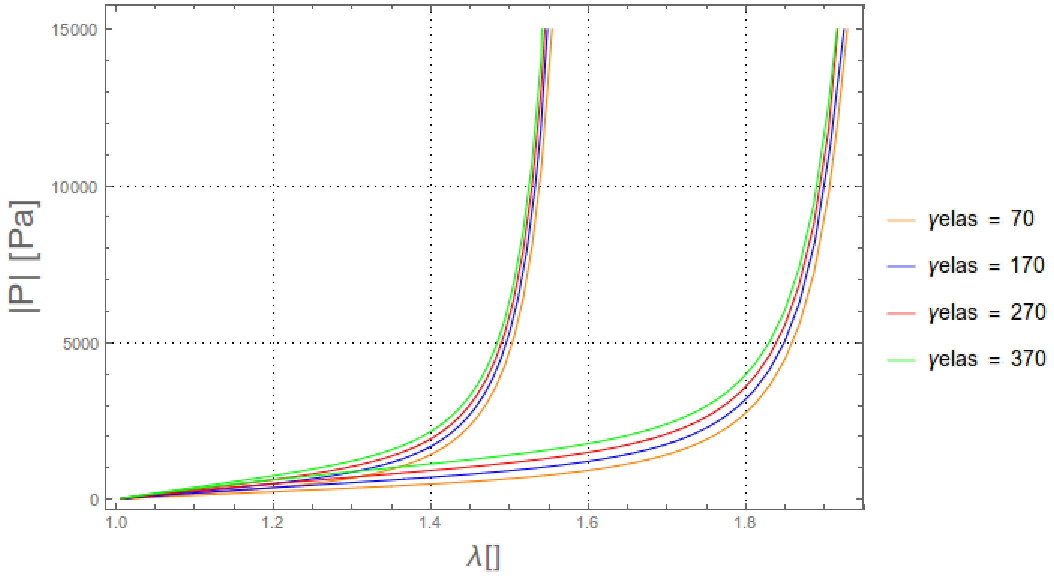

Fig. 9.1: Stretch vs stress at varying γ_{elas}.

Parameter	Stretch Ratio
γ_{elas}	Parallel:Perpendicular
70	1:1.241
170	1:1.244
270	1:1.241
370	1:1.243

Table 9.2: Parallel to perpendicular stretch ratios at varying γ_{elas}.

As has been touched on before, γ_{chn} has the effect of scaling the strain response of the collagen component of the model. It is therefore natural to expect that for larger values of γ_{chn} there is a greater response, as this translates to the idea that there are more fibres present to resist deformation. From Fig. 9.2, this is the response observed. The curves take on greater stress at lower stretch for greater values of γ_{chn}. γ_{chn} has negligible effect on the anisotropy as is seen by Table 9.3 as γ_{chn} has the effect of scaling the perpendicular and parallel responses equally.

Parameter	Stretch Ratio
γ_{chn}	Parallel:Perpendicular
1×10^{21}	1:1.245
4×10^{21}	1:1.248
7×10^{21}	1:1.247
10×10^{21}	1:1.246

Table 9.3: Parallel to perpendicular stretch ratios at varying γ_{chn}.

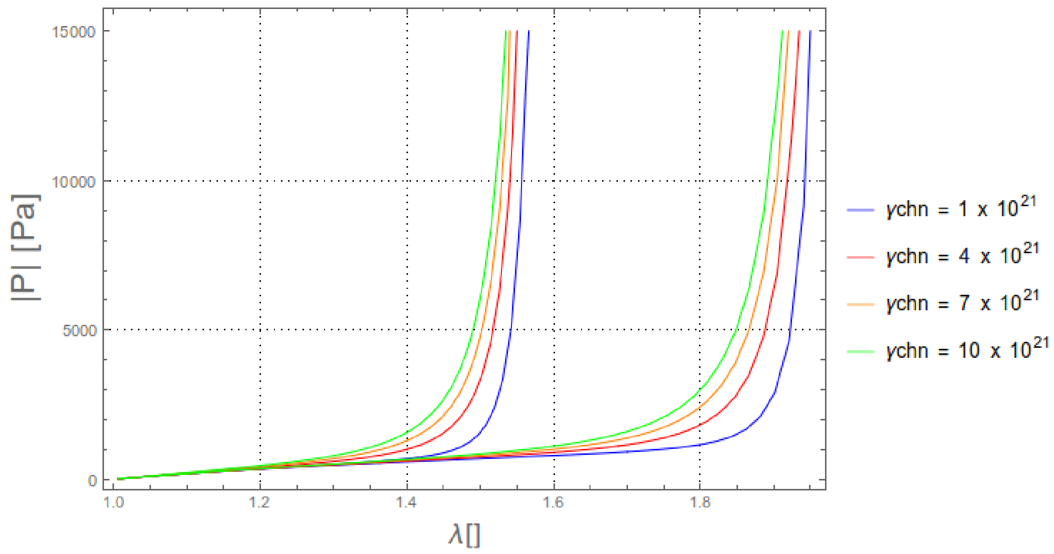

Fig. 9.2: Stretch vs stress at varying γ_{chn}.

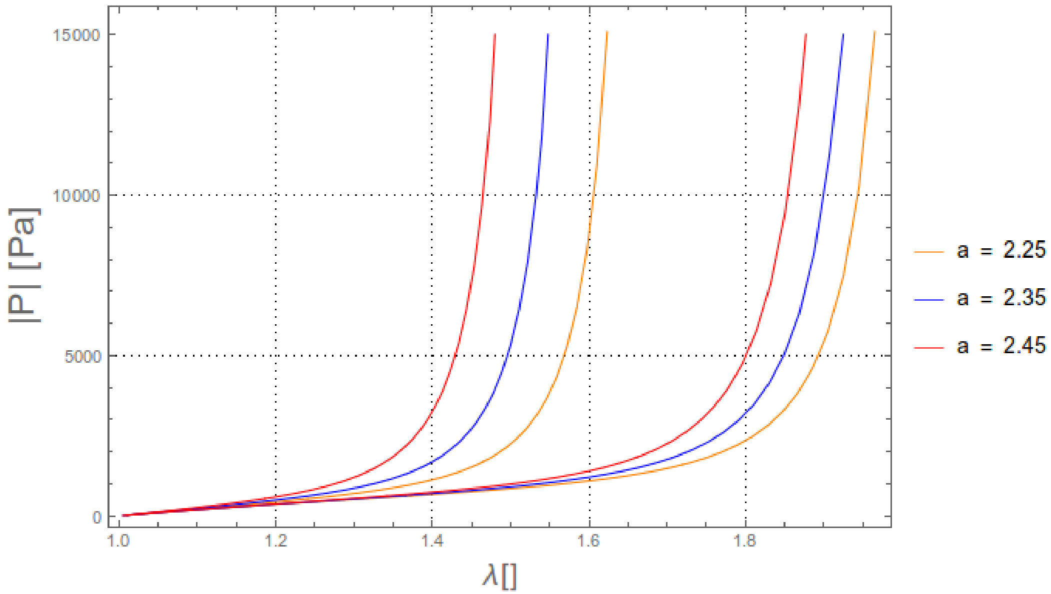

Fig. 9.3: Stretch vs stress at varying a.

Parameter	Stretch Ratio
a	Parallel:Perpendicular
2.25	1:1.211
2.35	1:1.244
2.45	1:1.268

Table 9.4: Parallel to perpendicular stretch ratios at varying a.

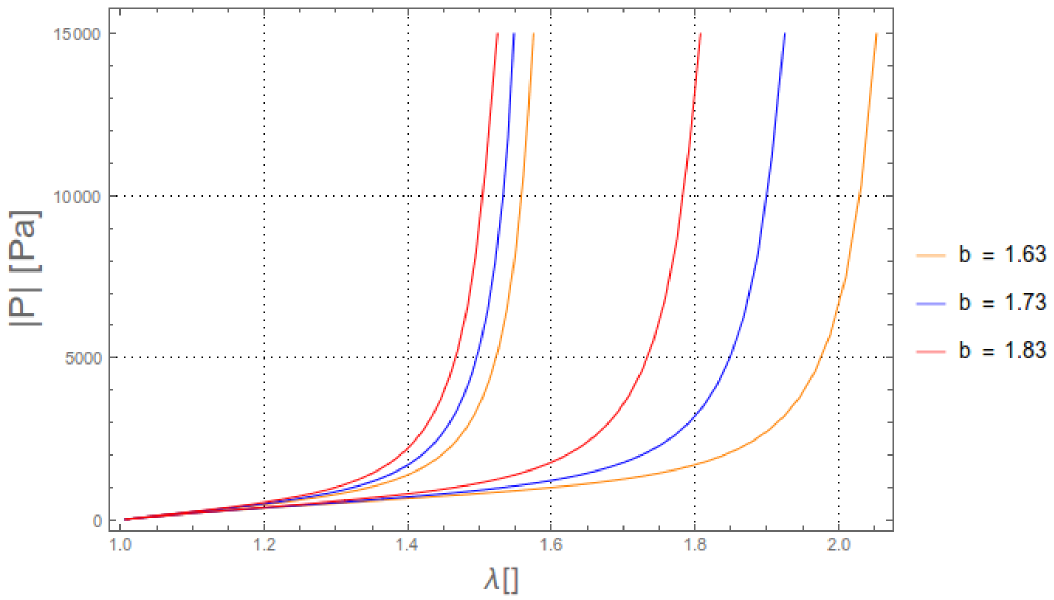

Fig. 9.4: Stretch vs stress at varying b.

Parameter	Stretch Ratio
b	Parallel:Perpendicular
1.63	1:1.303
1.73	1:1.244
1.83	1:1.186

Table 9.5: Parallel to perpendicular stretch ratios at varying b.

The effect of the cell dimensions a and b is two-fold. Firstly, their ratio to one another dictates the level of anisotropy. For the special case were $a : b = 1 : 1$, the collagen model's response is isotropic and the more this ratio deviates from $1 : 1$ the greater the level of anisotropy. This effect can be seen by Table 9.4 and Table 9.5. For increasing values of a, the response becomes more anisotropic while for decreasing values of b a similar response is observed. In both cases, i.e. an increase in a or a decrease in b, this represents an increased difference in the ratio between the two, thus furthering the level of anisotropy. Secondly, as a and b are used in the calculation of the end-to-end length initially and during deformation by Eq. (5.5) and Eq. (5.6), respectively, their initial values dictate the amount of allowable stretch before $r \to L$ and the locking type stretch is reached. Based on this, the behaviour observed in Fig. 9.3 and Fig. 9.4 is not unexpected. For greater values of a and b, the curves reached the end of the low-modulus portion at lower stretch values, both in the parallel fibre and perpendicular directions. Interestingly though, a had almost equal effect of the behaviour in both orientations, where the reduction in the obtained stretch was similar in the parallel and perpendicular directions for a 0.1 increase in a. Alternatively, for a 0.1 increase in b, the behaviour in the perpendicular direction was greatly affected whereas the parallel stretch obtained was minorly decreased.

9.1 Investigating Ageing via the Bulge Test

In order to investigate the effect of the skin thickness on the mechanical response, the bulge test as described and simulated in Sec. 7.1.4 was run for skin thicknesses of 0.3 cm, 0.4 cm and 0.5 cm. From Fig. 9.5 and Fig. 9.7, there is suggestion that the mechanical response of the model is unaffected by the the thickness of the simulated skin. For all three thicknesses the maximum obtained stretch in the parallel direction and the obtained apex height were practically identical. Some variation is observed at the transition between the low modulus portion and the linear region, where the thicker samples elicit a slightly stiffer response. Fig. 9.6 shows greater variation with skin thickness. The higher values of t result in a stiffer perpendicular response as lower stretch values are obtained at greater thicknesses.

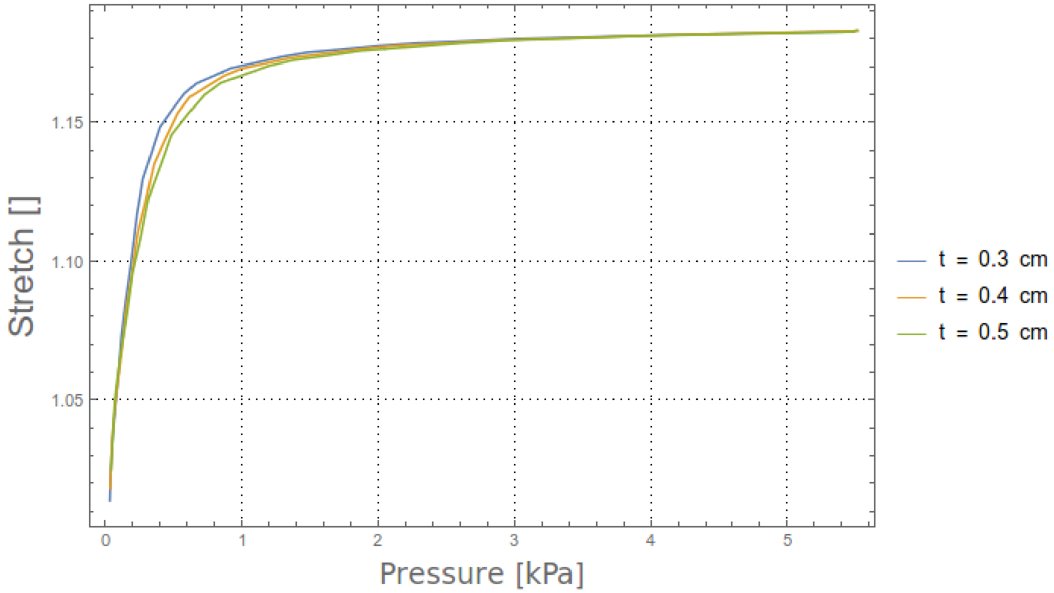

Fig. 9.5: Pressure vs parallel stretch at varying thicknesses.

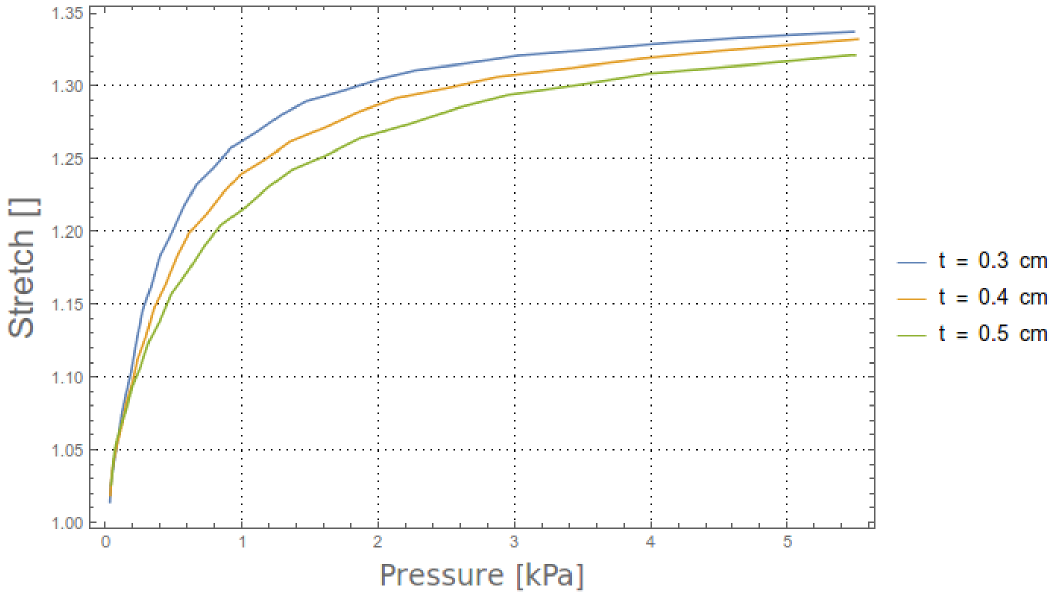

Fig. 9.6: Pressure vs perpendicular stretch at varying thicknesses.

The response of the apex height and parallel stretch suggest that the effect of the variation in thickness is ultimately negated by the effect of the collagen network. As the collagen chains approach the locking stretch, their effect dominates and supersedes any variation in skin thickness. The response on the perpendicular stretch is less obvious. The suggestion is that the maximum allowable stretch has not

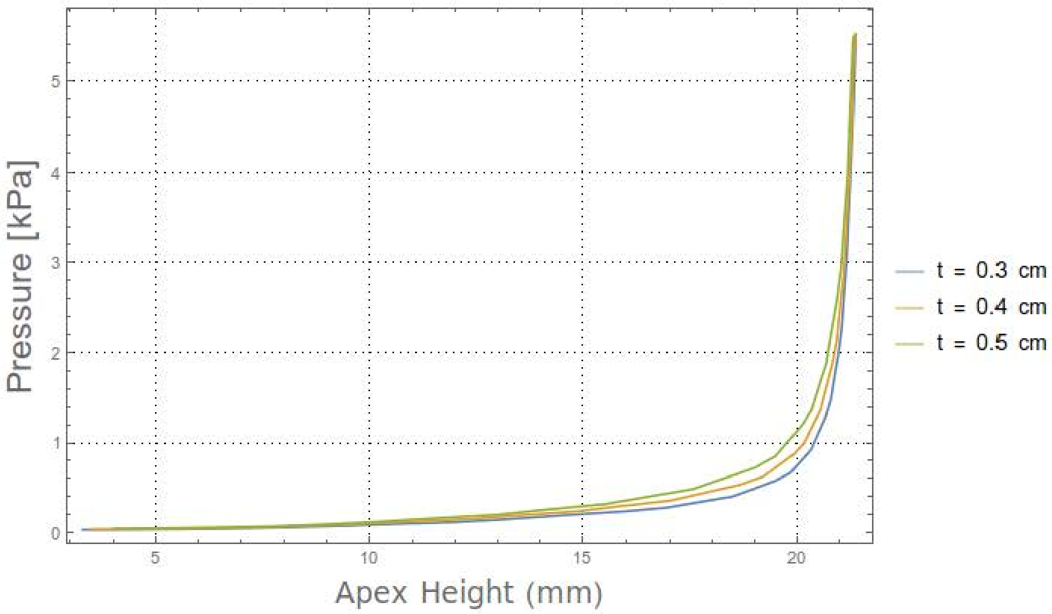

Fig. 9.7: Apex height vs pressure at varying thicknesses.

been reached in the perpendicular direction. Therefore the laxity in the collagen response that still exists along this axis allows for variations in skin thickness to play a more significant role.

It is interesting to note that similar mechanical responses can be elicited through different parameters, where increases in a, b and γ_{chn} result in increased stiffness. In capturing the mechanical response with ageing, it is thus plausible that all these factors could play an interlinked role and careful consideration is necessary to identify the correct ageing mechanisms. During the ageing process, the discussed parameters are taken to change as such:

- During the ageing process, the elastin network is observed to degrade. The loss of elastic integrity would logically lead to a reduced contribution from the elastin component of the described model. It is therefore natural that the value of γ_{elas} decrease with age. It should be noted though that as mentioned, elastin is a highly stable protein which undergoes little turnover before the age of 40. Thus γ_{elas} would remain constant for the first four decades and any change to occur thereafter.
- Within the current model, there is no natural parameter that describes the level of crosslinking at any point in time. It is believed that the increased crosslinking with age is one factor responsible for the increased stiffness of the skin. As observed in Fig. 9.2, by increasing γ_{chn} a stiffer response is illicited. Although γ_{chn} describes the number of fibres within a bundle, it represents the closest link between the observed increase in crosslinking with age and the model.
  Similarly though, there is no parameter within the model to describe the decrease in overall collagen density with age. It would be expected that a decrease in density would contribute to a decrease in the overall stiffness of the skin as the collagen network loses some integrity. Thus it is natural to assume that a decrease in γ_{chn} with age could be used to describe a loss of collagen.
  It is impossible to decode the complex interplay between these two factors as it is unclear as to which may be dominant. As discussed previously, according to Daly and Odland (1979) and Reihsner et al. (1995) the slope of the linear region remains constant with age. This suggests that the overall contribution between these two factors may be negligible. γ_{chn} is thus kept constant and the overall stiffening response of skin captured through alternative means.
- With age, due to dermal flattening and loss of elastic recoil, the collagen fibres are observed to "uncrimp". Through the chain network structure of the model, this is captured by adjustments to the end-to-end length of the collagen fibres through the parameters a and b. In Fig. 9.3 and Fig. 9.4, increasing a and b result in a reduction in the size of the low modulus portion prior to the onset of a rapid collagen response at lower stretches. With reference to Fig. 8.1, this is the expected behaviour with age. Thus by increasing a and b the model should be capable of capturing

the stiffening response.
Additionally, the anisotropic response of the skin is observed to change with age. Tonge et al. (2013a) reports a loss of anisotropy through observations of the bulge test. As the model will be compared to the bulge tests at various ages, it is this behaviour that is hoped to be captured. By reducing the ratio of $a : b$, either by increasing b or decreasing a or a combination of both, this should be obtained.

- Undeniably, there is a reduction in the thickness of the skin with age. Such an observation is backed by numerous sources in the literature, as mentioned in the previous chapter, but there is still much debate over the exact relationship between age and skin thinning. By figures Fig. 9.5, Fig. 9.6 and Fig. 9.7, the effect of the skin thickness is not significant and only plays a role along the perpendicular direction. Along this direction, larger skin thicknesses result in a stiffer response, which is counter to the expected response through ageing where despite observed thinning, a stiffer response is found. This suggests that the thickness of the skin is not responsible for the ageing response of skin. Nonetheless, alterations skin thickness will be accounted for in the forthcoming simulations.

9.1.1 Bulge Test with Ageing

The factors discussed in the previous section aim to provide a means by which to age the skin model in some continuous sense through the modification of a few choice parameters. Using this, the bulge test will be used to simulate an ageing skin response. The first step is to establish a relationship between these parameters and age. For this, parameter fits were found for the age 61 and 83 bulge test data. These specimens were chosen due to the broad age scope and as they were both from male donors, thus eliminating gender variability. In addition, the parameters found for the age 44 specimen will be used (Table 7.3). The age 43 parameters are omitted due to the suspected influence of UV ageing.

As before only the original network dimensions a and b, γ_{chn} and γ_{elas} were variable and the rest of the parameters kept constant at $L = 2.125, A = 1.82, \gamma_{gs} = 100\ \mathrm{N\,m^{-2}}$, $\beta = 4.5, \theta = 310$ K.

Parameter	Age 61	Age 83
a	3.55	3.65
b	1.25	1.287
γ_{chn}	$8.56 \times 10^{20}\ \mathrm{m^{-3}}$	$8.56 \times 10^{21}\ \mathrm{m^{-3}}$
γ_{elas}	$1000\ \mathrm{N\,m^{-2}}$	$500\ \mathrm{N\,m^{-2}}$

Table 9.6: 8-chain parameters, ages 61 and 83.

Adequate fits were found for both the 61 and 83 data. When compared to the age 44 data in Table 7.3, some trends can be noted. As expected, the value of γ_{elas} decreases almost linearly with age, with an approximate reduction of 100 $\mathrm{N\,m^{-2}}$ every five years. The cell dimensions a and b both increase with age, as predicted. Additionally the ratio between the two changes with age with $a : b = 4.313{:}1$, 2.84:1 and 2.836:1, at age 44, 61 and 83 respectively. This reduction, especially between age 44 and 61 is indicative of the expected reduction in anisotropy. The change in γ_{chn} is more difficult to interpret. There is a significant reduction from age 44 to 61 but the value at age 83 matches that at age 44. Such variation is difficult to deconstruct within an ageing context. As the value at 44 matches that at 83, it is assumed that there must be some individual factor present at age 61 that results in the observed difference, which is not part of the ageing process.

Using the a and b parameter values as found from the age 44, 61 and 83 fits, general ageing trends were established. It is clear that a mere three data points is insufficient in order to conclusively determine

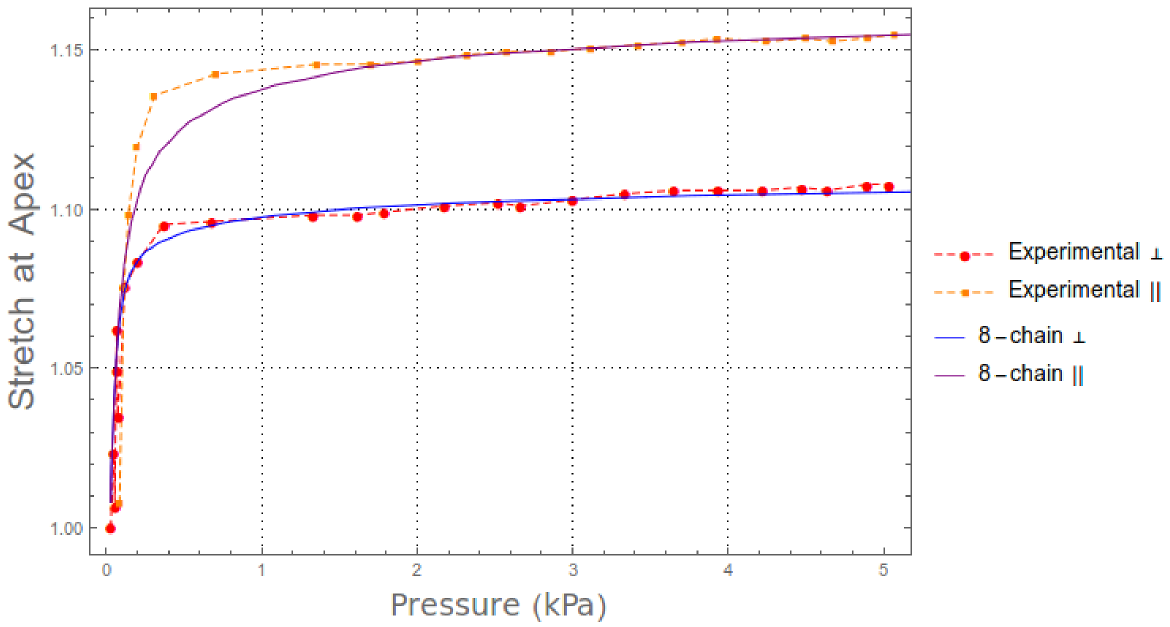

Fig. 9.8: Pressure vs stretch, age 61.

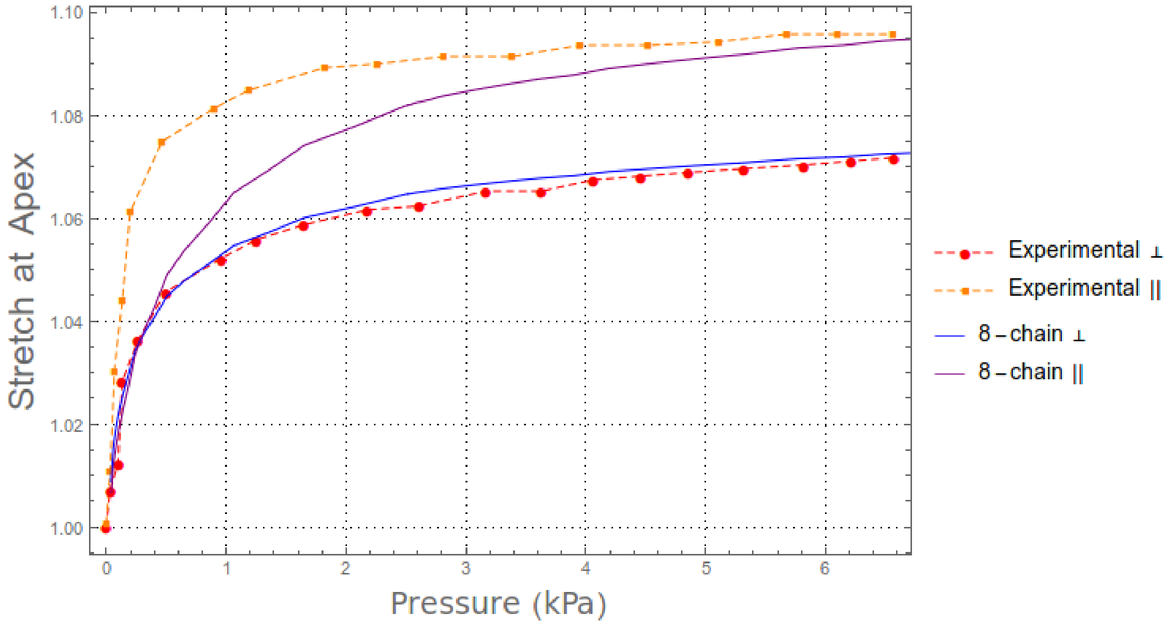

Fig. 9.9: Pressure vs stretch, age 83.

an ageing trend, but are adequate for the current proof on concept. Using MATLAB (Mathworks, 2014), shape-preserving fits were used to find a continuous evolution of a and b, as shown in Fig. 9.10 and Fig. 9.11. As expected, there is a general increase in both parameters with age. a evolves almost linearly with age whereas b undergoes a large increase between age 44 and 61 followed by a plateau. This suggests between age 44 and 61 there is a more significant loss of anisotropy due to a realignment or redistribution of the collagen network as compared to later in life.

The skin thickness data as presented in Table 7.2 for the ages of interest were used to acquire a linear equation for the skin thickness with age. From Fig. 9.12 it can observed that a very rough fit has been established due to highly irregular data. From the investigation into the effect of skin thickness on

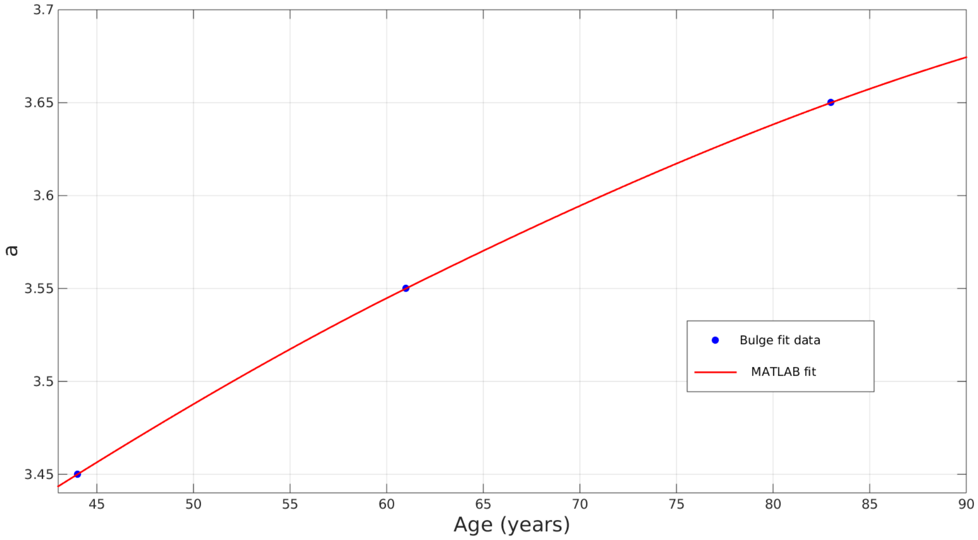

Fig. 9.10: Age vs a .

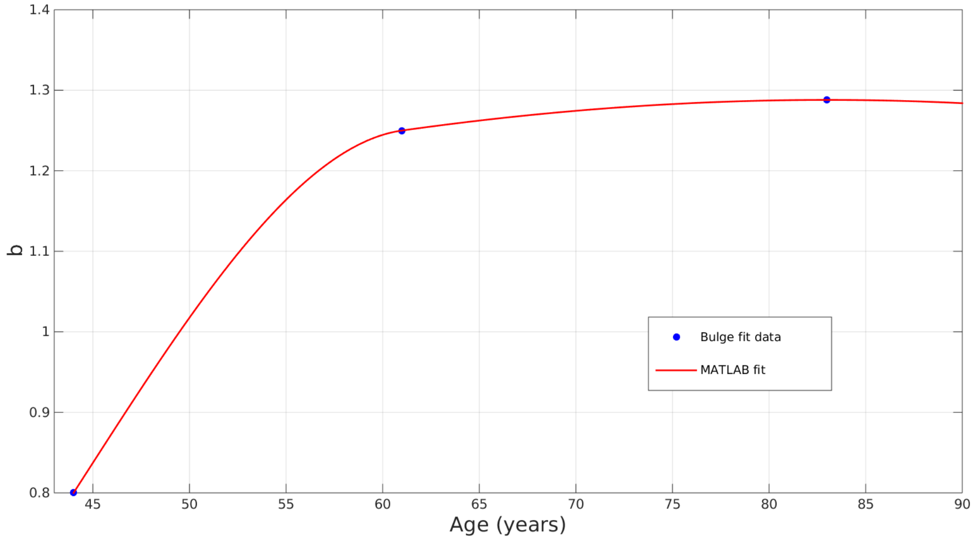

Fig. 9.11: Age vs b .

the stretch and apex height results, it is determined that such a fit should not significantly affect the ageing response. The linear fit is sufficient and follows the equation:

$$t = -0.0047\text{cm} \times \text{age} + 0.59\text{cm}. \tag{9.1}$$

The overall decrease in skin thickness is as found through the literature. With reference to Eq. (8.1), the gradient of the equation is comparable. The difference in the y-intercept value can is down to two possible factors; Eq. (8.1) accounts for thinning from the age of 60 while Eq. (9.1) does not account for the fact that thinning does not occur during earlier life.

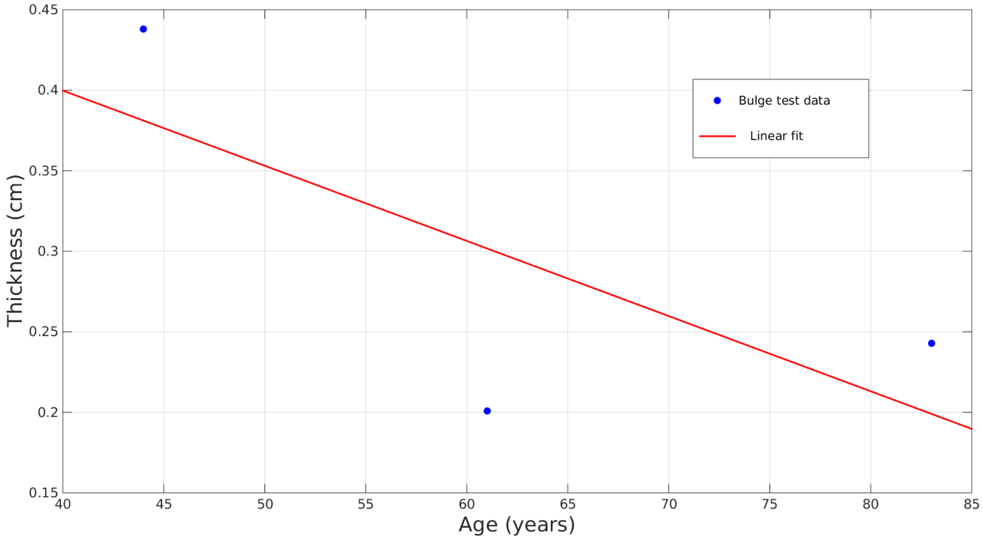

Fig. 9.12: Age vs skin thickness.

	Parameters		
Age	a	b	γ_{elas}
49	3.483	0.984	1200
54	3.513	1.14	1100
59	3.54	1.236	1000
64	3.564	1.26	900
69	3.587	1.273	800
74	3.613	1.282	700
79	3.634	1.287	600
84	3.654	1.288	500
89	3.671	1.285	400

Table 9.7: Modification of age dependent model parameters.

With the established trends, bulge test simulations were run at 5 year increments. Table 9.7 contains the adjustments to the parameters of interest. As mentioned, γ_{elas} decreases from 1300 $\mathrm{N\,m^{-2}}$ at age 44 by 100 $\mathrm{N\,m^{-2}}$ every 5 years.

In Fig. 9.13 and Fig. 9.14 the simulated evolution of the stretch behaviour with age is given, with comparison to the experimental data at ages 44, 61 and 83. As expected, the general trend is captured as the skin stiffens with age. It can be noted that the maximum stretch obtained drops significantly at ages 44 - 59, with less significant drops thereafter. This is to be expected primarily due to the trend in parameter b as given in Fig. 9.11, where there is an initial sharp increase followed by a plateau. The convergence of the stretch values between 59 and 89 is further due to the initial end-to-end length, r_0, approaching the contour length, L. As r_0 increases with age, the amount of allowable stretch is reduced. The evolution of the stretch values is mimicked by the evolution of the apex heights in Fig. 9.15. The obtainable height is reduced with increased stiffness, with a similar convergence of apex heights with later age.

Fig. 9.16, Fig. 9.18, Fig. 9.19 and Fig. 9.21 show the simulated contour profile of the bulge test for samples at 10 year age gaps, from 54 to 84 years. Fig. 9.17 and Fig. 9.20 show the experimental contour profiles of the age 61 and 83 specimens. It is important to note that in the experimental specimens the Langer lines were not aligned with the body axis. The Langer lines were oriented at 64° and $-24.6°$

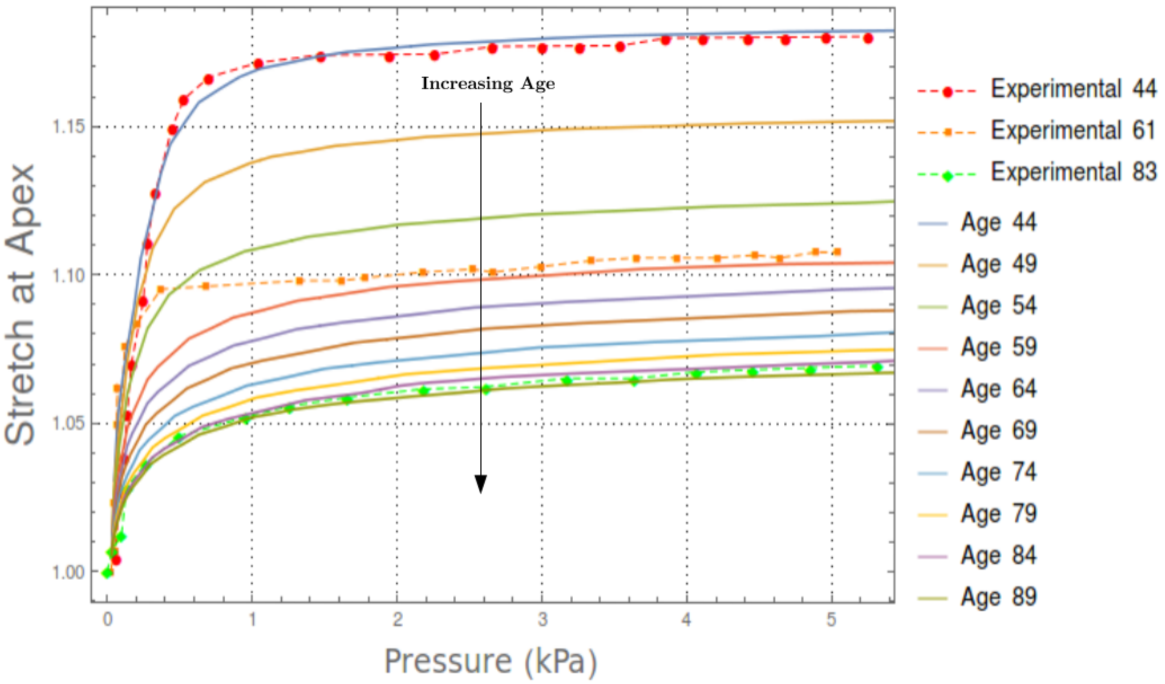

Fig. 9.13: Pressure vs parallel stretch at varying ages.

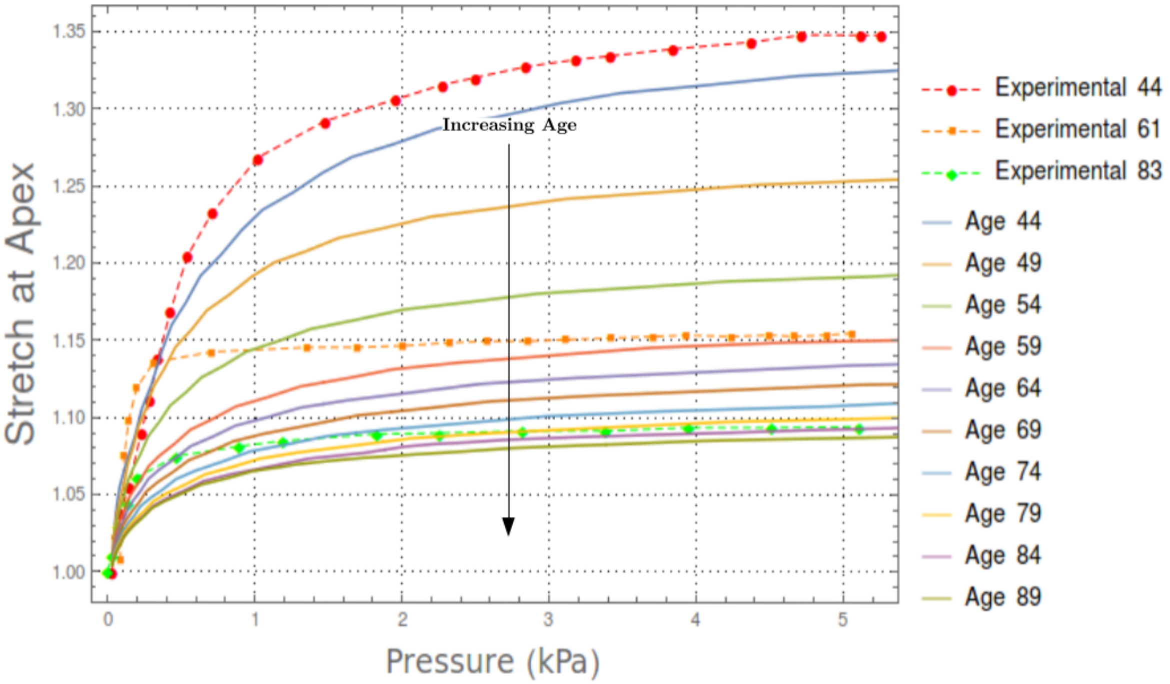

Fig. 9.14: Pressure vs perpendicular stretch at varying ages.

to the x-axis for the age 61 and 83 specimens, respectively, as indicated in the figures. This alteration in the orientation is reflected in the simulated results.

The profile comparison between the age 54 and 64 simulated and age 61 experimental results are very similar. The alteration in the fibre orientation is captured quite satisfactorily, with the resulting axial assymmetry in the X and Y components of displacement represented accurately. The Z component of displacement is acceptably captured, although there seems to be an over-estimation in the level of

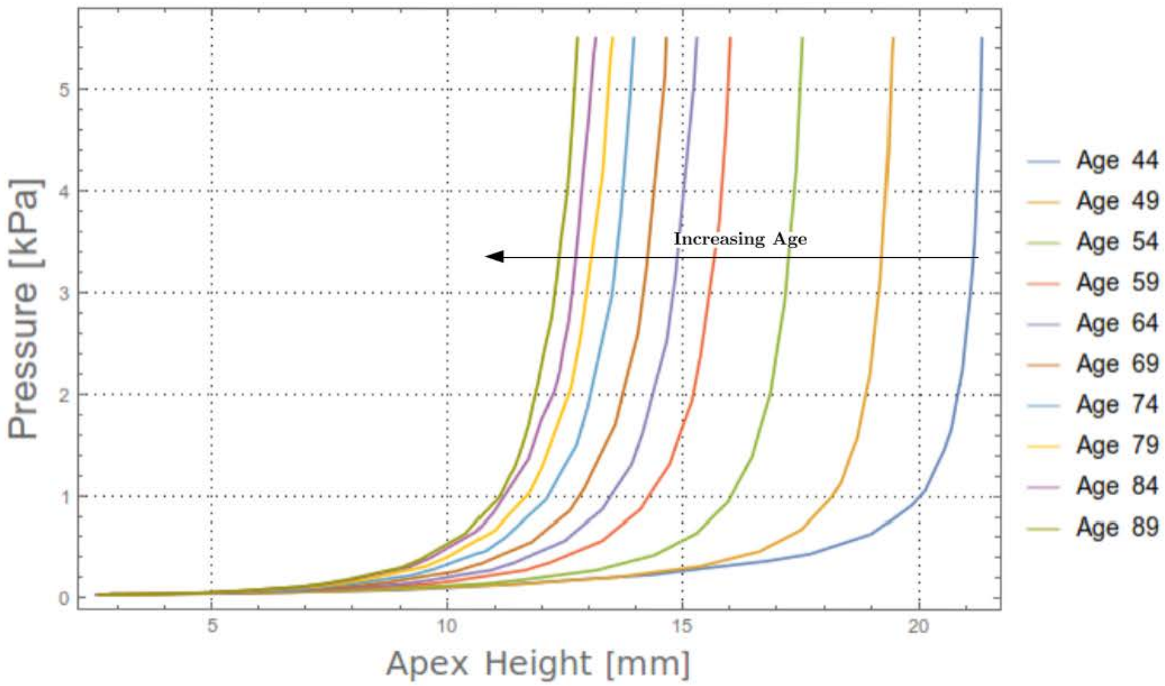

Fig. 9.15: Apex height vs pressure at varying ages.

anisotropy in the simulated results, compared to the age 61 specimen. In terms of the magnitude of the displacements, the Y components of the age 61 experiment and age 64 simulation are similar, but the simulations over-estimate the other two components. This is not all too surprising due to the poor quality of fit with the pressure-stretch data at age 61 as shown in Fig. 9.13 and Fig. 9.14

The age 74 and 84 simulations were orientated at $-24.6°$ to the positive x-axis in order to replicate the age 83 experimental contour plots. There is sufficient agreement in the general profile of the simulated results when compared to the experimental data. The only discrepancy lies in the X component of the experimental data as shown in Fig. 9.20a, where the lack of symmetry suggests a possible defect in the skin specimen, such as a non-uniform skin thickness or an irregularity on a constituent level, such as an inconsistent collagen distribution or dispersion. Despite this, the X and Y displacements of the age 84 simulated results are comparable to the experimental results, but there is again a minor over-estimation in the Z component.

Through this chapter, a structurally motivated means by which to "age" the constitutive model through modification to chosen parameters was presented. It was found that through adjustment to a limited number of parameters, an acceptable ageing type response could be captured. The majority of the ageing process was reproduced through modification to the collagen network, which is not unexpected due to the accepted idea that collagen is primarily responsible for the tensile response of the skin at large strain. Minor modification to the elastin contribution captured the ageing response at small strains.

Despite the general ageing trend being captured, there still exists some discrepancies. The poor quality of fit at age 61 could be due to individual variability, but could also suggest the presence of an additional factor not captured in the model. Additionally, the simulations consistently over-estimated the apex height compared to the experimental results, despite adequately replicating the maximal stretch results. Again this suggests an added stiffening factor:

- Crosslinking has been noted to play a role in the ageing process. The current model does not have a natural means by which to capture the contribution of increased crosslinking with age.

- UV damage compounds and exaggerates the effects of chronological ageing. It is unclear as to the extent to which the skin specimens used in the experimental bulge tests were exposed to UV during the lifetime of the donors. The presence of elastotic tissue would act to stiffen the skin.

As mentioned in Sec. 7.1.4, the guard ring may concurrently have unexpected effect on the deformation behaviour of the bulge experiments.

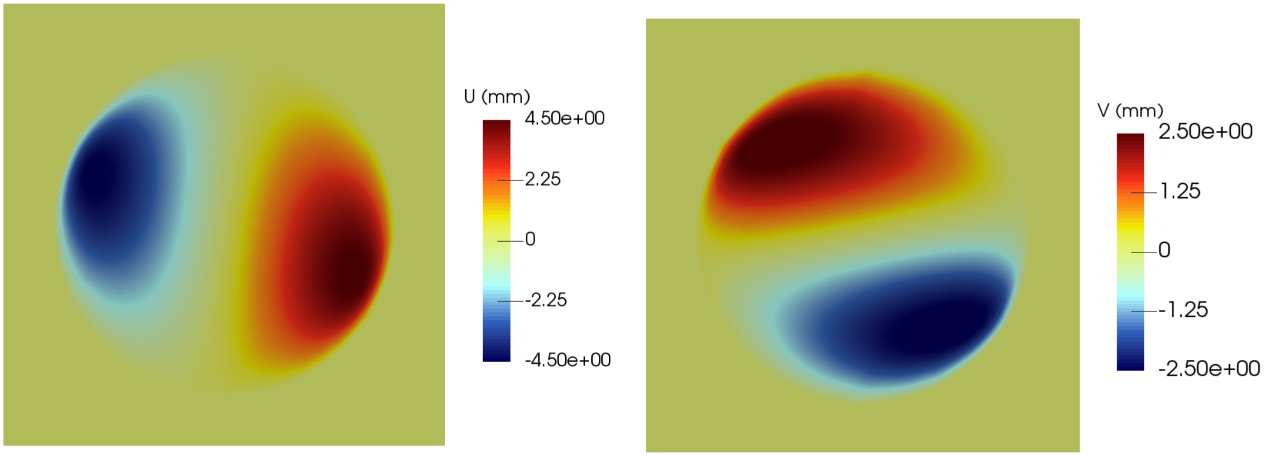

(a) X component of displacement.

(b) Y component of displacement.

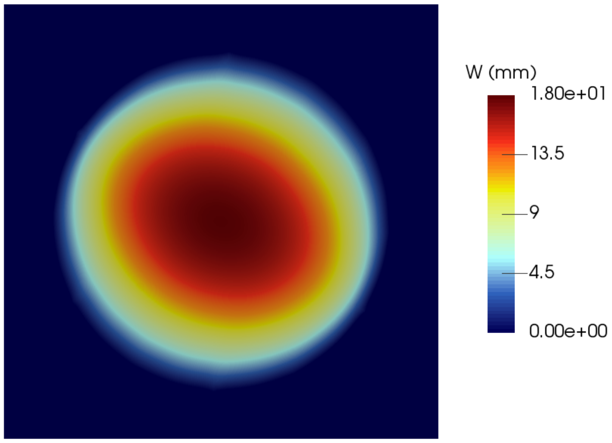

(c) Z component of displacement.

Fig. 9.16: Displacement comparison, simulated age 54, Langer lines at 64° to the positive x-axis.

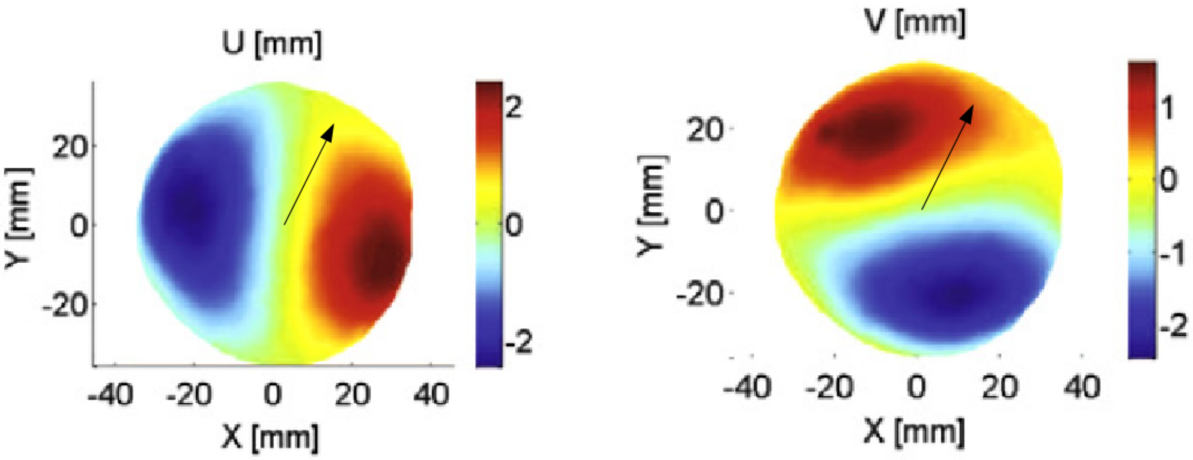

(a) X component of displacement.

(b) Y component of displacement.

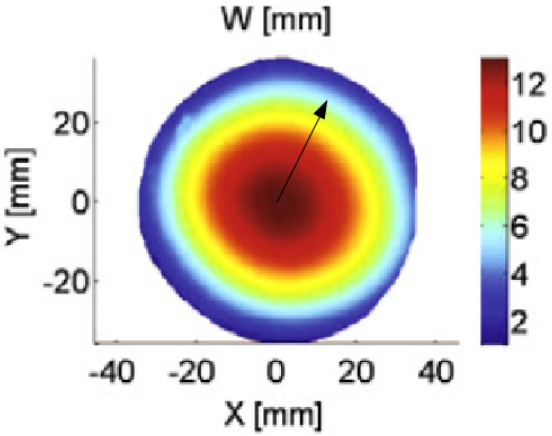

(c) Z component of displacement.

Fig. 9.17: Displacement comparison, experimental data age 61, Langer lines at 64° to the positive x-axis.

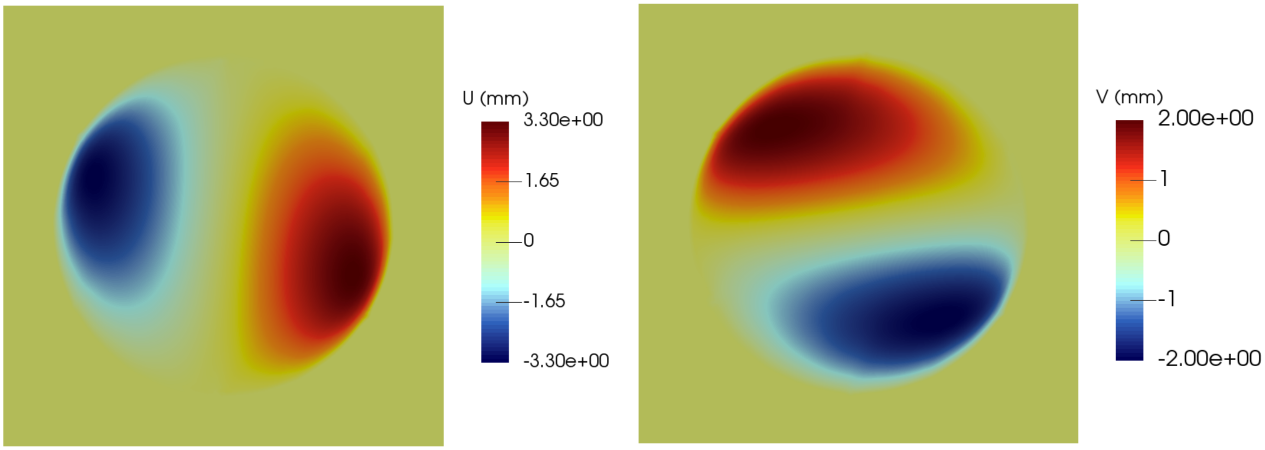

(a) X component of displacement.

(b) Y component of displacement.

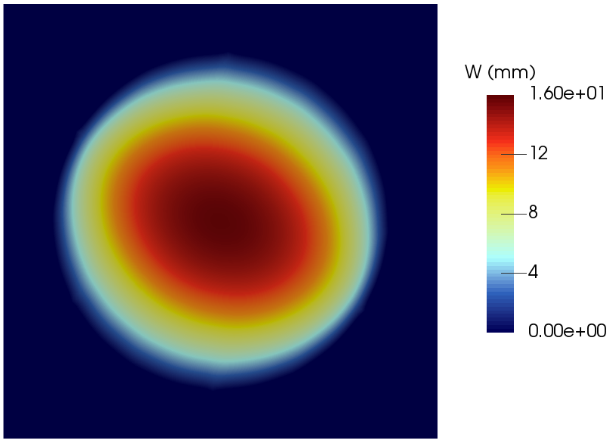

(c) Z component of displacement.

Fig. 9.18: Displacement comparison, simulated age 64, Langer lines at 64° to the positive x-axis.

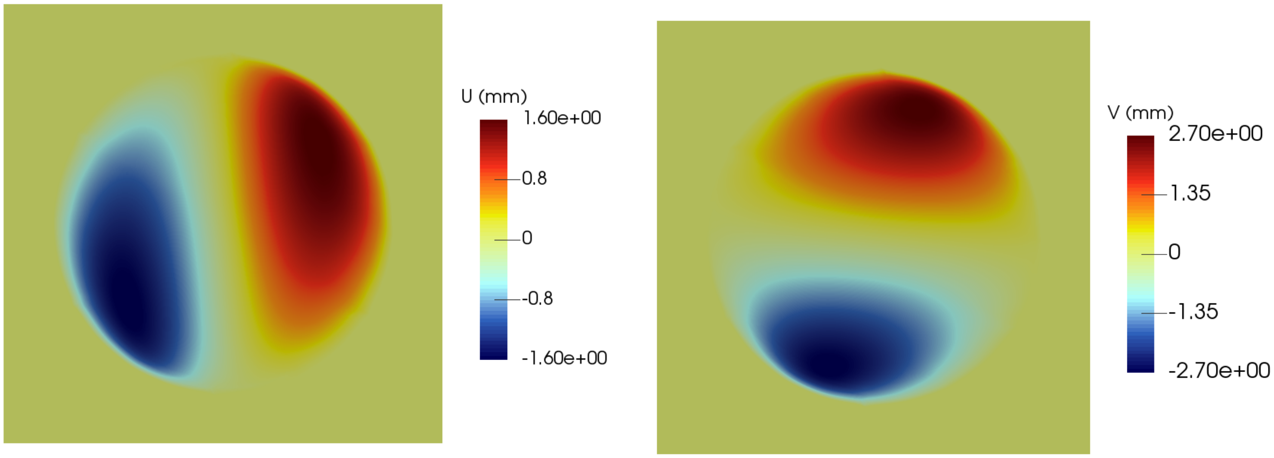

(a) X component of displacement.

(b) Y component of displacement.

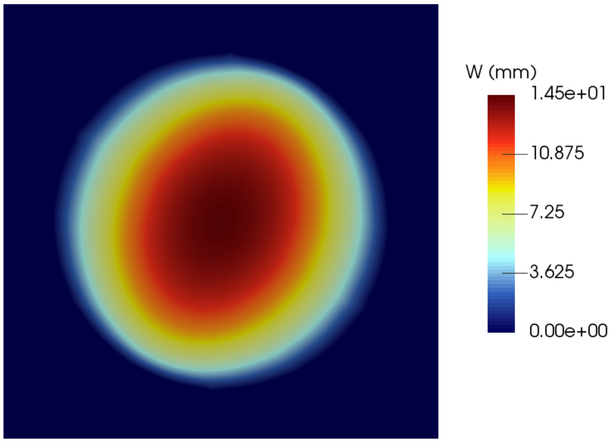

(c) Z component of displacement.

Fig. 9.19: Displacement comparison, simulated age 74, Langer lines at $-24.6°$ to the positive x-axis.

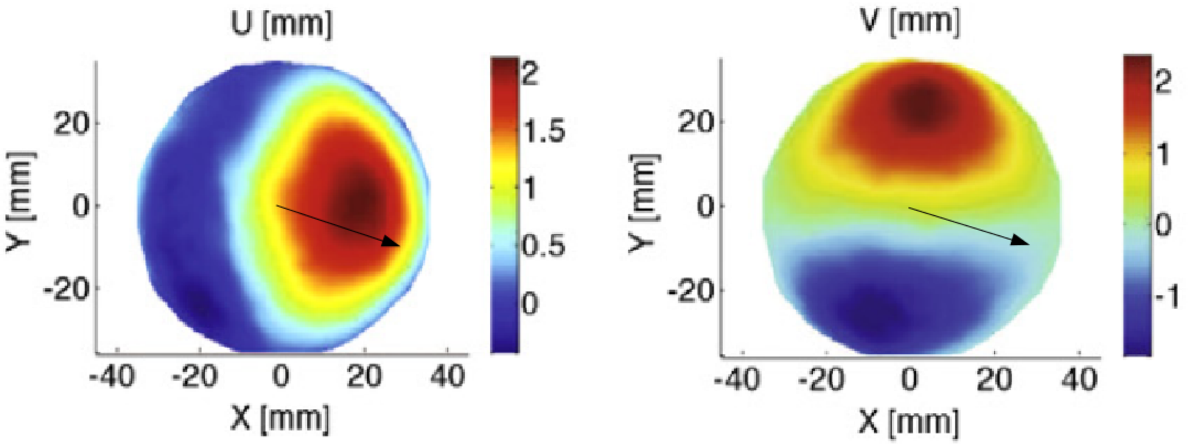

(a) X component of displacement.

(b) Y component of displacement.

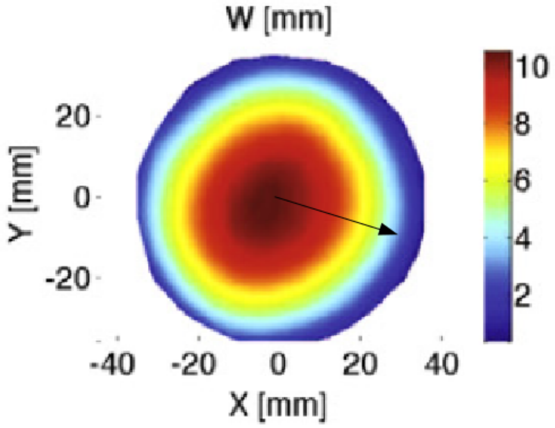

(c) Z component of displacement.

Fig. 9.20: Displacement comparison, experimental data age 83, Langer lines at −24.6° to the positive x-axis.

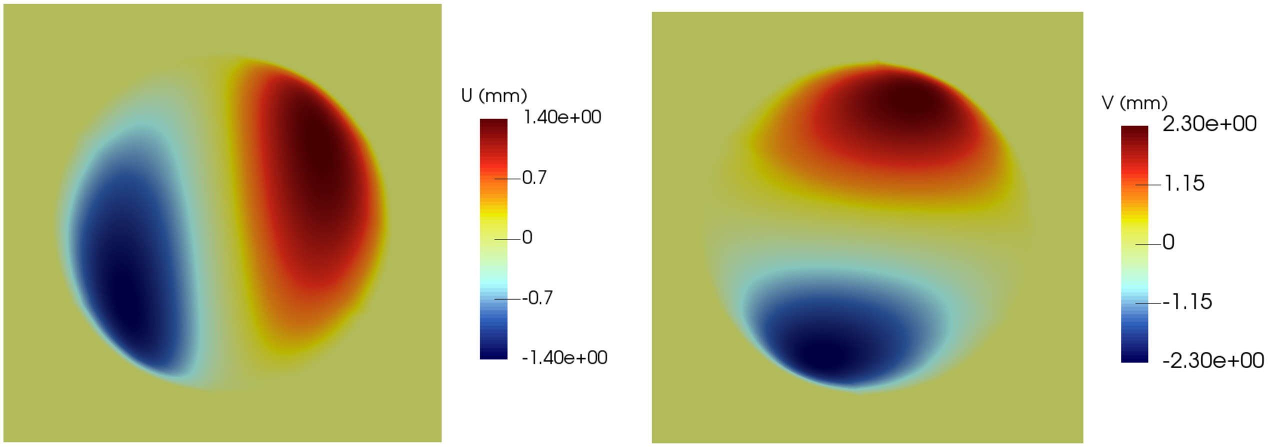

(a) X component of displacement.

(b) Y component of displacement.

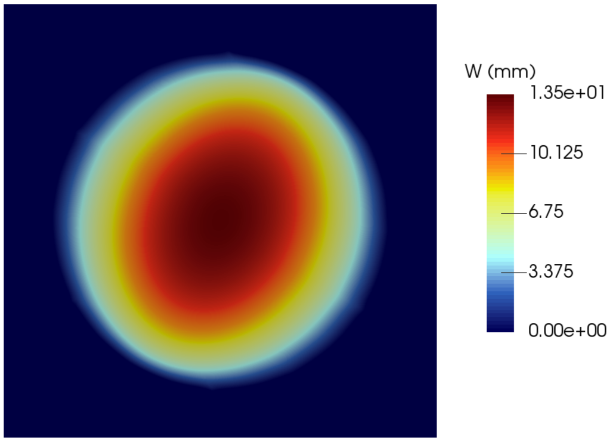

(c) Z component of displacement.

Fig. 9.21: Displacement comparison, simulated age 84, Langer lines at $-24.6°$ to the positive x-axis.

10

Discussion, Conclusion and Proposed Extension of the Model

10.1 Discussion and Conclusion

Ageing is one of life's absolutes. The steady progression of time results in the gradual decline of tissue condition and function. In an attempt to understand how the ageing process occurs within soft tissue, there has been an immense amount of experimental study. To date, a significant understanding has been established on a cellular level as to what instigates the effects of ageing, with all the downstream effectors that ultimately lead to soft tissue decline. Despite this, a great deal is still to be understood, with the only firm understanding being that ageing is a vastly complex and interconnected process.

One such soft tissue that has received much attention within the context of ageing is that of skin. Skin, being the point of contact with the outside world, is intrinsically linked to ones age. Additionally, it is subject to a vast array of external stresses, such as pollution and UV-exposure. Such factors generally compound and exaggerate the effects of ageing, which makes establishing the process of chronological ageing a difficult task.

Through the literature, there have been numerous attempts to resolve the mechanical response of skin, with and without the influence of age. Various experimentalists have devised multiple skin tests in the hope of forming a definitive characterisation of the behaviour of skin under loading. In general, the skin is highly nonlinear, anisotropic, viscoelastic, and exhibits nearly incompressible response to loading. The skin typically displays a *J-curve* under loading. Despite this general characterisation, it is abundantly clear that the extent to which these features are evoked is highly variable and dependent upon several factors such as race, gender and anatomical site, with age possibly having the most profound effect on the skin including the loss of elastic and viscoelastic properties. Despite the reduced stiffness in the low modulus portion of the J-curve, this portion is shortened resulting in an overall increase in stiffness.

In order to develop an appropriate skin model that could account for the level of variation found through experimental investigation, it was important that the microstructure of the skin be well understood. In general, the mechanical response of the skin is due to the constituents that make up the bulk of the dermal layer, specifically ground substance, elastin and collagen. As done previously by a number of authors, Buganza Tepole et al. (2012) and Kuhl et al. (2005) to name a few, a free energy is proposed for each constituent and the additive form of these results in the overall skin response. The ground substance and elastin contributions were modelled through an isotropic coupled form of the compressible neo-Hookean free energy. For collagen, as the primary load-bearing constituent it was necessary to adopt a structural model that was motivated by the fibrous nature of the collagen network, capable of capturing the inherent nonlinearity and anisotropy witnessed under finite deformation. For this, a wormlike chain model was found to be applicable.

The constitutive model was used to replicate the results of two mechanical tests: the tension test and the bulge test. The tension test offers a simple uniaxial test through which to test the directional response of the model. The model was able to closely replicate the experimental uniaxial rabbit skin data as established by Lanir and Fung (1974). The bulge test, as detailed by Tonge et al. (2013a) offered a more complicated loading condition through which to test the model. Through the application of a pressure loading condition, the stretch response of the skin specimens could the captured. The adopted constitutive model was found to adequately capture the resulting deformation and stretch.

Through the mechanical tests, confidence in the model was established independent of an ageing response. In order to incorporate ageing into the mechanical model, it was required that not only a firm understanding of what changes occur in the microstructure be established but also that these changes be mapped back the the constitutive parameters. Through the use of a structurally-based model, this task was naturally achievable. Several key aspects of skin ageing were identified, such as loss of integrity within the elastin network, dermal thinning and unravelling of the collagen network. These modifications were incorporated into the model in order to replicate the ageing process.

By informed modification to the constitutive parameters the ageing process was successfully replicated. The reduction in stiffness at low stretches (low modulus portion) through degradation of the elastin network was well captured through modification to the elastin free energy. The overall increase in stiffness was captured through modification of the collagen network dimensions. Despite this success there were some limitations:

- The model in its current form does not account for the crosslinking within the collagen network. Crosslinking prevents slippage between fibres and accordingly contributes toward the stiffness elicited by the collagen network under stretch. With age, crosslinking has been seen to increase which has often been attributed as a possible source of the increase in stiffness. An extension to the model would be to incorporate crosslinking through fibre-fibre interactions such as that presented in Limbert (2011). Additionally, the model does not directly account for the progressive loss of collagen and elastin with age.
- In order to incorporate an age-based modification to chosen model parameters, experimental bulge test data was used at ages 44, 61 and 83. At only three sample points, this does not represent an adequate range of data with which to make a conclusive parameter fit. Therefore, if a full ageing model were to be presented, it is necessary to include data from an statistically significant number of specimens over a large range of age groups. Additionally, experimental samples would need to controlled for several factors so as to limit variability. Of greatest importance would be control over anatomical site. Not only should skin from the same site of the patients be tested, but also controlled for influence of photoaging.
- The parameters through which to model ageing were chosen through informal reasoning done by the researchers. Although beyond the scope of this project, a formal sensitivity analysis would have aided in providing deeper insights into which parameters could additionally have been modified within an ageing context.

To conclude this thesis, a framework for a proposed extension to the skin model is detailed. This extension aims to incorporate the synthesis and degradation of collagen and elastin as discussed for chronological ageing in Chapter 3. Such a framework aims to capture a continuous model for ageing on the microscopic level through nano-scale processes. Furthermore, the incorporation of photoaging follows naturally from the structure presented.

10.2 A Model for Ageing

Not only was it essential to understand the anatomy of the skin's primary constituents, but the processes involved in their synthesis and degradation are key to establishing a structurally-motivated mechanical model. In the context of ageing, the ageing process could be postulated as a modification of the microstructure through factors and processes that govern the net turnover of the critical constituents. In this thesis, a microstructurally based model was presented that attempted to capture the contribution of the key constituents to the overall mechanical response of the skin. An ageing type response was further introduced through the modification of parameters that were motivated to be involved in the ageing response. The model proposed in the previous chapters has not incorporated the processes involved in the turnover of collagen and elastin that occurs through the ageing processes as discussed in Chapter 2 and Chapter 3, where an investigation was conducted into the enzymatic and nano-constituent processes involved in the ageing process. Various factors were identified as playing key roles in the synthesis and degradation of primary skin constituents, such as collagen and elastin.

Here, a potential extension to the skin model is presented as a possible framework for a continuous ageing response. Evolution equations for the nano-constituents and their influence on collagen and elastin are presented. Further ideas are put forth as to how this can be incorporated into the full skin model. With reference to Fig. 3.3, the focus will be on chronological ageing, while further ideas will be proposed for extension to a model that incorporates photoaging.

10.2.1 Biological Remodelling

In the literature, there has been increasing interest in the development of continuum models for the investigation of the response of biological materials to external stimuli. Such models are broadly classified into two categories:

- Continuum models for growth, i.e. a change in volume.
- Continuum models for remodelling, i.e. a change in constituent density and constitutive parameters.

There exists detailed literature on the concept of growth modelling (Himpel et al., 2005; Kuhl et al., 2003; Menzel and Kuhl, 2012), but the attention here is restricted to remodelling.

Continuum models for remodelling have been developed for bone and developed within the framework of continuum damage mechanics (Jacobs et al., 1995, 1997). Such models have been extended to describe softening behaviour in biological tissue (see e.g. Alastrué et al., 2007). Evolution equations for the density and the elasticity tensor follow from thermodynamic restrictions on the reduced dissipation inequality and are subject to classical Kuhn–Tucker constraints.

An alternative remodelling framework is that of *open-system thermodynamics*. This allows for isotropic remodelling via the introduction of density sources and fluxes (Kuhl et al., 2003; Kuhl and Steinmann, 2003; Menzel and Kuhl, 2012). The free energy Ψ, has added dependence on the density thereby allowing for a strengthening or weakening. Anisotropic remodelling has been considered by Waffenschmidt et al. (2012).

The general structure for remodelling is obtained through two coupled governing relations for momentum and mass, by adding the following dependencies to the free energy and introducing density source terms $\mathcal{R}_0$ into the density evolution relation, where:

$$\begin{aligned}\Psi &= \Psi(\mathbf{C}, \mathbf{v}_0, \rho_0)\\ \mathcal{R}_0 &= \mathcal{R}_0(\rho_0, \Psi).\end{aligned}$$

This framework has been successfully employed in various contexts within biological remodelling and more recently applied to soft tissue, in particular collagen turnover in arteries (Lafortune and Aris, 2015; Saez et al., 2013a). The work by Saez et al. (2013a) is especially relevant, as a theoretical and computational model for collagen turnover as a result of hypertension is proposed. Here, the model focused on the variation of the nano-constituent factors, such as TIMP, MMP and TGF-β. This change is driven by mechanical stimuli as a result of the muscular contractions. This provides an appropriate case study with which to motivate an ageing model.

Case study: collagen turnover due to hypertension

Hypertension is a chronic vascular disease where blood pressure becomes elevated. This increased pressure results in an increased mechanical load on the vasculature in the body. In an attempt to maintain a homoeostatic stress state, smooth muscle cells (SMCs) start to grow which results in the thickening of vessel walls. This growth is the result of alterations within the extracellular matrix (ECM) of vessel walls, primarily through changes in the deposition and degradation of collagen.

Extensive studies have shown that collagen deposition increases with hypertension. SMCs produce TGF-β and through added mechanical stress on the SMC, there is increased expression of TGF-β thus resulting in the up-regulation of collagen deposition. In terms of degradation of collagen, the ratio of MMP to TIMP is of primary concern. In hypertension, TIMP has been reported to increase, decreasing the total amount of MMP. Ultimately, collagen turnover increases as a result of hypertension and the strain imposed on the SMC.

A collagen free energy, Ψ_{col}, is proposed using the microsphere concept (Bazant and Oh, 1985) which homogenises the micro-scale response by means of an integral over the unit sphere. This allows for individual collagen fibril directions to be accounted for, the details of which can be found in Saez et al. (2013a).

The key aspect of this model is in how the collagen density, ρ, evolves. Density evolution introduces a mass source term $\mathcal{R}$ to the balance of mass, where mass fluxes are neglected here for the sake of simplicity. As proposed by Kuhl et al. (2005), $\mathcal{R}$ takes on the general form:

$$\dot{\rho} = \mathcal{R} = \left[\frac{\rho}{\rho^*}\right]^{-m} \Psi(\mathbf{C}) - \Psi^*, \tag{10.1}$$

where Ψ^* and ρ^* are the energy in the homoeostatic equilibrium state (also know as the attractor stimulus) and the initial density, respectively.

Additionally, Ψ_{col} takes on a density dependence, $\Psi_{col} = \Psi_{col}(\mathbf{C}, \mathbf{v}_0, \rho)$, generally through a weighted factor similar to that in Eq. (10.1). This either strengthens or weakens the collagen contribution to the overall mechanical response according to the presence of collagen within the soft tissue. Refer to Kuhl et al. (2003) for further details.

Through activation of the SMC, TGF-β and TIMP pathways are activated. It is these constituents that evolve according to Eq. (10.1). As mentioned, the system is driven by the mechanical loading on the SMCs which is captured through an energy, Ψ_{SMC} yielding source terms for TGF and TIMP:

$$\begin{aligned}
\mathcal{R}_{TGF-\beta} &= \gamma_{TGF-\beta}\left[\frac{\rho_{TGF-\beta}}{\rho^*_{TGF-\beta}}\right]^{-m_{TGF-\beta}} \Psi_{SMC} - \Psi^*_{TGF-\beta}, \\
\mathcal{R}_{TIMP} &= \gamma_{TIMP}\left[\frac{\rho_{TIMP}}{\rho^*_{TIMP}}\right]^{-m_{TIMP}} \Psi_{SMC} - \Psi^*_{TIMP},
\end{aligned}$$

where the $\gamma \in \mathbb{R}^+$ terms are parameters to govern the sensitivity to the SMC energy.

TIMP acts to inhibit and regulated MMP, thus MMP evolves inversely to TIMP through

$$\mathcal{R}_{MMP} = \gamma_{MMP}\mathcal{R}_{TIMP},$$

$\gamma_{MMP} \in \mathbb{R}^-$.

With these collagen sources defined, collagen thus evolves similarly to that discussed in the context of skin through:

$$\mathcal{R}_{col} = \gamma_+\mathcal{R}_{TGF-\beta} + \gamma_-\mathcal{R}_{MMP}.$$

The above system of time-dependent equations can be solved using a time discretisation scheme and linearised through a Newton scheme as discussed in Chapter 6 to establish the collagen density evolution. The parameter units and interpretation are presented in Table 10.1.

Parameter	Symbol	Units
TGF-β sensitivity to SMC energy	$\gamma_{TGF-\beta}$	-
TIMP sensitivity to SMC energy	γ_{TIMP}	-
MMP sensitivity to TIMP	γ_{MMP}	-
Collagen sensitivity to TGF-β	γ_{+}	-
Collagen sensitivity to MMP	γ_{-}	-
$m_{TGF-\beta}$	TGF-β nonlinear remodelling	-
m_{TIMP}	TIMP nonlinear remodelling	-
ρ^{*}_{TIMP}	initial TIMP density	$\mu g\,ml^{-1}$
$\rho^{*}_{TGF-\beta}$	initial TGF-β density	$\mu g\,ml^{-1}$
ρ^{*}_{MMP}	initial MMP density	$\mu g\,ml^{-1}$
ρ^{*}_{col}	initial collagen density	$\mu g\,ml^{-1}$
$\Psi^{*}_{TGF-\beta}$	homoeostatic equilibrium state of TGF-β	$N\,m^{-2}$
Ψ^{*}_{TIMP}	homoeostatic equilibrium state of TIMP	$N\,m^{-2}$

Table 10.1: Evolution equation parameters (Saez et al., 2013a).

10.2.2 A Model for Ageing

Saez et al. (2013a) gives a relevant idea on how to to account for collagen and elastin remodelling due to intrinsic and extrinsic ageing through microstructural motivation. The interplay between factors such as TGF-β and MMP are of primary concern and will need to be incorporated into an ageing model.

The primary difference between the model presented by Saez et al. (2013a) and an ageing model is how the processes are driven. In Saez et al., the stimulus is related to the elastic energy density where changes in collagen turnover occur through the mechanical loading of the SMCs of the vascular tissue. This offers a very natural driving process captured by the SMC free energy Ψ_{SMC}. The ageing process does not offer such an easy analogue. Ageing, and accordingly the effects on collagen and elastin turnover, do not evolve with some mechanical loading but instead due to a more innate process. Additionally, the system is driven toward a state of equilibrium through the inclusion of the homoeostatic equilibrium terms, $\Psi^{*}_{TGF-\beta}$ and Ψ^{*}_{TIMP}. Within an ageing context, it does not make sense for the system to be driven to a state of equilibrium as this would be analogous to saying that ageing "stops".

Due to the differences discussed in the previous paragraph, and in order to develop a meaningful ageing model several adjustments need to be made to the theory proposed by Saez. Of primary concern is the introduction of an alternative driving factor. In Chapter 3 it was found that through the loss of antioxidant defence with age, the level of ROS present in the skin increased. ROS accordingly was found to be a common factor in the evolution of the primary constituents that related to collagen and elastin turnover (see Fig. 3.3). Therefore it is proposed that ROS provides a mechanism with which to drive the ageing process.

With reference to Eq. (10.1), the evolution equations will be of the form:

$$\dot{\rho}^{\mathrm{rel}} = \mathcal{R},$$

where $\mathcal{R}$ represents the source term. Due to the fact that no initial values could be found through the literature for all the constituents that play a role in collagen and elastin turnover in the skin, it was decided that the relative quantities, ρ^{rel}, be used to describe the constituent evolution, where the relative quantities are the current values normalised by the the value at time $t = 0$, ρ^{*}:

$$\rho^{\text{rel}} = \frac{\rho}{\rho^{*}}. \tag{10.2}$$

This further avoids any dimensional and scale issues. Accurate initial values are also not of concern as the relative initial value is always 1.

An ageing model will attempt to replicate the process as depicted in Fig. 3.3 with ROS as the independent variable driving the evolution equations. The primary factors that are dependent on ROS as a driving factor are $TGF-\beta$ and TIMP. $TGF-\beta$ levels have been found to increase with ROS accumulation in the extracellular matrix while TIMP levels show a decline with ROS accumulation within the fibroblast cells, thus the source terms are given by

$$\mathcal{R}_{TGF} = \frac{\gamma^{+}_{TGF}}{\tau^{+}_{TGF}} \left[\frac{\rho^{max}_{TGF} - \rho^{\text{rel}}_{TGF}}{\rho^{max}_{TGF} - 1} \right]^{n_{TGF}} (\rho^{\text{rel}}_{ROS} - 1).$$

$$\mathcal{R}_{TIMP} = \frac{\gamma^{-}_{TIMP}}{\tau^{-}_{TGF}} \left[\frac{\rho^{\text{rel}}_{TIMP} - \rho^{min}_{TIMP}}{1 - \rho^{min}_{TIMP}} \right]^{m_{TIMP}} (\rho^{\text{rel}}_{ROS} - 1).$$

Additionally, through ROS and TIMP evolution, MMP levels will be affected. In order to simplify and reduce the number of the equations, the dependence on AP-1 as a governing factor in MMP turnover is absorbed into the dependence on ROS yielding a source term for MMP as

$$\begin{aligned} \mathcal{R}_{MMP} =& \frac{\gamma^{-}_{MMP}}{\tau^{-}_{MMP}} \left[\frac{\rho^{max}_{MMP} - \rho^{\text{rel}}_{MMP}}{\rho^{max}_{MMP} - 1} \right]^{m_{MMP}} (\rho^{\text{rel}}_{TIMP} - 1) \\ &+ \frac{\gamma^{+}_{MMP}}{\tau^{+}_{MMP}} \left[\frac{\rho^{max}_{MMP} - \rho^{\text{rel}}_{MMP}}{\rho^{max}_{MMP} - 1} \right]^{n_{MMP}} (\rho^{\text{rel}}_{ROS} - 1). \end{aligned}$$

Through a combination of the above, the relative collagen and elastin mass densities are given as:

$$\begin{aligned} \mathcal{R}_{col} =& \frac{\gamma^{-}_{col}}{\tau^{-}_{col}} \left[\frac{\rho^{\text{rel}}_{col} - \rho^{min}_{col}}{1 - \rho^{min}_{col}} \right]^{m_{col}} (\rho^{\text{rel}}_{MMP} - 1) \\ &+ \frac{\gamma^{+}_{col}}{\tau^{+}_{col}} \left[\frac{\rho^{max}_{col} - \rho^{\text{rel}}_{col}}{\rho^{max}_{col} - 1} \right]^{n_{col}} (\rho^{\text{rel}}_{TGF} - 1). \end{aligned} \tag{10.3}$$

$$\begin{aligned} \mathcal{R}_{elas} =& \frac{\gamma^{-}_{elas}}{\tau^{-}_{elas}} \left[\frac{\rho^{\text{rel}}_{elas} - \rho^{min}_{elas}}{1 - \rho^{min}_{elas}} \right]^{m_{elas}} (\rho^{\text{rel}}_{MMP} - 1) \\ &+ \frac{\gamma^{+}_{elas}}{\tau^{+}_{elas}} \left[\frac{\rho^{max}_{elas} - \rho_{elas}}{\rho^{max}_{elas} - 1} \right]^{n_{elas}} (\rho^{\text{rel}}_{TGF} - 1). \end{aligned} \tag{10.4}$$

It is necessary to introduce a further evolution equation in order to capture the reduction in collagen sensitivity to TGF-β. This can be done through a ROS dependent modification to γ^{+}_{col} through:

$$\mathcal{R}_{\gamma^{+}_{col}} = \frac{\gamma^{-}_{\gamma_{col}}}{\tau^{-}_{\gamma_{col}}} (\rho^{\text{rel}}_{ROS} - 1).$$

The parameter interpretations are as given in Table 10.2. τ has been introduced as an adaption speed parameter to allow for control over the reaction speed of one constituent realtive to another as well as ensuring dimensional consistency. The terms in the square brackets ensure that the relative constituent

Parameter	Symbol	Units
TGF-β sensitivity to ROS	$\gamma^{+}_{TGF-\beta}$	-
TIMP sensitivity to ROS	γ^{-}_{TIMP}	-
MMP sensitivity to TIMP	γ^{-}_{MMP}	-
MMP sensitivity to ROS	γ^{+}_{MMP}	-
Collagen sensitivity to TGF-β	γ^{+}_{col}	-
Collagen sensitivity to MMP	γ^{-}_{col}	-
Elastin sensitivity to TGF-β	γ^{+}_{elas}	-
Elastin sensitivity to MMP	γ^{-}_{elas}	-
m, n	nonlinear remodelling	-
τ	Adaption speed	years
ρ^{max}	Constituent relative maximum	-
ρ^{min}	Constituent relative minimum	-

Table 10.2: Evolution equation parameters.

amounts do not exceed or drop below any physical maximum, ρ^{max}, or minimum, ρ^{min} amounts.

Through the literature, it has been consistently found that the characteristics common to chronological ageing begin to manifest at around 40 years of age. Within the first four decades, ROS levels are relatively stable, where ROS production is balanced through oxidative defence. Thereafter, due to decline in the oxidative defence capabilities of the skin, ROS levels have been shown to gradually increase, with levels up to 4 times greater in aged skin compared to young skin.

As a simple model, a relative ROS evolution is proposed as depicted in Fig. 10.1 and governed by Eq. (10.5). ROS is chosen to remain stable until age 35 where it increases linearly with age according to

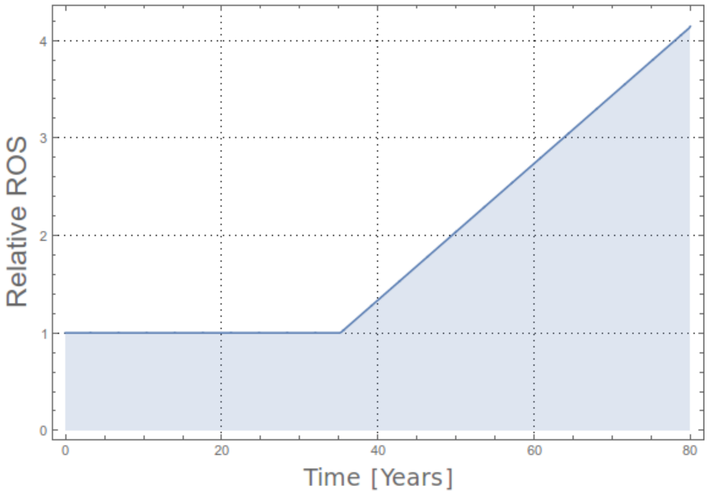

Fig. 10.1: Relative ROS evolution with time.

$$\rho^{\text{rel}}_{ROS} = \begin{cases} 1, \text{ if } t \leq 35 \\ 0.1(t-35)+1, \text{ if } t > 35 \end{cases} , \tag{10.5}$$

The parameter values are as give in Table 10.3. All τ values were set to 1 year and the nonlinear remodelling factors m and n were set to 0.8. Values for the relative minimum and maximum values of the various constituents were determined from various sources through the literature, as discussed in Chapters 3 and 8. Where values could not be found, intuitive values were proposed to replicate the expected constituent response. Without any evolution data from actual experiments with which to calibrate the equations, the proposed sensitivity parameters are again merely intuitive values with which to provide a “proof of concept”.

Parameter	Value
$\gamma^{+}_{TGF-\beta}$	0.005
γ^{-}_{TIMP}	-0.005
γ^{-}_{MMP}	-0.02
γ^{+}_{MMP}	0.1
γ^{+}_{col}	0.005
γ^{-}_{col}	-0.02
γ^{+}_{elas}	0.005
γ^{-}_{elas}	-0.01
$\gamma^{-}_{\gamma_{col}}$	-0.00003
$\rho^{max}_{TGF-\beta}$	4
ρ^{min}_{TIMP}	0.7
ρ^{max}_{MMP}	4
ρ^{max}_{col}	1.5
ρ^{min}_{col}	0.5
ρ^{max}_{elas}	3
ρ^{min}_{elas}	0.8

Table 10.3: Evolution equation parameter values.

In Fig. 10.2a, Fig. 10.2b and Fig. 10.2c the evolution of TGF-β, TIMP and MMP are depicted, respectively. Within the first simulated 35 years, there is no change in the relative amounts of each. Thereafter, there is a gradual decline in the level of TIMP while MMP and TGF-β increase, as understood from research. In Fig. 10.2d, the sensitivity of collagen to TGF-β is reduced through a decline in γ^{+}_{col}.

Through dependence on MMP and TGF-β, collagen and elastin levels decline as depicted in Fig. 10.3 and Fig. 10.4, respectively. As mentioned in Chapter 8, collagen has been shown to decline with age to approximately half the amount when compared to younger skin. As captured in Fig. 10.3, despite the increase in TGF-β, the combination of increased MMP and reduced TGF-β sensitivity results in the relative amount of collagen declining toward the proposed relative minimum. As the relative minimum of 0.5 is approached, the rate of collagen degradation decreases. The evolution of elastin mimics that of collagen, although due to the inherently stable nature of elastin, the relative loss of elastin is not as severe.

Fig. 10.2 - Fig. 10.4 provide an example of the evolution profile of the various constituents that have been identified to play a role in the ageing process. With this, it is essential to link the evolution of collagen and elastin back to the mechanical model. In order to accomplish this, inspiration is taken from that of the theory of *constrained mixtures.*

Constrained mixture theory involves the recognition that evolving constituent composition and organisation are innately linked to the overall mechanical behaviour of soft tissue. The primary idea behind a constrained mixture formulation is to pay attention to the individual constituents within a tissue

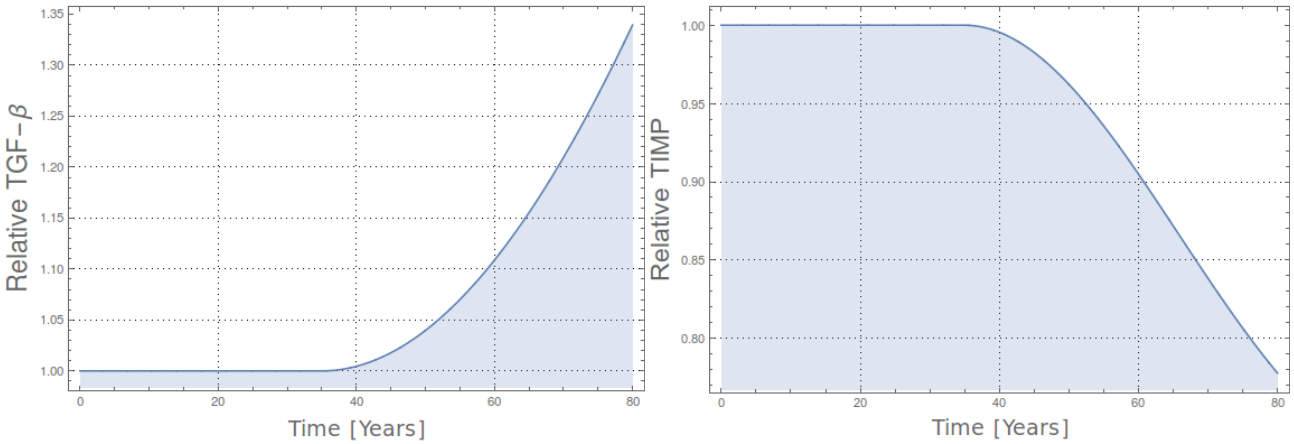

(a) Simulated TGF-β evolution with time.

(b) Simulated TIMP evolution with time.

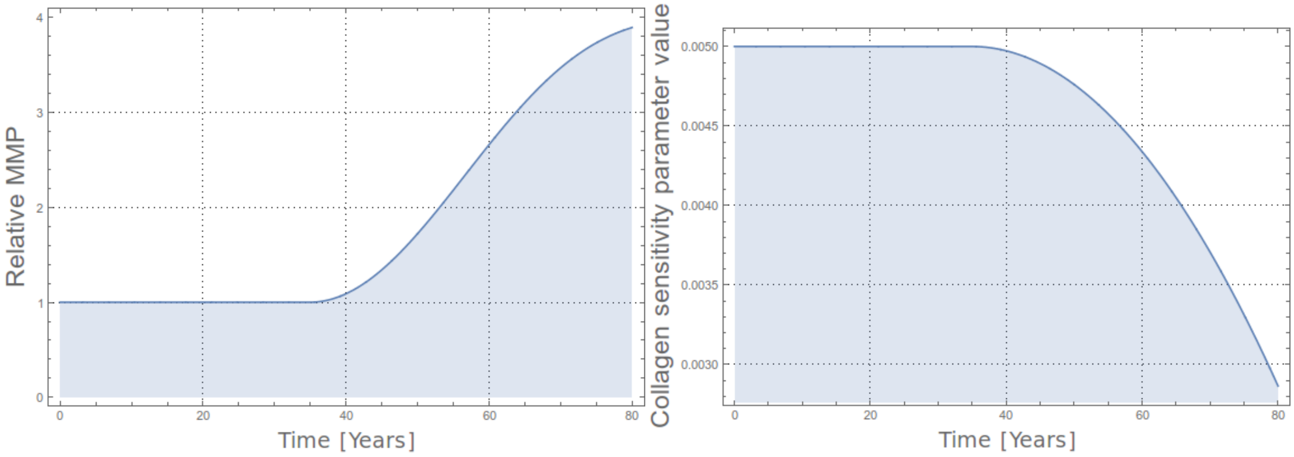

(c) Simulated MMP evolution with time.

(d) Simulated γ_{col}^{+} evolution with time.

Fig. 10.2: Evolution of nano-constituents TGF-β, TIMP and MMP according to evolution equations.

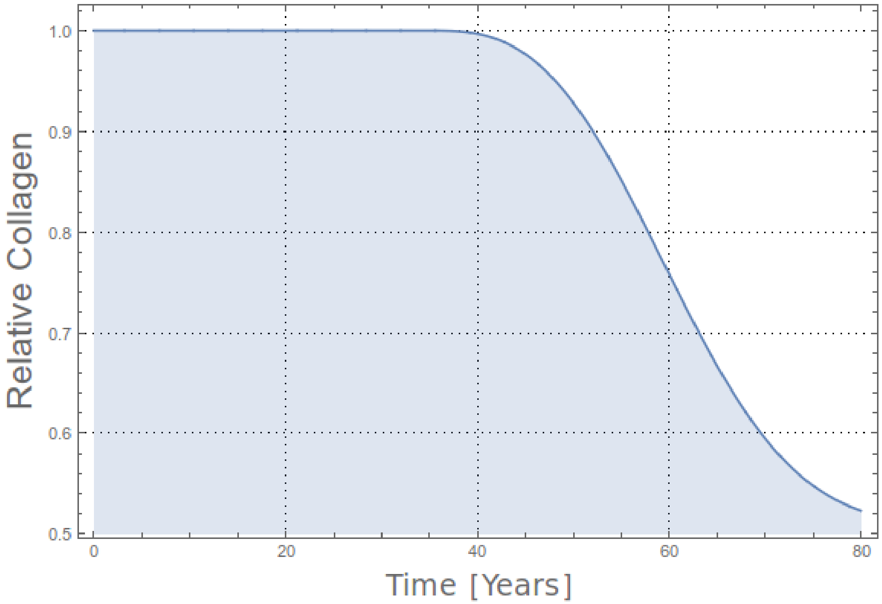

Fig. 10.3: Evolution of collagen with time.

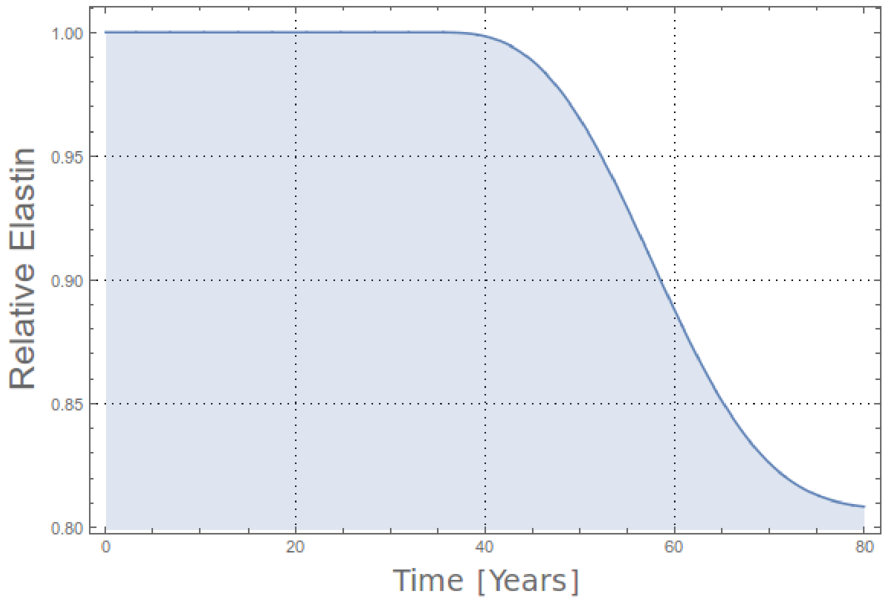

Fig. 10.4: Evolution of elastin with time.

through accounting for the turnover rates of the constituents of interest, rather than focus on the overall change of the tissue. Through the literature, it has been found that continuum-based mixture theory is highly applicable within the context of growth and remodelling models. Here, a full mixture theory is not proposed, but for a detailed overview, the reader is referred to Humphrey and Rajagopal (2003); Rouhi et al. (2007); Valentín and Holzapfel (2012); Valentín and Humphrey (2009); Valentín et al. (2011).

Denoting $\rho^{\mathrm{k}}(s)$ as the mass density of constituent k at time s, the free energy can accordingly be proposed as a function of the constituent mass densities,

$$\Psi = \Psi(\mathbf{F}, \rho^{\mathrm{k}}(s)).$$

This form follows a general rule of mixtures where weighted contributions are used to predict the mean response of a composite material. This is given as,

$$\Psi(\mathbf{F}, \rho^{\mathrm{k}}(s)) = \sum_{k} \frac{\rho^{\mathrm{k}}(s)}{\rho(s)} \Psi^{\mathrm{k}},$$

where $\rho(s) = \sum_k \rho^{\mathrm{k}}(s)$ and Ψ^{k} is the free energy contribution of constituent k. $\rho(s)$ is generally assumed to be constant (Valentín et al., 2011). Each constituent mass density $\rho^{\mathrm{k}}(s)$ can thus be allowed to adapt in time according to some stimulus. Evolution equations for each constituent can be proposed, in a manner similar to that proposed for the the contituent evolutions in in Sec. 10.2.1.

With this in mind, an adjusted model is proposed. As an extension to Eq. (5.1), each constituent free energy is weighted by a corresponding relative mass density (Eq. (10.2)),

$$\Psi = \rho^{\mathrm{rel}}_{gs} \Psi_{\mathrm{gs}} + \rho^{\mathrm{rel}}_{elas} \Psi_{\mathrm{elas}} + \rho^{\mathrm{rel}}_{col} \Psi_{\mathrm{col}}. \tag{10.6}$$

The choice of using relative density weightings is motivated by the idea that in the absence of constituent remodelling Eq. (10.6) reduces to Eq. (5.1). Eq. (10.3) and Eq. (10.4) can be used as evolution equations for the relative collagen and elastin contributions, respectively, while ρ^{rel}_{gs} evolves to ensure the overall density remains constant[1].

---

[1] $\rho^{\mathrm{rel}}|_{t=0} = \rho^{\mathrm{rel}}_{gs}|_{t=0} + \rho^{\mathrm{rel}}_{elas}|_{t=0} + \rho^{\mathrm{rel}}_{col}|_{t=0} = 3$
$\rho^{\mathrm{rel}}_{gs} = 3 - \rho^{\mathrm{rel}}_{elas} - \rho^{\mathrm{rel}}_{col}$

As mentioned, the model as presented in Eq. (5.1) does not have a natural connection to the amount of collagen and elastin present in the skin. This extension addresses this issue. Additionally, with the form of the collagen free energy as presented in Eq. (5.8), this allows γ_{chn} to be a representation of the level of crosslinking within the collagen network.

Beyond the use of open-system thermodynamics and mixture theory, more complex homogenisation schemes could be considered. Such schemes offer a means by which to average the properties of the micro-scale to model the macroscopic response, which would be particularly applicable within the context of the current presentation (Kouznetsova et al., 2001; Miehe, 2003; Miehe and Koch, 2002).

10.2.3 A Model for Photoageing

In Chapter 3 photoageing was presented as a processes that not only compounds the effects of chronological ageing, but often induces structural changes more severe than that observed under normal ageing. Due to this, the extension of the a mixture-type model to a one that accounts for photoageing is a logical next step.

From Fig. 3.3, the processes involved in chronological and photoageing are very similar, which makes the extension to account for photoageing a very natural one. The primary difference is the formation of what is referred to as elastotic tissue, which is similar to elastic tissue but highly disorganised and irregular. Thus a simple extension would be

$$\Psi = \rho_{\mathrm{gs}}^{\mathrm{rel}}\Psi_{\mathrm{gs}} + \rho_{\mathrm{elas}}^{\mathrm{rel}}\Psi_{\mathrm{elas}} + \rho_{\mathrm{col}}^{\mathrm{rel}}\Psi_{\mathrm{col}} + \rho_{\mathrm{elastotic}}^{\mathrm{rel}}\Psi_{\mathrm{elastotic}},$$

where $\Psi_{\mathrm{elastotic}}$ is an elastotic free energy. The form of $\Psi_{\mathrm{elastotic}}$ could be similar to that of that presented for the elastin free energy, but experimental data would be needed to make an informed decision.

The process would similarly be driven by ROS generation, where ROS would take on a form such as

$$ROS = ROS_{\mathrm{chrono}} + ROS_{\mathrm{UV}}$$

where ROS_{chrono} and ROS_{UV} are the ROS generated by the chronological and UV-exposure, respectively. ROS_{chrono} would take on a form as in Eq. (10.5) whereas ROS_{UV} would be motivated by Fig. 10.5 which shows the UVA doses at Sophia Antipolis in the south of France over a two year period (Rigel et al., 2004). Due to the elliptical nature of the orbit of the earth around the sun, the distance between the sun and the earth varies over the course of a year. Therefore intensity of UVR varies accordingly. In addition to this, geographical location and elevation play crucial roles in the amount of UVR exposure, which would need to be considered within a photoageing model.

The evolution equations for TGF-β, TIMP and MMP would accordingly need to include terms dependent on ROS_{UV}. Additionally, an evolution equation for elastotic tissue would need to be proposed which would be very similar to that of the elastin evolution equation, Eq. (10.4). Through this framework, photoageing could be accounted for.

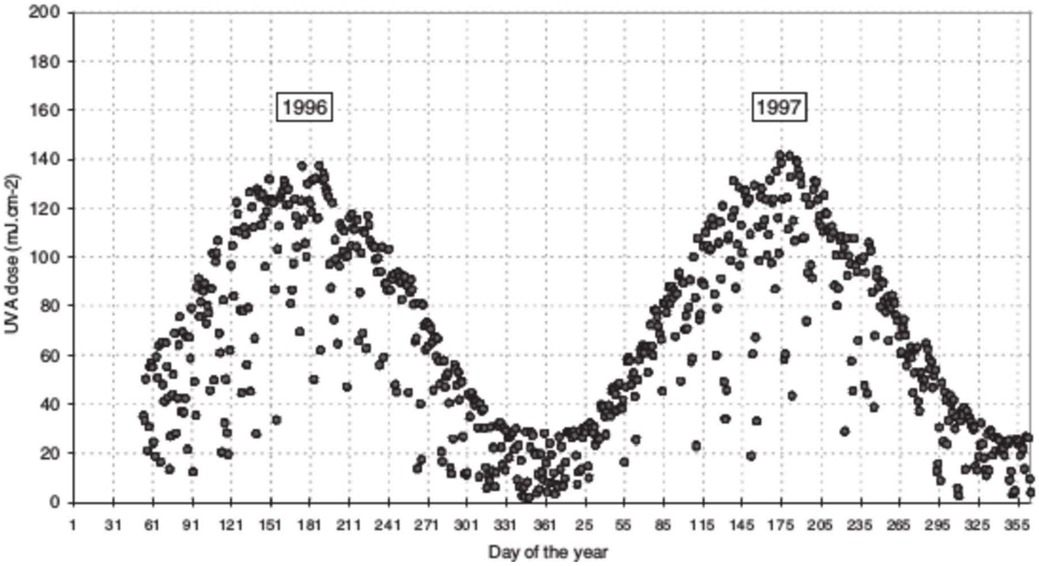

Fig. 10.5: UVA dose over a two year period at Sophia Antipolis in the south of France, extracted from Rigel et al. (2004)

References

Agache, P. G., Monneur, C., Leveque, J. L., Rigal, d. J., 1980. Mechanical properties and Young's modulus of human skin in vivo. *Archives of Dermatological Research* 269, 221–232.

Alastrué, V., Rodríguez, J. F., Calvo, B., Doblaré, M., 2007. Structural damage models for fibrous biological soft tissues. *International Journal of Solids and Structures* 44 (18-19), 5894–5911.

Alexander, H., Cook, T., 2006. Variations with age in the mechanical properties of human skin in vivo. *Journal of Tissue Viability* 16 (3), 6–11.

Arruda, E. M., Boyce, M. C., 1993. A three-dimensional constitutive model for the large stretch behavior of rubber elastic materials. *Journal of the Mechanics and Physics of Solids* 41, 389–412.

Bailey, A. J., 2001. Molecular mechanisms of ageing in connective tissues. *Mechanisms of Ageing and Development* 122, 735–755.

Bazant, Z. P., Oh, B., 1985. Microplane model for progressive fracture of concrete and rock. *Journal of Engineering Mechanics* 111 (4), 559–582.

Benedetto, A. V., 1998. The environment and skin aging. *Clinics in Dermatology* 16 (1), 129–139.

Bernstein, E. F., Chen, Y. Q., Kopp, J. B., Fisher, L., Brown, D. B., Hahn, P. J., Robey, F. a., Lakkakorpi, J., Uitto, J., 1996. Long-term sun exposure alters the collagen of thepapillary dermis. *Journal of the American Academy of Dermatology* 34 (2), 209–218.

Bernstein, E. F., Chen, Y. Q., Tamai, K., Shepley, K. J., Resnik, K. S., Zhang, H., Tuan, R., Mauviel, A., Uitto, J., 1994. Enhanced elastin and fibrillin gene expression in chronically photodamaged skin. *The Journal of Investigative Dermatology* 103 (2), 182–186.

Bischoff, J. E., Arruda, E. a., Grosh, K., 2002. A microstructurally based orthotropic hyperelastic constitutive law. *Journal of Applied Mechanics* 69, 570.

Bischoff, J. E., Arruda, E. M., Grosh, K., 2000. Finite element modeling of human skin using an isotropic, nonlinear elastic constitutive model. *Journal of Biomechanics* 33, 645–652.

Buganza Tepole, A., Gosain, A. K., Kuhl, E., 2012. Stretching skin: The physiological limit and beyond. *International Journal of Non-Linear Mechanics* 47, 938–949.

Choi, W. S., 2005. Involvement of TGF-beta in Skin Photoaging.

Choi, W. S., Mitsumoto, A., Kochevar, I. E., 2009. Involvement of reactive oxygen species in TGF-beta1-induced tropoelastin expression by human dermal fibroblasts. *Photochemistry and Photobiology* 85 (6), 1425–1433.

Chung, J. H., Kang, S., Varani, J., Lin, J., Fisher, G. J., Voorhees, J. J., 2000. Decreased extracellular-signal-regulated kinase and increased stress-activated MAP kinase activities in aged human skin in vivo. *Journal of Investigative Dermatology* 115 (2), 177–182.

Daly, C. H., Odland, G. F., 1979. Age-related changes in the mechanical properties of human skin. *The Journal of Investigative Dermatology* 73 (1), 84–87.

Diridollou, S., Vabre, V., Berson, M., Vaillant, L., Black, D., Lagarde, J., Gregoire, J., Gall, Y., Patat, F., 2001. Skin ageing: Changes of physical properties of human skin in vivo. *International Journal of Cosmetic Science* 23 (6), 353–362.

Escoffier, C., de Rigal, J., Rochefort, A., Vasselet, R., Lévêque, J. L., Agache, P. G., 1989. Age-related mechanical properties of human skin: an in vivo study. *The Journal of Investigative Dermatology* 93 (3), 353–357.

Fisher, G. J., Kang, S., Varani, J., Bata-Csorgo, Z., Wan, Y., Datta, S., Voorhees, J. J., 2002. Mechanisms of photoaging and chronological skin aging. *Archives of Dermatology* 138, 1462–1470.

Fligiel, S. E. G., Varani, J., Datta, S. C., Kang, S., Fisher, G. J., Voorhees, J. J., 2003. Collagen degradation in aged/photodamaged skin in vivo and after exposure to matrix metalloproteinase-1 in vitro. *Journal of Investigative Dermatology* 120 (5), 842–848.

Flynn, C., McCormack, B. A. O., 2010. Simulating the wrinkling and aging of skin with a multi-layer finite element model. *Journal of Biomechanics* 43 (3), 442–448.

Fung, Y. C., 1974. Biorheology of loose connective yissues, especially blood vessels. Springer Berlin Heidelberg, Berlin, Heidelberg, pp. 191–210.

Garikipati, K., Arruda, E. M., Grosh, K., Narayanan, H., Calve, S., 2004. A continuum treatment of growth in biological tissue: the coupling of mass transport and mechanics. *Journal of the Mechanics and Physics of Solids* 52 (7), 1595–1625.

Garikipati, K., Goktepe, S., Miehe, C., 2008. Elastica-based strain energy functions for soft biological tissue. *Journal of the Mechanics and Physics of Solids* 56 (4), 1693–1713.

Geerligs, M., 2006. In vitro mechanical characterization of human skin layers: stratum corneum, epidermis and hypodermis.

Giro, M. G., Oikarinen, A. I., Oikarinen, H., Sephel, G., Uitto, J., Davidson, J., 1985. Demonstration of elastin gene expression in human skin fibroblast cultures and reduced tropoelastin production by cells from a patient with atrophoderma. *The Journal of Clinical Investigation* 75, 672–678.

Green, E. M., Mansfield, J. C., Bell, J. S., Winlove, C. P., 2014. The structure and micromechanics of elastic tissue. *Interface focus* 4 (2), 20130058.

Griffiths, C., Russman, A., Majmudarm, G., Singer, R., Hamilton, T., Voorhees, J., 1993. Restoration of collagen formation in photodamaged human skin by tretinoin (retinoic acid). *New England Journal of Medicine* 328 (15), 1092–1096.

Harbour MedTech, 2016. The BriDGE Process - Creating a Stabalized Acellular Collagen Matrix. `www.harbormedtech.com/bridge,[Online;accessed-October-2016].`

Hekimi, S., Lapointe, J., Wen, Y., 2011. Taking a “good” look at free radicals in the aging process. *Trends in Cell Biology* 21 (10), 569–576.

Helfrich, Y. R., Sachs, D. L., Voorhees, J. J., 2008. Overview of skin aging and Photoaging. *Dermatology Nursing* 20 (3), 177–183.

Hendriks, F. M., Brokken, D., Oomens, C. W. J., Bader, D. L., Baaijens, F. P. T., 2006. The relative contributions of different skin layers to the mechanical behavior of human skin in vivo using suction experiments. *Medical Engineering and Physics* 28 (3), 259–266.

Hendriks, F. M., Brokken, D., van Eemeren, J. T. W. M., Oomens, C. W. J., Baaijens, F. P. T., Horsten, J. B. a. M., 2003. A numerical-experimental method to characterize the non-linear mechanical behaviour of human skin. *Skin Research and Technology* 9 (3), 274–283.

Henry, F., Piérard-Franchimont, C., Cauwenbergh, G., Piérard, G. E., 1997. Age-related changes in facial skin contours and rheology. *Journal of the American Geriatrics Society* 45 (2), 220–2.

Himpel, G., Kuhl, E., Menzel, A., Steinmann, P., 2005. Computational modelling of isotropic multiplicative growth. *CMES - Computer Modeling in Engineering and Sciences* 8 (2), 119–134.

Holzapfel, G. A., 2000. Nonlinear Solid Mechanics: A Continuum Approach for Engineering. John Wiley & Sons Ltd.

Humphrey, J. D., Rajagopal, K. R., 2003. A constrained mixture model for arterial adaptations to a sustained step change in blood flow. *Biomechanics and Modeling in Mechanobiology* 2 (2), 109–126.

Ibbotson, S. H., Moran, M. N., Nash, J. F., Kochevar, I. E., 1999. The effects of radicals compared with UVB as initiating species for the induction of chronic cutaneous photodamage. *Journal of Investigative Dermatology* 112 (6), 933–938.

Imokawa, G., Ishida, K., 2015. Biological mechanisms underlying the ultraviolet radiation-induced formation of skin wrinkling and sagging I: reduced skin elasticity, highly associated with enhanced dermal elastase activity, triggers wrinkling and sagging. *International Journal of Molecular Sciences* 16 (4), 7753–7775.

Jacobs, C. R., Levenston, M. E., Beaupré, G. S., Simo, J. C., Carter, D. R., 1995. Numerical instabilities in bone remodeling simulations: The advantages of a node-based finite element approach. *Journal of Biomechanics* 28 (4), 449–459.

Jacobs, C. R., Simo, J. C., Beaupré, G. S., Cartert, D. R., 1997. Adaptive bone remodeling incorporating simultaneous density and anisotropy considerations. *Journal of Biomechanics* 30 (96), 603–613.

Jenkins, G., 2002. Molecular mechanisms of skin aging. *Mechanisms of Ageing and Development* 123 (7), 801–810.

Jeyapalan, J. C., Sedivy, J. M., 2008. Cellular senescence and organismal aging. *Mechanisms of Ageing and Development* 129 (7-8), 467–474.

Kawaguchi, Y., Tanaka, H., Okada, T., Konishi, H., Takahashi, M., Ito, M., Asai, J., 1997. Effect of reactive oxygen species on the elastin mRNA expression in cultured human dermal fibroblasts. *Free Radical Biology & Medicine* 23 (1), 162–165.

Korelc, J., Wriggers, P., 2016. Automation of finite element methods. Springer, Switzerland.

Korlec, J., 2015. AceGen and AceFEM user manual. `http://symech.fgg.uni-lj.si,[Online; accessed-June-2015]`.

Kossodo, S., Wong, W.-R., Simon, G., Kochevar, I. E., 2004. Effects of UVR and UVR-induced cytokines on production of extracellular matrix proteins and proteases by dermal fibroblasts cultured in collagen gels. *Photochemistry and Photobiology* 79 (1), 86–93.

Kouznetsova, V., Brekelmans, W. A. M., Baaijens, F. P. T., 2001. Approach to micro-macro modeling of heterogeneous materials. *Computational Mechanics* 27 (1), 37–48.

Kratky, O., Porod, G., 1949. Röntgenuntersuchung gelöster fadenmoleküle. *Recueil des Travaux Chimiques des Pays-Bas* 68 (12), 1106–1122.

Kucich, U., Rosenbloom, J. C. J., Abrams, W. R., 2002. Transforming growth factor-beta stabilizes elastin mRNA by a pathway requiring active Smads, protein kinase C-delta, and p38. *American Journal of Respiratory Cell and Molecular Biology* 26 (2), 183–8.

Kuhl, E., Garikipati, K., Arruda, E. M., Grosh, K., 2005. Remodeling of biological tissue: Mechanically induced reorientation of a transversely isotropic chain network. *Journal of the Mechanics and Physics of Solids* 53, 1552–1573.

Kuhl, E., Holzapfel, G. A., 2007. A continuum model for remodeling in living structures. *Journal of Materials Science* 42 (21), 8811–8823.

Kuhl, E., Menzel, a., Steinmann, P., 2003. Computational modeling of growth. A critical review, a classification of concepts and two new consistent approaches. *Computational Mechanics* 32 (1-2), 71–88.

Kuhl, E., Steinmann, P., 2003. Theory and numerics of geometrically non-linear open system mechanics. *International Journal for Numerical Methods in Engineering* 58 (11), 1593–1615.

Kuhn, W., Grün, F., 1942. Beziehungen zwischen elastischen konstanten und dehnungsdoppelbrechung hochelastischer stoffe. *Kolloid-Zeitschrift* 101 (3), 248–271.

Kulbitska, V., 2015. Loose connective Tissues. `http://intranet.tdmu.edu.ua/data/kafedra/internal/histolog/classes_stud,[Online;accessed-February-2016]`.

Lafortune, P., Aris, R., 2015. Computational model of collagen turnover in carotid arteries during hypertension. *International Journal for Numerical Methods in Biomedical Engineering* 28 (1), 72–86.

Langer, K., 1861. On the anatomy and physiology of the skin - II. Skin tension. *British Journal of Plastic Surgery* 31, 93–106.

Lanir, Y., Fung, Y., 1974. Two-dimensional mechanical properties of rabbit skin II. Experimental results. *Journal of Biomechanics* 7 (2), 171–182.

Lapeer, R. J., Gasson, P. D., Karri, V., 2010. Simulating plastic surgery: From human skin tensile tests, through hyperelastic finite element models to real-time haptics. *Progress in Biophysics and Molecular Biology* 103 (2-3), 208–216.

Leveque, J. L., de Rigal, J., Agache, P. G., Monneur, C., 1980. Influence of ageing on the in vivo extensibility of human skin at a low stress. *Archives of Dermatological Research* 269 (2), 127–135.

Levi, K., 2009. Biomechanics of human stratum corneum: dry skin conditions, tissue damage and alleviation. Ph.D. thesis.

Limbert, G., 2011. A mesostructurally-based anisotropic continuum model for biological soft tissues-Decoupled invariant formulation. *Journal of the Mechanical Behavior of Biomedical Materials* 4 (8), 1637–1657.

Limbert, G., 2014. State-of-the-art constitutive models of skin biomechanics. In: Querleux, B. (Ed.), Computational Biophysics of the Skin. p. 558.

Limbert, G., Taylor, M., Middleton, J., 2004. Three-dimensional finite element modelling of the human ACL: Simulation of passive knee flexion with a stressed and stress-free ACL. *Journal of Biomechanics* 37 (11), 1723–1731.

López-Otín, C., Blasco, M. A., Partridge, L., Serrano, M., Kroemer, G., 2013. The hallmarks of aging.

Marko, J. F., Siggia, E. D., 1995. Stretching DNA. *Macromolecules* 28 (26), 8759–8770.

Marsden, J. E., Hughes, T. J. R., Carlson, D. E., 1984. Mathematical foundations of elasticity. Vol. 51.

Mathworks, 2014. Wolfram Mathematica. `www.mathworks.com,[Online;accessed-September-2015]`.

McBride, A., Bargmann, S., Pond, D., Limbert, G., 2016. Thermoelastic modelling of the skin at finite deformations. *Journal of Thermal Biology* 62, 201–209.

Mecham, R. P., 1991. Elastin synthesis and fiber assembly. *Annals of the New York Academy of Sciences* 624, 137–46.

Mecham, R. P., Broekelmann, T. J., Fliszar, C. J., Shapiro, S. D., Welgus, H. G., Senior, R. M., 1997. Elastin degradation by matrix metalloproteinases. *Journal of Biological Chemistry* 272 (29), 18071–18076.

Menzel, A., Kuhl, E., 2012. Frontiers in growth and remodeling. *Mechanics Research Communications* 42, 1–14.

Merker, K., Sitte, N., Grune, T., 2000. Hydrogen peroxide-mediated protein oxidation in young and old human MRC-5 fibroblasts. *Archives of Biochemistry and Biophysics* 375 (1), 50–54.

Miehe, C., 2003. Computational micro-to-macro transitions for discretized micro-structures of heterogeneous materials at finite strains based on the minimization of averaged incremental energy. *Computer Methods in Applied Mechanics and Engineering* 192 (5-6), 559–591.

Miehe, C., Koch, A., 2002. Computational micro-to-macro transitions of discretized microstructures undergoing small strains. *Archive of Applied Mechanics* 72 (4-5), 300–317.

Oomens, C. W., van Campen, D. H., Grootenboer, H. J., 1987. In vitro compression of a soft tissue layer on a rigid foundation. *Journal of Biomechanics* 20 (10), 923–935.

Oxlund, H., Andreassen, T. T., 1980. The roles of hyaluronic acid, collagen and elastin in the mechanical properties of connective tissues. *Journal of Anatomy* 131 (4), 611–20.

Oxlund, H., Manschot, J., Viidik, A., 1988. The role of elastin in the mechanical properties of skin. *Journal of Biomechanics* 21 (3), 213–218.

Pailler-Mattei, C., Bec, S., Zahouani, H., 2008. In vivo measurements of the elastic mechanical properties of human skin by indentation tests. *Medical Engineering and Physics* 30 (5), 599–606.

Pawlaczyk, M., Lelonkiewicz, M., Wieczorowski, M., 2013. Age-dependent biomechanical properties of the skin. *Postepy Dermatologii i Alergologii* 30 (5), 302–306.

Querleux, B. (Ed.), 2014. Computational Biophysics of the Skin. Pan Stanford Publishing.

Rabe, J. H., Mamelak, A. J., McElgunn, P. J. S., Morison, W. L., Sauder, D. N., 2006. Photoaging: Mechanisms and repair. *Journal of the American Academy of Dermatology* 55, 1–19.

Reihsner, R., Balogh, B., Menzel, E. J., 1995. Two-dimensional elastic properties of human skin in terms of an incremental model at the in vivo configuration. *Medical Engineering and Physics* 17 (4), 304–313.

Rigel, D. S., Weiss, R. A., Lim, H. W., Dover, J. S., 2004. Photoaging, 1st Edition. Marcel Dekker, Inc., New York.

Rittié, L., Fisher, G. J., 2002. UV-light-induced signal cascades and skin aging. *Ageing Research Reviews* 1, 705–720.

Rouhi, G., Epstein, M., Sudak, L., Herzog, W., 2007. Modeling bone resorbtion using mixture theory with chemical reactions. *Mechanics of Materials and Structures* 2 (6), 1141–1155.

Ruvolo Jr. E, C., Stamatas G, N., N, K., 2007. Skin viscoelasticity displays site- and age-dependent angular anisotropy. *Skin Pharmacology and Physiology* 20 (6), 313–321.

Saez, P., Peña, E., Martínez, M. A., Kuhl, E., 2013a. Computational modeling of hypertensive growth in the human carotid artery. *Computational Mechanics* 53 (6), 1183–1196.

Saez, P., Peña, E., Martínez, M. A., Kuhl, E., 2013b. Mathematical modeling of collagen turnover in biological tissue. *Journal of Mathematical Biology* 67 (6-7), 1765–1793.

Sanders, R., 1973. Torsional elasticity of human skin in vivo. *Pflügers Arch* 342, 255–260.

Scharffetter-Kochanek, K., Brenneisen, P., Wenk, J., Herrmann, G., Ma, W., Kuhr, L., Meewes, C., Wlaschek, M., 2000. Photoaging of the skin from phenotype to mechanisms. *Experimental Gerontology* 35 (3), 307–316.

Sephel, G. C., Davidson, J. M., 1986. Elastin production in human skin fibroblast cultures and its decline with age. *The Journal of Investigative Dermatology* 86 (3), 279–85.

Sherratt, M. J., 2009. Tissue elasticity and the ageing elastic fibre. *Age* 31 (4), 305–325.

Silver, F. H., Freeman, J. W., DeVore, D., 2001. Viscoelastic properties of human skin and processed dermis. *Skin Research and Technology* 7 (1), 18–23.

Silver, F. H., Kato, Y. P., Wasserman, A. J., 1992. Analysis of mammalian connective tissue: relationship between hierarchical structures and mechanical properties. *Journal of Long-term Effects of Medical Implants* 2 (2-3), 165–198.

Silver, F. H., Seehra, G. P., Freeman, J. W., DeVore, D., 2002. Viscoelastic properties of young and old human dermis: A proposed molecular mechanism for elastic energy storage in collagen and elastin. *Journal of Applied Polymer Science* 86 (8), 1978–1985.

Snedeker, J. G., Gautieri, A., 2014. The role of collagen crosslinks in ageing and diabetes - the good, the bad, and the ugly. *Muscles, Ligaments and Tendons Journal* 4 (3), 303–8.

Steinmann, P., Hossain, M., Possart, G., 2012. Hyperelastic models for rubber-like materials: Consistent tangent operators and suitability for Treloar's data. *Archive of Applied Mechanics* 82 (9), 1183–1217.

Tonge, T. K., Atlan, L. S., Voo, L. M., Nguyen, T. D., 2013a. Full-field bulge test for planar anisotropic tissues: Part I-Experimental methods applied to human skin tissue. *Acta Biomaterialia* 9 (4), 5913–5925.

Tonge, T. K., Voo, L. M., Nguyen, T. D., 2013b. Full-field bulge test for planar anisotropic tissues: Part II-A thin shell method for determining material parameters and comparison of two distributed fiber modeling approaches. *Acta Biomaterialia* 9 (4), 5926–5942.

Tregear, R. T., 1969. The mechanical properties of skin. *Journal of the Society of Cosmetic Chemists* 20, 467–477.

Treloar, L. R. G., 1944. Stress-strain data for vulcanised rubber under various types of deformation. *Rubber Chemistry and Technology* 17 (4), 813–825.

Uitto, J., 2008. The role of elastin and collagen in cutaneous aging: intrinsic aging versus photoexposure. *Journal of Drugs in Dermatology* 7 (2), 12–16.

Valentín, A., Holzapfel, G., 2012. Constrained mixture models as tools for testing competing hypothesis in arterial biomechanics: Survey. *Mechanics Research Communications* 29, 126–133.

Valentín, a., Humphrey, J. D., 2009. Evaluation of fundamental hypotheses underlying constrained mixture models of arterial growth and remodelling. *Philosophical transactions of the Royal Society A* 367 (1902), 3585–606.

Valentín, A., Humphrey, J. D., Holzapfel, G. A., 2011. A multi-layered computational model of coupled elastin degradation, vasoactive dysfunction, and collagenous stiffening in aortic aging. *Annals of Biomedical Engineering* 39 (7), 2027–2045.

Varani, J., 2010. Fibroblast aging: Intrinsic and extrinsic factors. *Drug Discovery Today: Therapeutic Strategies* 7 (3-4), 65–70.

Varani, J., Dame, M. K., Rittie, L., Fligiel, S. E. G., Kang, S., Fisher, G. J., Voorhees, J. J., 2006. Decreased collagen production in chronologically aged skin: roles of age-dependent alteration in fibroblast function and defective mechanical stimulation. *The American Journal of Pathology* 168 (6), 1861–1868.

Varani, J., Spearman, D., Perone, P., Fligiel, S. E., Datta, S. C., Wang, Z. Q., Shao, Y., Kang, S., Fisher, G. J., Voorhees, J. J., 2001. Inhibition of type I procollagen synthesis by damaged collagen in photoaged skin and by collagenase-degraded collagen in vitro. *The American Journal of Pathology* 158 (3), 931–942.

Vexler, A., Polyansky, I., Gorodetsky, R., 1999. Evaluation of skin viscoelasticity and anisotropy by measurement of speed of shear wave propagation with viscoelasticity skin analyzer. *Journal of Investigative Dermatology* 113 (5), 732–739.

Vogel, H. G., 1981. Directional variations of mechanical parameters in rat skin depending on maturation and age. *The Journal of Investigative Dermatology* 76 (6), 493–497.

Waffenschmidt, T., Menzel, A., Kuhl, E., 2012. Anisotropic density growth of bone - A computational micro-sphere approach. *International Journal of Solids and Structures* 49 (14), 1928–1946.

Wang, H., Kochevar, I. E., 2005. Involvement of UVB-induced reactive oxygen species in TGF-beta biosynthesis and activation in keratinocytes. *Free Radical Biology and Medicine* 38, 890–897.

Wolfram, 2016. Wolfram Mathematica. `/www.wolfram.com/mathematica,[Online; accessed-June-2015]`.

Xu, F., Lu, T., 2011. Introduction to Skin Biothermomechanics and Thermal Pain. Springer, Heidelberg.

Xu, F., Lu, T. J., Seffen, K. a., 2008. Biothermomechanics of skin tissues. *Journal of the Mechanics and Physics of Solids* 56, 1852–1884.